PARAMETRIC MODEL ORDER REDUCTION DEVELOPMENT FOR NAVIER-STOKES EQUATIONS FROM 2D CHAOTIC TO 3D TURBULENT FLOW PROBLEMS

BY

PING-HSUAN TSAI

DISSERTATION

Submitted in partial fulfillment of the requirements
for the degree of Doctor of Philosophy in Computer Science
in the Graduate College of the
University of Illinois Urbana-Champaign, 2023

Urbana, Illinois

Doctoral Committee:

Professor Paul Fischer, Chair
Professor Luke Olson
Associate Professor Edgar Solomonik
Professor Anthony Patera, MIT

Abstract

This work presents new developments for the application of parametric model-order reduction (pMOR) for engineering thermal-fluid applications. The pMOR technique is built on a reduced order model (ROM), in which the governing thermal-fluid transport equations are approximated by a low-dimensional system of ordinary differential equations involving relatively few ($N \approx 20$–200) time-dependent unknowns. Basis functions for the ROMs are derived from high-fidelity, full-order models (FOMs) typified by large-eddy simulations (LES) or direct numerical simulations (DNS) of turbulence that involve $\mathcal{N} \approx 10^6$–10^{11} unknowns. The goal of pMOR is to track quantities of interest as a function of input parameters, such as Reynolds or Rayleigh number, without rerunning the FOM. This dissertation addresses several outstanding challenges in the application of pMOR to engineering problems, including: developing a time-averaged error indicator for thermal-fluids systems; improved stabilization strategies for ROM-based simulations of turbulence; and an efficient low-rank, symmetry-preserving, tensor decomposition for the ROM advection operator that alleviates the leading-order, $O(N^3)$, computational complexity in time-advancement of ROMs.

To my parents and my wife, for their love and support.

Acknowledgments

This work would not have been possible without the support of many people. First, I would like to thank my advisor, Prof. Paul Fischer, who mentored and guided me through my graduate studies and, at the same time, provided the freedom to pursue different ideas that culminated in this work.

I am also grateful to my Ph.D. committee for insightful comments on my preliminary thesis proposal and the final dissertation. Their feedback has been instrumental in improving my approach to writing and presenting my research and has shaped my critical thinking as a researcher.

My Ph.D. journey at the University of Illinois has also been successful due to continued support from peers and mentors whom I have interacted with. I want to thank Li, Kento, Dimitrios, Yu-Hsiang, Viral, Nick, and Thilina for providing me with insight whenever I reached out to discuss problems in their area of expertise.

And finally, thanks to my parents, friends, and my wife, who always gave their love and support.

Table of Contents

Chapter 1: Introduction

Fluid-thermal analysis plays a critical role in understanding and predicting of many important phenomena for engineering and science applications, including engine design, cooling mechanisms in nuclear reactors, fundamentals of stellar convection, and cooling of biological systems. In the early developmental phase of this discipline, rigorous mathematical models, including the Navier-Stokes equations (NSE), were established and used in conjunction with the energy transport equation to accurately represent the thermal states of the flow measured in experimental setups.

A significant challenge with the mathematical formulation is that the governing equations are nonlinear partial differential equations (PDEs) in three space dimensions and time, which makes their solution challenging to obtain, even in simple geometries. For problems involving complex geometry or with variable material properties, it is generally necessary to resort to numerical solution of the governing system of PDEs on a computer using numerical methods. At elevated Reynolds numbers, even simple configurations can require a numerical approach if the flow transitions to turbulence. Numerical discretizations, including finite difference, finite volume, finite element, and spectral methods, have been demonstrated to provide high-fidelity solutions for the NSE with geometry, properties, initial conditions, and boundary conditions relevant to engineering applications. This field, known as computational fluid dynamics (CFD), has become ubiquitous to the point that it is widely accessible by engineers.

Modern high-performance computing and numerical algorithms have significantly increased the computational capacity to solve a given CFD problem. Despite continued advances in these areas, direct numerical (DNS), large-eddy (LES), and even unsteady Reynolds-averaged Navier-Stokes (uRANS) simulations of turbulent thermal transport remain too costly for routine analysis and design of many thermal-fluid systems when hundreds of cases must be considered. With current standard practice, each simulation incurs as much expense as its predecessor, as there is no information sharing between the two calculations. Parametric model-order reduction (pMOR) is one of the promising approaches to overcome this issue and provide a rapid turn-around tool for engineering query. pMOR is designed to leverage (expensive) high-fidelity simulations, referred to as full-order models or FOMs, by extracting the principal features of the underlying flow fields and building a reduced order model (ROM) or suite of ROMs [1, 2, 3, 4, 5, 6, 7, 8]. The ROMs are used to estimate the system behavior over a range of parametric inputs (e.g., inlet flow rates, thermal loading, or Reynolds number).

While FOMs for turbulent flows can require $\mathcal{N} = 10^7 - 10^{11}$ degrees of freedom, ROMs offer the potential to represent the flow dynamics governing the behavior of quantities of interest

(QOIs) with only $N \approx 10^2$–10^3 basis functions. In this work, we focus on the Galerkin ROM (G-ROM) for the NS and energy transport equations in which the reduced bases functions are obtained from proper orthogonal decompositions (PODs) [9, 10] of the high-fidelity velocity and temperature fields.

The overall objective of *parametric model-order reduction* (pMOR) is to use the ROMs to inexpensively explore the parametric dependencies of the QOIs. To realize this goal, pMOR must address two problems: First, the ROMs must be able to solve the *reproduction problem*. That is, they must be able to accurately reproduce quantities of interest (QOIs) generated by the originating FOM. Second, they should be able to solve the *parametric problem*, in which the ROMs are used to evaluate QOIs in the (parametric) neighborhood of the originating problem. To make the overall process efficient, pMOR should be equipped with error indicators to assess its fidelity at any given parameter, which allows one to optimally choose the training parameter thus minimizing the number of expensive FOMs required for effective parametric analysis.

While pMOR is a promising approach for engineering analysis and design [8, 11, 12, 13], there are three main challenges when applying pMOR for turbulent flows.

(1) It is well known that even the reproduction problem is challenging for the standard G-ROM at high Reynolds numbers after the flow transitions to turbulence. To capture the complex dynamics of the turbulent flow, a relatively large number (on the order of hundreds and even thousands [14, Table II]) of ROM basis functions are needed. Thus, the resulting G-ROM is relatively high-dimensional, and its computational cost is prohibitive to be used in realistic applications, such as control of turbulent flows. The reduced advection tensor reduction requires the storage of N^3 entries with a corresponding work of $2N^3$ operations per timestep. While $N = 100$, with a cost of two million operations per step and a million words in memory, may be tolerable, $N = 400$ with a cost of 128 million operations and 64 million words quickly make pMOR inefficient.

(2) To mitigate this issue, the standard G-ROM is often constructed with relatively few basis functions. The resulting G-ROM is appealing because it is low-dimensional and computationally efficient. It is, however, inaccurate. This inaccuracy can stem from a lack of stability and approximation qualities in the ROM or from spatio-temporal chaos intrinsic to the turbulent system. Regarding stability, the low-mode ROM basis functions, which typically represent the bulk of the solution energy, tend to be smooth, and therefore incapable of effectively dissipating energy through high-wavenumber-diffusive mechanisms (i.e., represented by $\nu\nabla^2\mathbf{u}$ in the NSE). Without including this dissipation mechanism, the under-resolved G-ROM (i.e., the G-ROM that does not include enough basis functions to capture the underlying complex dynamics) generally yields spurious numerical oscillations.

Thus, in the numerical simulation of turbulent flows, these efficient, low-dimensional ROMs are generally equipped with ROM closures (see the review in [14]) and stabilizations (see, e.g., [15, 16, 17]).

Another issue that can deteriorate ROM accuracy is the lack of reproducibility in the FOM. For example, in spatio-temporal chaotic problems, time-averaged statistics are often not reproducible in the FOM due to the temporal chaos. In this case, one cannot expect the ROM, even if it is stable, to accurately reproduce the FOM results. In Chapter 3, we demonstrate that the (potentially high) variance in the full-order model provides a lower bound on the pMOR error.

(3) An error indicator is required to optimally select the training parameters to minimize the number of expensive FOM simulations. However, developing an error-indicated pMOR for an unsteady problem remains an open research issue for several reasons: (i) efficient and rigorous error estimates are usually not achievable, (ii) there could be multiple well-defined attractors, and (iii) temporal instability needs to be considered.

The subject of this dissertation is to (i) develop and investigate stabilization methods for the ROM in the context of turbulent flows, (ii) mitigate the $\mathcal{O}(N^3)$ computational cost due to the nonlinear term to enable a larger N values for turbulent flows and (iii) develop an error indicator specific to pMOR in turbulent-thermal transport applications.

1.1 Literature Survey

In this section, we present a historical overview of the ROM stabilization method, the error-indicated pMOR, and the hyper-reduction techniques for alleviating the cost of evaluating the nonlinear term.

1.1.1 Stabilization Methods

Over the years, several strategies have been devised to alleviate numerical instabilities in Galerkin-based ROMs for high Reynolds flows. These include: (i) employing data-driven limiters to bound the G-ROM dynamics [17], (ii) employing regularization to stabilize ROMs, (iii) modifying the approximation space [7, 18, 19], (iv) including dissipation via a closure model [6, 20], (v) calibration methods [21], (vi) employing a minimum residual formulation [22, 23] and (vii) generating the reduced space through Dynamic Mode Decomposition [24, 25]. In this work, stabilization strategies (i) and (ii) are the main focus.

The first type of stabilization strategy is the constrained-evolution ROM (C-ROM) proposed in [17] for the NSE. The idea is to replace the reduced linear systems with the constrained

minimization problem, with the constraints being the observed limit from the snapshots. It was shown that the C-ROM can reproduce/predict (long-time) QOIs for 2D chaotic flows [17]. In this work, we extend the method for the energy equation and apply it to heat transfer problems [26, 27].

The second type of stabilization strategy is regularized ROMs (Reg-ROMs). The idea behind regularization is to use explicit spatial filtering to stabilize ROMs and enable their use in advection-dominated flows. The two Reg-ROMs in current use are (i) the Leray ROM (L-ROM), in which the velocity component of the convective term of the Navier-Stokes equations is filtered, and (ii) the evolve-filter-relax ROM (EFR-ROM), which filters an intermediate approximation of the Navier-Stokes equations, and then relaxes it. It has been shown in the 1D, periodic Kuramoto-Sivashinsky equations, the 2D and the 3D flow past a circular cylinder that the L-ROM [26, 28, 29, 30] and the EFR-ROM [28, 30] can alleviate the spurious numerical oscillations and significantly increase the standard ROM accuracy. Reg-ROM has an attractive feature of ease of implementation despite the optimal choice of regularization (e.g., number of modes to truncate or filter order, filter radius, and relaxation parameter) is not known a priori.

In this work, we push forward the development of Reg-ROMs for turbulent heat transfer problems. We propose a new Reg-ROM, the time-relaxation ROM (TR-ROM), and investigate the three Reg-ROMs in the 3D Rayleigh-Bénard convection [26], the turbulent channel flow, and the T-junction. We also investigate the three Reg-ROMs' predictive power and the optimal parameters' robustness. In addition, we conduct sensitivity studies of the three Reg-ROMs with respect to the parameters.

1.1.2 Error-Indicated pMOR

There has been significant work on the error-indicated pMOR developments. Efficient and rigorous error estimation for the elliptic and the parabolic equation has been developed in [1, 2, 31, 32]. In [33], the author has developed an error indicator based on the residual for the steady Stokes and the NSE. In the context of the NSE coupled with the energy equation, rigorous error estimation has been developed for the *steady* Boussinesq equations [34, 35, 36, 37, 38]. Error-indicated pMOR for the unsteady problem remains an open research issue for several reasons: (i) efficient and rigorous error estimates are usually not achievable, (ii) there could be multiple well-defined attractors, and (iii) temporal instability needs to be considered. To our knowledge, there are few error-indicated pMOR developments for the unsteady parameterized Boussinesq equations. In [39], the authors develop rigorous a posteriori error bounds applied to a 2D Rayleigh-Bénard problem parameterized with the

Grashof number Gr and the domain angle with respect to gravity, θ_g. However, due to exponential instability in time, the rigor is not for very high Gr and large final times. In [40], the authors overcame the high Gr issue by considering a space-time formulation, which enabled effective long-time certification of a reduced basis approximation of noncoercive PDEs. However, the approach is limited due to the considerable offline computational effort because only one snapshot is generated from one FOM solve due to the formulation. For example, to cover the parameter space, 125 FOMs are solved during the offline in their case. Fick *et al.* [17] developed a POD-hGreedy pMOR to study challenging incompressible flow using a time-averaged error indicator. The authors showed that the error indicator is highly correlated with the error in mean flow prediction and can be efficiently computed through an offline/online strategy.

Considering the methodology has a high potential for routine analysis and design of turbulent flows that are characteristic of thermal-hydraulic systems. In this work, we further extend the error indicator for the energy equation and Leray regularization and demonstrate that the resulting error-indicated pMOR can accurately and efficiently predict QOIs in a 2D unsteady natural convection with the presence of bifurcations.

1.1.3 Cost Reduction for the Nonlinear Term

For nonlinear problems, due to the nonlinear operators or nonaffine parameter dependence, ROMs are no longer efficient because evaluating the nonlinear term depends on the FOM degrees of freedom. Existing techniques for addressing the nonlinear evaluation cost in the ROMs includes the EIM [41], the discrete empirical interpolation method (DEIM) [42, 43, 44], the missing point estimation [45], and the gappy POD [23]. These 'hyper-reduction' techniques can effectively evaluate nonlinear terms and enable the application of pMOR to nonlinear problems.

Although the advection operator in the Navier-Stokes equations (NSE) is nonlinear, it is only of polynomial type. Hence, the evaluation cost of the nonlinear term is already independent of the FOM degrees of freedom. In fact, a 3rd-order advection tensor can be precomputed in the offline and in the online, the evaluation of the nonlinear term can be done by a tensor contraction with $2N^3$ operations per timestep

However, turbulent flows (e.g., the turbulent channel flow [46, 47]) are notoriously hard for the standard G-ROM. To capture the complex dynamics of the turbulent flow, standard ROMs require a relatively large number (on the order of hundreds and even thousands [14, Table II]) of reduced basis functions to achieve good accuracy. Although the resulting G-ROM is still relatively low-dimensional compared to the FOM, its computational cost becomes

prohibitive due to the 3rd-order convection tensor contraction cost $\mathcal{O}(N^3)$. The 3rd-order tensor requires the storage of N^3 entries with a corresponding work of $2N^3$ operations per timestep. While $N = 100$, with a cost of two million operations per step and a million words in memory, may be tolerable, $N = 400$ with a cost of 128 million in operations and 64 million words quickly makes ROMs inefficient. Hence, using such ROMs in realistic applications, such as control of turbulent flows, is impossible. Hyper-reduction techniques such as DEIM have been applied to the nonlinear term in the steady NSE and the NSE to reduce the computational cost in [48, 49].

In this work, we focus on the scenario where G-ROM requires large N values and investigate the potential of the tensor decomposition for reducing the tensor contraction cost. Tensor decomposition has been widely used as a low-rank approximation for reducing the cost at the FOM level. For example, in [50], a low-rank tensor decomposition algorithm has been developed for the numerical solution of a distributed optimal control problem constrained by two-dimensional time-dependent Navier-Stokes equations with a stochastic inflow. Other decompositions such as hierarchical Tucker decomposition and tensor train have also been applied to other types of equations, such as Vlasov equation [51, 52], Fokker–Planck equation [53] and Boltzmann equation [54]. Dynamical low-rank approximation has been used to compute low-rank approximations to time-dependent large data matrices or solutions of large matrix differential equations [55, 56].

Regarding the ROM, tensor decomposition has only been used for extracting multiple space-time basis vectors from each training simulation via tensor decomposition [57]. In [58], the author considered the windowed space-time least-squares Petrov-Galerkin method (WST-LSPG) for model reduction of nonlinear parameterized dynamical systems and proposes constructing space-time bases using tensor decompositions for each window.

In this work, we propose a novel approach that utilizes the CANDECOMC/PARAFAC decomposition (CPD), a tensor decomposition technique, to accelerate the G-ROM by approximating the ROM advection tensor by a sum of R rank-1 tensors.

1.2 Organization and Thesis Contribution

This dissertation presents several strategies to advance the state-of-the-art Galerkin-based ROMs for simulating turbulent flows. These approaches aim to enhance ROMs' analysis and design capabilities in industry applications.

The contributions of this dissertation include the following:

1. In Chapter 3, the time-averaged error indicator proposed in [17] is further extended

for the energy equation and Leray regularization. Furthermore, we demonstrate that spatio-temporal chaos can lead to a lack of reproducibility in both the full-order and the reduced-order models and that the full-order model's variance provides a lower bound on the pMOR error in these cases. Most of the methods developed in this chapter appear in a recent publication in Frontiers in Physics [27].

2. In Chapter 4, a new regularized reduced-order model (Reg-ROM) based on time-relaxation is proposed and is compared with G-ROM and with existing ROM regularization strategies, including one based on a Leray model and one using an evolve-filter-relax update procedure. A detailed study of the Reg-ROMs and their filter parameters is conducted in the context of turbulent flows.

3. In Chapter 5, a novel approach using the CANDECOMC/PARAFAC decomposition (CPD) is proposed to mitigate the $\mathcal{O}(N^3)$ cost for the scenario of large N values. In addition, two conditions are derived for the CP decomposition to preserve the skew symmetry. A comparison between the singular value decomposition and the CP decomposition is also conducted.

Although not described in this document, we also note that the software developed as part of this dissertation is open source and is being used within the CFD community.

Chapter 2: Promise of the Parametric Model Order Reduction

This chapter presents basic steps toward realizing parametric model order reduction (pMOR) for buoyancy-driven turbulent flows at modest Rayleigh numbers. We introduce the Galerkin formulation for the full-order model (FOM) in Section 2.1. Subsequently, we introduce the proper orthogonal decomposition and the standard Galerkin ROM for the Boussinesq equations in Section 2.2. Section 2.3 presents the MOR workflow and practical considerations. The success of ROM reconstruction and pMOR is demonstrated through the 2D flow past a cylinder and the Orr-Sommerfeld problem in Sections 2.4–2.5. Although not described in this document, we also note that the software developed as part of this dissertation is open source and is being used within the CFD community.

The focus then turns to addressing challenges encountered in higher Rayleigh numbers. Here, ROMs suffer from inadequate dissipation due to the absence of high-wavenumber functions in the POD approximation space. To tackle this issue, we explore two stabilization strategies in Section 2.6. The first is a Leray-type regularization [28, 59], in which we mollify the nonlinear advection term by regularizing the *advecting field* (only). The second is based on the constrained-evolution approach of [17], in which the snapshot data (introduced below) is reused to set limits on the basis coefficients to keep the system's dynamics near the observed attractor. We demonstrate the relative success of these regularization approaches for the two-dimensional lid-driven cavity and the three-dimensional Rayleigh-Bénard convection in box-type geometries at Rayleigh numbers as high as 10^7 in Section 2.7. Portions of this chapter appear in the paper "Towards model order reduction for fluid-thermal analysis" published in Nuclear Engineering and Design [26].

2.1 Galerkin Formulation for the Full-Order Model

Our point of departure is the Boussinesq approximation for buoyancy-driven flow,

$$\frac{\partial \boldsymbol{u}}{\partial t} + (\boldsymbol{u}\cdot\nabla)\boldsymbol{u} + \nabla p \;=\; \nu\nabla^2\boldsymbol{u} + \eta\, T\boldsymbol{g}(\theta_g), \quad \nabla\cdot\boldsymbol{u} \;=\; 0, \tag{2.1}$$

$$\frac{\partial T}{\partial t} + (\boldsymbol{u}\cdot\nabla)T \;=\; \kappa\nabla^2 T, \tag{2.2}$$

subject to appropriate Dirichlet or Neumann boundary conditions for the velocity, $\boldsymbol{u}$, and temperature, T. Here p is the pressure, $\boldsymbol{g}(\theta_g)$ is the unit vector represents the direction of the buoyancy force and it is defined by $\boldsymbol{g}(\theta_g) = \cos(\theta_g)\hat{\imath} + \sin(\theta_g)\hat{\jmath}$, with θ_g the angle of the domain with respect to the gravity. Here, ν, η, and κ are problem parameters based on the

nondimensionalization of the problem.

The FOM is constructed through the spectral element method (SEM) and the P_q–P_{q-2} velocity-pressure coupling [60], where the velocity is represented as a tensor-product Lagrange polynomial of degree q in the reference element $\hat{\Omega} := [-1, 1]^2$ while the pressure is of degree $q-2$. The solution in $\Omega = \bigcup_e \Omega^e$ consists of local representations of $\boldsymbol{u}$, p, and T that are mapped from $\hat{\Omega}$ to Ω^e for each element, $e = 1, \ldots, E$. The FOM simulations are performed using the spectral element code Nek5000/RS [61, 62].

For any $\boldsymbol{u}(\mathbf{x}, t)$, we have a corresponding vector of basis coefficients $\underline{\mathbf{u}} = [\boldsymbol{u}_1 \ldots \boldsymbol{u}_{\mathcal{N}}]^T$ such that

$$\boldsymbol{u}(\mathbf{x}, t) = \sum_{j=1}^{\mathcal{N}} \boldsymbol{u}_j(t)\phi_j(\mathbf{x}) \in \mathbf{X}_0^{\mathcal{N}} \subset \mathbf{H}_0^1, \tag{2.3}$$

with $\phi_j(\mathbf{x})$ the underlying spectral element basis functions spanning the FOM approximation space, $\mathbf{X}_0^{\mathcal{N}}$. Because the SEM is nodal-based, each $\boldsymbol{u}_j(t)$ represents the two velocity components at grid point $\mathbf{x}_j$ in the spectral element mesh at time t. Similarly, the temperature is given by

$$T(\mathbf{x}, t) = \sum_{j=1}^{\bar{\mathcal{N}}} T_j(t)\phi_j(\mathbf{x}) \in X_0^{\mathcal{N}} \subset \mathcal{H}_0^1. \tag{2.4}$$

Here, $\mathcal{H}^1$ is the set of square-integrable functions on Ω whose gradient is also square-integrable and $X^{\mathcal{N}} \subset \mathcal{H}^1$ is the finite dimensional SEM approximation space spanned by $\{\phi_j(\mathbf{x})\}$. $\mathcal{H}_0^1$ is the set of functions in $\mathcal{H}^1$ that vanish wherever Dirichlet conditions associated with (3.2) are applied on the domain boundary $\partial\Omega$ and $\mathcal{H}_b^1$ is the set of functions in $\mathcal{H}^1$ that satisfy the prescribed Dirichlet conditions for temperature. Bold-face indicates that the space is spanned by vector-valued functions having d components ($d = 2$ or 3) and, in the case of $\mathbf{X}_0^{\mathcal{N}} \subset \mathbf{H}_0^1$, that the functions vanish where Dirichlet conditions are applied for (4.18). The pressure p is in $Y^{\mathcal{N}} \subset \mathcal{L}^2(\Omega)$, which is the space of piecewise continuous functions on Ω such that $\int_\Omega p^2 \, d\mathbf{x} < \infty$. For convenience, we denote $\bar{\mathbf{Z}}^{\mathcal{N}} = (\mathbf{X}^{\mathcal{N}}, Y^{\mathcal{N}}, X^{\mathcal{N}})$ as the collection of the relevant finite-dimensional spaces and will add a subscript 0 or b where required to explicitly indicate the imposed boundary conditions.

Both the FOM and ROM are cast within the same Galerkin framework. To begin, we introduce several inner products for elements in the FOM space, $\bar{\mathbf{Z}}^{\mathcal{N}}$. For any pair of scalar fields $(p, q) \in \mathcal{L}^2(\Omega)$ and d-dimensional vector fields, $\boldsymbol{v}(\mathbf{x}) = [v_1(\mathbf{x}) \ldots v_d(\mathbf{x})]$, $\boldsymbol{u}(\mathbf{x}) = [u_1(\mathbf{x}) \ldots u_d(\mathbf{x})]$ whose components are also in $\mathcal{L}^2$, let

$$(q, p) \coloneqq \int_\Omega q\, p \, d\mathbf{x}, \qquad (\boldsymbol{v}, \boldsymbol{u}) \coloneqq \int_\Omega (v_1 u_1 + \cdots + v_d u_d) \, d\mathbf{x}. \tag{2.5}$$

Further, for $S,\, T \in X^{\mathcal{N}}$ and $\boldsymbol{v},\, \boldsymbol{u} \in \mathbf{X}^{\mathcal{N}}$, let

$$a(S,T) \coloneqq (\nabla S, \nabla T)\,, \qquad a(\boldsymbol{v},\boldsymbol{u}) \coloneqq (\nabla \boldsymbol{v}, \nabla \boldsymbol{u})\,, \tag{2.6}$$

$$c(S,\boldsymbol{u},T) \coloneqq (S, \boldsymbol{u}\cdot\nabla T)\,, \qquad c(\boldsymbol{v},\boldsymbol{u},\mathbf{w}) \coloneqq (\boldsymbol{v}, \boldsymbol{u}\cdot\nabla \mathbf{w})\,. \tag{2.7}$$

For the FOM, we consider the (semi-discrete) weak form of (4.18)–(3.2) [63], *Find* $(\widetilde{\mathbf{u}},\ p,\ \widetilde{T}) \in \bar{\mathbf{Z}}_b^{\mathcal{N}}$ *such that, for all* $(\boldsymbol{v},\ q,\ S) \in \bar{\mathbf{Z}}_0^{\mathcal{N}}$,

$$\left(\boldsymbol{v}, \frac{\partial \widetilde{\mathbf{u}}}{\partial t}\right) + \nu\, a(\boldsymbol{v},\widetilde{\mathbf{u}}) - (\nabla\cdot\boldsymbol{v}, p) = -c\,(\boldsymbol{v},\widetilde{\mathbf{u}},\widetilde{\mathbf{u}}) + \eta\left(\boldsymbol{v}, \boldsymbol{g}(\theta_g)\widetilde{T}\right), \tag{2.8}$$

$$-\,(q, \nabla\cdot\widetilde{\mathbf{u}}) \qquad\qquad = 0, \tag{2.9}$$

$$\left(S, \frac{\partial \widetilde{T}}{\partial t}\right) + \kappa\, a(S,\widetilde{T}) \qquad\qquad = -c\left(S,\widetilde{\mathbf{u}},\widetilde{T}\right). \tag{2.10}$$

Here, we have introduced $\widetilde{\mathbf{u}} = \boldsymbol{u} + \boldsymbol{u}_0(\mathbf{x})$ and $\widetilde{T} = T + T_0(\mathbf{x})$ as functions that have been augmented by (potentially trivial) lifting functions, $\boldsymbol{u}_0$ and T_0, which are functions of space only. If these functions satisfy the (time-independent) boundary conditions, then one can account for inhomogeneous boundary conditions by moving them to the right-hand side. In the case of the ROM, the lifting functions can also provide an initial approximation to the solution. In the sequel, our principal unknowns will be $\boldsymbol{u}$ and T.

Following [64], we consider a semi-implicit scheme BDFk/EXTk to discretize (2.8)–(2.10) in time; kth-order backward differencing (BDFk) is used for the time-derivative term, kth-order extrapolation (EXTk) is used for the advection and buoyancy terms and implicit treatment on the dissipation terms. As discussed in [64], $k = 3$ is used to ensure the imaginary eigenvalues associated with skew-symmetric advection operator are within the stability region of the BDFk/EXTk time-stepper. Denoting the solution at time $t^n = \Delta t \cdot n$ as $(\widetilde{\mathbf{u}}^n, p^n, \widetilde{T}^n)$, the full discretization of the FOM reads *Find* $(\boldsymbol{u}^n, p^n, T^n) \in \bar{\mathbf{Z}}_0^{\mathcal{N}}$ *such that, for all* $(\boldsymbol{v}, q, S) \in \bar{\mathbf{Z}}_0^{\mathcal{N}}$,

$$\frac{\beta_0}{\Delta t}(\boldsymbol{v},\boldsymbol{u}^n) + \nu\, a(\boldsymbol{v},\boldsymbol{u}^n) - (\nabla\cdot\boldsymbol{v}, p^n) = (\boldsymbol{v}, \mathbf{f}^n), \tag{2.11}$$

$$-\,(q, \nabla\cdot\boldsymbol{u}^n) \qquad\qquad = (q, \nabla\cdot\boldsymbol{u}_0)\,, \tag{2.12}$$

$$\frac{\beta_0}{\Delta t}\,(S, T^n) + \kappa\, a(S,T^n) \qquad\qquad = (S, Q^n). \tag{2.13}$$

Equations (2.11)–(2.13) represent a linear unsteady Stokes plus unsteady heat equation to be solved at each time-step t^n. The inhomogeneous terms comprise the BDF, advection,

buoyancy and lifting terms

$$(\boldsymbol{v}, \mathbf{f}^n) \coloneqq -\sum_{s=1}^{k} \left[\frac{\beta_s}{\Delta t}(\boldsymbol{v}, \boldsymbol{u}^{n-s}) + \alpha_s \left(c(\boldsymbol{v}, \widetilde{\mathbf{u}}^{n-s}, \widetilde{\mathbf{u}}^{n-s}) - \eta(\boldsymbol{v}, \boldsymbol{g}(\theta_g)\widetilde{T}^{n-s}) \right) \right] - \nu a(\boldsymbol{v}, \boldsymbol{u}_0), \quad (2.14)$$

$$(S, Q^n) \coloneqq -\sum_{s=1}^{k} \left[\frac{\beta_s}{\Delta t}(S, T^{n-s}) + \alpha_s c(S, \widetilde{\mathbf{u}}^{n-s}, \widetilde{T}^{n-s}) \right] - \kappa a(S, T_0). \quad (2.15)$$

Here, the β_ss and α_ss are the respective sth-order BDF and extrapolation coefficients for the BDFs/EXTs time-stepper [64]. Note that the right-hand side of (2.12) will be zero if $\boldsymbol{u}_0$ is divergence free or at least satisfies the weak divergence-free condition (2.9).

Under the assumption that $\nabla \cdot \boldsymbol{u}_0 = 0$, the compact matrix form [60, 65, 66] for (2.11)–(2.15) is

$$\begin{bmatrix} \mathbf{H} & -\mathbf{D}^T \\ -\mathbf{D} & 0 \end{bmatrix} \begin{pmatrix} \underline{\mathbf{u}}^n \\ \underline{p}^n \end{pmatrix} = \begin{pmatrix} \underline{\hat{\mathbf{f}}}(\widetilde{\mathbf{u}}^n, \widetilde{T}^n; \theta_g) \\ 0 \end{pmatrix}, \quad (2.16)$$

$$H_\kappa \, \underline{T}^n = \underline{\hat{Q}}(\widetilde{\mathbf{u}}^n, \widetilde{T}^n). \quad (2.17)$$

Here, $\underline{\mathbf{u}}^n$, $\underline{p}^n$, and $\underline{T}^n$ are the vectors of spectral element basis coefficients. The corresponding block matrices are

$$\mathbf{H} = \begin{bmatrix} H_\nu & \\ & H_\nu \end{bmatrix}, \qquad \mathbf{D} = [D_1 \;\; D_2], \quad (2.18)$$

with $H_\nu = \frac{\beta_0}{\Delta t} M + \nu A$ and $H_\kappa = \frac{\beta_0}{\Delta t} M + \kappa A$, with matrices M and A defined below. The velocity data vectors are $\underline{\hat{\mathbf{f}}}(\widetilde{\mathbf{u}}^n, \widetilde{T}^n; \theta_g) = [\underline{\hat{f}}_1 \;\; \underline{\hat{f}}_2]^T$, with

$$\underline{\hat{f}}_m \coloneqq -\sum_{s=1}^{k} \left[\frac{\beta_s}{\Delta t} M \underline{u}_m^{n-s} + \alpha_s \left(C(\underline{\widetilde{\mathbf{u}}}^{n-s}) \underline{\widetilde{u}}_m^{n-s} - \eta g_m M \underline{\widetilde{T}}^{n-s} \right) \right] - \nu A \underline{u}_{m,0}, \quad m = 1, 2. \quad (2.19)$$

where $g_1 = \cos(\theta_g)$ and $g_2 = \sin(\theta_g)$ represent the parametric forcing. The thermal load in (2.17) is

$$\underline{\hat{Q}}(\widetilde{\mathbf{u}}^n, \widetilde{T}^n) \coloneqq -\sum_{s=1}^{k} \left[\frac{\beta_s}{\Delta t} M \underline{\widetilde{T}}^{n-s} + \alpha_s C(\underline{\widetilde{\mathbf{u}}}^{n-s}) \underline{\widetilde{T}}^{n-s} \right] - \kappa A \underline{T}_0. \quad (2.20)$$

Entries of the respective stiffness, mass, convection, and gradient matrices are

$$A_{ij} = \int_\Omega \nabla\phi_i \nabla\phi_j \, d\mathbf{x}, \tag{2.21}$$

$$M_{ij} = \int_\Omega \phi_i \phi_j \, d\mathbf{x}, \tag{2.22}$$

$$C_{ij}(\mathbf{w}) = \int_\Omega \phi_i \cdot (\mathbf{w} \cdot \nabla)\phi_j \, d\mathbf{x}, \tag{2.23}$$

$$D_{m,ij} = \int_\Omega \psi_i \frac{\partial \phi_j}{\partial x_m} \, d\mathbf{x}, \quad m = 1, 2. \tag{2.24}$$

Note that $\{\phi_i(\mathbf{x})\}$ forms the spectral element velocity/temperature basis while $\{\psi_i(\mathbf{x})\}$ constitutes the pressure basis.

2.2 Galerkin Reduced Order Model

The Galerkin ROM (G-ROM) for the Boussinesq equations starts with a collection of K snapshots for velocity, $\boldsymbol{u}^k(\mathbf{x}) := \boldsymbol{u}(\mathbf{x}, t^k) - \boldsymbol{u}_b$ and for temperature, $T^k(\mathbf{x}) := T(\mathbf{x}, t^k) - T_b$ corresponding to numerical solutions of the full-order model (FOM) at well-separated timepoints, t^k, minus *base states*, $\boldsymbol{u}_b(\mathbf{x})$ and $T_b(\mathbf{x})$. The base states (typically time-averaged FOM solutions) satisfy any prescribed inhomogeneous boundary conditions, which are presently assumed to be time-independent.

2.2.1 POD Bases

We follow the standard proper orthogonal decomposition (POD) procedure [67, 68] to construct the reduced basis. For the velocity, we collect the snapshots into the a matrix $\mathbf{U}_K = [\underline{\mathbf{u}}^1 \dots \underline{\mathbf{u}}^K]$. From these, one forms the Gramian, $\mathbf{U} \in \mathbb{R}^{K\times K}$, with $\mathbf{U}_{k,k'} := (\boldsymbol{u}^k, \boldsymbol{u}^{k'})_{L^2}$, where $(\boldsymbol{v}, \boldsymbol{u})_{L^2} := \int_\Omega \boldsymbol{v} \cdot \boldsymbol{u} \, dV$ is the L^2 inner product. One could also consider the H^1 norm and H^1 semi-norm which have been considered in [69] and [17, 26].

The basis functions $\{\underline{\boldsymbol{\varphi}}_n\}$ for the ROM derive from the first N eigenmodes of $\mathbf{U}_K$,

$$\mathbf{U}_K \underline{z}_k = \lambda_k \underline{z}_k, \quad \underline{z}_k \in \mathbb{R}^K, \quad \lambda_1 \geq \cdots \geq \lambda_K \geq 0 \tag{2.25}$$

$$\underline{\boldsymbol{\varphi}}_n := \mathbf{U}_K \underline{z}_n, \quad n = 1, \dots, N < K. \tag{2.26}$$

The continuous functions in the SEM space corresponding to $\underline{\boldsymbol{\varphi}}_n$ are $\boldsymbol{\varphi}_n(\mathbf{x}) := \sum_{j=1}^{\mathcal{N}} (\underline{\boldsymbol{\varphi}}_n)_j \phi_j(\mathbf{x})$.

We perform a similar procedure for temperature, generating $\overline{T}_K := [\underline{T}^1 \dots \underline{T}^K]$ and associated Gramian, $\overline{T}$, having entries $\overline{T}_{k,k'} := (T^k, T^{k'})_{L^2}$. We then solve the $K \times K$

eigenproblem,

$$\overline{T}_K \underline{\tau}_k \;=\; \lambda_k \underline{\tau}_k, \quad \underline{\tau}_k \in \mathbb{R}^K, \quad \lambda_1 \geq \cdots \geq \lambda_K \geq 0, \tag{2.27}$$

and define

$$\underline{\theta}_n \;:=\; \overline{T}_K \underline{\tau}_n, \quad n = 1, \ldots, N < K. \tag{2.28}$$

The continuous functions in the SEM space corresponding to $\underline{\tau}_n$ are $\theta_n(\mathbf{x}) := \sum_{j=1}^{\mathcal{N}} (\underline{\theta}_n)_j \phi_j(\mathbf{x})$.

Remark 2.1. We note that the POD construction provides a set of basis vectors $\boldsymbol{Z} := [\underline{\boldsymbol{\varphi}}_1 \ldots \underline{\boldsymbol{\varphi}}_N]$ that minimizes the average distance between $\boldsymbol{Z}$ and $\mathbf{U}_K$ in the chosen inner-product (here, $(\cdot,\cdot)_{L^2}$) for any rank-N subset of U_K. Thus, the motivation for POD is its approximation property, which uniformly distributes the error across the snapshot set. That property is not dependent on the subsequent choice of time-evolution of the ROM nor any particular feature of the Navier-Stokes or Boussinesq equations. One could, however, consider other norms that might favor the minimization of errors in one or more QOIs, which is a topic for future consideration.

Remark 2.2. In the procedures that follow, we treat the velocity and temperature as independent state vectors. One could alternatively work with snapshot sets that combine the velocity and temperature into a single vector and thus form the Gramian from $\mathbf{Q}_K = [\underline{\boldsymbol{q}}^1 \ldots \underline{\boldsymbol{q}}^K]$, where $\underline{\boldsymbol{q}}^k := [\underline{\mathbf{u}}^k \, \underline{T}^k]$. This approach reduces the online evaluation cost of the ROM by a factor of two because one has one-half the number of variables to track. The principal drawback of using a coupled system is that one then has no mechanism to ensure that the temperature is bounded by its extremal boundary values (where such bounds are meaningful).

2.2.2 Galerkin Formulation

Within the Galerkin framework of the preceding section it is relatively straightforward to develop Galerkin-based ROM (G-ROM). With the reduced basis sets in hand, $\boldsymbol{\varphi}_j(\mathbf{x}) \in \mathbf{X}^N \subset \mathbf{X}^{\mathcal{N}}$, $\theta_j(\mathbf{x}) \in X^N \subset X^{\mathcal{N}}$, the Galerkin formulation follows by inserting the reduced-basis

expansions,

$$\widetilde{\mathbf{u}}_{\mathrm{r}}(x,t) = \boldsymbol{\varphi}_0(\mathbf{x}) + \sum_{j=1}^{N} \boldsymbol{\varphi}_j(\mathbf{x}) u_{\mathrm{r},j}(t) \ \in \mathbf{X}_b^N \tag{2.29}$$

$$\widetilde{T}_{\mathrm{r}}(x,t) = \theta_0(\mathbf{x}) + \sum_{j=1}^{N} \theta_j(\mathbf{x}) T_{\mathrm{r},j}(t) \ \in X_b^N, \tag{2.30}$$

into (2.8)–(2.10) and require equality for all $(\boldsymbol{v}, S)$ in $\boldsymbol{Z}_0^N$. In order to set the boundary conditions, we have augmented the trial (approximation) spaces $\mathbf{X}^N$ and X^N with the *base states* $\boldsymbol{\varphi}_0 \coloneqq \boldsymbol{u}_b$ and $\theta_0 \coloneqq T_b$. The coefficients for these terms are prescribed: $u_{\mathrm{r},0} \equiv T_{\mathrm{r},0} \equiv 1$. The corresponding test spaces, $\mathbf{X}_0^N \coloneqq \{\boldsymbol{\varphi}_j\}_{j=1}^N$ and $X_0^N \coloneqq \{\theta_j\}_{j=1}^N$, satisfying homogeneous boundary conditions, as is standard for Galerkin formulation. The reduced space $\boldsymbol{Z}_0^N \coloneqq (\mathbf{X}_0^N, X_0^N)$ is typically based on a linear combination of full spectral element solutions of (2.16)–(2.17), such as snapshots at certain time-points, t^n, or solutions at various parametric values. Under these conditions and with a carefully chosen $\boldsymbol{u}_0$, $\mathbf{X}^N$ is a set of velocity-space functions that are (weakly) divergence-free and the pressure terms drop out of (2.8)–(2.9). We also note that $\boldsymbol{\varphi}_j$ and θ_j are *modal*, not nodal, basis functions.

In weak form, the problem can be stated as *Find* $\widetilde{\mathbf{u}}_r \in \mathbf{X}_b^N$, $\widetilde{T}_r \in X_b^N$, *such that, for all* $\boldsymbol{v} \in \mathbf{X}_0^N$, $S \in X_0^N$,

$$\int_\Omega \boldsymbol{v} \cdot \frac{d\widetilde{\mathbf{u}}_{\mathrm{r}}}{dt}\, dV + \nu \int_\Omega \nabla \boldsymbol{v} : \nabla \widetilde{\mathbf{u}}_{\mathrm{r}}\, dV = -\int_\Omega \boldsymbol{v} \cdot (\widetilde{\mathbf{u}}_{\mathrm{r}} \cdot \nabla)\, \widetilde{\mathbf{u}}_{\mathrm{r}}\, dV \ + \ \eta \int_\Omega \boldsymbol{v} \cdot (\widetilde{T}_{\mathrm{r}} \boldsymbol{g}(\theta_g))\, dV, \tag{2.31}$$

$$\int_\Omega S \frac{d\widetilde{T}_{\mathrm{r}}}{dt}\, dV + \kappa \int_\Omega \nabla S \cdot \nabla \widetilde{T}_{\mathrm{r}}\, dV = -\int_\Omega S\, (\widetilde{\mathbf{u}}_{\mathrm{r}} \cdot \nabla)\, \widetilde{T}_{\mathrm{r}}\, dV \ + \ \kappa \int_{\partial\Omega_f} S \nabla \widetilde{T}_{\mathrm{r}} \cdot \hat{\mathbf{n}}\, dA. \tag{2.32}$$

We remark that the presence of the surface integral in (2.32) admits the possibility of an inhomogeneous surface flux $q_s \coloneqq \kappa \nabla \widetilde{T}_{\mathrm{r}} \cdot \hat{\mathbf{n}}$ on some part of the domain boundary $\partial\Omega_f \subset \partial\Omega$. If $\boldsymbol{\varphi}_0$ and θ_0 satisfy the prescribed Dirichlet conditions, then $\widetilde{\mathbf{u}}_{\mathrm{r}}$ and $\widetilde{T}_{\mathrm{r}}$ will satisfy these conditions as well. Note that the pressure term vanishes from (2.31) due to integration-by-parts because the test functions are weakly divergence-free and homogeneous on the boundary. The continuity equation of the Navier-Stokes equations is also removed because Z_b consists solely of weakly divergence-free basis functions.

For temporal discretization of (2.31)–(2.32), we use a semi-implicit scheme with kth-order backward differencing (BDFk) for the time derivative, implicit treatment of the negative-definite dissipation terms, and kth-order extrapolation (EXTk) of the advection and buoyancy terms. We typically use $k = 3$ to ensure that the imaginary eigenvalues associated with skew-

symmetric advection operator are within the stability region of the BDFk/EXTk timestepper, as discussed in [70].

When fully discretized in space and time, we get the following systems for the ROM basis coefficients $\underline{u}_{\mathrm{r}}^n$ and $\underline{T}_{\mathrm{r}}^n$ at timepoint t^n,

$$\left(\frac{\beta_0}{\Delta t}B_u + \nu\, A_u\right)\underline{u}_{\mathrm{r}}^n = -\sum_{i=1}^{k}\alpha_i\left[C_u\left(\widetilde{\underline{u}}_{\mathrm{r}}\right)\widetilde{\underline{u}}_{\mathrm{r}} \;-\eta\, B_{uT}\widetilde{\underline{T}}_{\mathrm{r}}\right]^{n-i} - B_u\sum_{i=1}^{k}\frac{\beta_i}{\Delta t}\underline{u}_{\mathrm{r}}^{n-i} \;-\; \nu\underline{a}_{u,0}, \tag{2.33}$$

$$\left(\frac{\beta_0}{\Delta t}B_T + \kappa\, A_T\right)\underline{T}_{\mathrm{r}}^n = -\sum_{i=1}^{k}\alpha_i\left[C_T(\widetilde{\underline{u}}_{\mathrm{r}})\,\widetilde{\underline{T}}_{\mathrm{r}}\right]^{n-i} - B_T\sum_{i=1}^{k}\frac{\beta_i}{\Delta t}\underline{T}_{\mathrm{r}}^{n-i} - \kappa\,\underline{a}_{T,0} + \underline{q}_s. \tag{2.34}$$

Here, $\widetilde{\underline{u}}_{\mathrm{r}}$ and $\widetilde{\underline{T}}_{\mathrm{r}}$ are the augmented basis vectors that include the base states for $\underline{u}_{\mathrm{r}}$ and $\underline{T}_{\mathrm{r}}$; α_i and β_i are the respective BDFk/EXTk coefficients (e.g., for k=2, $\alpha_1 = 2$, $\alpha_2 = -1$, $\beta_0 = \frac{3}{2}$, $\beta_1 = -\frac{4}{2}$, and $\beta_2 = \frac{1}{2}$). A, B, and C represent the respective stiffness, mass, and advection operators, with entries

$$A_{u,ij} = \int_\Omega \nabla\boldsymbol{\varphi}_i : \nabla\boldsymbol{\varphi}_j\, dV \tag{2.35}$$

$$B_{u,ij} = \int_\Omega \boldsymbol{\varphi}_i \cdot \boldsymbol{\varphi}_j\, dV \tag{2.36}$$

$$C_{u,ikj} = \int_\Omega \boldsymbol{\varphi}_i \cdot (\boldsymbol{\varphi}_k \cdot \nabla)\boldsymbol{\varphi}_j\, dV \tag{2.37}$$

$$A_{T,ij} = \int_\Omega \nabla\theta_i \cdot \nabla\theta_j\, dV \tag{2.38}$$

$$B_{T,ij} = \int_\Omega \theta_i\theta_j\, dV \tag{2.39}$$

$$C_{T,ikj} = \int_\Omega \theta_i \cdot (\boldsymbol{\varphi}_k \cdot \nabla)\theta_j\, dV. \tag{2.40}$$

$$B_{uT,ij} = \int_\Omega \boldsymbol{\varphi}_i \cdot \boldsymbol{g}(\theta_g)\theta_j\, dV \tag{2.41}$$

$$\underline{q}_{s,i} = \int_{\partial\Omega_f} \theta_i\, q_s\, dA \tag{2.42}$$

Remark 2.3. We note that, in the case of fixed geometries, the divergence and pressure terms drop out of (2.31) because the ROM basis is weakly divergence-free. For ROMs that include the pressure approximation, see, e.g., [8, 12, 71, 72, 73].

We have applied the G-ROM (2.33)–(2.34) for several cases, including the basic test problem of two-dimensional flow past a cylinder at Reynolds number $Re_D = 100$, for which $N \approx 20$ provides a sufficient number of modes for accurate reproduction of the flow field and

the drag history to four significant digits. As stated earlier, however, our objective is not to reconstruct the flow field. Instead, we aim to predict QOIs at parameter points p not in the training set $\mathcal{P}_{\text{anchor}}$ from which we draw our approximating bases. In Section 2.4, we illustrate the use of the G-ROM for the reproduction of the aforementioned cylinder problem and demonstrate the pMOR through the cylinder problem and the Orr-Sommerfeld problem in Section 2.5.

2.3 Model Order Reduction Workflow and Practical Considerations

The pMOR procedure consists of offline and online stages. In the offline stage, the first step is to collect the data (snapshots) by solving the full-order models, as discussed in Section 2.1, at parameters of interest using highly optimized CFD code Nek5000/RS. The choice of computational resources, ranging from a workstation to a supercomputer, depends on the complexity of the full-order model. The computational memory for this step, depending on the FOM solver, typically requires an allocation of 400 FOM vector of size $\mathcal{N}$.

The second step is to construct the reduced basis using POD with the collected snapshots, which generally involves forming the Gramian, solving its eigenvalue problem and multiplying the snapshot matrix with the eigenvectors, as discussed in Section 2.2.1. During the development of this work, we realized that we underestimate the amount of computational resources required in this step, especially when dealing with 3D turbulent flow problems. The bottleneck is the computational memory requirement for forming the Gramian, which requires loading all the snapshots resulting in an allocation of 1000–4000 FOM vectors of size $\mathcal{N}$. The choice of computational resources is immediately limited to either a campus cluster or a supercomputer. In addition, this step could require more computational resources, that is the number of nodes and wall-clock time than solving the FOM. Moreover, the bottleneck also limits the amount of snapshots that can be used for industrial applications which usually have degrees of freedom $\mathcal{N} > 10^9$. One way to bypass this bottleneck is to consider a memory-efficient offline generation developed in [16] that could be run on a modest-sized workstation.

The third step is to use the reduced basis to construct the reduced operators for the NSE and the energy equations, as discssued in Section 2.2.2. The computational memory is less intense than the second step, requiring an allocation of N FOM vectors of size $\mathcal{N}$. However, forming the advection tensor due to the nonlinear term in the NSE could still require fair amount of wall-clock time on HPC platforms. Moreover, with the time-averaged error indicator, which will be discussed in Section 2.5, an allocation of $2(N+1)^2 + 6(N+1)$ FOM vectors of size $\mathcal{N}$ for linear functionals is required. In addition, it requires solving

$(N+1)^2+4(N+1)$ Stokes and $(N+1)^2+2(N+1)$ Poisson problems for the Riesz representers. The amount of computational memory and resources could be more intense than the second step with $N > 45$. An alternative approach is to consider the "direct" approach which will be discussed in Section 2.5. While use of the direct approach requires access to the FOM machinery in order to generate an error indicator, we note that such access is readily available during the pMOR training/construction phase. The advantage of this approach is that the number of Stokes/Poisson solves scales as the number of points in the training space, which is typically less than N^2.

In the online stage, the requirement for computational memory and resources is low because it only requires loading the reduced operators and solve the reduced system, which only depends on the ROM size N instead of FOM size $\mathcal{N}$. In summary, the bottlenecks in the second and the third step needed to be addressed in order to consider error-indicated pMOR for industrial applications.

2.4 Reproduction Problem

We first demonstrate the reproduction problem using the G-ROM on the problem of 2D flow past a cylinder at $\mathrm{Re} = 100$. This is a canonical test case for ROMs due to its robust and low-dimensional attractor, manifesting as a von Karman vortex street for $\mathrm{Re} = \mathrm{UD}/\nu > 34.37$ [74]. The computational domain is $\Omega = [-2.5 : 17]D \times [-5 : 5]D$, with the unit-diameter cylinder centered at $[0, 0]$.

The reduced basis $\{\boldsymbol{\varphi}_i\}_{i=1}^N$ for the G-ROM (5.3) is constructed by applying POD procedure to $K = 100$ snapshots collected over 100 convective time units (D/U), after von Karman vortex street is developed. The zeroth mode $\boldsymbol{\varphi}_0$ is set to be the mean velocity field of the snapshot collection time window. Already with $N = 20$ POD basis, the reduced space contains more than 99% of the total energy of the snapshots. The initial condition for the G-ROM and the CPD-ROM is obtained by projecting the lifted snapshot at $t = 500$ (in convective time units) onto the reduced space.

The total drag on the cylinder is defined as:

$$\boldsymbol{F}_D = \oint_\Gamma (-\nu \nabla \boldsymbol{u} + p) d\boldsymbol{A}. \tag{2.43}$$

where Γ is the surface of the cylinder. We consider the total drag in the x-direction as the QOI. To compute the pressure drag, we consider the method described in [16] which does not require solving the reduced pressure system. We refer [75] for solving a pressure ROM to compute the pressure drag.

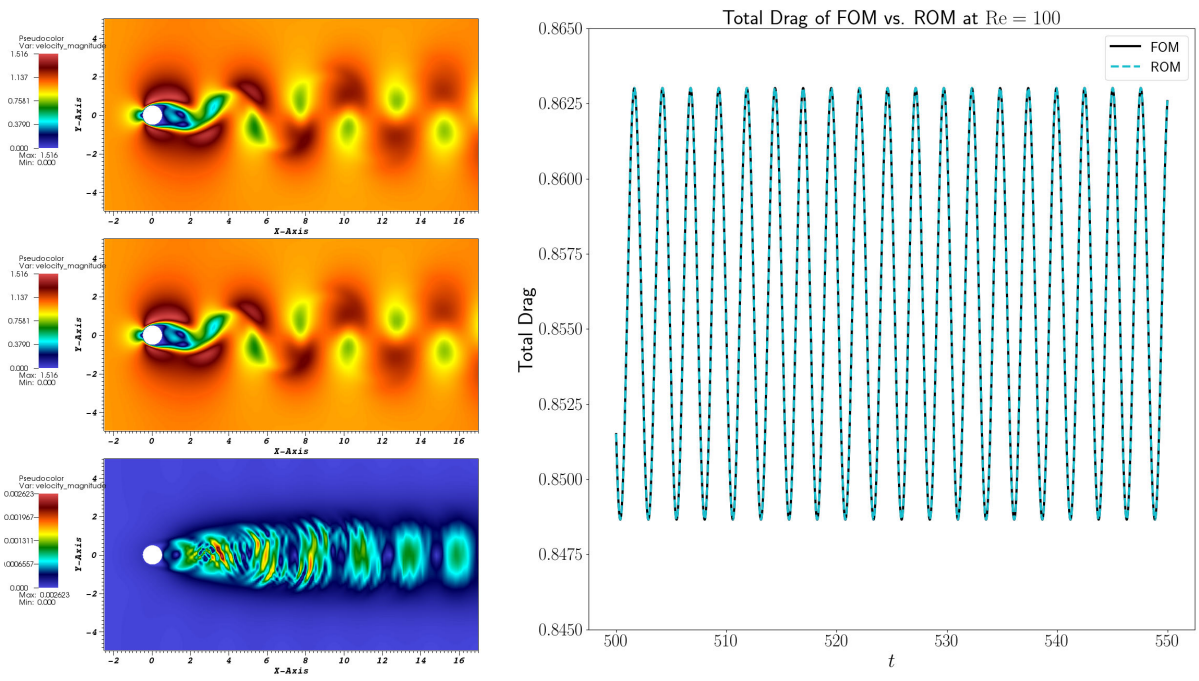

Figure 2.1: Reconstruction results with ROM with $N = 20$ at $\mathrm{Re} = 100$: (Left) Magnitude of instantaneous velocity of the FOM (top) and the G-ROM (middle) at the same time instance and point-wise difference between the two (bottom) with maximum difference $\approx 3e-3$. (Right) Total drag comparison between the FOM and the G-ROM.

Fig. 2.1 shows the reproduction results of the G-ROM. The G-ROM accurately captures the velocity solution and also the phase and period of the drag in the FOM.

Moreover, the G-ROM only requires $N = 20$ degress of freedom compared to the FOM degress of freedom $\mathcal{N} = 32,768$. Already, to simulate 500 CTUs, it takes 30 minutes for the FOM and the G-ROM is able to run $10,000$ CTUs in 20 seconds. Although this example is a trivial cases for MOR, it demonstrate a significant reduction in the degrees of freedom and computational time.

2.5 Parametric Model Order Reduction

Given that the parameters and QOIs for thermal-fluids applications are highly case specific, we introduce pMOR in this section. Specifically, we consider using the pMOR to estimate the critical Reynolds number for the 2D flow past a cylinder and Orr-Sommerfeld problem.

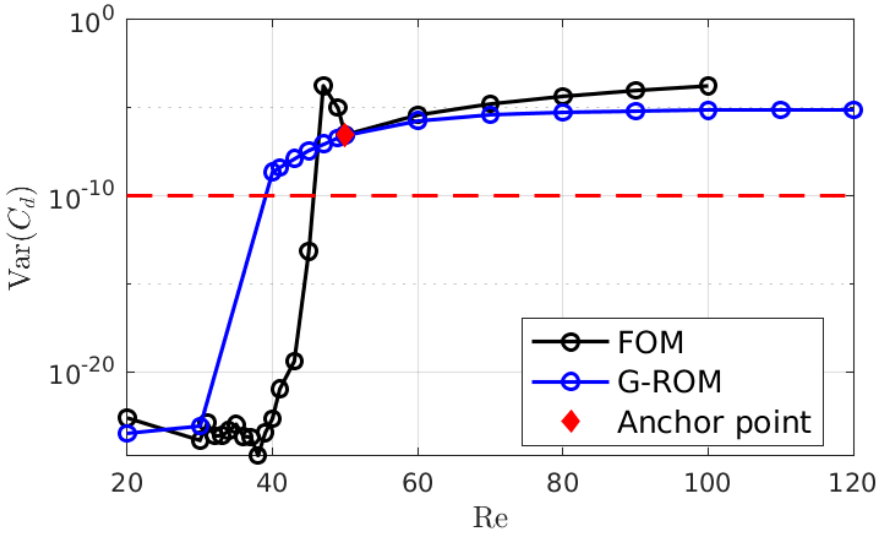

Figure 2.2: pMOR results with one anchor point in 2D flow past a cylinder at Re = 50: Variance of the drag coefficient C_d, $\mathrm{Var}(C_d)$ for the FOM and the G-ROM. G-ROM is constructed using one anchor point at Re = 50 with $N = 20$. $\mathrm{Var}(C_d) \leq 10^{-10}$ is used as the criteria to determine the flow is motionless.

2.5.1 Flow Past a Cylinder

We first consider the aforementioned cylinder problem to demonstrate pMOR. Re = 50 is selected as the single anchor (training) point to construct the G-ROM. The reduced basis is then constructed using the POD procedure with $K = 500$ snapshots from the time interval $[501, 1000]$. The G-ROM (2.31) is constructed using $N = 20$ modes.

With this setup, we adjust the parameters in (2.31) to run the ROM for $\mathrm{Re} \in [20,\ 120]$. Our goal is to use the variance of the drag coefficient C_d, $\mathrm{Var}(C_d)$ to estimate the critical Reynolds number $\mathrm{Re}_{\mathrm{critical}}$.

Fig. 2.2 shows the variance of the drag coefficient for the FOM and the G-ROM at several Re. We use the criteria $\mathrm{Var}(C_d) \leq 10^{-10}$ to determine the flow is motionless. With this criteria, $\mathrm{Re}_{\mathrm{critical}} = 47$ is found with the FOM and $\mathrm{Re}_{\mathrm{critical}} = 40$ is found with the pMOR. With one anchor point at Re = 50, the pMOR does a remarkably job in estimating the critical Reynolds number. Moreover, it takes 2000 (sec) per FOM run while it only take 10 (sec) per G-ROM run.

2.5.2 Orr-Sommerfeld Problem

We consider the evolution of small amplitude disturbances in channel flow [76, 77]. In this study the disturbance is taken to be an eigensolution of the Orr-Sommerfeld equation. The

Table 2.1: Reproduction results in Orr-Sommerfeld problem at Re = 7500: $error$ and $error_g$ for both FOM and ROM at $t = 200$.

	t	$\frac{E(t)}{E(0)}$	$e^{(2\omega_i t)}$	$error$	$error_g$
FOM	200	2.44363736	2.44486586	-1.22850700E-03	5.77317855E-04
ROM	200	2.44354848	2.44486586	-1.31738592E-03	4.36671759E-04

advantage of using this problem as a test case is that it has known solutions from linear theory. The geometry consists of two walls separated by a distance $2h$ with periodic boundary conditions in the streamwise direction at $x = 0$ and $x = 2\pi$. The initial condition is

$$u^0(x, y) = 1 - (\frac{y}{h})^2 + \epsilon\hat{u} \tag{2.44}$$

$$v^0(x, y) = \epsilon\hat{v}, \tag{2.45}$$

where $(\hat{u}, \hat{v})$ corresponds to the only unstable eigensolution (wave number unity) of the Orr-Sommerfeld equation. The Reynolds number is $Re = U_c h/\nu = 7500$, based upon the centerline velocity, $U_c = 1$. A constant body force is applied to sustain the mean flow. The perturbation velocity is normalized to $|\hat{u}| = 1$ and ϵ is set to .00001.

According to the linear theory, the energy of the perturbation:

$$E(t) = \int_0^{2\pi} \int_{-1}^{1} \{(1 - y^2 - u)^2 + v^2\}\, dy\, dx \tag{2.46}$$

should grow as $e^{2\omega_i t}$, where $\omega_i = .002234976$. Following [77], we take as a measure of error the quantity: $error(t) = e^{2\omega_i t} - E(t_i)/E(0)$, where $E(t)$ is derived from the FOM and ROM solution at time $t = 200$. In addition, we compute the error in the growth rate at time $t = 200$ according to

$$error_g = \frac{1}{\omega_i} \left| \omega_i - \frac{1}{2\Delta t} \ln \left(\frac{E(200)}{E(200 - \Delta t)} \right) \right| \tag{2.47}$$

Table 2.1 shows the $error$ and $error_g$ for both FOM and ROM at $t = 200$. The growth-rate error for the ROM is about 0.04%, while for the FOM it is about 0.06%.

For pMOR, we can use this case to estimate the critical Reynolds number. To this end, Re = 7500 is selected as the single anchor (training) point to construct the G-ROM. The reduced basis is then constructed using the POD procedure with $K = 200$ snapshots. The G-ROM (2.31) is constructed using just $N = 2$ modes. (The 0th-mode in this case is the base parabolic profile of the Orr-Sommerfeld problem.)

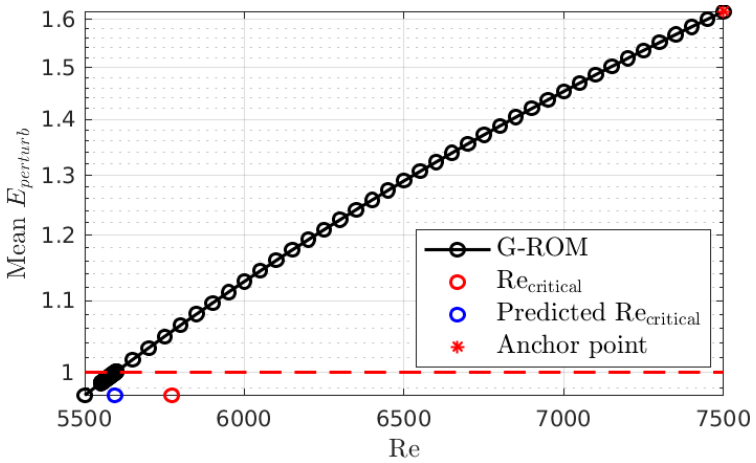

Figure 2.3: pMOR results with one anchor point at Re = 7500 in Orr-Sommerfeld problem: unstable eigensolution of the Orr-Sommerfeld equation, E_{perturb}, for the G-ROM. The anchor point used to construct the G-ROM is Re = 7500 and denoted as the red star sign. The $\mathrm{Re}_{\mathrm{critical}}$ for the linear stability analysis and G-ROM are denoted as red and blue circles. $E_{perturb} < 1$ is used as the criteria to determine the $\mathrm{Re}_{\mathrm{critical}}$.

With this setup, we adjust the parameters in (2.31) to run the ROM for $\mathrm{Re} \in [5500,\ 7500]$. We measure the mean energy of the unstable eigensolution of the Orr-Sommerfeld equation, $E_{\mathrm{perturb}} := E(t)/E(0)$ to estimate the critical Reynolds number $\mathrm{Re}_{\mathrm{critical}}$.

Fig. 2.3 shows the E_{perturb} for the ROM for $\mathrm{Re} \in [5500,\ 7500]$. The anchor point is denoted as the star sign. We use the criteria $E_{\mathrm{perturb}} < 1$, which indicates that the perturbation mode decays, to determine the $\mathrm{Re}_{\mathrm{critical}}$. With this criteria, $\mathrm{Re}_{\mathrm{critical}} = 5595$ is found with the G-ROM. Compared to the $\mathrm{Re}_{\mathrm{critical}} = 5772.6$ derived from the linear stability analysis. Again we find the pMOR is able to do a remarkable job in estimating the critical Reynolds number.

2.6 Stabilization

A significant issue with the standard G-ROM at higher Reynolds numbers is that (2.33)–(2.34) can deviate substantially from the projection of the modes onto the FOM due to the presence of potentially spurious attractors. This unstable behavior is an artifact of modal truncation (often manifest as energy pile-up in the high wavenumber modal coefficients) and relates to the well-known closure problem in LES and other turbulence-modeling scenarios [17, 78]. The smoothness of the approximating modes $\{\boldsymbol{\varphi}_n\}$ prevents generation of adequate dissipation (through $Re^{-1}(\boldsymbol{\varphi}_j, \boldsymbol{\varphi}_j)_A$) unless the corresponding coefficients have large amplitude. One can potentially resolve this issue by increasing N to the point where the reduced bases include modes capable of dissipating the energy. For turbulent flows, however, the number of

required modes can be quite high, particularly in light of the $O(N^3)$ costs associated with the advection operators C_u and C_T. Hence, for engineering applications, some closure model is typically required to dissipate energy or otherwise stabilize the ROM.

In this chapter, we present two stabilization approaches. The first is a relatively simple Leray-type regularization introduced in the ROM context by Wells *et al.* [28]. The second is the constraint-based ROM of Fick and co-workers [17].

2.6.1 Leray Regularization

The idea behind Leray regularization is filter the *advecting* field in the Navier-Stokes equations and energy equation through a low-pass filter function F:

$$\frac{\partial \widetilde{\mathbf{u}}}{\partial t} + (\overline{\mathbf{u}} \cdot \nabla)\widetilde{\mathbf{u}} + \nabla p \;=\; \nu \nabla^2 \widetilde{\mathbf{u}} + \eta\, \widetilde{T}\hat{\boldsymbol{g}}, \quad \nabla \cdot \widetilde{\mathbf{u}} \;=\; 0, \tag{2.48}$$

$$\frac{\partial \widetilde{T}}{\partial t} + (\overline{\mathbf{u}} \cdot \nabla)\widetilde{T} \;=\; \kappa \nabla^2 \widetilde{T}, \tag{2.49}$$

where $\overline{\mathbf{u}} = F(\widetilde{\mathbf{u}})$ is the result of some sort of smoothing or regularization of the current velocity field. As noted by Guermond *et al.* [79, 80], even just a small amount of regularization suffices to make gains in proving existence and uniqueness of the solution in the continuous case, a task that remains insurmountable for the full Navier-Stokes equations. Thus, Leray regularization is of interest both from a numerical (and physical) stabilization viewpoint and from a theoretical perspective.

The formulation of the G-ROM with Leray regularization would be to replace $\widetilde{\mathbf{u}}_\mathrm{r}$ by $\overline{\mathbf{u}}_\mathrm{r}$ in the momentum equation (2.31) and similarly in the energy equation (2.32) to yield

$$\int_\Omega \boldsymbol{v} \cdot \frac{d\widetilde{\mathbf{u}}_\mathrm{r}}{dt}\, dV + \nu \int_\Omega \nabla \boldsymbol{v} : \nabla \widetilde{\mathbf{u}}_\mathrm{r}\, dV = -\int_\Omega \boldsymbol{v} \cdot (\overline{\mathbf{u}}_\mathrm{r} \cdot \nabla)\, \widetilde{\mathbf{u}}_\mathrm{r}\, dV \;+\; \eta \int_\Omega \boldsymbol{v} \cdot (\widetilde{T}_\mathrm{r}\hat{\boldsymbol{g}})\, dV, \tag{2.50}$$

$$\int_\Omega S \frac{d\widetilde{T}_\mathrm{r}}{dt}\, dV + \kappa \int_\Omega \nabla S \cdot \nabla \widetilde{T}_\mathrm{r}\, dV = -\int_\Omega S\, (\overline{\mathbf{u}}_\mathrm{r} \cdot \nabla)\, \widetilde{T}_\mathrm{r}\, dV \;+\; \kappa \int_{\partial\Omega_f} S \nabla \widetilde{T}_\mathrm{r} \cdot \hat{\mathbf{n}}\, dA. \tag{2.51}$$

Throughout the dissertation, we interchangeably use the terms Leray ROM or L-ROM to refer (2.50–2.51).

Wells *et al.* [28] consider several possible filters to map $\widetilde{\mathbf{u}}_\mathrm{r}$ to $\overline{\mathbf{u}}_\mathrm{r}$. The simplest one, suggested by one of the authors , is to treat the POD modes as one would do with Fourier bases (personal communication, 2019). That is, one can simply damp out the amplitudes of the higher modes when constructing $\overline{\mathbf{u}}_\mathrm{r}$ in (2.50–2.51). One improvement is to consider a PDE- or (differential-) based filter (2.52), which is characterized by a filter width, δ [81]

and readily implemented in the POD bases by using (2.35) and (2.36). Following [28, 29], such filters are developed in a POD context as follows: *Given* $\widetilde{\mathbf{u}}_r = \sum_{j=1}^{N} u_{r,j}\boldsymbol{\varphi}_j(\mathbf{x})$, *find* $\overline{\boldsymbol{u}}_r(\mathbf{x}) = \sum_{j=1}^{N} \overline{u}_{r,j}\boldsymbol{\varphi}_j(\mathbf{x})$ *such that*

$$\left(\overline{\boldsymbol{u}}_{\mathrm{r}} - \delta^2 \Delta \overline{\boldsymbol{u}}_{\mathrm{r}}, \boldsymbol{\varphi}_i\right) = \left(\widetilde{\mathbf{u}}_{\mathrm{r}}, \boldsymbol{\varphi}_i\right) \qquad \forall\, i = 1, \ldots N, \tag{2.52}$$

where δ is the filter radius. This approach was shown in [28] to be superior to simple modal damping for three-dimensional flow past a cylinder at $Re = 1000$.

In the following Leray ROM examples, we consider a sharp cut-off filter in which we set a few of the highest-numbered basis coefficients to zero when constructing the advector, $\overline{\mathbf{u}}_{\mathrm{r}}$. Notice that this approach, while blunt, also has the advantage of reducing the leading-order $O(N^3)$ cost of evaluating the advection terms. As seen in the examples at the end of this section, simple Leray regularization is remarkably effective and merits further development.

In Chapter 3, we investigate Leray ROM with the differential filter (2.52) in a 2D unsteady parametric convection problem. In Chapter 4, we further investigate the differential and the higher-order algebraic filters with three regularized ROMs (Reg-ROMs) in turbulent channel flow and T-junction, including the Leray ROM introduced here.

2.6.2 Constrained Optimization

As an alternative to explicitly adding dissipation or other closure terms, Fick *et al.* [17] suggest a novel strategy of replacing the equality (2.33–2.34) with constrained minimization problems at each timestep that would keep the dynamical system near the attractors observed in the snapshot set.

The standard G-ROM (2.33–2.34) requires the following systems to be solved for the velocity and the temperature at each timestep,

$$H_u \underline{u}_{\mathrm{r}}^n = \underline{g}^n, \quad H_T \underline{T}_{\mathrm{r}}^n = \underline{Q}^n, \tag{2.53}$$

where the Helmholtz matrices are defined as,

$$H_u := \frac{\beta_0}{\Delta t} B_u \; + \; \nu\, A_u, \quad H_T := \frac{\beta_0}{\Delta t} B_T \; + \; \kappa\, A_T, \tag{2.54}$$

with B_u, B_T, A_u and A_T defined in (2.35–2.36) and (2.38–2.39). We note that H_u and H_T

are symmetric positive definite matrices. The right-hand sides are defined as

$$\underline{g}^n = -\sum_{i=1}^{k} \left[\frac{\beta_i}{\Delta t} B_u \underline{u}^{n-i} + \alpha_i \left(C_u \left(\widetilde{\underline{u}}_{\mathrm{r}} \right) \widetilde{\underline{u}}_{\mathrm{r}} - \eta \, B_{uT} \widetilde{\underline{T}}_{\mathrm{r}} \right)^{n-i} \right] - \nu \underline{a}_0. \tag{2.55}$$

$$\underline{Q}^n = -\sum_{i=1}^{k} \left[B_T \sum_{i=1}^{k} \frac{\beta_i}{\Delta t} \underline{T}_{\mathrm{r}}^{n-i} + \alpha_i \left(C_T \left(\widetilde{\underline{u}}_{\mathrm{r}} \right) \widetilde{\underline{T}}_{\mathrm{r}} \right)^{n-i} \right] - \kappa \, \underline{a}_{T,0} + \underline{q}_s. \tag{2.56}$$

The idea behind the constrained formulation is to use information from the snapshot set to establish *a priori* bounds on the basis coefficients $\underline{u}_{\mathrm{r}}^n$ and $\underline{T}_{\mathrm{r}}^n$ by replacing (2.53) with the constrained optimization problems,

$$\underline{u}_{\mathrm{r}}^n = \arg \min_{\underline{u}_{\mathrm{r}} \in \mathbb{R}^N} \frac{1}{2} \| H_u \underline{u}_{\mathrm{r}} - \underline{g}^n \|_2^2, \quad \text{s.t. } m_{u,j} \leq u_{\mathrm{r},j}^n \leq M_{u,j}, \tag{2.57}$$

$$\underline{T}_{\mathrm{r}}^n = \arg \min_{\underline{T}_{\mathrm{r}} \in \mathbb{R}^N} \frac{1}{2} \| H_T \underline{T}_{\mathrm{r}} - \underline{Q}^n \|_2^2, \quad \text{s.t. } m_{T,j} \leq T_{\mathrm{r},j}^n \leq M_{T,j}. \tag{2.58}$$

where the constraints on the basis coefficients $u_{\mathrm{r},j}^n$ and $T_{\mathrm{r},j}^n$, $j = 1, \cdots, N$ are derived from the observation snapshot set, $\mathbf{U}_K$ and $\overline{T}_K$, defined in Section 2.2.1. The constraint bounds are $m_{u,j} = \min_{\underline{\boldsymbol{u}}_k \in \mathbf{U}_K} (\boldsymbol{\varphi}_i, \boldsymbol{u}_k)$ and $M_{u,j} = \max_{\underline{\boldsymbol{u}}_k \in \mathbf{U}_K} (\boldsymbol{\varphi}_i, \boldsymbol{u}_k)$. The constraint bounds for the temperature are defined similarly with $m_{T,j} = \min_{\underline{T}_k \in \overline{T}_K} (\theta_i, T_k)$ and $M_{T,j} = \max_{\underline{T}_k \in \overline{T}_K} (\theta_i, T_k)$. These bounds amount to the ranges observed in the snapshot space. Hence it is making further use of the snapshot information. In this dissertation, we interchangeably use the terms constrained ROM or C-ROM to refer to (2.57–2.58).

2.7 Results for Stabilized Methods

In the following, we compare stabilized ROM (i.e., Leray-ROM and constrained ROM) with unstabilized ROM (i.e., Galerkin ROM) in three examples. We reiterate that our Leray ROM examples do not represent an exhaustive study of this approach, but are included merely to show the potential of this remarkably simple strategy, as put forth in [28]. A thorough investigation of the regularized ROMs in Chapter 4.

2.7.1 2D Lid-Driven Cavity

Following [17], we consider the following unsteady lid-driven cavity problem using parameter $\nu = \frac{1}{\mathrm{Re}}$ and $\eta = 0$ subject to steady boundary conditions.

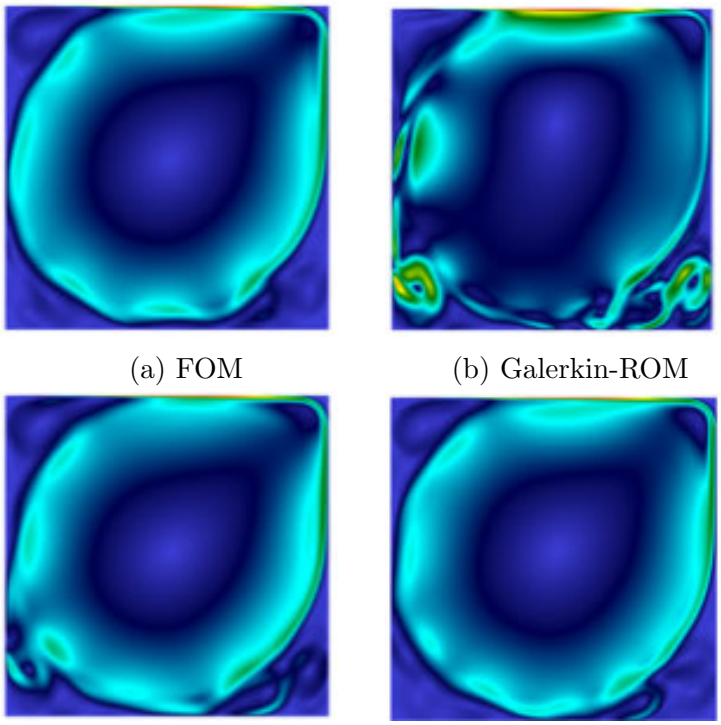

(a) FOM (b) Galerkin-ROM

(c) Leray-ROM (d) Constrained-ROM

Figure 2.4: 2D lid-driven cavity at $\mathrm{Re} = 30,000$: Velocity magnitude comparison at $t = 1740$ between the FOM, Galerkin, Leray, and constrained ROMs with $N = 20$.

$$\begin{cases} \boldsymbol{u} = \boldsymbol{u}_b & \text{on } \Gamma_{top} \times \mathcal{R}_+, \\ \boldsymbol{u} = 0 & \text{on } \partial\Omega \backslash \Gamma_{top} \times \mathcal{R}_+, \\ \boldsymbol{u} = 0 & \text{on } \Omega \times \{0\}, \end{cases} \tag{2.59}$$

where $\boldsymbol{u} : \Omega \times \mathcal{R}_+ \to \mathcal{R}^2$ is a two-dimensional vector field, $\Omega = [-1, 1]^2$, $\Gamma_{top} = \{\mathbf{x} \in \bar{\Omega} : x_2 = 1\}$, the Dirichlet datum is given by

$$\boldsymbol{u}_b(\mathbf{x}) = \begin{bmatrix} (1 - x_1^2)^2 \\ 0 \end{bmatrix}. \tag{2.60}$$

The FOM results were produced using Nek5000 [61] with 256 spectral elements of order $N = 7$ at $\mathrm{Re} = 30,000$. In order to generate the ROM solution, we collect 500 snapshots at the sampling times $\{t_s^k = 500 + \Delta t_s k\}_{k=1}^K$ with $\Delta t_s = 1$ and $K = 500$, where the data are taken from the statistically steady state solution. For the lid-driven cavity problem, we also apply the Leray regularization for the ROM. The velocity magnitude at time $t = 1740$ is shown in Fig. 2.4 for the FOM, Galerkin ROM, Leray ROM, and constrained ROM, each using $N = 20$.

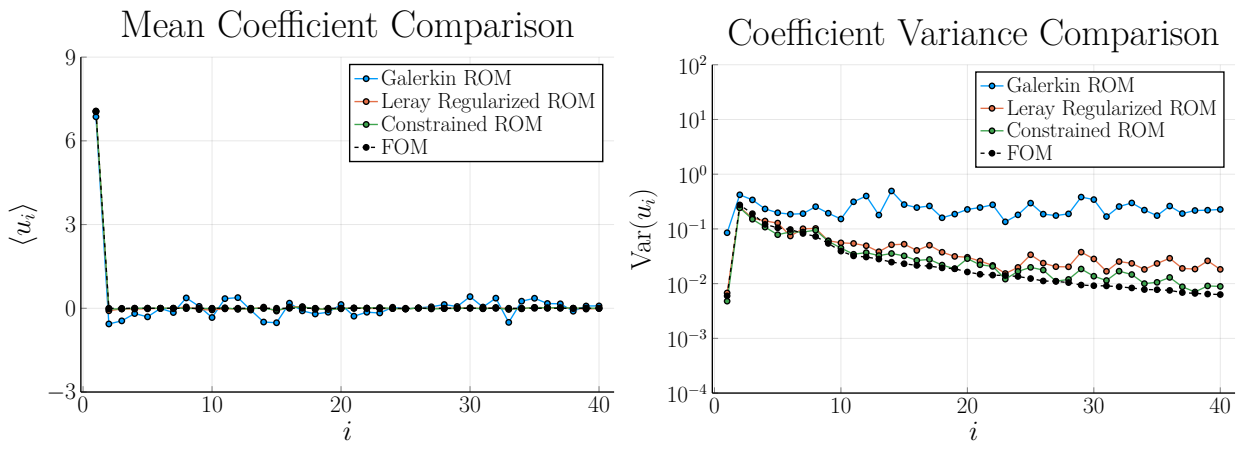

(a) Mean coefficient

(b) Coefficient variance

Figure 2.5: 2D lid-driven cavity at $\mathrm{Re} = 30,000$: Behavior of the sample mean and variance of the coefficients $\{u^n_{\mathrm{r},i}\}_i$ for the FOM, Galerkin, Leray and constrained ROMs with $N = 40$.

In Fig. 2.5, the sample mean and variance for the FOM, Galerkin, Leray, and constrained ROMs are compared. We found the results of the Leray and the constrained ROMs are superior to those of the Galerkin ROM.

In Fig. 2.6b, the estimated turbulent kinetic energy (TKE) of the FOM, Galerkin, Leray, and constrained ROMs with $N = 40$ are compared in which the TKE is defined as

$$\mathrm{TKE}(t) = \frac{1}{2} \int_\Omega \|\boldsymbol{u}(x,t) - \langle \boldsymbol{u} \rangle(x)\|_2^2, \tag{2.61}$$

where $\|\cdot\|_2$ is the Euclidean norm [1].

For the Leray ROM, the last 50% of the modes are set to zero. Note that the percentage of modes to be filtered is not known beforehand. For this problem, we have tried filtering out 10%, 20%, 30%, 40% and 50%, and found that 50% produced the most accurate results. The question of optimal filter choice depends on the number of POD modes and on the problem and will be a topic of future study.

To further demonstrate the effects of stabilization, we plot the coefficient behavior versus time. Figure 2.6a clearly shows that, without regularization, the coefficient for the first POD basis function ventures out of the range observed in the data. Other spurious phenomena include effects such as false stable steady flows.

As thermal transport is one of our principal motivators, we consider an energy transport problem using parameter $\kappa = \frac{1}{\mathrm{Re}}$ with the solution to the lid-driven cavity problem as the

[1]Technically, because these flows are not turbulent the TKE should be referred to as velocity variance. Because the is more widely used and the mathematical formulation is the same in either case, we prefer to use the more widely recognized appellation, TKE

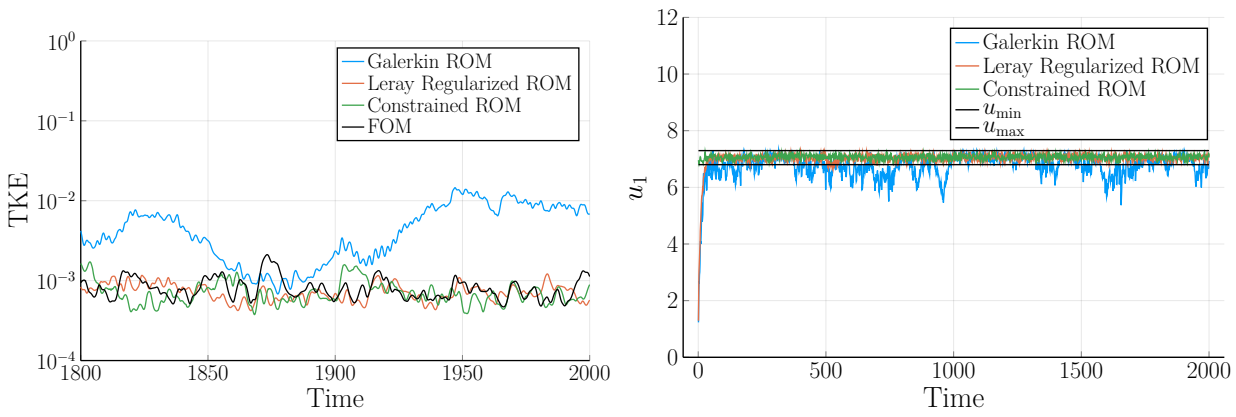

(a) TKE behavior in time

(b) First mode behavior in time

Figure 2.6: 2D lid-driven cavity at $\mathrm{Re} = 30,000$: (a) TKE behavior comparison for the FOM, Galerkin, Leray and constrained ROMs with $N = 40$; (b) Comparison of the first mode behavior for various stabilization techniques with $N = 40$.

advecting field. The thermal boundary conditions are:

$$\begin{cases} T(x,-1,t) = 0, \\ T(x,1,t) = 1, \\ T(x,-1,t) = T(x,1,t) = 1. \end{cases} \tag{2.62}$$

The QOI is the Nusselt number, which is the mean temperature gradient

$$Nu = \frac{\int_{\Gamma_{top}} \nabla T \cdot \hat{n} dS}{\int_{\Gamma_{top}} dS}. \tag{2.63}$$

In Fig. 2.7, the Nu history for the FOM and the G-ROM is presented for different values of N. We observe that, even with the standard Galerkin approach, the accuracy of the QOI can be recovered as the number of modes increases from $N = 10$ to 80. Figure 2.8, however, illustrates that both the L-ROM and the C-ROM can achieve accurate Nu with much lower N (as low as 10) than the G-ROM.

2.7.2 3D Rayleigh-Bénard Convection

Three-dimensional thermal transients are of great importance to many thermal-hydraulic design questions and are thus of primary interest in our own ROM development efforts. Here, we test the ROM strategies on a 3D Rayleigh-Bénard problem in a box with aspect ratios $W : W : H$, where $W = 1$ and $H = 4$. The parameters are $Pr = 0.71$ and

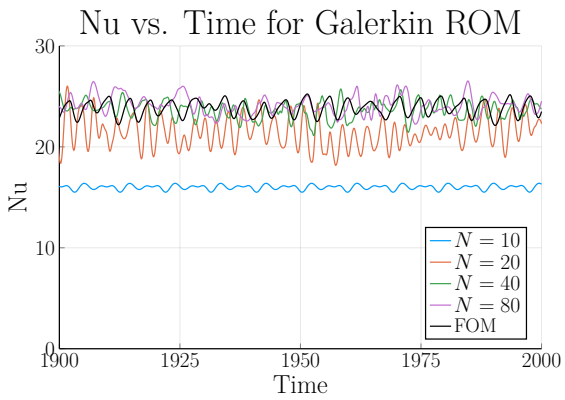

Figure 2.7: 2D heated lid-driven cavity: Nusselt number history for the Galerkin ROM with various N values.

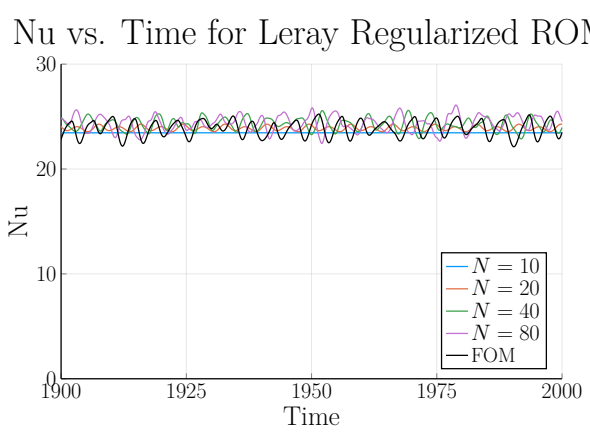

(a) Nu behavior of Leray ROM

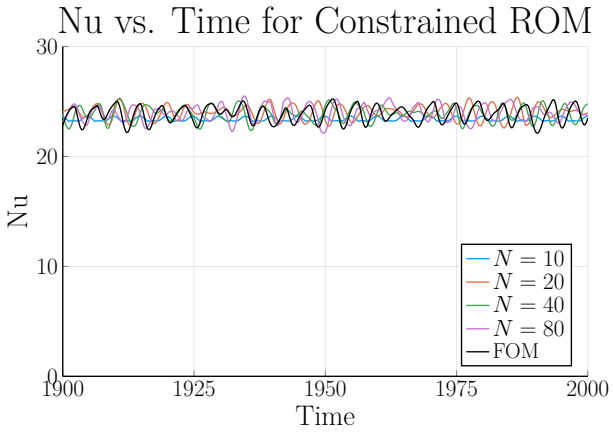

(b) Nu behavior of constrained ROM

Figure 2.8: 2D heated lid-driven cavity: Nusselt number vs. time for the (a) Leray ROM and (b) the constrained ROM for various N values.

$Ra = 1.1e5, 1.1e6$ and $1.1e7$, which are implemented in (2.1)–(3.2) in convective time units by setting $\nu = (Pr/Ra)^{\frac{1}{2}}$, $\kappa = (Pr\,Ra)^{-\frac{1}{2}}$, and $\eta = 1$. The boundary conditions for velocity are no-slip on all walls. For temperature, the side-walls are insulated ($\nabla T \cdot \hat{\mathbf{n}} = 0$) and constant temperature on top and bottom, $T(x, y, z = \mp 2) = \pm 1$. Our FOM is based on the formulation in Nek5000 using an $8 \times 8 \times 32$ array ($x \times y \times z$) of 9th-order spectral elements. The FOM is based on 3rd-order semi-implicit timestepping with variable Δt set such that the Courant number is approximately 0.5 throughout the simulation, including the thermal transient.

Because this flow is three-dimensional and run at relatively high Rayleigh numbers the number of degrees of freedom is much greater than in the previous examples and these cases thus present a greater challenge for reduced-order modeling. Figure 2.9 gives some indication

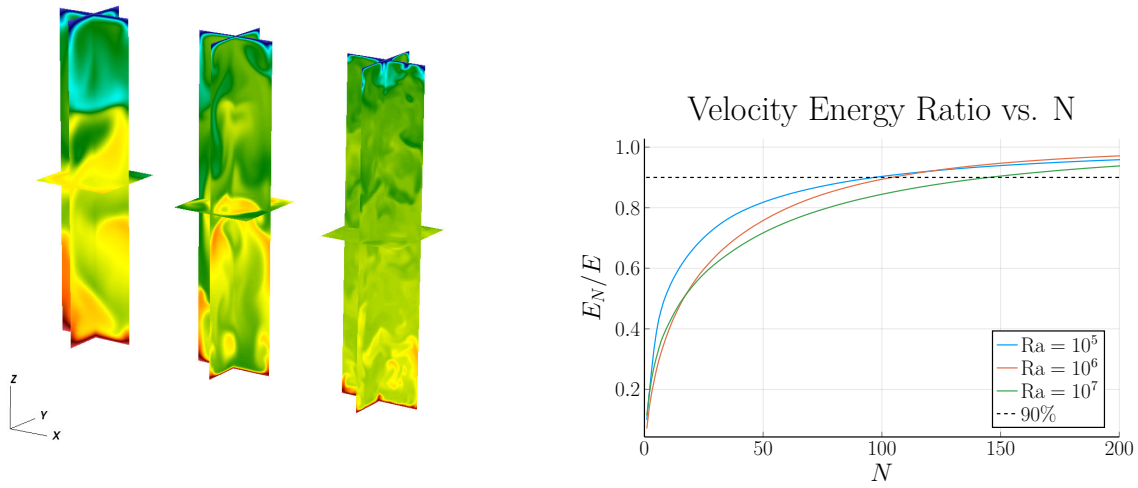

Figure 2.9: (Left) Cross section at $x = 0$, $y = 0$ and $z = 0$ for FOM temperature at time $t = 1292$ with $Ra = 1.1e5, 1.1e6$ and $1.1e7$. (Right) Cumulative energy contribution of velocity POD modes for various Rayleigh numbers. The dotted line represents $E_N/E = 0.9$ where $E_N = \sum_{j=1}^{N} \lambda_j^2$ and $E = \sum_{j=1}^{K} \lambda_j^2$ where K is the number of snapshots and λ_i are the i-th eigenvalue of the Gramian.

of the number of active modes in the system in the fully-developed (statistically steady-state) regime as a function of Ra. On the left, we plot instantaneous temperature distributions from the FOM, and on the right we plot the fraction of energy, E_N/E captured by the POD bases from 1000 snapshots taken in the fully-developed flow regime. Here, $E_N = \sum_{j=1}^{N}(\boldsymbol{\varphi}_j, \boldsymbol{\varphi}_j)$, and $E := E_{1000}$.

From Fig. 2.9, right, we see that about 150 modes are required to capture 90% of the energy at $Ra = 1.1e7$. We have computed the critical Rayleigh number for this case (the point at which $\|\boldsymbol{u}\| > 0$) and find $Ra_c \approx 1559$, which makes the corresponding ratios for our three cases to be $r = Ra/Ra_c \approx 70$, 700, and 7000. Sirovich and Deane [82] find that $N \approx 200$ modes are required for $E_N/E = 90\%$ when $r = 30$, which is a significantly more pessimistic outcome than our findings. Their case, however, corresponded to a unit-cube domain with periodic boundary conditions, which would support more degrees of freedom than our relatively narrow domain with walls. More recently, Puragliesi and Leriche [83] examined the spectrum for $Ra = 10^9$ in a unit cube with homogeneous Dirichlet conditions on all walls for the case where the side walls were differentially heated ($T(x = \pm\frac{1}{2}, y, z) = \pm\frac{1}{2}$.). In this case, they found that $N = 30$ sufficed to capture 90% of the energy. More importantly, Puragliesi and Leriche noted that the basis vectors that account for the majority of the heat flux are not the most energetic POD eigenfunctions, which implies that there is potential for

a more judicious choice of basis functions when pMOR is employed for thermal transport problems.

In the present case, we are particularly interested in using the ROM (and, ultimately, pMOR) to capture thermal transients as rise time is of great interest in many thermal-hydraulics applications. To this end, we take as our QOI the mean temperature

$$\langle T \rangle(t)_{xyz} \quad := \quad \frac{\int_\Omega T(\mathbf{x}, t)\, dV}{\int_\Omega \, dV}. \tag{2.64}$$

The FOM starts with random fluctuations across all ($\mathcal{N} \approx 1.5$M) gridpoints, uniformly distributed on $[-1, 0]$. This "cold" flow is then subject to boundary conditions ± 1 at time $t = 0+$, such that the mean should rise to $\langle T \rangle(t)_{xyz} \approx 0$. For the ROM, we take as the base state the first of the snapshots, which occurs at time $t \approx 1$.

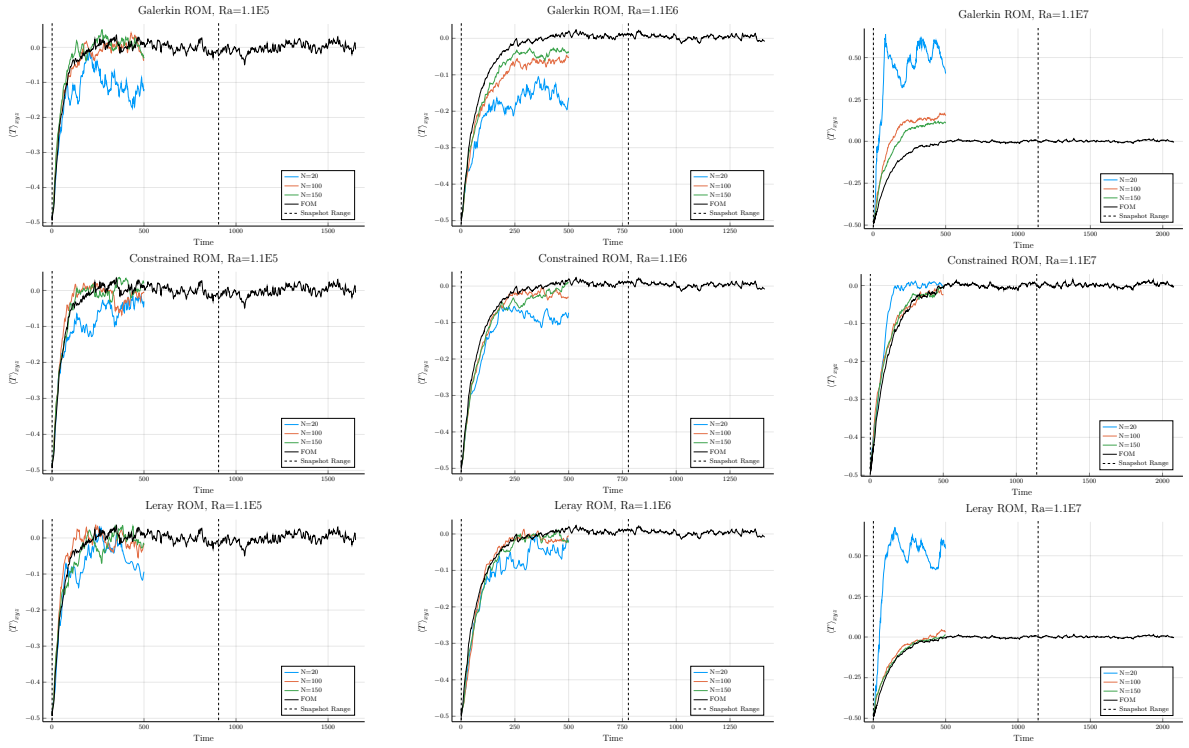

Figure 2.10: 3D Rayleigh-Bénard convection: Average temperature vs. time with $Ra = 1.1e5, 1.1e6$ and $1.1e7$ for the Galerkin, constrained, and Leray ROMs with various N values. 70% of modes are filtered out in Leray ROM. 1000 snapshots are taken between the two vertical dotted lines which includes the transient and statistically steady state region.

Fig. 2.10 shows the transient behavior of $\langle T \rangle(t)_{xyz}$ for the Galerkin, constrained, and Leray ROMs at each of the three Rayleigh numbers. For Leray, we have tried filtering 10%, 30%, 50% and 70% of the modes report the results for the 70% case. Note that for different Ra,

the optimal percentage to be filtered is different. For $Ra = 1.1e5$, all three formulations do a reasonable job of tracking the rise times for $N \geq 100$ modes. For $N = 20$, the Galerkin and constrained ROM do not do well while, surprisingly, the Leray ROM is able to produce a mean temperature that is comparable to constrained ROM. Furthermore, with 50% filtering (not shown), the Leray ROM with $N = 20$ is able to produce a even better mean temperature and is comparable to $N \geq 100$ modes. For $Ra = 1.1e6$, only the constrained and Leray ROM are able to track the QOI for $N = 100$ and 150. Moreover, the Leray ROM with 50% and 70% of modes filtered are able to track the QOI for $N = 20$. For $Ra = 1.1e7$, the Leray ROM is not stable for $N = 20$ with 70% of modes filtered (nor with 10%, 30% or 50%). While not terribly accurate in predicting the rise time, the constrained ROM is the only case that is stable for $N = 20$. Both the constrained and Leray approaches are accurate for $N \geq 100$.

In Fig. 2.11, left, we compare $\langle T \rangle$ for $Ra = 1.1e7$ with 1000 snapshots taken in the statistically steady-state region, using the average of the snapshots as the base mode. As the figure shows, without constraints, the mean temperature has more oscillations due to the lack of dissipation. For $N = 20$, the constrained and Leray ROMs produce a better QOI than the Galerkin ROM with $N = 100$. We also plot in the column on the right of Fig. 2.11 the turbulent kinetic energy (TKE) without zeroth mode, which we denote as $E_J := \frac{1}{2}\sum_{j=1}^{N} u_j^2$. We can see clearly that, even with $N = 100$, the Galerkin ROM drastically over-predicts the TKE. Note that we also observe over-prediction of TKE in the Leray ROM. In this case, even the constrained case shows an over-prediction of the TKE by about a factor of 2–3, which indicates that more modes are likely needed to capture this particular QOI. The fact that the thermal QOIs of Fig. 2.10 are in good agreement with the FOM is supportive of the suggestions of Puragliesi and Leriche [83] that TKE is not necessarily directly correlated with the modes governing thermal transport.

2.8 Conclusions

In this chapter, we have presented key components towards the development of a reduced-order modeling (ROM) capability, aiming to harness the output of high-fidelity simulations on leadership computing facilities for thermal-hydraulic design studies.

For the parametric problem, we have demonstrated the effectiveness of the p-greedy model-order reduction procedure in the 2D flow past a cylinder and the Tollmien-Schlichting waves and its capability of predicting quantities of interests such as drag coefficient and its variance and the critical Reynolds numbers.

At higher Rayleigh (or Reynolds) numbers, stabilization is required for the Galerkin ROM. We have demonstrated that Leray and constraint-based regularization generate more stable

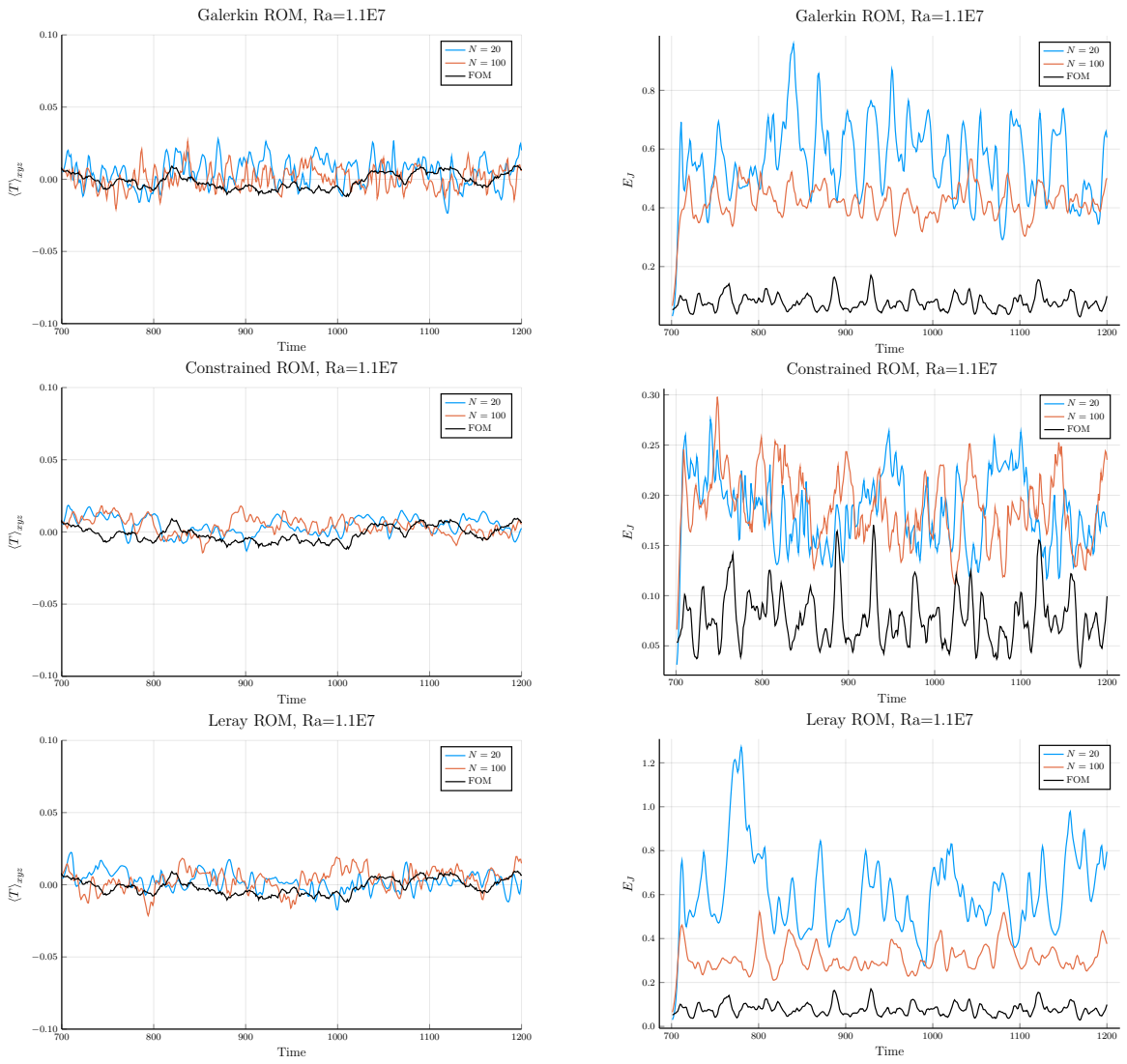

Figure 2.11: 3D Rayleigh-Bénard convection: Left: Average temperature vs. time with $Ra = 1.1e7$ for the Galerkin, constrained, and Leray ROMs with various N values. Right: Turbulent kinetic energy (TKE) without the zeroth mode vs. time with $Ra = 1.1e7$ for the Galerkin, constrained and Leray ROMs with various N values. 70% of modes are filtered out in Leray ROM.

and accurate solutions than the standard Galerkin ROM formulation. Examples demonstrated that the constraint-based approach, which incorporates prior information about the long-time attractor in the ROM, can produce accurate transient solutions in 3D Rayleigh-Bénard convection at $Ra = 1.1e7$.

Despite the success of the methods shown here, several developments remain to make pMOR viable for analysis and engineering design in turbulent-thermal transport applications: (1) Development of error indicators specific to pMOR in turbulent-thermal transport applications.

(2) Stabilization methods for turbulent flows. (3) Mitigation of the $\mathcal{O}(N^3)$ computational cost to enable the use of larger N values for turbulent flows. We address the three tasks in the following Chapters.

Chapter 3: Error-Indicated Parametric Model Order Reduction for Unsteady Convection

In this chapter, we develop a time-averaged error indicator with POD-hGreedy to drive the parametric model order reduction (pMOR) for a challenging 2D natural convection problem in a high-aspect ratio slot parameterized with the Prandtl number, Rayleigh number, and slot angle with respect to the gravity. The time-averaged error indicator is investigated with several reduced-order models (ROMs) and is extended to accommodate the energy equation and Leray regularization. Our numerical results demonstrated that Leray-regularized Galerkin ROMs provide a robust solution approach for this class of flows, and the error-indicated pMOR can efficiently predict several QOIs, even in the presence of a bifurcation. Finally, we show that spatio-temporal chaos can lead to a lack of reproducibility in both the full-order and the reduced-order models and that the full-order model's variance provides a lower bound on the pMOR error in these cases.

The chapter is organized as follows. In section 3.1, we introduce the model problem and governing equations. In section 3.2, we consider the solution reproduction problem and assess the performance of the ROMs. The parametric problem is discussed starting in section 3.3. We first introduce POD-hGreedy algorithms in section 3.3.1 with some remarks on applying POD-pGreedy to this model problem at the end of the section. We then introduce the time-averaged error indicator with thermal extension in section 3.3.2. A straightforward integration with Leray regularization is also shown in the same section. In sections 3.3.3 and 3.3.4, we present the pMOR results with θ_g variation and Ra variation. In section 3.4, we discuss the spatio-temporal chaos and multiple states issues found in this model problem. Finally, we conclude the chapter in section 3.5. Most of the contents in this chapter appear in the paper "Parametric model-order-reduction development for unsteady convection" published in Frontiers in Physics [27].

3.1 A Parametrized Natural Convection Problem

We start with the Boussinesq equations for buoyancy-driven flow [84],

$$\frac{\partial \boldsymbol{u}}{\partial t} + (\boldsymbol{u}\cdot\nabla)\boldsymbol{u} + \nabla p = \nu\nabla^2\boldsymbol{u} + T\boldsymbol{g}(\theta_g), \qquad \nabla\cdot\boldsymbol{u} = 0, \tag{3.1}$$

$$\frac{\partial T}{\partial t} + (\boldsymbol{u}\cdot\nabla)T = \kappa\nabla^2 T, \tag{3.2}$$

where $\boldsymbol{u}$ is the velocity, p is the pressure, T is the temperature and $\boldsymbol{g}(\theta_g)$ is the unit vector represents the direction of the buoyancy force and it is defined by $\boldsymbol{g}(\theta_g) = \cos(\theta_g)\hat{\imath} + \sin(\theta_g)\hat{\jmath}$, with θ_g the angle of the slot with respect to the gravity. The velocity boundary conditions are no-slip ($\boldsymbol{u} = 0$). The temperature boundary conditions are no-flux (insulated) on the top and bottom, heated ($T = 1$) on the left wall, and cooled ($T = -1$) on the right wall. The initial conditions are $\boldsymbol{u} = 0$ and $T = 0$.

In our non-dimensional setting, we set $\nu = (\mathrm{Pr}/\mathrm{Ra})^{1/2}$ and $\kappa = (\mathrm{Pr}\,\mathrm{Ra})^{-1/2}$. The Rayleigh number, $\mathrm{Ra} = \rho\beta g H^3 \Delta T/(\nu\kappa)$, represents the ratio of buoyancy force to thermal and momentum diffusive force The Prandtl number $\mathrm{Pr} = \nu/\kappa$, reflects the relative importance of momentum diffusivity compared to thermal diffusivity. With this nondimensionalization the characteristic velocity is $U_c = \sqrt{\beta g H \Delta T}$, the characteristic length is the slot width H, and the reference time is $t_r = H/U_c$. The temperature is made dimensionless by subtracting the temperature on the right wall and scaling with $\Delta T = 2$. We note that U_c is sometimes referred to as the "free-fall" velocity, indicating that one might expect $\|\boldsymbol{u}\| \approx 1$, with only a weak dependence on Ra. While that expectation is realized for $\theta_g = 0$, we in fact see much larger velocities ($\|\boldsymbol{u}\| \approx 40$) for $\theta_g = 90°$ because the domain height $L = 40H$ in that case.

The problem is characterized by four parameters, the Rayleigh number, Ra, the Prandtl number, Pr, the slot angle with respect to gravity, θ_g, and the aspect-ratio, Γ. However, for small aspect ratios, $\Gamma \leq 8$, we find the flow is rather simple. Hence in this work, we focus on the more challenging case of $\Gamma = 40$ with ($\mathrm{Pr},\ \mathrm{Ra},\ \theta_\mathrm{g}$) as the parameter space.

Figure 3.1 **A** illustrates the problem configuration. The aspect ratio is defined as $\Gamma = L/H$, where H is the width of the slot and L is the height of the slot. We take $H = 1$ and $L = 40$ throughout the study. With $\theta_g = 0°$ the flow corresponds to standard Rayleigh-Bénard convection, 90° corresponds to vertical slot convection, and $\theta_g = 180°$ leads to a pure conduction solution with the cold side on the bottom of the horizontal slot. Figure 3.1 **B** illustrates representative mean (or steady) temperature fields for 19 uniformly-spaced $\theta_g \in [0°,\ 180°]$ at $\mathrm{Ra} = 10^4$ and $\mathrm{Pr} = 7.2$. Figure 3.1 **C** shows the mean temperature field for 6 uniformly-spaced $\mathrm{Ra} \in [2 \times 10^5,\ 7 \times 10^5]$ at $\theta_g = 90°$ and $\mathrm{Pr} = 7.2$. The configuration has many interesting applications. For example, it represents energy-efficient double-glazed windows, in which the sealed air gap between the two panes acts as an added layer of insulation. Finding the optimum angle θ_g that enhances the heat transfer is an important question. Convection in a tilted fluid layer is also of meteorological and oceanographic interest. More information on the impact of θ_g and Γ on heat transport and flow organization for this configuration can be found in [85].

For unsteady problems, the QOIs are the mean flow, mean Nu, standard deviation in Nu, mean TKE and mean temperature fluctuation. The symbol $\langle\cdot\rangle$ is used to indicate a

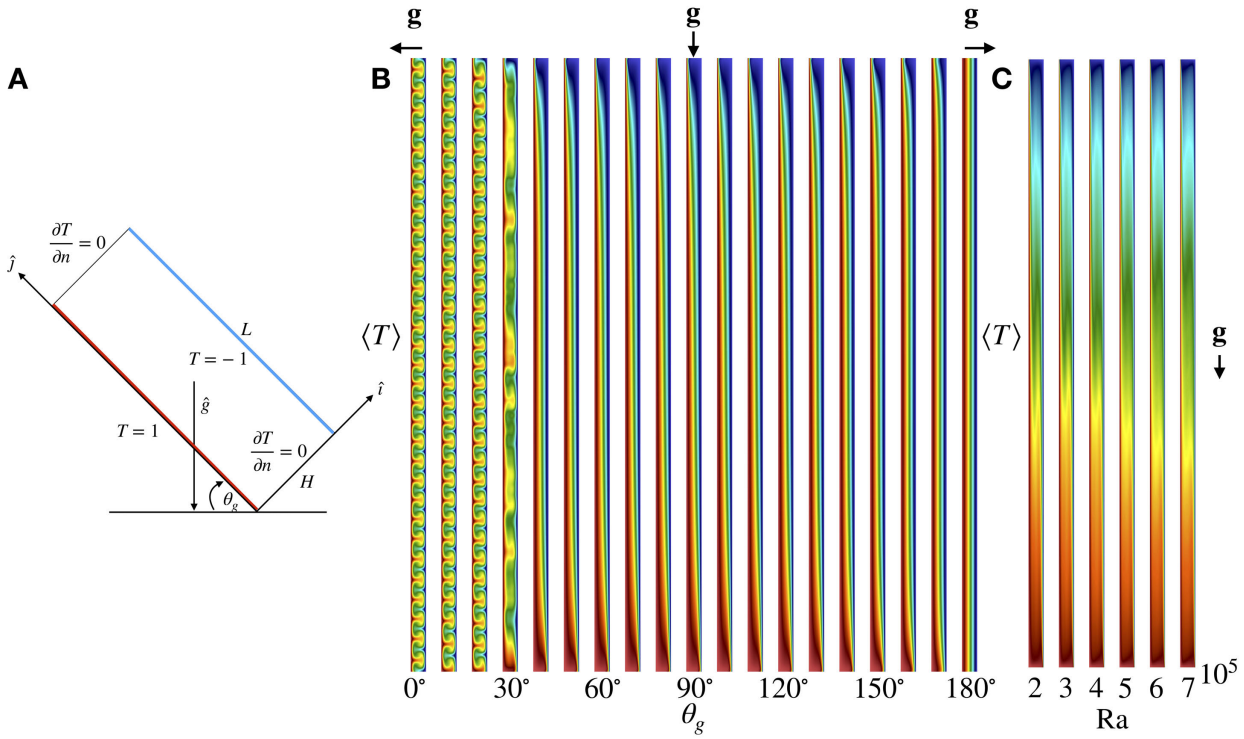

Figure 3.1: **(A)**: Problem configuration. **(B)**: FOM mean (or steady) temperature for 19 uniformly-spaced $\theta_g \in [0°,\ 180°]$ at $\mathrm{Ra} = 10^4$ and $\mathrm{Pr} = 7.2$. **(C)**: FOM mean temperature for 6 uniformly-spaced $\mathrm{Ra} \in [2 \times 10^5,\ 7 \times 10^5]$ at $\theta_g = 90°$ and $\mathrm{Pr} = 7.2$.

time-averaged quantity. The mean velocity and temperature field are defined as:

$$\langle \boldsymbol{u} \rangle = \frac{1}{J - J_0} \sum_{j=J_0+1}^{J} \boldsymbol{u}(t^j), \qquad \langle T \rangle = \frac{1}{J - J_0} \sum_{j=J_0+1}^{J} T(t^j), \tag{3.3}$$

with $t^j = j\Delta t$ and Δt being the time step. The selection of J_0 is based on when the solution reaches it statistically steady state. The mean quantities are then averaged over 500 CTUs, with the time scale defined above. The instantaneous Nusselt number is defined as

$$\mathrm{Nu}(t) = \frac{q''_w}{k(\Delta T)/H}, \tag{3.4}$$

with $q''_w = -\int_{\partial\Omega_h} k \nabla T \cdot \hat{\mathbf{n}}\, dS$ being the integrated heat flux on the heated wall, $\partial\Omega_h$. The mean Nu and the its standard deviation are then defined as

$$\langle \mathrm{Nu} \rangle \coloneqq \frac{1}{J - J_0} \sum_{j=J_0+1}^{J} \mathrm{Nu}(t^j), \quad \mathrm{Std}(\mathrm{Nu}) \coloneqq \sqrt{\frac{1}{J - J_0} \sum_{j=J_0+1}^{J} \big(\mathrm{Nu}(t^j) - \langle \mathrm{Nu} \rangle\big)}. \tag{3.5}$$

The mean TKE and mean temperature fluctuation are defined as

$$\langle \text{TKE} \rangle = \frac{1}{2(J-J_0)} \sum_{j=J_0+1}^{J} \|\boldsymbol{u}(t^j) - \langle \boldsymbol{u} \rangle\|_{L^2}^2, \quad \langle T_{\text{fluc}} \rangle = \frac{1}{J-J_0} \sum_{j=J_0+1}^{J} \|T(t^j) - \langle T \rangle\|_{L^2}^2. \tag{3.6}$$

For steady problems, the QOIs are simply the steady solutions to (4.18)–(3.2) and the corresponding Nu using (3.4).

In the current FOMs for the slot problem we use $E = 516$ elements (an array of 6×86 in the $H \times L$ directions), of order $q = 9$, for a total of $\mathcal{N} \approx 42000$ grid points. The FOM simulations are performed using the open-source code Nek5000 [61].

3.2 The Solution Reproduction Problem

As the first step towards the development of a ROM for the parametric problem, we start with the solution reproduction problem. In this section, we consider the solution reproduction problems for $\text{Ra} = 2 \times 10^5,\ 7 \times 10^5$ at $\text{Pr} = 7.2$ and $\theta_g = 90°$, where the solutions are chaotic. We assess the performance of the G-ROM (2.31–2.32), the C-ROM (2.57–2.58) and the LDF-ROM (2.50–2.51) with differential filter introduced in Sections 2.1 and 2.6 through the accuracy of the mean field and the QOIs. The mean field is computed by averaging the POD coefficients and reconstructing with the POD basis. The QOIs are the mean Nu and Std(Nu), which are estimated through (3.5), and the mean TKE and mean temperature fluctuation, estimated through (3.6). The quantities are averaged over 500 CTUs.

Although of limited practical interest, the solution reproduction problem is an important step towards the development of a MOR procedure for the parametric problem. The reproduction results for spatio-temporal chaotic flow are presented and discussed in section 3.4.1.

3.2.1 Numerical Results

Results for $\text{Ra} = 2 \times 10^5$ are shown in Figs. 3.2 **A**–**D**. The performances of the G-ROM, the C-ROM and the LDF-ROM are indicated by blue, orange, green solid line. In the LDF-ROM, the radius of the differential filter is $\delta = 0.015625$. Figure 3.2 **A** shows the behavior of the relative $\mathcal{H}^1$ error in the mean flow prediction versus N. We observe less than 1% error in the C-ROM with small N. The error in the G-ROM and the LDF-ROM decreases as N increases and eventually reaches 1% with $N = 100$. Similar trends for the mean Nu, the Std(Nu) and the mean temperature fluctuation are observed in Figures 3.2 **B**–**D**. The FOM data is denoted as black solid line. For the mean Nu prediction, we observe around 0.1%

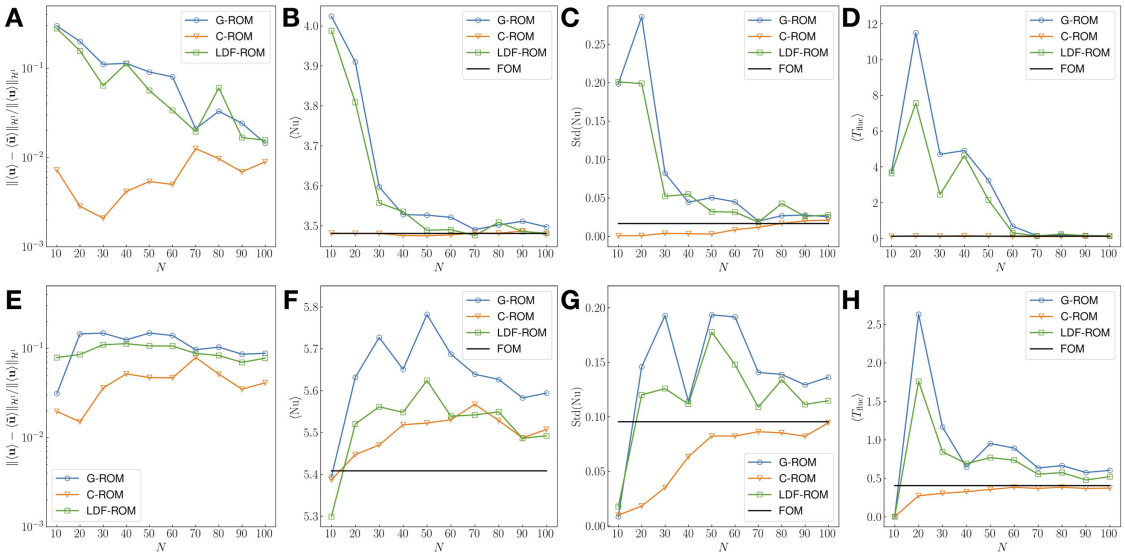

Figure 3.2: The solution reproduction problem at $\theta_g = 90°$ and Pr = 7.2: Performance comparison between G-ROM, C-ROM and LDF-ROM. **(A–D)**: behavior of the relative $\mathcal{H}^1$ error in mean flow prediction, predicted mean Nu, Std(Nu), and mean temperature fluctuation as a function of number of modes, N at Ra $= 2 \times 10^5$ ($\delta = 0.015625$ in the LDF-ROM). **(E–H)**: performance for the same quantities at Ra $= 7 \times 10^5$ ($\delta = 0.03125$ in the LDF-ROM).

error in the C-ROM for almost all N. The error in G-ROM and LDF-ROM decreases as N increases and the LDF-ROM has error around 0.01% with $N = 100$. For the Std(Nu) and the mean temperature fluctuation prediction, we observe convergence in both QOIs with the G-ROM and the LDF-ROM. For the C-ROM, the predictions are in good agreement with the FOM data for all values of N. Behaviors of the same quantities for Ra $= 7 \times 10^5$ are shown in Figs. 3.2 **E–H**. In the LDF-ROM, the radius of the differential filter is $\delta = 0.03125$. We still observe convergence in the mean flow and QOIs but it is much slower because the flow is more chaotic. The error in the mean flow is around 10% in the G-ROM and the prediction in QOIs are over-estimated and less accurate than for the other methods. With the LDF-ROM, the predictions are slightly better. The C-ROM is still the most effective and has 5% error in mean flow prediction. Although the prediction in mean Nu is only as good as the LDF-ROM, the Std(Nu) and mean temperature fluctuation are bounded from above for all values of N and converge to the correct value as N increases.

Note that the differential filter radius δ selected for the two Ra yields the best accuracy in mean flow among the five differential filter radius $\delta = 0.25,\ 0.125,\ 0.0625,\ 0.03125,\ 0.015625$. Besides, we find $\delta = 0.015625$ yield the best results at smaller Ra and as Ra increases, results of $\delta = 0.03125$ becomes better and are comparable with $\delta = 0.015625$ at Ra $= 7 \times 10^5$. The

tendency is reasonable because the flow is more chaotic as Ra increases, therefore one should expect a larger δ to stabilize the flow.

From the results, we observe the mean flow and QOIs converge with N for all ROMs. With higher Ra, convergence in those quantities is much slower and a larger N is required to reach to the same accuracy as in the lower Ra case. Note that, because of the $O(N^3)$ online costs, requiring a large value of N for convergence might require off-line resources for timely simulation, which would greatly diminish the intrinsic advantage of the ROM/pMOR framework. This potentiality highlights the importance of stabilization methods. Indeed, we find that the C-ROM is able to predict the mean flow and QOIs with a better accuracy with smaller N. On the other hand, although the LDF-ROM is not as effective as the C-ROM, and only slightly better than the G-ROM, it will play a key role in the pMOR presented in section 3.3, especially in the parametric problem with θ_g variation.

3.3 The Parametric Problem

The pMOR development is broken into two sets of parametric problems: (i) problem parameterized with θ_g at higher Ra. (ii) problem parameterized with Ra. In the first set, a bifurcation is observed and the solution space is a blend of steady and unsteady solutions. In the second set, no bifurcation is observed and the solutions are all unsteady.

By proceeding in this manner, we are able to isolate several difficulties and eventually come up with an important observation for the pMOR: Accurate prediction ($< 10\%$) with pMOR is achievable if the solution in the parametric space is either only chaotic or the spatio-temporal chaos is not significant, regardless a bifurcation exists or not. Once the spatio-temporal chaos becomes significant, the performance of the pMOR deteriorates and the maximum errors of the mean flow and QOIs are dominated by the flow chaos.

We turn now to study the performance of pMOR for the slot problem with the G-ROM, the C-ROM, and the LDF-ROM. Two sets of parameterization are considered. With $\mathrm{Pr} = 7.2$ fixed, we seek to estimate the solution and QOIs of (2.8) and (2.10) for: (i) $\theta_g \in \mathcal{P} = [0^\circ,\ 180^\circ]$ at multiple Ra, and (ii) $\mathrm{Ra} \in \mathcal{P} = [2 \times 10^5,\ 7 \times 10^5]$ with $\theta_g = 90^\circ$. Throughout, we take the lifting functions to be the zero velocity field and the heat conduction solution.

For efficient selection of the pMOR anchor points we consider the POD-hGreedy algorithm proposed in [17] which combines POD in time with Greedy in parameter. The term Greedy refers to the optimization strategy of basing anchor point selection on the training point that exhibits the largest value in the error estimate. Error-indicated selection of the anchor points reduces the number of FOM solves and is thus critical for the feasibility of pMOR. Here, the error indicator corresponds to the dual norm of the residual associated with the

time-averaged momentum and energy equations.

The section is organized as follows. In section 3.3.1 we present the POD-hGreedy algorithm. In section 3.3.2, we extend the time-averaged error indicator introduced in [17] to accommodate the energy equation and Leray regularization. Finally, in sections 3.3.3 and 3.3.4, we present the numerical results.

3.3.1 POD-hGreedy Algorithm

In this section, we present the POD-hGreedy algorithm for the construction of the reduced spaces $\{\mathbf{X}_{0,\ell}^N, X_{0,\ell}^N\}_{\ell=1}^L$, and the partition $\{\mathcal{I}_\ell\}_{\ell=1}^L$ of $\mathcal{P}$, based on the results of L full-order simulations associated with the parameters $p_1^*, \ldots, p_L^*$. The algorithm is similar to the one in [17] but with extensions for thermal fields.

To begin, we introduce the discretized parameter space $\mathcal{P}_{\text{train}} = \{p_i\}_{i=1}^{n_{\text{train}}}$, $p_1 \leq \ldots \leq p_{n_{\text{train}}}$, the integers L which fix the maximum number of offline solves, the integer $n_{\text{cand}} < L$, which is the number of ROM evaluations performed online for a given value of the parameters, and an error indicator Δ. The error indicator takes as input sequences $\{\overline{\mathbf{u}}_{\text{r}}^n\}_{n=0}^J$ and $\{\overline{T}_{\text{r}}^n\}_{n=0}^J$ and the value of the parameter, p^*, and returns an estimate of the error in the prediction of the mean flow. We formally present the indicator in section 3.3.2.

Algorithm 3.1 presents the computational procedure for both offline and online stage. The offline procedure starts with an anchor point that could either be selected randomly from the training space $\mathcal{P}_{\text{train}}$ or be user specified. At each iteration ℓ, a FOM simulation at the anchor point p_ℓ^* is conducted and returns a set of snapshots. The snapshot set is then processed through POD and returns the first N orthonormalized POD modes. The value of N is determined by reproduction problem at the anchor point. The ROM and the error indicator, Δ_ℓ, are then built with the reduced spaces $\mathbf{X}_{0,\ell}^N$ and $X_{0,\ell}^N$. The coefficients and the error estimates are then computed for each $p \in \mathcal{P}_{\text{train}}$ and the next anchor point is identified as the parameter that has the maximum value in the current (including previous) error estimate. The procedure starts again with the new selected anchor point. If the error indicator is sufficiently small over all points in $\mathcal{P}_{\text{train}}$ or the procedure reaches the maximum number of FOM solves L, the offline stage terminates.

Given the ROM/anchor point data $(\mathbf{X}_{0,\ell}^N, X_{0,\ell}^N, p_\ell^*)$ for $\ell = 1, \ldots, L$, and error indicator, Δ, the hGreedy online stage starts with finding the n_{cand} candidate anchor points nearest to the test parameter p. The ROMs associated to the candidate anchor points are then used to compute the coefficients and error estimate at p. The coefficients are then returned based on the ROM that has smallest error estimate. The POD-hGreedy approach is analogous to h-refinement in the finite element method in that the POD bases are not shared between

anchor points. Convergence is therefore expected to be linear in the distance from the nearest anchor point.

Algorithm 3.1: POD-hGreedy algorithm for the construction of $\{\mathbf{X}_{0,\ell}^N, X_{0,\ell}^N, \mathcal{I}_\ell\}_l$.

Offline stage: $[\{\mathbf{X}_{0,\ell}^N, X_{0,\ell}^N\}_{\ell=1}^L] = \text{Offline}\ (\mathcal{P}_{\text{train}},\ L,\ \Delta)$.

Inputs: $\mathcal{P}_{\text{train}} = \{p_i\}_{i=1}^{n_{\text{train}}}$ = discretized parameter space, L = maximum number of offline solves, Δ = error indicator defined in (3.11).

Output: $\{(\mathbf{X}_{0,\ell}^N, X_{0,\ell}^N, p_\ell^*)\}_{\ell=1}^L$ = reduced space/anchor point pairs.

p_1^* = smallest p in $\mathcal{P}_{\text{train}}$.

for $\ell = 1, \ldots, L$ **do**

  $[\{(\boldsymbol{u}^k(p_\ell^*), T^k(p_\ell^*))\}_{k=1}^K] = \text{DNS-solver}\ (p_\ell^*)$.

  $[\{(\boldsymbol{\varphi}_{n,\ell}, \theta_{n,\ell})\}_{n=1}^N] = \text{POD}\ (\{(\boldsymbol{u}^k(p_\ell^*), T^k(p_\ell^*))\}_{k=1}^K, N)$.

  Define $\mathbf{X}_{0,\ell}^N = \text{span}\{\boldsymbol{\varphi}_{n,\ell}\}_{n=1}^N$, $X_{0,\ell}^N = \text{span}\{\theta_{n,\ell}\}_{n=1}^N$, build the ROM operators and error indicator Δ_ℓ.

  for $i = 1, \ldots, n_{train}$ **do**

    $[\{(\boldsymbol{u}_{\text{r}}^j(p_i), T_{\text{r}}^j(p_i))\}_{j=0}^J] = \text{ROM-solver}\ (p_i, \mathbf{X}_{0,\ell}^N, X_{0,\ell}^N)$.

    Compute the weak dual norm Δ_ℓ at p_i.

  end

  $p_{\ell+1}^* = \arg\max_{p\in\mathcal{P}_{\text{train}}} \min\{\Delta_{\ell'}(p)\}_{\ell'=1}^{\ell}$.

end

Online stage: $[\{\boldsymbol{u}_{\text{r}}^j, T_{\text{r}}^j\}_j] = \text{Online}\ (\{(\mathbf{X}_{0,\ell}^N, X_{0,\ell}^N, p_\ell^*)\}_{\ell=1}^L, \Delta, n_{\text{cand}}, p)$.

Inputs: $\{(\mathbf{X}_{0,\ell}^N, X_{0,\ell}^N, p_\ell^*)\}_{\ell=1}^L$ = reduced space/anchor point pairs, n_{cand} = online ROM evaluations, p = input parameter.

Output: $\{\boldsymbol{u}_{\text{r}}^j, T_{\text{r}}^j\}_j$ = solution estimate.

for $i = 1$ **to** n_{cand} **do**

  Find the n_{cand} candidate anchors nearest to $p : p_1^*, \ldots, p_{n_{\text{cand}}}^*$.

  $[\{u_{\text{r},(i)}^j, T_{\text{r},(i)}^j\}_{j=0}^J] = \text{ROM-solver}\ (p_i^*, \mathbf{X}_{0,(i)}^N, X_{0,(i)}^N)$.

  Compute the error estimate $\Delta_{(i)}(p)$.

end

Return $\{(u_{\text{r}}^j, T_{\text{r}}^j) = (u_{\text{r},(i^*)}^j, T_{\text{r},(i^*)}^j)\}_j$, where i^* is the minimizer of $\{\Delta_{(i)}(p)\}_i$.

Another strategy is the POD-pGreedy algorithm, following the definitions of [86], as first proposed in [87] and analyzed in [88]. The algorithm combines data from different parameters to generate a single reduced basis set that covers the entire parameter space $\mathcal{P}$. The procedure is similar to Algorithm 3.1 but with few differences:

- The reduced bases are shared between anchor points. POD is still used to construct the new basis but the collected snapshot set is projected onto the orthogonal complement of the existing basis.

- In the online/training stage, only one ROM is used instead of a set of ROMs and there is no need to check for the nearest anchor points.
- The anchor point is selected based on the single error estimate Δ in current iteration, rather than the individual estimates for each ROM.

Although it has a better convergence rate than POD-hGreedy, POD-pGreedy can easily fail for unsteady problems. Combining modes at different anchor points, especially ones whose solution exhibits different physics, can easily lead to instability and deteriorate the performance, as noted in [17]. Moreover, stabilizations that work for POD-hGreedy can fail in the POD-pGreedy approach. For example, in the C-ROM, it is not clear how to construct the constraints for the combined basis. A naive approach is to apply POD to all the snapshots at anchor points. However, this approach is inefficient and can be limited by the computer storage requirements during the offline phase. Leray regularization with the projection filter (i.e., trivially truncated basis set for the advector) is also limited because the combined basis is no longer ordered in a Fourier-like, energy-decaying, sequence. To address this, one could apply POD to all the snapshots that have been collected but this approach is again limited by the storage and therefore not practical. An alternative is to consider the differential filter, denoted as the LDF-ROM here. Once the radius δ is specified, it will filter right amount of energy in each basis.

3.3.2 A Time-Averaged Error Indicator

In this section, we extend the time-averaged error indicator proposed in [17] to accommodate the energy equation and Leray regularization. The error indicator is based on the dual norm of the discrete time-averaged residual. Given the ROM solution sequence $\{\widetilde{\mathbf{u}}_{\mathrm{r}}^n\}_{n=J_0+1}^J$ and $\{\widetilde{T}_{\mathrm{r}}^n\}_{n=J_0+1}^J$ and the parameters of interest $\underline{p} = (\nu, \theta_g, \kappa)$, the discrete time-averaged residual for velocity and temperature are defined as: [2]

$$\langle R_u \rangle(\{\widetilde{\mathbf{u}}_{\mathrm{r}}^n\}_{n=J_0}^J, \boldsymbol{v}; \nu, \theta_g) := \frac{1}{J - J_0} \sum_{n=J_0+1}^{J} r_u(\widetilde{\mathbf{u}}_{\mathrm{r}}^n, \boldsymbol{v}; \nu, \theta_g), \quad \forall\ \boldsymbol{v} \in \mathbf{V}_{\mathrm{div}}, \tag{3.7}$$

$$\langle R_T \rangle(\{\widetilde{T}_{\mathrm{r}}^n\}_{n=J_0}^J, S; \kappa) := \frac{1}{J - J_0} \sum_{n=J_0+1}^{J} r_T(\widetilde{T}_{\mathrm{r}}^n, S; \kappa), \quad \forall\ S \in X_0^{\mathcal{N}}, \tag{3.8}$$

[2] In [39], the velocity and temperature residuals are coupled because the velocity-temperature solutions are obtained through a coupled Newton's method. Here, we do not couple the residuals because we solve (2.16)–(2.17) separately.

where $r_u(\widetilde{\mathbf{u}}_{\mathrm{r}}^n, \boldsymbol{v}; \nu, \theta_g) \in \mathbf{V}'_{\mathrm{div}}$ (dual space of $\mathbf{V}_{\mathrm{div}}$) and $r_T(\widetilde{T}_{\mathrm{r}}^n, S; \kappa) \in X_0^{\mathcal{N}\prime}$ (dual space of $X_0^{\mathcal{N}}$) are the residual associated with (2.53) at time t^n and defined as

$$\begin{aligned} r_u(\widetilde{\mathbf{u}}_{\mathrm{r}}^n, \boldsymbol{v}; \nu, \theta_g) = &\sum_{s=1}^{3} \alpha_s \left[(\boldsymbol{v}, \boldsymbol{g}(\theta_g)\widetilde{T}_{\mathrm{r}}^{n-s}) - c\left(\boldsymbol{v}, \widetilde{\mathbf{u}}_{\mathrm{r}}^{n-s}, \widetilde{\mathbf{u}}_{\mathrm{r}}^{n-s}\right) \right] \\ &- \sum_{s=0}^{3} \frac{\beta_s}{\Delta t}(\boldsymbol{v}, \widetilde{\mathbf{u}}_{\mathrm{r}}^{n-s}) - \nu a(\boldsymbol{v}, \widetilde{\mathbf{u}}_{\mathrm{r}}^n), \end{aligned} \tag{3.9}$$

$$r_T(\widetilde{T}_{\mathrm{r}}^n, S; \kappa) = -\sum_{s=1}^{3} \alpha_s c(S, \widetilde{\mathbf{u}}_{\mathrm{r}}^{n-s}, \widetilde{T}_{\mathrm{r}}^{n-s}) - \sum_{s=0}^{3} \frac{\beta_s}{\Delta t}(S, \widetilde{T}_{\mathrm{r}}^{n-s}) - \kappa(S, \widetilde{T}_{\mathrm{r}}^n). \tag{3.10}$$

Note for simplicity, we assume only BDF3/EXT3 is used for time discretization in (3.9)–(3.10). Besides, the residual is defined over $\mathbf{V}_{\mathrm{div}} \coloneqq \{\boldsymbol{v} | \boldsymbol{v} \in \mathbf{X}_0^{\mathcal{N}}, \nabla \cdot \boldsymbol{v} = 0\}$ and $X_0^{\mathcal{N}}$, rather than $\mathbf{X}_0^N \subset \mathcal{H}_0^1$ and X_0^N, because we measure our reduced-basis error relative to the FOM.

We define the *time-averaged error indicator*, $\Delta : \otimes_{n=J_0}^{J} \mathbf{X}^N \times X^N \times \mathcal{P} \to \mathbb{R}_+$, as follows:

$$\Delta(\{\widetilde{\mathbf{u}}_{\mathrm{r}}^n, \widetilde{T}_{\mathrm{r}}^n\}_{n=J_0}^{J}; \underline{p}) \coloneqq \sqrt{\|\langle R_u \rangle(\{\widetilde{\mathbf{u}}_{\mathrm{r}}^n\}_{n=J_0}^{J}, \cdot; \nu, \theta_g)\|_{\mathbf{V}'_{\mathrm{div}}}^2 + \|\langle R_T \rangle(\{\widetilde{T}_{\mathrm{r}}^n\}_{n=J_0}^{J}, \cdot; \kappa)\|_{X_0^{\mathcal{N}\prime}}^2}. \tag{3.11}$$

The residuals (3.9)–(3.10) can be further expressed in the matrix-vector form because the spaces $\mathbf{V}_{\mathrm{div}}$ and $X_0^{\mathcal{N}}$ are finite dimensional,

$$r_u(\widetilde{\mathbf{u}}_{\mathrm{r}}^n, \boldsymbol{v}; \nu, \theta_g) = \underline{\mathbf{v}}^T \underline{\mathbf{r}}_u^n = \underline{\mathbf{v}}^T \underline{\hat{\mathbf{f}}}(\widetilde{\mathbf{u}}_{\mathrm{r}}^n, \widetilde{T}_{\mathrm{r}}^n; \theta_g) - \underline{\mathbf{v}}^T \mathbf{H} \mathbf{B} \underline{\tilde{u}}_{\mathrm{r}}^n, \quad \forall\ \underline{\mathbf{v}} \in \mathbb{R}^{2\mathcal{N}}, \tag{3.12}$$

$$r_T(\widetilde{T}_{\mathrm{r}}^n, S; \kappa) = \underline{S}^T \underline{r}_T^n = \underline{S}^T \underline{\hat{Q}}(\widetilde{\mathbf{u}}_{\mathrm{r}}^n, \widetilde{T}_{\mathrm{r}}^n) - \underline{S}^T H_\kappa B \underline{\widetilde{T}}_{\mathrm{r}}^n, \quad \forall\ \underline{S} \in \mathbb{R}^{\mathcal{N}}. \tag{3.13}$$

where the matrices $\mathbf{B}$ and B are defined as

$$\mathbf{B}_{ij} = \boldsymbol{\varphi}_j(\mathbf{x}_i), \qquad B_{ij} = \theta_j(\mathbf{x}_i), \tag{3.14}$$

where the $\mathbf{x}_i$s are the spectral element nodal points. $\mathbf{H}$ and H_κ are the FOM velocity and thermal Helmholtz matrices defined in (2.18) and $\underline{\hat{\mathbf{f}}}$ and $\underline{\hat{Q}}$ are the velocity data and thermal loading vectors defined in (2.19–2.20). The matrix-vector version of the discrete time-averaged

residual (3.7)–(3.8) is then expressed as

$$\langle R_u\rangle(\{\widetilde{\mathbf{u}}_{\mathrm{r}}^n\}_{n=J_0}^J, \boldsymbol{v}; \nu, \theta_g) = \underline{\mathbf{v}}^T \underline{\mathbf{R}}_u = \underline{\mathbf{v}}^T \left(\frac{1}{J-J_0} \sum_{n=J_0+1}^{J} \underline{\hat{\mathbf{f}}}(\widetilde{\mathbf{u}}_{\mathrm{r}}^n, \widetilde{T}_{\mathrm{r}}^n; \theta_g) - \mathbf{H}\mathbf{B}\underline{\tilde{u}}_{\mathrm{r}}^n \right), \tag{3.15}$$

$$\langle R_T\rangle(\{\widetilde{T}_{\mathrm{r}}^n\}_{n=J_0}^J, S; \kappa) = \underline{S}^T \underline{R}_T = \underline{S}^T \left(\frac{1}{J-J_0} \sum_{n=J_0+1}^{J} \underline{\hat{Q}}(\widetilde{\mathbf{u}}_{\mathrm{r}}^n, \widetilde{T}_{\mathrm{r}}^n) - H_\kappa B \underline{\widetilde{T}}_{\mathrm{r}}^n \right), \tag{3.16}$$

$\forall\ \underline{\mathbf{v}} \in \mathbb{R}^{2\mathcal{N}}$ and $\forall\ \underline{S} \in \mathbb{R}^{\mathcal{N}}$. The norm of the residual is closely related to the error and it is tempting to use $\|\underline{R}_u\|_2$ and $\|\underline{R}_T\|_2$ to estimate the error. However, this is not correct because $\langle R_u\rangle(\{\widetilde{\mathbf{u}}_{\mathrm{r}}^n\}_{n=J_0}^J, \cdot; \nu, \theta_g) : \mathbf{V}_{\mathrm{div}} \to \mathbb{R}$ and $\langle R_T\rangle(\{\widetilde{T}_{\mathrm{r}}^n\}_{n=J_0}^J, \cdot; \kappa) : X_0^{\mathcal{N}} \to \mathbb{R}$ are bounded *linear* functionals whose size is appropriately measured through the dual norm:

$$\|\langle R_u\rangle(\{\widetilde{\mathbf{u}}_{\mathrm{r}}^n\}_{n=J_0}^J, \cdot; \nu, \theta_g)\|_{\mathbf{V}_{\mathrm{div}}'} = \sup_{\boldsymbol{v}\in\mathbf{V}_{\mathrm{div}}} \frac{\langle R_u\rangle(\{\widetilde{\mathbf{u}}_{\mathrm{r}}^n\}_{n=J_0}^J, \boldsymbol{v}; \nu, \theta_g)}{\|\boldsymbol{v}\|_{\mathbf{V}_{\mathrm{div}}}}, \tag{3.17}$$

$$\|\langle R_T\rangle(\{\widetilde{T}_{\mathrm{r}}^n\}_{n=J_0}^J, \cdot; \kappa)\|_{X_0^{\mathcal{N}}} = \sup_{S\in X_0^{\mathcal{N}\prime}} \frac{\langle R_T\rangle(\{\widetilde{T}_{\mathrm{r}}^n\}_{n=J_0}^J, S; \kappa)}{\|S\|_{X_0^{\mathcal{N}}}}. \tag{3.18}$$

Thanks to the Riesz representation theorem, there exist a unique $\langle \hat{\mathbf{R}}_u\rangle \in \mathbf{V}_{\mathrm{div}}$ and $\langle \hat{R}_T\rangle \in X_0^{\mathcal{N}}$ such that

$$(\langle \hat{\mathbf{R}}_u\rangle, \boldsymbol{v})_{\mathbf{V}_{\mathrm{div}}} = \langle R_u\rangle(\{\widetilde{\mathbf{u}}_{\mathrm{r}}^n\}_{n=J_0}^J, \boldsymbol{v}; \nu, \theta_g), \quad \forall\ \boldsymbol{v} \in \mathbf{V}_{\mathrm{div}}, \tag{3.19}$$

$$(\langle \hat{R}_T\rangle, S)_{X_0^{\mathcal{N}}} = \langle R_T\rangle(\{\widetilde{T}_{\mathrm{r}}^n\}_{n=J_0}^J, S; \kappa), \quad \forall\ S \in X_0^{\mathcal{N}}. \tag{3.20}$$

It thus follows that

$$\|\langle R_u\rangle(\{\widetilde{\mathbf{u}}_{\mathrm{r}}^n\}_{n=J_0}^J, \cdot; \nu, \theta_g)\|_{\mathbf{V}_{\mathrm{div}}'} = \|\langle \hat{\mathbf{R}}_u\rangle\|_{\mathbf{V}_{\mathrm{div}}}, \tag{3.21}$$

$$\|\langle R_T\rangle(\{\widetilde{T}_{\mathrm{r}}^n\}_{n=J_0}^J, \cdot; \kappa)\|_{X_0^{\mathcal{N}\prime}} = \|\langle \hat{R}_T\rangle\|_{X_0^{\mathcal{N}}}. \tag{3.22}$$

(3.19)–(3.20) allows one to compute the Riesz representers $\langle \hat{\mathbf{R}}_u\rangle$ and $\langle \hat{R}_T\rangle$ and (3.21)–(3.22) allows one to evaluate the dual norm of the residual through Riesz representation without computing the supremum.

In practice, determination of the Riesz representers, $\langle \hat{\mathbf{R}}_u\rangle$ and $\langle \hat{R}_T\rangle$, is relatively straightforward because the coarse (i.e., ROM) and truth (FOM) representations live in finite-dimensional spaces, meaning that there is a direct linear-algebra problem to be solved for the Riesz representers. Expanding (3.19)–(3.20), we have the corresponding linear algebra

statement,

$$\begin{bmatrix} \mathbf{A} & -\mathbf{D}^T \\ -\mathbf{D} & 0 \end{bmatrix} \begin{pmatrix} \langle \hat{\underline{\mathbf{R}}}_u \rangle \\ \underline{p} \end{pmatrix} = \begin{pmatrix} \underline{\mathbf{R}}_u \\ 0 \end{pmatrix}, \tag{3.23}$$

$$A \langle \hat{\underline{R}}_T \rangle = \underline{R}_T. \tag{3.24}$$

Here, $\mathbf{A}$ corresponds to $\mathbf{H}$ introduced in (2.18) with $\beta_0 = 0$ and $\nu = 1$. We remark that the essential difference between the velocity and temperature representers is that the former satisfies the divergence-free constraint by virtue of the 2×2 block system in (3.23). Evaluation of the error indicator Δ entails solving (3.23)–(3.24), computing the corresponding $\mathcal{H}^1$ norms of the outputs, and ultimately using these results in (3.11).

While use of the direct approach requires access to the FOM machinery in order to generate an error indicator, we note that such access is readily available during the pMOR training/construction phase. The advantage of this approach is that the number of Stokes/Poisson solves scales as the number of points in the training space, which is typically less than N^2. The other is through the offline/online computational decomposition which takes the advantage of the affine decomposition and expands the residual. By expanding the residuals $\langle R_u \rangle$ and $\langle R_T \rangle$, $2(N+1)^2 + 6(N+1)$ linear functionals are derived, where $2(N+1)^2$ is due to the convection term in the Navier-Stokes and energy equations. Applying the Riesz representation theorem to each linear functional, we end up solving $2(N+1)^2 + 6(N+1)$ Riesz representers, where $(N+1)^2 + 4(N+1)$ of them are solved through Stokes problems and $(N+1)^2 + 2(N+1)$ of them are solved through Poisson problems. Note that the Riesz representers must be stored in order to accomplish the decomposition and each is a vector of size $\mathcal{N}$ because it lives in the FOM space. For example, if $N = 60$, one would have to store at least 7200 vectors of size $\mathcal{N}$ which can be prohibitive, even for large multicore workstations. Even if there is no storage limitation, the offline cost is quite high when N is large as it scales quadratically. Once it is done, the online cost is $\mathcal{O}(N^2 J + N^4)$, where $\mathcal{O}(N^2 J)$ is to solve (2.53) and $\mathcal{O}(N^4)$ is required to compute the error estimate. Further details of the decomposition are provided in [17].

Time-Averaged Error Indicator with Leray Regularization The integration of the time-averaged error indicator Δ with Leray regularization is rather straightforward. Recall the difference between the G-ROM (2.31–2.32) and the LDF-ROM (2.50–2.51) is simply the advecting field being filtered. Hence, the residuals $r_u(\widetilde{\mathbf{u}}_{\mathrm{r}}^n, \boldsymbol{v}; \nu, \theta_g)$ and $r_T(\widetilde{T}_{\mathrm{r}}^n, S; \kappa)$ for all

$n = J_0 + 1, \ldots, J$ are simply modified with the filtered advecting field,

$$r_u(\widetilde{\mathbf{u}}_{\mathrm{r}}^n, \boldsymbol{v}; \nu, \theta_g) = \sum_{s=1}^{3} \alpha_s \left[(\boldsymbol{v}, \boldsymbol{g}(\theta_g)\widetilde{T}_{\mathrm{r}}^{n-s}) - c\left(\boldsymbol{v}, \overline{\mathbf{u}}_{\mathrm{r}}^{n-s}, \widetilde{\mathbf{u}}_{\mathrm{r}}^{n-s}\right) \right] - \sum_{s=0}^{3} \frac{\beta_s}{\Delta t}(\boldsymbol{v}, \boldsymbol{u}_{\mathrm{r}}^{n-s}) - \nu a(\boldsymbol{v}, \widetilde{\mathbf{u}}_{\mathrm{r}}^n), \tag{3.25}$$

$$r_T(\widetilde{T}_{\mathrm{r}}^n, S; \kappa) = -\sum_{s=1}^{3} \alpha_s c\left(S, \overline{\mathbf{u}}_{\mathrm{r}}^{n-s}, \widetilde{T}_{\mathrm{r}}^{n-s}\right) - \sum_{s=0}^{3} \frac{\beta_s}{\Delta t}(S, T_{\mathrm{r}}^{n-s}) - \kappa a(S, \widetilde{T}_{\mathrm{r}}^n), \tag{3.26}$$

for all $\boldsymbol{v} \in \mathbf{V}_{\mathrm{div}}$ and $S \in X_0^{\mathcal{N}}$. The corresponding time-averaged error indicator Δ is then defined based on the modified residuals (3.25)–(3.26).

3.3.3 pMOR Results: θ_g Variation

In this section, we consider the parametric problem parameterized with θ_g at $\mathrm{Pr} = 7.2$. The problem has three characteristics: bifurcation, spatio-temporal chaos over a certain range of θ_g, and a solution manifold that is a blend of steady and unsteady solutions. To identify the major pMOR challenges for this case, three values of Ra are considered:

1. $\mathrm{Ra} = 1 \times 10^4$ where the FOM is steady except at $\theta_g = 30°$.
2. $\mathrm{Ra} = 8 \times 10^4$ where the FOM is unsteady for $\theta_g \in [0°,\ 70°]$ and steady for $\theta_g \in [80°,\ 180°]$.
3. $\mathrm{Ra} = 3 \times 10^5$ where the FOM is unsteady for $\theta_g \in [0°,\ 120°]$ and steady for $\theta_g \in [130°,\ 180°]$.

In each case, the ROM is constructed through Algorithm 3.1. In order to assess performance, we generate FOM data for $\theta_g = 0°, 10°, \ldots, 180°$ ($n_{\mathrm{train}} = 19$ data points). The FOM solution is obtained by solving (4.18)–(3.2). For parameters where the problem is steady, the solution and the Nu are collected after the solution difference between ten time steps is less than 10^{-6}. For unsteady problems, the mean flow, mean Nu, Std(Nu), mean TKE and mean temperature fluctuation are averaged over 500 CTUs after the solution has reached a statistically steady state.

$\mathrm{Ra} = 1 \times 10^4$ To examine the feasibility of the pMOR (Algorithm 3.1) in the unsteady case, we begin with $\mathrm{Ra} = 1 \times 10^4$, in which only one unsteady solution is introduced at $\theta_g = 30°$.

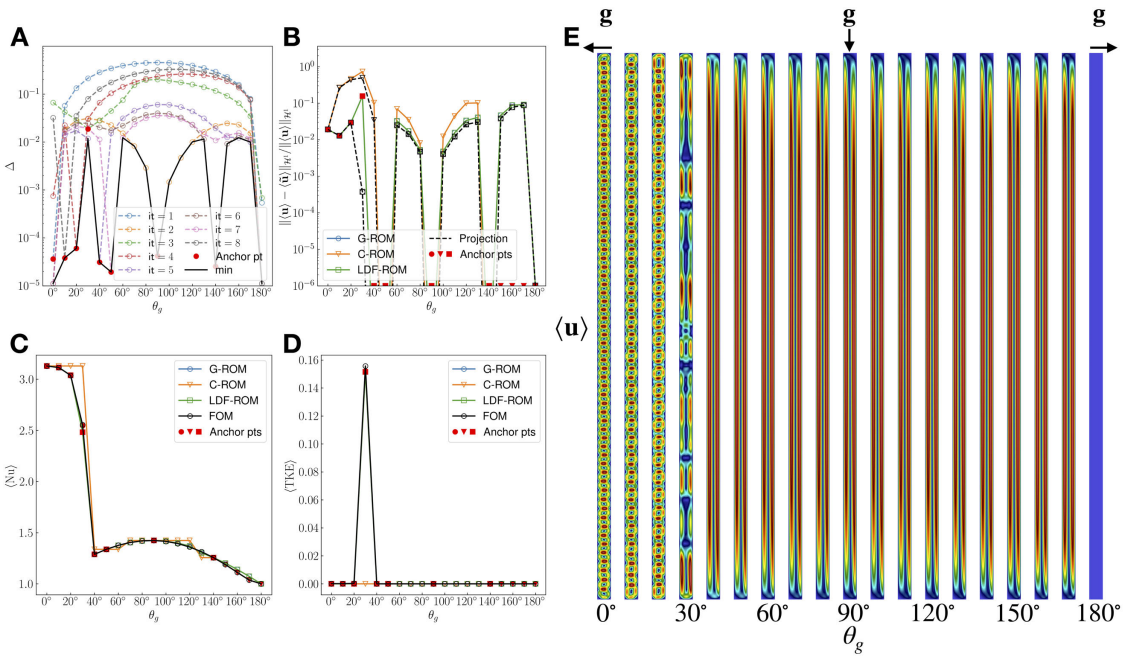

Figure 3.3: The parametric problem parameterized with θ_g at $\mathrm{Ra} = 1 \times 10^4$ and $\mathrm{Pr} = 7.2$: POD-hGreedy performance comparison between the G-ROM, the C-ROM and the LDF ROM. **(A)**: behavior of the error indicator Δ defined in (3.11) for eight iterations with G-ROM. **(B–D)**: behavior of the relative $\mathcal{H}^1$ error in predicted solution, mean Nu and mean TKE with θ_g based on eight anchor points. ($N = 1$ for all $\theta_g \in \mathcal{P}_{\text{anchor}}$ except $N = 70$ at $\theta^*_{g,3} = 30°$.) **(E)**: mean (or steady) velocity magnitude for 19 uniformly-spaced $\theta_g \in [0°,\ 180°]$. (The corresponding temperature solutions are in Fig. 3.1 **B**.)

Figure 3.3 **E** shows the steady (or mean) velocity magnitude for 19 uniformly-space training points $\theta_g = 0°,\ 10°, \ldots, 180°$. The corresponding temperature distributions are in Fig. 3.1 **B**. At $\theta_g = 180°$, we observe no flow and the temperature is simply the conduction solution. As θ_g decreases, we observe slot convection and then about $\theta_g = 40°$ there is a bifurcation to the wavy flow and rolls in the velocity. Moreover, we observe spatial-temporal chaos at $\theta_g = 30°$. Figures 3.3 **A**–**D** show the results of the application of Algorithms 3.1 for the construction of the G-ROM, C-ROM and LDF-ROM for the pMOR. The algorithm starts with $\theta^*_{g,1} = 0°$ and is performed with $L = 8$ iterations.

Figure 3.3 **A** demonstrates the selection process of anchor points (denoted by red circles) for the G-ROM case. We briefly walk through the process: At the first iteration, the error estimate $\Delta_1(\theta_g)$ for $\theta_g \in \mathcal{P}_{\text{train}}$ is computed (blue dashed line). With the largest error estimate, $\theta_g = 90°$ is then identified as the second anchor point. The third anchor point is then selected from $\theta_g \in \mathcal{P}_{\text{train}}$ which maximizes the error estimate $\Delta_{1,2}(\theta_g) := \min\{\Delta_1(\theta_g), \Delta_2(\theta_g)\}$ over $\mathcal{P}_{\text{train}}$. (We reiterate that minimizing over the individual error estimates is a property of the h-Greedy process—there is not a single unifying error estimate as is the case for p-Greedy.) The

process continues until the error estimate reaches the desired tolerance or the number of offline solves reaches its maximum. The black solid line denotes the minimum of all error estimates computed up to current iteration. In this case, it represents $\min\{\Delta_1(\theta_g), \ldots, \Delta_8(\theta_g)\}$. Note that the error estimate at $\theta_g = 180°$ in each model $\Delta_\ell(\theta_g = 180°)$ is small due to the choice of lift function.

From Fig. 3.3 **A**, we observe the error estimate is small at anchor points where the problem is steady. On the other hand, although the error estimate $\Delta_3(\theta_g)$ (greed line) is small at $\theta^*_{g,3} = 30°$ compared to other points in $\mathcal{P}_{\text{train}}$, it is not as small as the estimate at other anchor points. Because of the unsteadiness, it can't reach the same magnitude as in the steady cases.

Following this procedure for the other cases, we present models results for the G-ROM, C-ROM and LDF-ROM cases, denoted respectively blue, orange, green solid lines in Figs. 3.3 **B**–**D**. The behavior of the relative $\mathcal{H}^1$ error in the predicted solution is shown in Fig. 3.3 **B**. The corresponding Galerkin projection is denoted as the black dashed line. We found that the G-ROM and the LDF-ROM have a similar performance: the error in the solution is nearly identical to the Galerkin projection for cases where the problem is steady, including those that are not in the $\mathcal{P}_{\text{anchor}}$. The maximum error is at $\theta_g = 30°$ where the problem is unsteady. Both methods have around 15% error in the mean flow. Note that at $\theta_g = 30°$, the number of modes N is carefully selected because the ROM diverges after certain N due to the spatio-temporal chaos (15% error with $N = 70$, 17% error with $N = 80$ and 23% error with $N = 90$). On the other hand, the mean solution prediction made by the C-ROM has 73% in maximum error and in order for the C-ROM to reach same accuracy as in the G-ROM and the LDF-ROM, two more iterations are required. Already, with this modest $\text{Ra} = 1 \times 10^4$, we find C-ROM is less efficient than G-ROM and LDF-ROM. The pMOR behavior for mean Nu and mean TKE are shown along with the FOM results in Figs. 3.3 **C**–**D**. Again, the G-ROM and the LDF-ROM are able to make accurate predictions while the C-ROM has maximum 22% error in mean Nu and in particular is unable to capture the peak in mean TKE at $\theta_g = 30°$.

Before closing this section, we highlight some observations with respect to the solution manifolds.

- The solutions at $\theta_g \in [0°,\ 30°]$ are Rayleigh-Bénard with differing numbers of rolls, analogous to orthogonal sine and cosine functions at different wave numbers. Therefore, there is little hope in reproducing the solution except at selected anchor points. QOIs such as mean Nu, however, are less sensitive to precise mean flow fields and are therefore more tractable.

- At $\theta_g = 170°$ and $\theta_g = 180°$ the thermal metrics are not too different despite the $\mathcal{O}(1)$

difference in velocity solutions.

The first issue is resolved by the error indicator picking $\theta_g \in [0°,\ 30°]$ as anchor points. The second issue can be a source of error as Ra increases. With $\theta_g = 160°$ as an anchor point and the solution at $\theta_g = 180°$ as the lift function, the error at $\theta_g = 170°$ is 9% for $\mathrm{Ra} = 1 \times 10^4$, 16% for $\mathrm{Ra} = 8 \times 10^4$, and 19% for $\mathrm{Ra} = 3 \times 10^5$.

$\mathrm{Ra} = 8 \times 10^4$ Figure 3.4 shows pMOR results analogous to Fig. 3.3 for the case $\mathrm{Ra} = 8 \times 10^4$. Here, we consider only the G-ROM and the LDF-ROM. The algorithm starts with $\theta^*_{g,1} = 0°$ and terminates at $L = 6$ iterations. Figures 3.4 **E**–**F** show the FOM mean (or steady) temperature and velocity solution at the training points. (In an actual pMOR, these FOMs would of course not be computed *a priori*.) With this Ra, the bifurcation occurs at $\theta_g = 40°$. Moreover, we observe spatio-temporal chaos for $\theta_g \in [0°,30°]$ with the lower values being more chaotic.

The anchor-point selection process with the LDF-ROM is demonstrated in Fig. 3.4 **A**. Starting with $\theta^*_{g,1} = 0°$ the peak error in first iteration is at 110°, which is chosen to be $\theta^*_{g,2}$, and so on. Again, we find the error indicator is small at anchor points where the problem is steady and that it is larger where it is unsteady ($\theta_g \in [0°,\ 60°]$). Nonetheless, the error indicator is still able to identify where solution changes rapidly and select most of the anchor points in the region $[0°,\ 40°]$.

The behaviors of the relative $\mathcal{H}^1$ error in the predicted solution with θ_g using the G-ROM and the LDF-ROM are shown in Fig. 3.4 **B**. For $\theta_g \in [80°,\ 180°]$, where the solution is steady, we find the estimation is almost identical to the Galerkin projection in both models. On the other hand, for $\theta_g \in [0°,\ 70°]$, where the solution is unsteady, we find the error at anchor points $\theta_g = 0°,\ \theta_g = 10°$ is large due to the spatio-temporal chaos. The maximum error is around 19% at $\theta_g = 10°$ with the LDF-ROM while 69% at $\theta_g = 40°$ with the G-ROM. Although the maximum error in the G-ROM can be reduced by further iterations of the algorithm, the error will eventually be dominated by the high reproduction error arising from spatio-temporal chaos at $\theta_g = 0°$ and 10°.

The behavior for mean Nu and mean TKE are shown in Fig.3.4 **C**–**D** for the G-ROM and the LDF-ROM. Despite large errors in the mean flow prediction at $\theta_g = 0°,\ 10°$, the LDF-ROM is able to predict mean Nu with a maximum error around 5% whereas the G-ROM has maximum error around 28%. In addition, the LDF-ROM is able to predict a more accurate mean TKE than the G-ROM.

$\mathrm{Ra} = 3 \times 10^5$ For $(\mathrm{Pr}, \mathrm{Ra}) = (7.2, 3 \times 10^5)$ the flow is quite chaotic (similar to what is found for $\mathrm{Pr} = .71$ at lower Ra). Figures 3.5 **E**–**F** show the mean (or steady) temperature

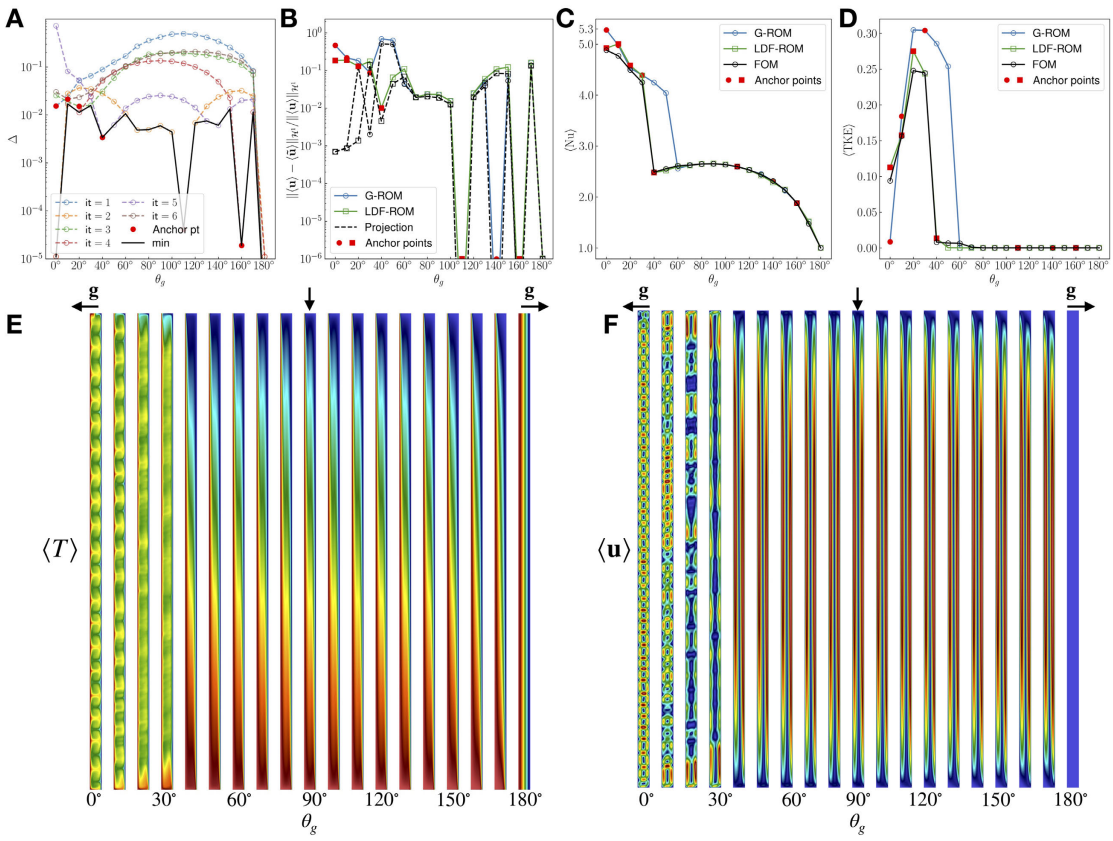

Figure 3.4: The parametric problem parameterized with θ_g at $\mathrm{Ra} = 8 \times 10^4$ and $\mathrm{Pr} = 7.2$: POD-hGreedy performance comparison between the G-ROM and the LDF ROM. **(A)**: behavior of the error indicator Δ defined in (3.11) for six iterations with LDF-ROM. **(B–D)**: behavior of the relative $\mathcal{H}^1$ error in predicted solution, mean Nu, and mean TKE with θ_g based on six anchor points. ($N = 100$ at $\theta_g = 0°,\ 20°$, $N = 80$ at $\theta_g = 10°,\ 30°,\ 40°$, $N = 1$ at $\theta_g = 110°,\ 140°,\ 160°$.) **(E–F)**: mean (or steady) temperature and velocity solution for 19 uniformly spaced $\theta_g \in [0°,\ 180°]$.

and velocity solution at $\theta_g = 0°,\ 10°, \ldots, 180°$ (19 data points). This time, the bifurcation occurs at $\theta_g = 60°$. We use this elevated Rayleigh-number case to explore the behavior of the h-Greedy pMOR convergence by considering application of the algorithm to two different training sets, $\mathcal{P}_1 = [60°,\ 70°, \ldots,\ 180°]$ and $\mathcal{P}_2 = [0°,\ 10°, \ldots,\ 180°]$. The set $\mathcal{P}_1$ excludes the spatio-temporal chaotic regime while $\mathcal{P}_2$ spans the full range of flow phenomena.

The anchor point selection process for $\mathcal{P}_1$ with LDF-ROM is demonstrated in Fig. 3.5 **A**, starting with $\theta^*_{g,1} = 60°$ and proceeding for $L = 5$ iterations. Again, we observe that the error estimate at the anchor points, $\theta^*_{g,1} = 60°$, $\theta^*_{g,3} = 80°$ and $\theta^*_{g,5} = 120°$ are larger than other anchor points because of unsteadiness. The behavior of the relative $\mathcal{H}^1$ error in predicted solution is shown in Fig. 3.5 **B**. For $\theta_g \in [130°,\ 180°]$, where the solution is steady, the ROM estimates at the anchor points are almost identical to the Galerkin

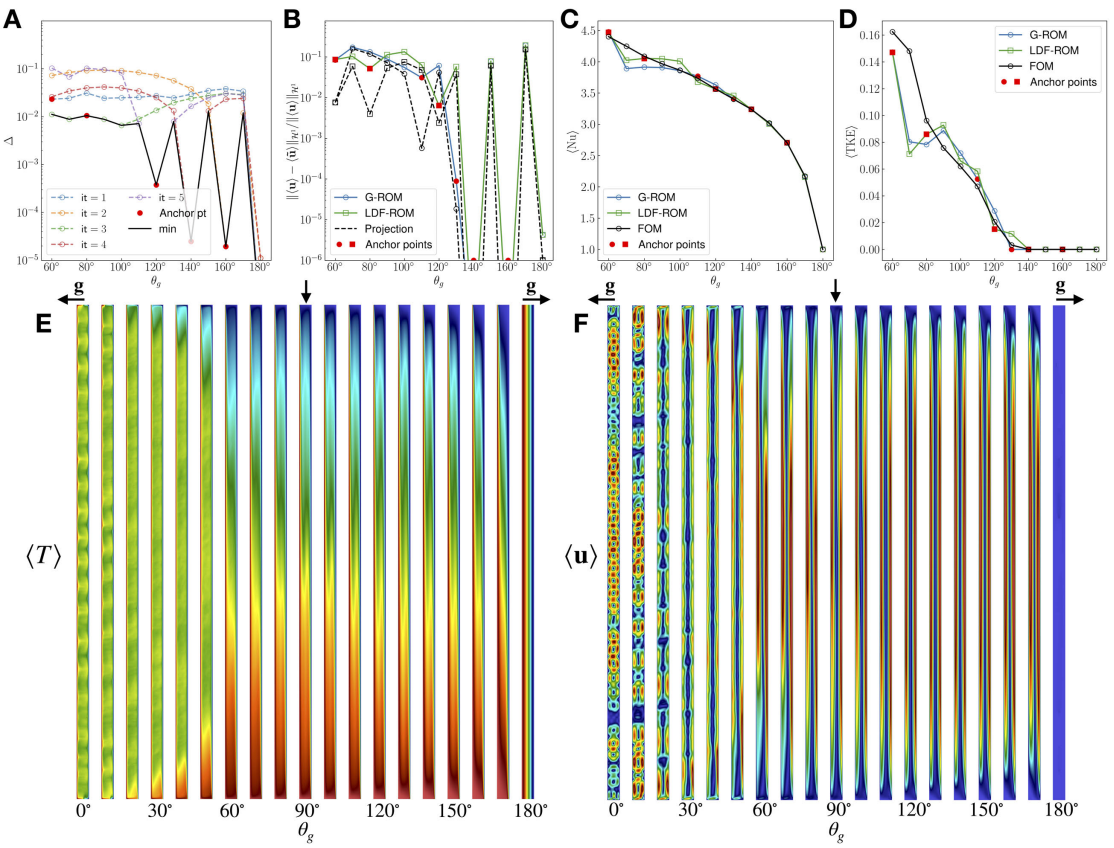

Figure 3.5: The parametric problem parameterized with $\theta_g \in [60°,\ 180°]$ at $\mathrm{Ra} = 3 \times 10^5$ and $\mathrm{Pr} = 7.2$: POD-hGreedy performance comparison between the G-ROM and the LDF-ROM. **(A)**: behavior of the error indicator Δ defined in (3.11) for five iterations with LDF-ROM. **(B–D)**: behavior of the relative $\mathcal{H}^1$ error in predicted solution, mean Nu and mean TKE with θ_g based on five anchor points. ($N = 80$ at $\theta_g = 60°,\ 80°,\ 110°$, $N = 50$ at $\theta_g = 120°$ and $N = 1$ at $\theta_g = 130°,\ 140°,\ 160°$.) **(E–F)**: mean (or steady) temperature and velocity solution for 19 uniformly spaced $\theta_g \in [0°,\ 180°]$.

projection. For $\theta_g \in [60°,\ 120°]$, where the solution is unsteady, the errors at the anchor points ($\theta_g = 60°,\ 80°,\ 110°,\ 120°$) are less than 10%. However, because of the irregular solution manifold, there is a 20% maximum error at $\theta_g = 170°$, despite the ROM being based on the nearby $\theta_g = 160°$ anchor point.

The behavior of the mean Nu and mean TKE are shown in Figs. 3.5 **C–D**. The maximum error in the predicted mean Nu is around 5% with LDF-ROM and 8% with G-ROM. The mean TKE estimation is also reasonable but is underestimated at $\theta_g = 70°$.

Next we examine the same problem configuration but with the full parameter space $\mathcal{P}_2$. The problem now includes spatio-temporal chaos for $\theta_g \in [0°,\ 40°]$ with the lower values being more chaotic. Fig. 3.6 show the results of the application of Algorithm 3.1 for the construction of the LDF-ROM for the parametric problem with $\mathcal{P}_2$. The algorithm starts

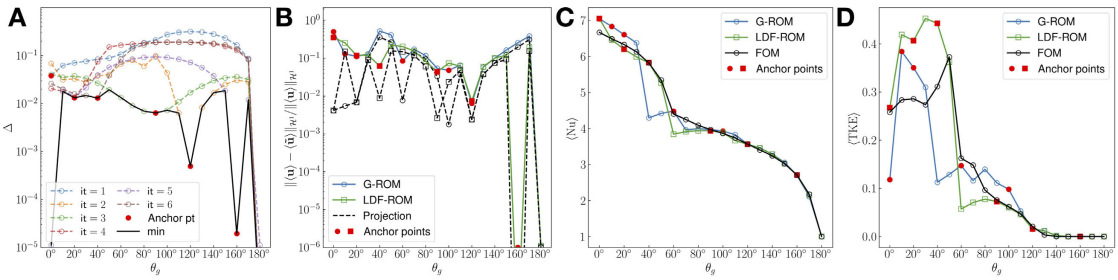

Figure 3.6: The parametric problem parameterized with $\theta_g \in [60°,\ 180°]$ at $\mathrm{Ra} = 3 \times 10^5$ and $\mathrm{Pr} = 7.2$: POD-hGreedy performance comparison between the G-ROM and the LDF-ROM. **(A)**: behavior of the error indicator Δ defined in (3.11) for five iterations with LDF-ROM. **(B–D)**: behavior of the relative $\mathcal{H}^1$ error in predicted solution, mean Nu and mean TKE with θ_g based on five anchor points. ($N = 80$ at $\theta_g = 10°,\ 20°,\ 40°,\ 60°,\ 90°,\ 100°$, $N = 70$ at $\theta_g = 0°$, $N = 50$ at $\theta_g = 120°$ and $N = 1$ at $\theta_g = 160°$.)

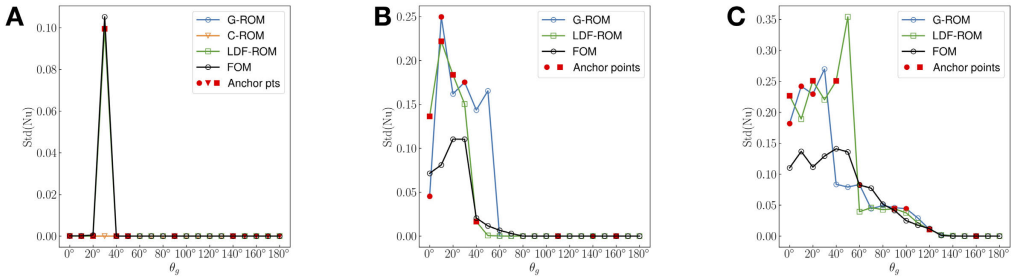

Figure 3.7: Behavior of the predicted Std(Nu) with θ_g. **(A)**: The G-ROM, the C-ROM and the LDF-ROM estimation at $\mathrm{Ra} = 1 \times 10^4$ with eight anchor points. **(B)**: The G-ROM and the LDF-ROM estimation at $\mathrm{Ra} = 8 \times 10^4$ with six anchor points. **(C)**: The G-ROM and the LDF-ROM estimation at $\mathrm{Ra} = 3 \times 10^5$ with six anchor points.

with $\theta^*_{g,1} = 0°$ and is performed with $L = 6$ iterations. The anchor point selection process is demonstrated in Fig. 3.6 **A**. We observe the same issue as in the previous cases, where unsteadiness leads to larger error estimates than with the steady regimes.

The relative $\mathcal{H}^1$ error in predicted solution is shown in Fig. 3.6 **B**. Again we find the estimation is almost identical to the Galerkin projection for $\theta_g \in [130°,\ 180°]$ where the solution is steady. For $\theta_g \in [0°,\ 120°]$ where the solution is unsteady, the errors at anchor points $\theta_g = 20°,\ 40°,\ 90°,\ 120°$ are less than 10% but 35% at $\theta_g = 0°$, which corresponds to "simple" Rayleigh-Bénard convection. Note that 35% is the error after carefully chosen N and spatial radius δ in Leray filtering. The corresponding mean Nu and mean TKE behavior are shown in Figs. 3.6 **C–D**. The maximum error in the predicted mean Nu is around 12%. For mean TKE, the estimation for $\theta_g \in [60°,\ 180°]$ is acceptable, while it is overestimated for $\theta_g \in [0°,\ 50°]$.

We are also aware that in some applications, the Std(Nu) could be considered as QOI.

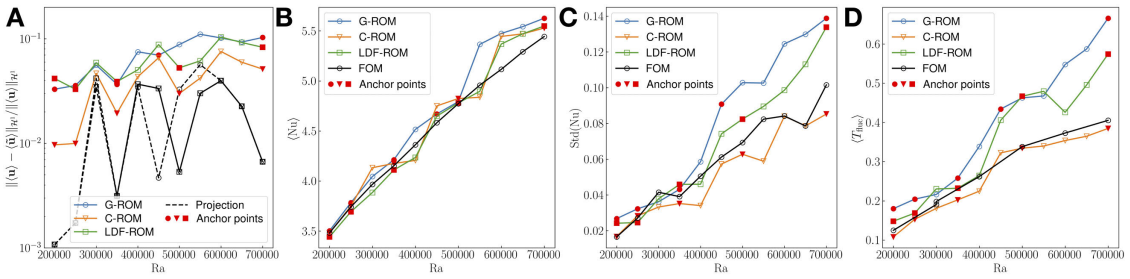

Figure 3.8: The parametric problem parameterized with Ra at $\theta_g = 90°$ and Pr = 7.2: POD-hGreedy performance comparison between the G-ROM, the C-ROM and the LDF ROM. **(A–D)**: behavior of the relative $\mathcal{H}^1$ error in predicted mean flow, predicted mean Nu, Std(Nu) and mean temperature fluctuation based on five anchor points. ($N = 80$, $\mathrm{Ra}_1^* = 2 \times 10^5$, $\mathrm{Ra}_2^* = 7 \times 10^5$, $\mathrm{Ra}_3^* = 2.5 \times 10^5$, $\mathrm{Ra}_4^* = 3.5 \times 10^5$, $\mathrm{Ra}_5^* = 5 \times 10^5$ for the C-ROM and the LDF-ROM and $\mathrm{Ra}_5^* = 4.5 \times 10^5$ for the G-ROM.)

However, comparing to the mean Nu and mean TKE, we find Std(Nu) is in general a more challenging QOI. Figure 3.7 shows the predicted Std(Nu) in the three Ra cases. We observe accurate prediction in $\mathrm{Ra} = 1 \times 10^4$ case. However, unlike the mean TKE, the Std(Nu) soon becomes intractable with $\mathrm{Ra} = 8 \times 10^4$ even with Leray regularization and is even worse in $\mathrm{Ra} = 3 \times 10^5$.

3.3.4 pMOR Results: Ra Variation

In this section, we consider the slot problem at $\theta_g = 90°$ and Pr = 7.2 with the parametric space defined by $\mathrm{Ra} \in \mathcal{P} = [2 \times 10^5,\ 7 \times 10^5]$. Unlike the problem with θ_g variation, all solutions are unsteady and there is no parametric bifurcation. In order to assess performance, we generate FOM data, including mean flow, mean Nu, Std(Nu), mean TKE and mean temperature fluctuation, for $\mathrm{Ra} = 2 \times 10^5,\ 2.5 \times 10^5, \ldots,\ 7 \times 10^5$ ($n_{\text{train}} = 11$ data points). The quantities are averaged over 500 CTUs once the solution reaches the statistically steady state.

Figure 3.8 shows the results of the application of Algorithm 3.1 for the pMOR using the G-ROM, the C-ROM and the LDF-ROM. The solid line denotes the performance of the reduced model which minimizes the error indicator, and thus is selected by the Greedy procedure (cf. Algorithm 3.1, $n_{\text{cand}} = 2$). Anchor points are denoted as red circle while FOM data is denoted as black solid line. The algorithm starts with $\mathrm{Ra}_1^* = 2 \times 10^5$ and is performed with $L = 5$ iterations. The number of POD basis N with anchor points are listed in the figure caption.

Figure 3.8 **A** shows the behavior of the relative $\mathcal{H}^1$ error in mean flow prediction with Ra.

First, we observe the errors at the anchor points are less than 10% with the C-ROM and the LDF-ROM while the G-ROM has 10% error at $\mathrm{Ra}_2^* = 7 \times 10^5$. The maximum error is roughly 11% in the G-ROM, 10% in the LDF-ROM and 8% in the C-ROM. Comparing with the Galerkin projection error (denoted by the black dashed line), the pMOR accuracy is seen to be quite satisfactory throughout $\mathcal{P}$.

Figure 3.8 **B** shows the behavior of the predicted mean Nu with Ra. At the anchor points, we observe good agreement between ROMs and FOM and that stabilization does improve its accuracy. The maximum relative error is roughly 8% in the G-ROM, 6.5% in the C-ROM and 5% in the LDF-ROM. Figures 3.8 **C**–**D** show the behavior of the predicted Std(Nu) and mean temperature fluctuation. In both QOIs, we find the C-ROM outperforms the other two models. At $\mathrm{Ra} = 7 \times 10^5$, the LDF-ROM is only slightly better than the G-ROM.

This parametric space is in general more tractable than those involving variation in θ_g. This outcome might be anticipated by observing the mean temperature fields shown in Fig. 3.1 **C**, which suggests that the solution manifold with respect to Ra is quite smooth. This is also reflected in the QOIs, for example, the mean Nu, Std(Nu) and mean temperature fluctuation behave almost linearly as Ra increases.

3.4 Discussion

In this section, we investigate some of the flow behaviors exhibited by the FOM to better understand how they influence the relative performance of the ROMs. We note that we cannot, in general, expect a ROM to be able to predict FOM behavior if the flow itself is not predictable. Thus, variability in the FOM provides an anticipated lower bound on ROM performance for the reproduction problem.

3.4.1 Spatio-Temporal Chaos

Even though our 2D model problem generates only laminar flows, pMOR is quite challenging in this application for several reasons: (i) there is bifurcation in θ_g parameter space; (ii) the solution can be multivalued, even at steady state; and (iii) the solution exhibits spatio-temporal chaos at several points in the parameter space. As our initial efforts happened to be focused in one of the spatio-temporal chaos regimes, we decided to map out a larger space to identify where pMOR could succeed, where it would have difficulty, and where it *a priori* could not succeed. Table 3.1 reflects a broad range of flow regimes identified inside the high-aspect ratio slot from hundreds of FOM simulations conducted at multiple Ra, θ_g with $\mathrm{Pr} = 0.07,\ 0.71,\ 7.2$. We categorize the flow into six types: (i) motionless, (ii) steady, (iii)

Table 3.1: Distribution of six flow types with Ra and θ_g at Pr = 0.07, 0.71, 7.2.

flow \Pr	Pr = 0.07	Pr = 0.71	Pr = 7.2
motionless	$\mathrm{Ra} < 1.1 \times 10^3$, $\theta_g = 0°$	$\mathrm{Ra} < 8.75 \times 10^2$, $\theta_g = 0°$	$\mathrm{Ra} < 9 \times 10^2$, $\theta_g = 0°$
steady	$\mathrm{Ra} = 10^3, \theta_g = 90°$ $\mathrm{Ra} = 10^4, \theta_g \in [0°,\ 40°] \cup [170°,\ 180°]$	$\mathrm{Ra} = 10^3, \theta_g \in [0°,\ 180°]$ $\mathrm{Ra} = 10^4, \theta_g \in [0°,\ 30°] \cup [70°,\ 80°] \cup [120°,\ 180°]$ $\mathrm{Ra} = 1.5 \times 10^4,\ \theta_g = 90°$	$\mathrm{Ra} = 10^3, \theta_g \in [0°,\ 180°]$ $\mathrm{Ra} = 10^4, \theta_g \in [0°,\ 180°] \backslash \{30°\}$ $\mathrm{Ra} \in [2 \times 10^4,\ 10^5],\ \theta_g = 90°$ $\mathrm{Ra} = 8 \times 10^4, \theta_g \in [80°,\ 180°]$ $\mathrm{Ra} = 3 \times 10^5, \theta_g \in [130°, 180°]$
periodic	$\mathrm{Ra} \in [5 \times 10^3,\ 7 \times 10^3],\ \theta_g = 90°$	$\mathrm{Ra} = 10^4,\ 1.75 \times 10^4,\ \theta_g = 90°$	N\A
quasi-periodic	$\mathrm{Ra} = 10^4,\ \theta_g \in [50°,\ 110°]$ $\mathrm{Ra} = 8 \times 10^3,\ 9 \times 10^3,\ 2 \times 10^4,\ \theta_g = 90°$	$\mathrm{Ra} \in [1.8 \times 10^4,\ 2 \times 10^4],\ \theta_g = 90°$	N\A
chaotic	$\mathrm{Ra} = 10^4,\ \theta_g \in [120°,\ 160°]$ $\mathrm{Ra} \in [6 \times 10^4,\ 1.5 \times 10^5],\ \theta_g = 90°$	N\A	$\mathrm{Ra} = 8 \times 10^4, \theta_g \in [40°,\ 70°]$ $\mathrm{Ra} = 3 \times 10^5, \theta_g \in [50°,\ 120°]$ $\mathrm{Ra} \in [2 \times 10^5,\ 8 \times 10^5], \theta_g = 90°$
spatio-temporal chaotic	$\mathrm{Ra} \in [3 \times 10^4,\ 5 \times 10^4],\ \theta_g = 90°$	$\mathrm{Ra} = 10^4,\ \theta_g \in [40°,\ 60°] \cup [100°,\ 110°]$ $\mathrm{Ra} = 1.25 \times 10^4,\ \theta_g = 90°$ $\mathrm{Ra} \in [2.05 \times 10^4,\ 3 \times 10^5],\ \theta_g = 90°$	$\mathrm{Ra} = 10^4,\ \theta_g = 30°$ $\mathrm{Ra} = 8 \times 10^4, \theta_g \in [0°,\ 30°]$ $\mathrm{Ra} = 3 \times 10^5, \theta_g \in [0°,\ 40°]$ $\mathrm{Ra} \in [2 \times 10^5,\ 8 \times 10^5], \theta_g = 0°,\ 10°$

periodic, (iv) quasi-periodic, (v) chaotic and (vi) spatio-temporal chaotic. We identify the flow regimes by examining the (mean) solution field and the energy and Nu histories. Such analysis can readily distinguish the motionless, steady and periodic flow cases. Even though the energy and Nu analysis seem to be a reliable way to distinguish the quasi-periodic and chaotic flow, it is only a heuristic—a more rigorous analysis is through computing the power spectrum of Nu or energy [89]. Tools such as Lyapunov exponent and fractal dimension are probably the most widely used diagnostic for chaotic systems [90, 91]. The first five types of low have consistent mean flow in differing time windows, each averaged over 500 convective time units (CTUs). We define a flow to be spatio-temporal chaotic [92] if its mean solution is not consistent in at least three different time windows. This type of flow has strong irregularities in both space and time and has been observed in Rayleigh Bénard convection and in other complex dynamical systems [93]. To characterize spatio-temporal chaos, one could also consider Lyapunov exponents at each grid point. A detail analysis of spatio-temporal chaos is beyond the scope. A comprehensive review on this topic can be found in [94].

As discussed above, we classify a flow to be spatio-temporal chaotic by examining its consistency in mean flow over various time windows. (We use this simple metric here for convenience—we have also examined the flow fields and the time traces of multiple QOIs.) We further explore how lack of consistency influences four QOIs, mean Nu, Std(Nu), mean temperature fluctuation, and mean TKE, at three successive time windows, W1, W2 and W3. These quantities are used to indicate the variability in the FOM. As with the preceding cases, we consider averaging times of 500 CTUs for each of the three windows. The starting time for W1 differs with given parameters as some cases take a longer time to reach a statistically steady state. For example, for Pr = 0.71 at $\mathrm{Ra} = 1.8 \times 10^4$ and $\theta_g = 90°$, the flow is chaotic until 6000 CTUs and then becomes periodic. Figures 3.9 **A**–**D** show the behavior of the

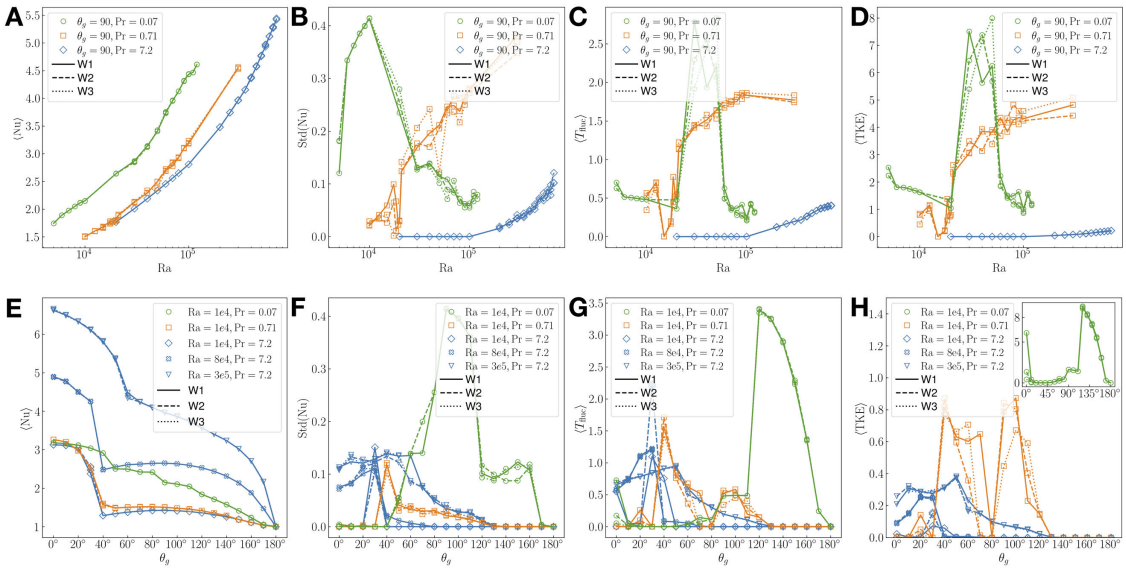

Figure 3.9: Parametric variability in the FOM: green–Pr = 0.07, orange–Pr = 0.71, and blue–Pr = 7.2. Each plot reveals absence/presence of chaotic effects by presenting statistics taken over three time windows, W1, W2, and W3. **(A–D)**: *Ra*-dependence of mean Nu, Std(Nu), mean temperature fluctuation, and mean TKE computed over time windows W1, W2 and W3. **(E–H)**: θ_g-dependence at fixed Ra.

four QOIs with Ra at three Pr for $\theta_g = 90°$. Pr = 0.07 is denoted as green line, Pr = 0.71 is denoted as orange line, while Pr = 7.2 is denoted as blue line. Window W1 is denoted by a solid line, W2 by a dashed line, and W3 by a dotted line.

From Figs. 3.9 **A–D** we can see the following:

- For Pr = 0.07 the QOIs are fairly consistent except for Ra $\in [3 \times 10^4,\ 5 \times 10^4]$.
- For Pr = 0.71, we find large variability in Std(Nu), mean temperature fluctuation and mean TKE for Ra $> 2 \times 10^4$.
- Pr = 7.2 exhibits the least variability.

For Ra where we find that the QOI variability is high, we have also examined the mean flow at multiple time windows and found that those are also inconsistent. In all cases, the mean Nu is quite repeatable.

Figures 3.9 **E–H** show the behavior of the same QOIs as a function of θ_g. For Pr = 7.2, we consider three different values of Ra. We find for most of the θ_g, the variability is small except for small θ_g where we also report spatio-temporal chaotic flow. For Pr = 0.07, we find the QOIs has small variability with Ra $= 1 \times 10^4$. However, for Pr = 0.71, we find large variability, especially in the mean TKE. Not only it has spatio-temporal chaotic flow (for

example $\theta_g = 100°$), but also the solution manifold is not smooth. By varying $\theta_g = 80°$ to $\theta_g = 100°$, the solution changes from steady to periodic then spatio-temporal chaotic.

From Figs. 3.9 **E**–**H** we observe the following:

- For $\mathrm{Pr} = 0.07$, Std(Nu) exhibits up to 50% variability (e.g., at $\theta_g = 70°$) while $\langle T_{\mathrm{fluc}} \rangle$ and $\langle \mathrm{TKE} \rangle$ have orders-of-magnitude relative variability at $\theta_g = 0°$.
- For $\mathrm{Pr} = 0.71$, $\langle T_{\mathrm{fluc}} \rangle$ and $\langle \mathrm{TKE} \rangle$ exhibit significant variability for $\theta_g \in [60°, 110°]$.
- For $\mathrm{Pr} = 7.2$, the most notable variation is at $\theta_g = 30°$ for Std(Nu), $\langle T_{\mathrm{fluc}} \rangle$, and $\langle \mathrm{TKE} \rangle$ at $\mathrm{Ra} = 10^4$. Remarkably, the higher Rayleigh number cases do not exhibit as much variance.

As in **A**–**D**, the mean Nu is seen to be a repeatable QOI. It is worth noting the real challenge and sensitivity of this class of problems is illustrated in Fig. 3.9 **H**. Here, we observe for the $(\mathrm{Pr}, \mathrm{Ra}) = (0.71, 10^4)$ case that the flow alternates from steady to unsteady at multiple points along the one-dimensional θ_g parameter space as indicated by several distinct zeros in the TKE.

In Fig. 3.10, we further explore the influence of spatio-temporal chaos by examining the mean-flow distributions and ROM performance for $(\mathrm{Pr}, \mathrm{Ra}) = (7.2, 3.5 \times 10^4)$ at $\theta_g = 0°$ and $\theta_g = 20°$. Figures 3.10 **A**–**C** show the behavior of the $\mathcal{H}^1$ error and mean Nu predictions as a function of N, along with the mean-velocity magnitude distributions over seven time windows for $\theta_g = 0°$. Figure 3.10 **D**–**F** show the same quantities but with $\theta_g = 20°$ and only three time windows. In Fig. 3.10 **C**, we observe that for $\theta_g = 0°$ the number of rolls in the mean velocity field changes across different time windows. Similar changes are observed, to a lesser extent, at $\theta_g = 20°$. Hence, both solutions are categorized as spatio-temporal chaotic flow, but the $\theta_g = 0°$ case is more significant. Comparing the mean flow error and mean Nu, we observe that the ROM convergence for the reproduction problem is slower (or nonexistent) at $\theta_g = 0°$, while the convergence behavior is more favorable at $\theta_g = 20°$.

We have also computed the relative error between FOM mean flows across seven time windows for the two values of θ_g. The maximum relative $\mathcal{H}^1$ error is 34% for $\theta_g = 0°$ and 10% for $\theta_g = 20°$. These FOM discrepancies can be considered as a bound on the predictive capabilities of the ROM. Indeed, the values of 34% and 10% are consistent with the lower bounds realized in Figs. 3.10 **A** and **D**.

In Figure 3.11, we examine the influence of Prandtl number by comparing results for $\mathrm{Pr} = 0.71$ and 7.2 at $(\mathrm{Ra}, \theta_{\mathrm{g}}) = (3 \times 10^5, 90°)$. Figures 3.11 **A**–**D** show the convergence behavior for the $\mathcal{H}^1$ error and mean Nu as well as mean temperature and x-velocity fields at three time windows for $\mathrm{Pr} = 0.71$, while **E**–**H** show the same quantities for $\mathrm{Pr} = 7.2$.

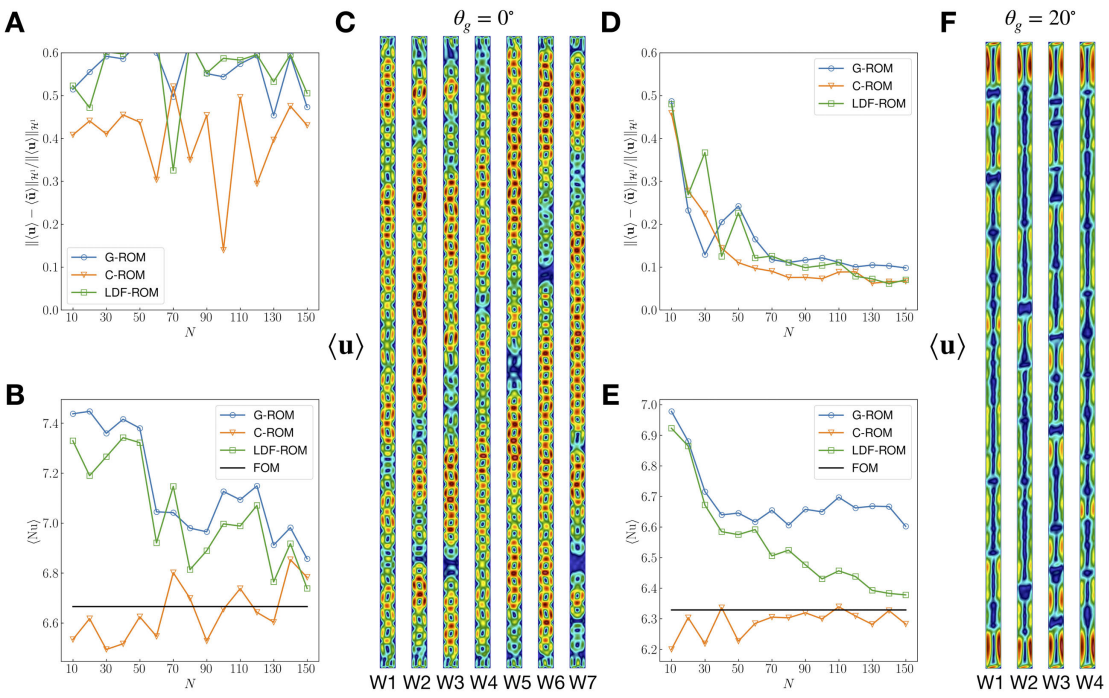

Figure 3.10: ROM performance comparison between problem having significant ($\theta_g = 0°$) and less significant ($\theta_g = 20°$) spatio-temporal chaotic flow at Pr = 7.2 and Ra = 3×10^5. **(A–C)**: Behavior of the relative $\mathcal{H}^1$ error and mean Nu as a functions of N and magnitude of the mean velocity at multiple time windows W1, . . . , W7 at $\theta_g = 0°$. **(D–F)**: performance for the same quantities at $\theta_g = 20°$.

From the mean fields, we observe that the number of rolls and its position changes with time window at Pr = 0.71, while minimal variance is observed at Pr = 7.2. Hence the solution at Pr = 0.71 is considered to be spatio-temporal chaotic while only chaotic at Pr = 7.2. Comparing the behavior of the relative $\mathcal{H}^1$ error in the mean flow and mean Nu, we observe convergence issues in the ROM at Pr = 0.71, while the same metrics converge at Pr = 7.2. We further compute the relative variance between two FOM mean flows across seven time windows for the two considered θ_g. The maximum relative $\mathcal{H}^1$ error is 14% for Pr = 0.71 and only 1% for Pr = 7.2. This again explains why the approximation errors are different between the two cases. Considering these variance levels as a lower bound for the ROM, we can view 20% error in the C-ROM as acceptable. On the other hand, the approximation error for Pr = 7.2 is able to reach below 10%.

In summary, the results of this section show that convergence issues and variations in the QOIs in the ROM can have high a correlation with the flow being spatio-temporal chaotic. From Table 3.1 and Fig. 3.9, we see that Pr = 0.71 has a more complicated solution manifold found with the other two Prandtl numbers and also exhibits spatio-temporal chaos at a

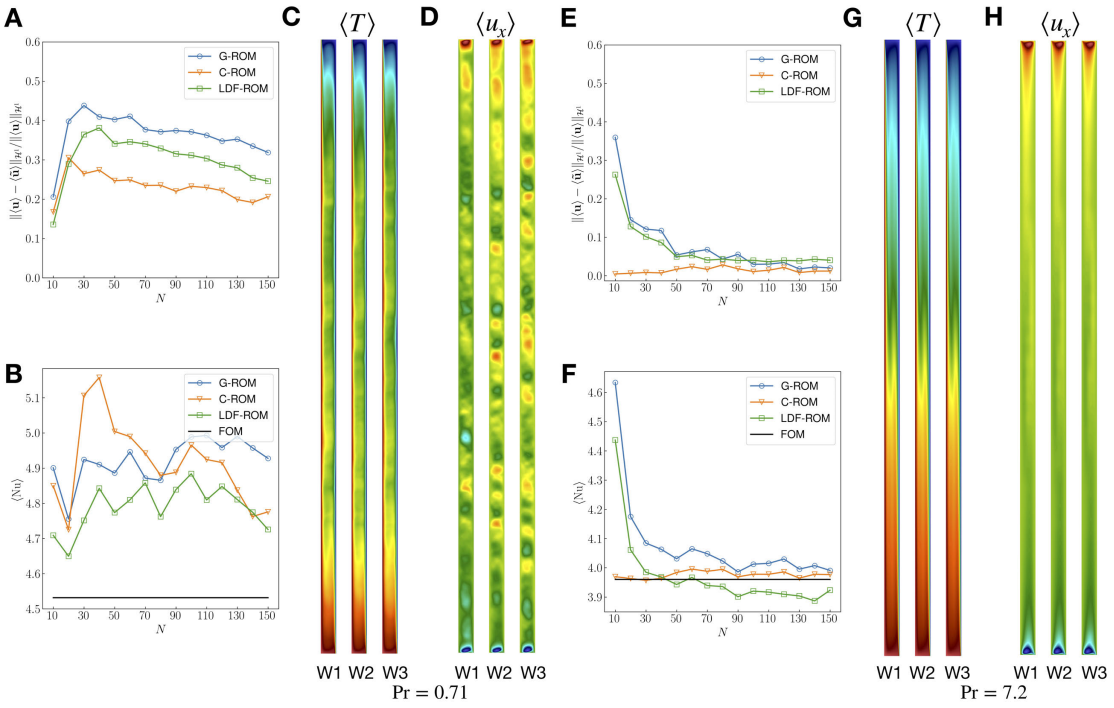

Figure 3.11: ROM performance comparison between Pr = 0.71 and Pr = 7.2 at Ra = 3×10^5 and $\theta_g = 90°$. **(A–D)**: Behavior of the relative $\mathcal{H}^1$ error and mean Nu as a functions of N, temperature and mean x-velocity at three time windows, W1, W2 and W3 at Pr = 0.71. **(E–H)**: performance for the same quantities at Pr = 7.2.

relatively small Rayleigh number, Ra = 10^4.

3.4.2 Multiple Steady-State Solutions

In this section, we report the existence of multiple steady-state solutions observed for the case $(\theta_g, \text{Ra})=(0°, 10^4)$. The variations are characterized by different numbers of recirculation rolls, which are induced by using different initial conditions. Figure 3.12 shows steady temperature solutions generated by starting with steady solutions, χ_n from other values of $\theta_g = n°$, save for the χ_{90} case, which corresponds to a single snapshot of the unsteady flow/temperature field at $\theta_g = 90°$. Multiple steady states are also observed for this Prandtl number at $\theta_g = 10°$ and 20° and have been reported by other authors as well [37, 85, 95].

For solution reproduction, the multiplicity of the solutions is not an issue as long as the ROM uses the same initial condition as the FOM. However, for parametric problem, these multiple states could easily lead to an incorrect (or at least, unexpected or unverifiable) conclusion. For example, if the ROM anchor at $\theta_g = 10°$ is used to approximate the solution at $\theta_g = 0°$. With the initial condition at $\theta_g = 10°$, the approximate solution will be the third

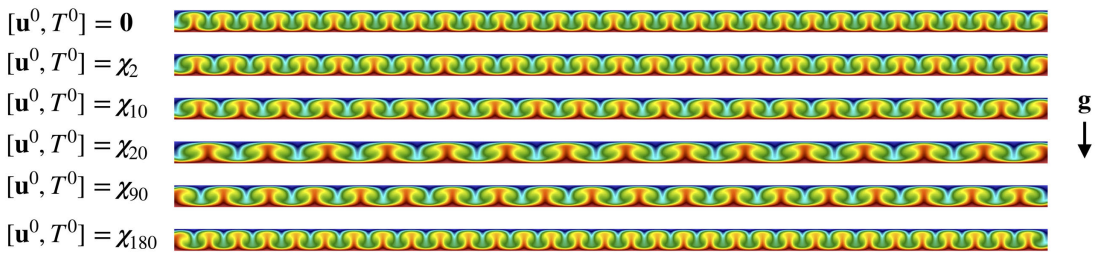

Figure 3.12: Different steady temperature solutions at $\theta_g = 0°$, $\mathrm{Ra} = 1 \times 10^4$ and $\mathrm{Pr} = 0.71$. The solutions were computed from different initial conditions, $\boldsymbol{\chi}_n$, corresponding to FOM solutions at $\theta_g = n°$. For $n = 2,\ 10,\ 20$, and 180 the solution is steady, whereas $\boldsymbol{\chi}_{90}$ is simply a snapshot from the $\theta_g = 90°$ case.

temperature solution shown in Fig. 3.12. However, if one collects the FOM data at θ_g with zero initial condition, one will consider the first temperature solution as the truth solution. As we could consider those roll solutions as sine and cosine functions, the first and third solution are nearly orthogonal; their difference is $\mathcal{O}(1)$ and one would thus conclude that the pMOR had failed when it in fact had generated a valid solution.

3.4.3 Discussion Summary

We have noted in Table 3.1 the broad range of flow regimes encountered for the tilted slot problem and illuminated a correlation between the flow states and predictive power of the MOR/pMOR framework. The cases with spatio-temporal chaos are generally the most challenging for model-order reduction and the pMOR errors are found to be (approximately) bounded from below by the variance observed in successive FOM simulations performed at the same parametric point. The development of the pMOR thus needs to be performed with care.

Two parameterizations were considered: (i) θ_g-variation, where a bifurcation exists and solution space is a blend of unsteady and steady solutions, and (ii) Ra-variation, where no bifurcation exists and one finds only unsteady solutions. In the θ_g-variation problem, accurate prediction in mean flow and other QOIs by the pMOR was demonstrated in the $\mathrm{Ra} = 1 \times 10^4$ and $\mathrm{Ra} = 8 \times 10^4$ cases. In high Ra cases, acceptable prediction of Nu is achieved with the LDF-ROM but a small mean-flow error is not realizable because of spatio-temporal chaos.

The results also indicate that the LDF-ROM is a better candidate for for parametric problems with bifurcation than the C-ROM. This observation is new, yet consistent with the results of [17], where the authors show that the C-ROM is effective for parametric problems that do not have a bifurcation. For the parametric problem parameterized with Ra, without

spatio-temporal chaos, we find that pMOR with any of the three methods, the G-ROM, the C-ROM, or the LDF-ROM, is able to predict the mean flow quite well. In this case, the C-ROM is the most accurate in mean flow prediction and other targeted QOIs. This result is not surprising given that the solution manifold does not have a bifurcation. Lastly, we remark that Std(Nu) is generally the most challenging QOI of those explored here.

From the results, we are able to make an important observation. For parametric problems where pMOR is successful (e.g., errors $< 10\%$), the solution is either only chaotic (e.g., Ra variation with $\theta_g = 90°$) or the solution does not have significant spatio-temporal chaos (e.g., θ_g variation with $\mathrm{Ra} = 1 \times 10^4,\ 8 \times 10^4$). Once the spatio-temporal chaos becomes significant, the predictive power of pMOR deteriorates and the maximum errors are dominated by variance in the truth solution.

Although not shown here, we have also applied POD-pGreedy to this problem. In the parametric problem parameterized with θ_g, it works only in the steady case $\mathrm{Ra} = 1 \times 10^3$. Once the unsteady solution emerges, for example at $\mathrm{Ra} = 1 \times 10^4$, combining modes associated with different values of θ_g leads to an unstable ROM even with the Leray regularization. Although no rigorous proof is given, we hypothesize that the issue is due to the bifurcation in solution behavior. This point was also suggested in [17], which empirically showed that combining modes associated with qualitatively different behaviors might lead to poor prediction. By contrast, when the current problem is parameterized with Ra we find that POD-pGreedy is more efficient than the h-refinement approach.

3.5 Conclusions

In this chapter, an error-indicated pMOR is applied to a 2D unsteady natural convection in a tilted high-aspect ratio slot. We first considered the solution reproduction problem (non-predictive case) to demonstrate the convergence of the ROMs and the effectiveness of the stabilization methods. We next addressed the parametric problem (predictive case) to validate the error indicator and, more broadly, the stabilized POD-hGreedy procedures. Principal contributions include, (i) extension of the error indicator proposed in [17] to buoyancy-driven flows; (ii) demonstration that Leray-regularized Galerkin ROMs provide a robust solution approach for this class of flows; (iii) identification of spatio-temporal chaos as a source of irreproducibility in both the FOM and the ROM and that the variance in the FOM provides a lower bound on the pMOR error in these cases; (iv) observation that accurate prediction ($< 10\%$) with pMOR is achievable if the solution in the parametric space is either only chaotic or the spatio-temporal chaos is not significant, regardless of whether a bifurcation exists or not. Once the spatio-temporal chaos becomes significant, the performance of the

pMOR deteriorates and the maximum errors of the mean flow and QOIs are dominated by the flow chaos.

We also highlight a number of challenges that are particularly relevant for buoyancy-driven flows and which should be taken into consideration in the design of pMOR strategies for 3D buoyancy driven turbulent flow. First, one needs to be aware of potential convergence issues for the mean flow and other QOI predictions when the FOM exhibits large-scale spatio-temporal chaos. Second, it is difficult to combine modes associated with different flow regimes, especially for the *p*Greedy case. Third, even relatively simple (e.g., steady) flows can exhibit multiple states at a given parameter. And fourth, there are large offline costs both in terms of computational time and required storage for error indicator and $O(N^4)$ costs for online-only error indicators.[3]

We outline potential next steps in pMOR development for this class of problems.

- *Extension to higher dimensional parameter space.* In this work, we considered only one-dimensional parameter space because the pMOR behavior needed to be carefully diagnosed; however higher dimensional parameter spaces are more interesting for engineering applications.

- *hp-Greedy with a bifurcation detection technique.* Although we find the LDF-ROM is more efficient than the C-ROM for parametric problems that have a bifurcation, the *h*-refinement strategy considered here might require an infeasible number of offline simulations as the dimension of the parameter space increases. To tackle complex parametrizations, more advanced sampling strategies that combine *h*- and *p*-refinement [86], potentially with bifurcation detection, could be beneficial [96].

[3]The $O(N^4)$ costs, which arise from the rank-3 advection tensor, might be mitigated by an $O(N^2)$ approximation to the advection operator, such as suggested in [41].

Chapter 4: Regularized Reduced Order Models

In this chapter, we investigate the performance of regularized reduced order models (Reg-ROMs) in contrast to that of classic the POD Galerkin ROM (G-ROM). The regularized models include (i) the Leray ROM (L-ROM), in which the convecting field is filtered; (ii) the evolve-filter-relax ROM (EFR-ROM), which evolves the solution by a standard G-ROM update followed by a relaxation (or filtering) step; and (iii) a time-relaxation ROM (TR-ROM), which adds an energy dissipation term to the right-hand side of the reduced model of the evolution (i.e., Navier-Stokes and energy) equations. Models (i) and (ii) have been the subject of prior investigations, including [26, 28, 29, 30] for the L-ROM and [28, 30] for the EFR-ROM. Model (iii), the main focus of this chapter, is new in the ROM context, but has it roots in LES methods [97, 98, 99, 100, 101, 102]

The main test case for this comparative investigation is turbulent channel flow. We consider friction Reynolds numbers $\mathrm{Re}_\tau = 180$ and 395 in both the reproduction and predictive regimes. To ensure a thorough assessment of the new TR-ROM, we compare it with the two other Reg-ROMs in current use. For each Reg-ROM, we investigate two different filters: (i) the differential filter (DF); and (ii) a new higher-order algebraic filter. We expect the three Reg-ROMs to alleviate the G-ROM spurious numerical oscillations and yield more accurate results with a negligible modest computational overhead. We also compare the three Reg-ROMs with the classical G-ROM, (i.e., the ROM that does not use any stabilization or closure), and with the projection error, which is the error with respect to the projection of the FOM solution onto the space spanned by the ROM basis functions.

It is well known that, in numerical simulation of turbulent flows, the parameters used in the computational setting can have a significant effect on the ROM results. Thus, to ensure a fair assessment of the Reg-ROMs, we perform a sensitivity study of the numerical results with respect to the following parameters: (i) the number of ROM basis functions, N, used to construct the ROM; (ii) the filter order, m; (iii) the filter radius, δ; (iv) the relaxation parameter, χ; and (v) the time interval.

At the end of the chapter, we investigate the performance of the G-ROM and the three Reg-ROMs for a nuclear engineering application, namely, thermal striping in a T-junction [103]. For each ROM, we explore the time history of temperature at multiple stations along the axis downstream of the T-junction where two confluent flows of differing temperatures meet.

The numerical investigation reveals that all three Reg-ROMs significantly improve accuracy compared to the classical G-ROM and the projection error without substantial computational

cost increase. In addition, the new TR-ROM outperforms L-ROM and EFR-ROM with optimal parameters in each of the reproduction and predictive regimes, at each Re_τ. Moreover, the higher-order algebraic filter with filter order $m = 1$ generally produces the best results across most N values, while with $m > 1$ is more effective for small N and lower Reynolds numbers ($\mathrm{Re}_\tau = 180$). Sensitivity studies also show the predictive capability of the three Reg-ROMs. However, all three Reg-ROMs are sensitive to the relaxation parameter (χ) and filter radius (δ). Finally, the investigation of the higher-order algebraic filter shows that it is indeed a spatial filter and its behavior is consistent with spatial filtering in the SEM settings, where larger m values dampen higher-index modes while having less impact on lower-index modes.

The rest of the chapter is organized as follows: In Sections 4.1–4.3, we introduce three regularized ROMs, i.e., the Leray-ROM (L-ROM), evolve-filter-relax ROM (EFR-ROM), and the new time relaxation ROM (TR-ROM). In Section 4.4, we describe the two ROM spatial filters that we use to construct the Reg-ROMs: the classical differential filter and the higher-order algebraic filter. In Section 4.5, we present a numerical investigation of the higher-order algebraic filter. In Section 4.6, we perform a numerical investigation of the three Reg-ROMs in the numerical simulation of the turbulent channel flow at friction Reynolds numbers $\mathrm{Re}_\tau = 180$ and 395. As a benchmark for our numerical investigation, we use DNS results. For comparison purposes, we also use the standard G-ROM. In our investigation, we assess the accuracy of the three Reg-ROMs and their sensitivity with respect to parameters in both the reproduction and the predictive regimes. In Section 4.7, we consider application of the ROMs to the T-junction problem. In Section 4.6, we present the conclusions of our numerical investigation and we outline directions for future developments of Reg-ROMs in the context of turbulent flows.

4.1 Leray ROM

The *Leray ROM (L-ROM)* [26, 28] modifies the standard G-ROM weak formulation (2.31) as follows: *Find* $\widetilde{\mathbf{u}}_r$ *of the form* (2.29) *such that,* $\forall\, i = 1, \ldots N$,

$$\left(\frac{\partial \widetilde{\mathbf{u}}_\mathrm{r}}{\partial t}, \boldsymbol{\varphi}_i\right) + Re^{-1}\ (\nabla \widetilde{\mathbf{u}}_\mathrm{r}, \nabla \boldsymbol{\varphi}_i) + \left((\overline{\boldsymbol{u}}_\mathrm{r} \cdot \nabla)\widetilde{\mathbf{u}}_\mathrm{r}, \boldsymbol{\varphi}_i\right) = 0 \tag{4.1}$$

where $\overline{\boldsymbol{u}}_\mathrm{r}$ is a regularized advecting field that derives from filtering the ROM velocity with one of the ROM spatial filters that will be introduced in Section 4.4, that is, DF (4.13) or HOAF (4.14).

L-ROM (4.1) is a Reg-ROM, because it leverages spatial filtering of the convective term of

the G-ROM (i.e., it replaces $(\widetilde{\mathbf{u}}_\mathrm{r} \cdot \nabla)\widetilde{\mathbf{u}}_\mathrm{r}$ with $(\overline{\boldsymbol{u}}_\mathrm{r} \cdot \nabla)\widetilde{\mathbf{u}}_\mathrm{r}$) in order to smooth out the G-ROM's spurious numerical oscillations in the convection-dominated, under-resolved regime.

In a more general setting, the Leray model was first introduced by Jean Leray in 1934 as a theoretical tool to prove existence of weak solutions of the NSE [104]. As a computational tool, Leray regularization was first used in [105] as a stabilization strategy for under-resolved simulations of turbulent flows with classical numerical discretizations [97]. As noted by Guermond and co-authors [79, 80], when a differential filter is used, the Leray model is similar to the NS-α model of Foias, Holm, and Titi [106]. Leray regularization was first used in the context of reduced order models in [29] for the Kuramoto-Sivashinsky equations. For fluid flows, L-ROM was first used in [28] for the 3D flow past a circular cylinder at $Re = 1000$. Since then, L-ROM has been successfully used as a stabilization technique for various under-resolved flows: the NSE [107, 108], the stochastic NSE [109, 110], and the quasigeostrophic equations [111, 112]. To our knowledge, L-ROM has never been used for reduced-order models of turbulent channel flow.

4.2 Evolve-Filter-Relax ROM

The *evolve-filter-relax ROM (EFR-ROM)*, introduced in [28, 109], consists of three steps. *Given the EFR-ROM approximation at the current time step, $\widetilde{\mathbf{u}}_r^n$, find the EFR-ROM approximation at the next time step, $\widetilde{\mathbf{u}}_r^{n+1}$, as follows.*

(I) *Evolve*: *Find $\widetilde{\mathbf{w}}_r$ of the form (2.29) such that, $\forall\, i = 1, \ldots N$,*

$$\left(\frac{\widetilde{\mathbf{w}}_\mathrm{r}^{n+1} - \widetilde{\mathbf{u}}_\mathrm{r}^{n}}{\Delta t}, \boldsymbol{\varphi}_i\right) + Re^{-1}\,(\nabla\widetilde{\mathbf{u}}_\mathrm{r}^{n}, \nabla\boldsymbol{\varphi}_i) + \left((\widetilde{\mathbf{u}}_\mathrm{r}^{n} \cdot \nabla)\widetilde{\mathbf{u}}_\mathrm{r}^{n}, \boldsymbol{\varphi}_i\right) = 0 \tag{4.2}$$

(II) *Filter*: $$\widetilde{\mathbf{w}}_\mathrm{r}^{n+1} \longmapsto \overline{\mathbf{w}}_\mathrm{r}^{n+1} \tag{4.3}$$

(III) *Relax*: $$\widetilde{\mathbf{u}}_\mathrm{r}^{n+1} = (1-\chi)\,\widetilde{\mathbf{w}}_\mathrm{r}^{n+1} + \chi\,\overline{\mathbf{w}}_\mathrm{r}^{n+1}. \tag{4.4}$$

In Step (I) of the EFR-ROM, called the evolve step, one step of the standard G-ROM time discretization is used to advance the current EFR-ROM approximation, $\widetilde{\mathbf{u}}_\mathrm{r}^{n}$, to an intermediate EFR-ROM approximation, $\widetilde{\mathbf{w}}_\mathrm{r}^{n+1}$. In Step (II), called the filter step, one of the two ROM spatial filters will be presented in Section 4.4 is used to filter the intermediate EFR-ROM approximation obtained in Step (I) and obtain a smoother approximation, without spurious numerical oscillations. Finally, in Step (III), called the relax step, the EFR-ROM

approximation at the next time step is defined as a convex combination of the unfiltered intermediate EFR-ROM approximation obtained in Step (I), $\widetilde{\mathbf{w}}_{\mathrm{r}}^{n+1}$, and its filtered counterpart, $\overline{\mathbf{w}}_{\mathrm{r}}^{n+1}$. The goal of the relax step is to adjust the amount of dissipation introduced in the filter step by using a relaxation parameter, $0 \leq \chi \leq 1$. By varying χ, one can produce a range of filter strengths, from no filtering at all ($\chi = 0$) to maximum filtering ($\chi = 1$). We note that the numerical investigation in [30] has shown that EFR-ROM is sensitive with respect to χ.

The EFR strategy is well developed for classical numerical discretizations, for example, in the context of finite element method [97], and the spectral and spectral element methods [113, 114]. In reduced order modeling, the evolve-filter ROM was introduced in [28] and EFR-ROM in [109]. Since then, EFR-ROM has been developed in several directions, for example, the FOM-ROM consistency [30] and feedback control [115].

4.3 Time Relaxation ROM

In this work, we propose a new type of Reg-ROM: the *time-relaxation ROM (TR-ROM)*: *Find* $\widetilde{\mathbf{u}}_r$ *of the form* (2.29) *such that,* $\forall\, i = 1, \ldots N$,

$$\left(\frac{\partial \widetilde{\mathbf{u}}_{\mathrm{r}}}{\partial t}, \boldsymbol{\varphi}_i\right) + \frac{1}{\mathrm{Re}}\left(\nabla \widetilde{\mathbf{u}}_{\mathrm{r}}, \nabla \boldsymbol{\varphi}_i\right) + \left((\widetilde{\mathbf{u}}_{\mathrm{r}} \cdot \nabla)\widetilde{\mathbf{u}}_{\mathrm{r}}, \boldsymbol{\varphi}_i\right) + \left(\chi(\widetilde{\mathbf{u}}_{\mathrm{r}} - \overline{\boldsymbol{u}}_{\mathrm{r}}), \boldsymbol{\varphi}_i\right) = 0, \tag{4.5}$$

where χ is the time-relaxation parameter, and $\overline{\boldsymbol{u}}_{\mathrm{r}}$ is the ROM velocity filtered with one of the ROM spatial filters will be introduced in Section 4.4, that is, DF (4.13) or HOAF (4.14).

Time-relaxation has been used as a regularization/stabilization strategy at a FOM level [97, Chapter 5] (see also [98, 99, 100, 101, 102]). To our knowledge, this is the first use of time-relaxation stabilization in the ROM context.

To understand the role of the time relaxation term, we consider $\widetilde{\mathbf{u}}_{\mathrm{r}}$ as test function in TR-ROM (4.5), which is the usual approach in energy-stability analysis. With this choice, the last term on the left-hand side of (4.5) can be written as follows:

$$(\chi(\widetilde{\mathbf{u}}_{\mathrm{r}} - \overline{\boldsymbol{u}}_{\mathrm{r}}), \widetilde{\mathbf{u}}_{\mathrm{r}}) = \chi(\widetilde{\mathbf{u}}'_{\mathrm{r}}, \widetilde{\mathbf{u}}_{\mathrm{r}}), \tag{4.6}$$

where $\widetilde{\mathbf{u}}'_{\mathrm{r}}$ represents the fluctuations of $\widetilde{\mathbf{u}}_{\mathrm{r}}$ around $\overline{\boldsymbol{u}}_{\mathrm{r}}$:

$$\widetilde{\mathbf{u}}'_{\mathrm{r}} := \widetilde{\mathbf{u}}_{\mathrm{r}} - \overline{\boldsymbol{u}}_{\mathrm{r}}. \tag{4.7}$$

Using the decomposition (4.7), the inner product in the time relaxation term (4.6) becomes:

$$(\widetilde{\mathbf{u}}'_{\mathrm{r}}, \widetilde{\mathbf{u}}_{\mathrm{r}}) = (\widetilde{\mathbf{u}}'_{\mathrm{r}}, \widetilde{\mathbf{u}}'_{\mathrm{r}}) + (\widetilde{\mathbf{u}}'_{\mathrm{r}}, \overline{\boldsymbol{u}}_{\mathrm{r}}). \tag{4.8}$$

The first term on the right-hand side of (4.8) has a clear physical interpretation: It is a dissipative term acting only on the fluctuations. To understand the role played by the second term on the right-hand side of (4.8), we distinguish two cases:

Case 1: DF. When DF is used to construct TR-ROM, we can use (4.12) and (4.7) to formally write the following:

$$\widetilde{\mathbf{u}}'_{\mathrm{r}} = \widetilde{\mathbf{u}}_{\mathrm{r}} - \overline{\boldsymbol{u}}_{\mathrm{r}} = -\delta^2 \Delta \overline{\boldsymbol{u}}_{\mathrm{r}}. \tag{4.9}$$

Using (4.9) in the last term in (4.8), we obtain the following:

$$\begin{aligned}
(\widetilde{\mathbf{u}}'_{\mathrm{r}}, \widetilde{\mathbf{u}}_{\mathrm{r}}) &= (\widetilde{\mathbf{u}}'_{\mathrm{r}}, \widetilde{\mathbf{u}}'_{\mathrm{r}}) + (\widetilde{\mathbf{u}}'_{\mathrm{r}}, \overline{\boldsymbol{u}}_{\mathrm{r}}) \\
&= (\widetilde{\mathbf{u}}'_{\mathrm{r}}, \widetilde{\mathbf{u}}'_{\mathrm{r}}) - \delta^2 (\Delta \overline{\boldsymbol{u}}_{\mathrm{r}}, \overline{\boldsymbol{u}}_{\mathrm{r}}) \\
&\overset{\overline{\boldsymbol{u}}_{\mathrm{r}}=0 \text{ on } \partial\Omega}{=} (\widetilde{\mathbf{u}}'_{\mathrm{r}}, \widetilde{\mathbf{u}}'_{\mathrm{r}}) + \delta^2 (\nabla \overline{\boldsymbol{u}}_{\mathrm{r}}, \nabla \overline{\boldsymbol{u}}_{\mathrm{r}}) \\
&\overset{(4.9)}{=} \delta^4 (\Delta \overline{\boldsymbol{u}}_{\mathrm{r}}, \Delta \overline{\boldsymbol{u}}_{\mathrm{r}}) + \delta^2 (\nabla \overline{\boldsymbol{u}}_{\mathrm{r}}, \nabla \overline{\boldsymbol{u}}_{\mathrm{r}}).
\end{aligned} \tag{4.10}$$

Equality (4.10) shows that the TR-ROM term in (4.6) is a dissipative term that has two components: The first component can be interpreted either as a dissipation term acting on the fluctuations or as a hyper-viscosity term acting on the averages. The second component is a diffusion term acting on the averages.

Case 2: HOAF. The HOAF is a high-order algebraic filter (4.14) that does not have a direct interpretation as a differential operator (primarily because of ambiguity related to boundary conditions). When HOAF (4.14) is used to construct TR-ROM, we cannot use the above approach to interpret the TR-ROM term because HOAF cannot be easily written in terms of the spatial derivative operators. However, we can (optimistically) expect behavior of the following form for a $2m$th-order filter,

$$\begin{aligned}
(\widetilde{\mathbf{u}}'_{\mathrm{r}}, \widetilde{\mathbf{u}}_{\mathrm{r}}) &= (\widetilde{\mathbf{u}}'_{\mathrm{r}}, \widetilde{\mathbf{u}}'_{\mathrm{r}}) + \delta^{2m} (\nabla^m \overline{\boldsymbol{u}}_{\mathrm{r}}, \nabla^m \overline{\boldsymbol{u}}_{\mathrm{r}}) \\
&= \delta^{4m} (\Delta^m \overline{\boldsymbol{u}}_{\mathrm{r}}, \Delta^m \overline{\boldsymbol{u}}_{\mathrm{r}}) + \delta^{2m} (\nabla^m \overline{\boldsymbol{u}}_{\mathrm{r}}, \nabla^m \overline{\boldsymbol{u}}_{\mathrm{r}}),
\end{aligned} \tag{4.11}$$

which has the same physical interpretation as that in the DF case and which is in fact exact if the domain is periodic in all directions.

A numerical comparison of the DF and the HOAF will be presented in Section 4.5, and an

investigation of their effect on the TR-ROM results will be presented in Section 4.6.

4.4 ROM Filters

In this section, we present the two ROM spatial filters that are used to construct the Reg-ROMs in Sections 4.1–4.3: the classical algebraic filter (Section 4.4.1) and the higher-order algebraic filter (Section 4.4.2).

4.4.1 ROM Differential Filter (DF)

The first ROM spatial filter we investigate is the *ROM differential filter (DF)*: *Given* $\boldsymbol{u}_r = \sum_{j=1}^{N} u_{r,j}\boldsymbol{\varphi}_j(\mathbf{x})$, *find* $\overline{\boldsymbol{u}}_r(\mathbf{x}) = \sum_{j=1}^{N} \overline{u}_{r,j}\boldsymbol{\varphi}_j(\mathbf{x})$ *such that*

$$\left(\overline{\boldsymbol{u}}_{\mathrm{r}} - \delta^2 \Delta \overline{\boldsymbol{u}}_{\mathrm{r}}, \boldsymbol{\varphi}_i\right) = \left(\boldsymbol{u}_{\mathrm{r}}, \boldsymbol{\varphi}_i\right) \qquad \forall\, i = 1, \ldots N, \tag{4.12}$$

where δ is the filter radius. The DF weak form (4.12) yields the following linear system:

$$\left(\mathbb{I} + \delta^2 A\right) \underline{\overline{u}}_{\mathrm{r}} = \underline{u}_{\mathrm{r}}, \tag{4.13}$$

where $\underline{u}_t r$ and $\underline{\overline{u}}_{\mathrm{r}}$ are the vector of ROM coefficients of $\boldsymbol{u}_r$ and $\overline{\boldsymbol{u}}_{\mathrm{r}}$, and $\mathbb{I}$ and A are the identity and ROM stiffness matrices, respectively. We note that, in general, the inverse of the ROM mass matrix, B^{-1}, is accompanied with A, but because the POD basis considered here is orthonormal in the L^2 norm, B is simply identity matrix and therefore ignored. We note that the expansions for $\boldsymbol{u}_{\mathrm{r}}$ and $\overline{\boldsymbol{u}}_{\mathrm{r}}$ do not include the zeroth mode, $\boldsymbol{\varphi}_0$. This is in contrast with the expansion (2.29), which does include $\boldsymbol{\varphi}_0$. The reason for not including $\boldsymbol{\varphi}_0$ in our expansions is that, because this strategy was shown in [28] to yield more accurate results.

We emphasize that (4.13) is a low-dimensional, $N \times N$ linear system, whose computational overhead is negligible. Thus, the DF stabilizes the G-ROM without significantly increasing the computational cost.

The DF was used in large eddy simulation of turbulent flows with classical numerical discretizations [97, 116]. In reduced order modeling, the DF was used to develop Reg-ROMs for the Kuramoto-Sivashinsky equation [29], the NSE [28, 30], and the quasi-geostrophich equations [111].

4.4.2 ROM Higher-Order Differential Filter (HOAF)

The second filter we investigate is the *higher-order algebraic filter (HOAF)*: *Given* $\boldsymbol{u}_r = \sum_{j=1}^{N} u_{r,j}\boldsymbol{\varphi}_j(\mathbf{x})$, *find* $\overline{\boldsymbol{u}}_r(\mathbf{x}) = \sum_{j=1}^{N} \overline{u}_{r,j}\boldsymbol{\varphi}_j(\mathbf{x})$ *such that*

$$H_m\underline{\overline{u}}_{\mathrm{r}} := \left(\mathbb{I} + \delta^{2m}A^m\right)\underline{\overline{u}}_{\mathrm{r}} = \underline{u}_{\mathrm{r}}, \tag{4.14}$$

where $\underline{u}_{\mathrm{r}}$ and $\underline{\overline{u}}_{\mathrm{r}}$ are the vectors of ROM basis coefficients of $\boldsymbol{u}_{\mathrm{r}}$ and $\overline{\boldsymbol{u}}_{\mathrm{r}}$, respectively, and m is a positive integer. Again the expansions for $\boldsymbol{u}_{\mathrm{r}}$ and $\overline{\boldsymbol{u}}_{\mathrm{r}}$ do not include the zeroth mode, $\boldsymbol{\varphi}_0$ as explained in Section 4.4.1. As explained in [113] in the Fourier setting, the role of the exponent m is to control the percentage of filtering at different wavenumbers: As m increases, the amount of filtering increases for the high wavenumber components and decreases for the low wavenumber components.

We note that the HOAF (4.14) is a low-dimensional, $N \times N$ linear system, just as the DF (4.13). Thus, Reg-ROMs with the HOAF are efficient.

Remark 4.1 (Notation Convention)**.** We also note that, for $m = 1$, the linear systems (4.14) and (4.13) are identical. Thus, DF can be considered a particular case of the HOAF with $m = 1$. In what follows, for notational convenience, we will use the linear system (4.14) for both the HOAF and the DF, and we will only specify the m value to differentiate between the two: $m = 1$ for the DF and $m \geq 2$ for the HOAF.

Remark 4.2. The HOAF (4.14) was proposed in [109] and was based on the HOAF introduced by Fischer and Mullen [113] in a spectral element method (SEM) setting. We also note that the HOAF used in [109] has a δ scaling that is dimensionally inconsistent. This is rectified in (4.14).

Remark 4.3 (Nomenclature)**.** In [109], the HOAF (4.14) was called the higher-order differential filter, to be consistent with the SEM nomenclature. The HOAF is related to, but slightly different from, the spatial discretization of a higher-order differential operator. (They are the same in the periodic case.) Thus, for clarity, in this dissertation we call the operator in (4.14) the high-order algebraic filter: The term A^m yields the high-order algebraic character of the operator (4.14), and the numerical investigation in Section 4.5 shows that the operator (4.14) acts like a spatial filter.

4.5 HOAF Numerical Investigation

In this section, we investigate the HOAF (4.14) in one- and two-dimensional spectral element (SEM) setting and a POD setting. In particular, we like to know whether the HOAF is a

spatial filter by examing if the output $\overline{\boldsymbol{u}}$ is smoother compared to the input, $\boldsymbol{u}$. We also study the role of the exponent m in the HOAF.

Note that we consider only integers $m \geq 2$ because, as explained in Remark 4.1, the standard (low-order) DF (4.13) can be considered as a particular case of the HOAF with $m = 1$. Thus, to distinguish between the DF and the HOAF, in this section we exclusively consider $m \geq 2$ in the HOAF.

In addition, we note that a similar numerical investigation was carried out in the SEM setting in [113], where it was shown that the HOAF (4.14) is a spatial filter that attenuates the high wavenumber components of the input field. Furthermore, it was also shown that the exponent m in HOAF (4.14) controls the percentage of filtering at different wavenumbers: As m increases, the amount of filtering increases for the high wavenumber components of the input field, and decreases for the low wavenumber components [113, Figure 1].

One-Dimensional SEM Setting. We consider the spatial domain $\Omega = [0, 1]$ and construct the HOAF (4.14) using a SEM discretization that consists of a 64 array of 7th-order spectral elements. Note that, in the SEM setting, instead of A^m we use $(B^{-1}A)^m$ in (4.14), and $\underline{u}$ and $\overline{\underline{u}}$ are the SEM basis coefficients for the input (unfiltered) and output (filtered) functions, respectively.

We construct an input function u that has both low and high wavenumber components:

$$u(x) = 0.5\sin(2\pi x) + 0.5\sin(10\pi x) + 2\sin(20\pi x), \tag{4.15}$$

and set the filter radius δ to be 0.025. We then consider four m values and compare the corresponding HOAF output $\overline{u}$ with the input function u in Fig. 4.1. The $m = 1$ results show that, although HOAF has attenuated the high wavenumber ($k = 20$) component of the input function, that component is still visible. However, as we increase the HOAF order (i.e., use $m = 2, 3, 4$), the high wavenumber component of the input function starts to significantly decrease. In fact, for $m = 4$, the high wavenumber component is practically eliminated. We also note that the medium wavenumber ($k = 10$) component of the input function is affected differently by the different m values: For $m = 1$, the medium wavenumber component is slightly attenuated. In contrast, for $m = 4$, the medium wavenumber component remains unchanged. Finally, the low wavenumber ($k = 2$) component of the input function is practically unaffected by the HOAF order. Thus, the results in Fig. 4.1 suggest that, as expected, using the classical DF (i.e., HOAF with $m = 1$) attenuates the medium and high wavenumber components of the input function. The higher-order HOAF (i.e., HOAF with $m = 2, 3, 4$) attenuates more the high wavenumber component, and almost not at all the

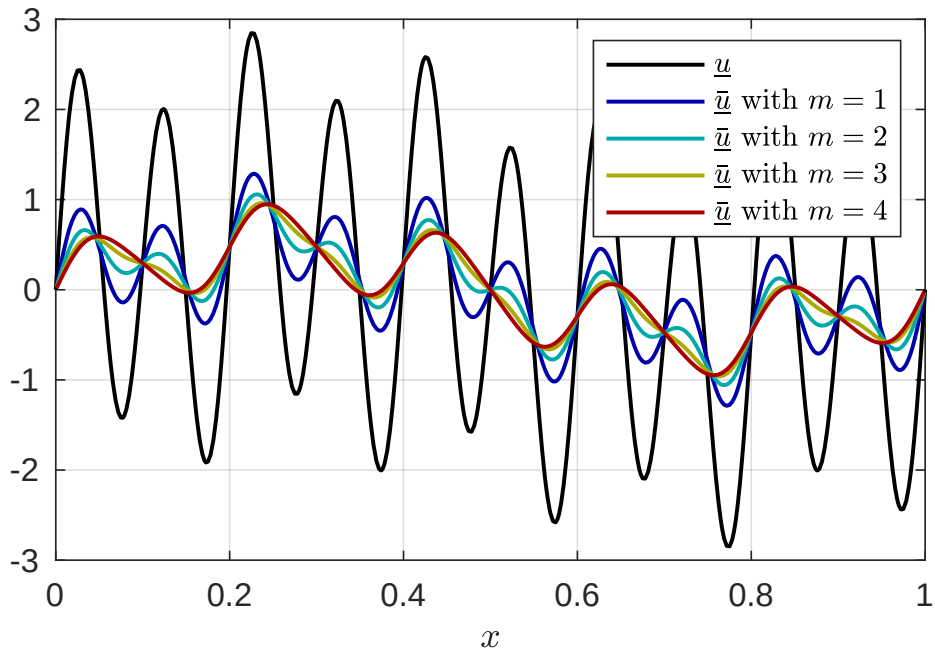

Figure 4.1: Comparison of the input function $u(x) = 0.5\sin(2\pi x) + 0.5\sin(10\pi x) + 2\sin(20\pi x)$ and four HOAF outputs $\overline{u}$ that correspond to $m = 1,\ 2,\ 3,\ 4$, and $\delta = 0.025$.

medium wavenumber component.

Two-Dimensional SEM Setting. We consider the spatial domain $\Omega = [0,1]^2$ and construct the HOAF (4.14) using a SEM discretization that consists of a 12×12 array of 7th-order spectral elements. We construct an input function u that has low and high wavenumber components:

$$u(x,y) = 0.5\sin(2\pi x)\sin(2\pi y) + \sin(4\pi x)\sin(4\pi y) + 2\sin(6\pi x)\sin(6\pi y), \tag{4.16}$$

and set filter radius δ to be 0.06. We then consider three m values and compare the corresponding HOAF output $\overline{u}$ with the input function u in Fig. 4.2. The $m = 1$ results show that, although HOAF has attenuated the high wavenumber ($(k_1, k_2) = (6,6)$ component of the input function, that component is still visible. However, as we increase the HOAF order (i.e., use $m = 2, 3$), the high wavenumber component of the input function starts to significantly decrease. We also note that the medium wavenumber ($(k_1, k_2) = (4,4)$) component of the input function is affected differently by the different m values: For $m = 1$, the medium wavenumber component is slightly attenuated. In contrast, for $m = 3$, the medium wavenumber component remains unchanged. Finally, the low wavenumber

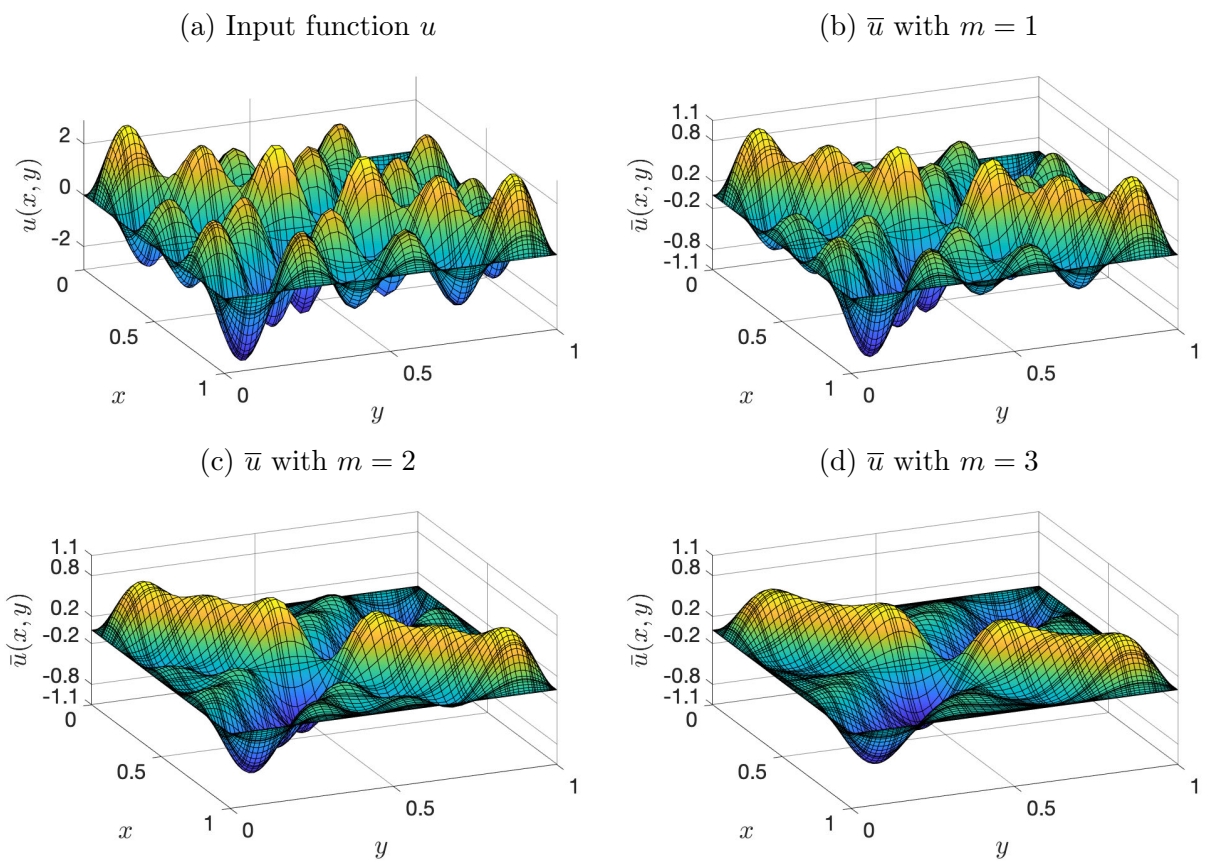

Figure 4.2: Comparison of the input function $u(x,y) = 0.5\sin(2\pi x)\sin(2\pi y) + \sin(4\pi x)\sin(4\pi y) + 2\sin(6\pi x)\sin(6\pi y)$ and three HOAF outputs $\overline{u}$ corresponding to $m = 1,\ 2,\ 3$ with $\delta = 0.06$.

$((k_1, k_2) = (2,2))$ component of the input function is unaffected by the HOAF order. Thus, the results in Fig. 4.2 again suggest that the classical DF (i.e., HOAF with $m = 1$) attenuates the medium and high wavenumber components of the input function. The higher-order HOAF (i.e., HOAF with $m = 2, 3$) attenuates more the high wavenumber component, and almost not at all the medium wavenumber component.

POD Setting. Here, we investigate the HOAF (4.14) in a POD setting. Specifically, we consider the POD basis set for the turbulent channel flow at $\mathrm{Re}_\tau = 180$ as detailed in Section 4.6.

The HOAF is constructed with $N = 100$ using an L^2-based POD basis. To understand the impact of the HOAF (4.14) on each POD basis, we specifically construct the input coefficient vector $\underline{u}$ as a unit vector (i.e., $\underline{u} = [1, \ldots, 1]^T$). The resulting output vector $\underline{\overline{u}}$ thus indicates how much each POD basis is damped by the HOAF.

In our first case, the $N = 100$ mode POD basis is derived from 2000 snapshots taken over 25 convective time units ($25 \times H/\bar{U}$, where H is the channel half-height and $\bar{U}$ is the bulk velocity). Fig. 4.3 displays the coefficient magnitude of the input $\underline{u}$ (black) and $\overline{\underline{u}}$ associated with the four m values (multi-colored) and $\delta = 0.0475$. Here, we see the expected behavior that increasing m yields a sharper drop in the transfer function ($\bar{u}_i/u_i$) for high mode numbers, i, with less suppression of the low mode numbers, which is consistent with an interpretation of the POD modes as "Fourier" modes. Note that all of the curves cross at $\bar{u}_i/u_i \approx 1/2$ near $i = 60$, which implies that modes with $i < 60$ have characteristic length scales $\lambda_i > \delta = 0.0775$, given that we expect

$$\frac{\bar{u}_i}{u_i} \sim \frac{1}{1 + (\delta/\lambda_i)^{2m}} . \tag{4.17}$$

Thus, we see that, in this case, the HOAF provides a convenient means to associate a length scale with each mode.

Unfortunately, not all snapshot/POD basis sets lend themselves to the easy interpretation of the preceding example. Fig. 4.4 displays the coefficient magnitude of the input $\underline{u}$ and four $\overline{\underline{u}}$ with $m = 1,\ 2,\ 3,\ 4$ and $\delta = 0.08125$ for the case of $N = 100$ derived from 2000 snapshots sampled uniformly over 500 convective time units. In general, for $i \geq 36$, larger m (higher-order filter) leads to larger damping in $\overline{u}_i$ while for $i \leq 34$, larger m leads to smaller damping in $\overline{u}_i$, but the ranking is no longer as obvious as in the case of Fig. 4.3.

We suspect that the root cause of the irregularity is that the snapshots are highly decorrelated in this case. The snapshots are effectively random, despite being solutions of the NSE. We have made some preliminary investigations into this phenomenon through a linear-algebraic model where we attempt to reconstruct low-rank eigenmodes of a discrete Laplace operator from a random 400×399 matrix. Such an approach leads to relatively poor approximations even for wavenumbers as low as $k = 3$. With a modest amount of regularization, however, the basis set yields better approximation properties. We intend to pursue this analogy further in future work.

Fig. 4.5 illustrates the physical-space effect of the HOAF for $m = 1,\ 2,\ 3,\ 4$ and $\delta = 0.0475$. Here we plot the physical space output—the sum of all the basis functions—weighted by the coefficients given in Fig. 4.3. It is clear that the filtered field $\overline{u}$ is smoother as m increases.

Fig. 4.6 illustrates the physical-space effect of the HOAF for $m = 1,\ 2,\ 3,\ 4$ and $\delta = 0.08125$. Here we plot the physical space output—the sum of all the basis functions—weighted by the coefficients given in Fig. 4.4. It is clear that the filtered field $\overline{u}$ is smoother as m increases.

Overall, these results show that the HOAF in the POD setting has a similar behavior as in the SEM setting, that is, larger m values tend to damp the higher modes more and have

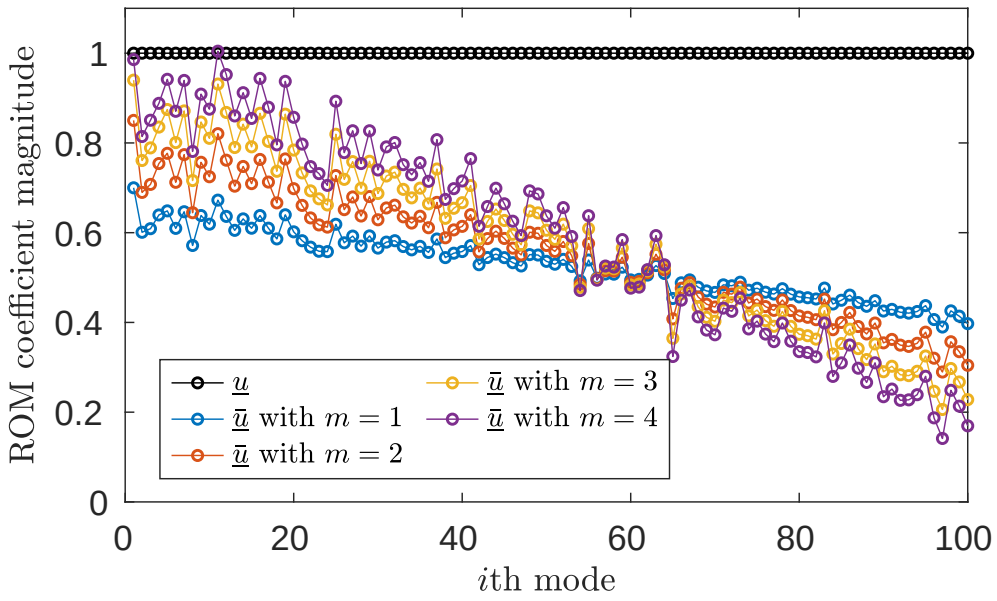

Figure 4.3: Comparison of the ROM coefficient magnitude of the input $\underline{u}$ and output $\overline{\underline{u}}$ associated with $m = 1,\ 2,\ 3,\ 4$. The HOAF (4.14) is formed using $N = 100$ L^2 POD basis constructed using 2000 snapshots over the first 25 CTUs and the filter radius $\delta = 0.0475$.

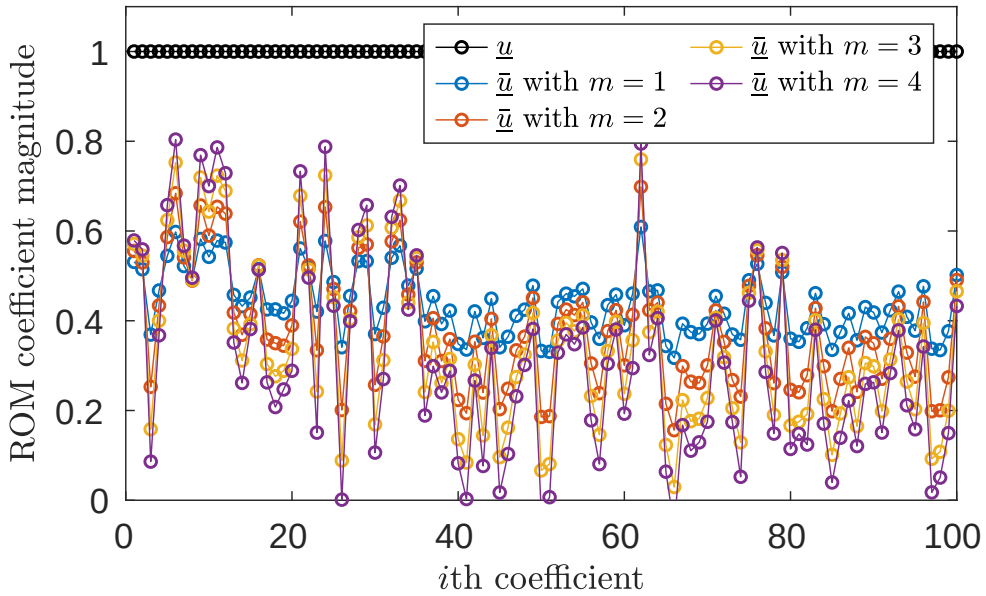

Figure 4.4: Comparison of the coefficient magnitude of the input $\underline{u}$ and output $\overline{\underline{u}}$ associated with $m = 1,\ 2,\ 3,\ 4$. The HOAF (4.14) is formed using $N = 100$ POD basis constructed using snapshots in 500 CTUs time interval and $\delta = 0.08125$.

less impact on the lower modes compared to smaller m values. However, unlike in the SEM setting where the low-wave number modes are usually undamped regardless of the m value,

(a) $\overline{u}$ with $m = 1$ (b) $\overline{u}$ with $m = 2$

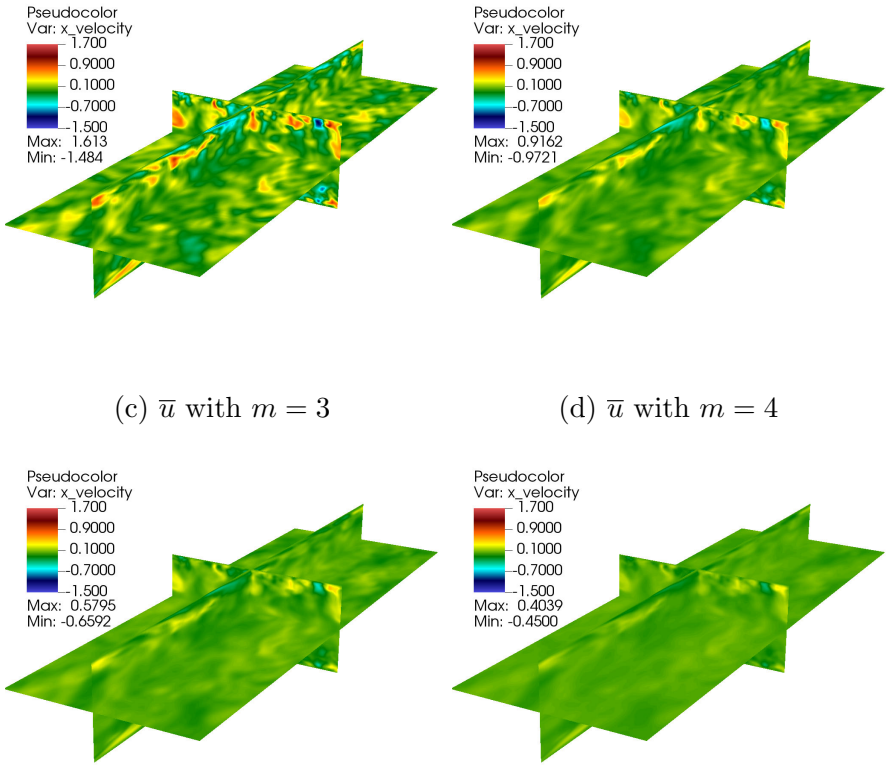

(c) $\overline{u}$ with $m = 3$ (d) $\overline{u}$ with $m = 4$

Figure 4.5: Comparison of streamwise component of the filtered function $\overline{\boldsymbol{u}}$ with $m = 1,\ 2,\ 3,\ 4$, and $\delta = 0.0475$. The display range is fixed to be $[-1.5,\ 1.7]$ and the maximum and minimum magnitudes are reported in the legend.

all POD modes are damped in the POD setting.

In this numerical investigation we exclusively used an L^2 POD basis, which is the most popular choice in reduced order modeling. We note, however, that the H_0^1 POD basis could provide a clearer illustration of the HOAF spatial filtering capabilities. Indeed, as highlighted in [17], the H_0^1 POD basis is better in capturing the small-scale structures and distinguishing them from the large-scale structures in the solution compared to the L^2 POD basis. Hence, we anticipate more distinct results in the filtered coefficients when the HOAF is constructed by using the H_0^1 POD basis.

(a) $\overline{u}$ with $m = 1$ (b) $\overline{u}$ with $m = 2$

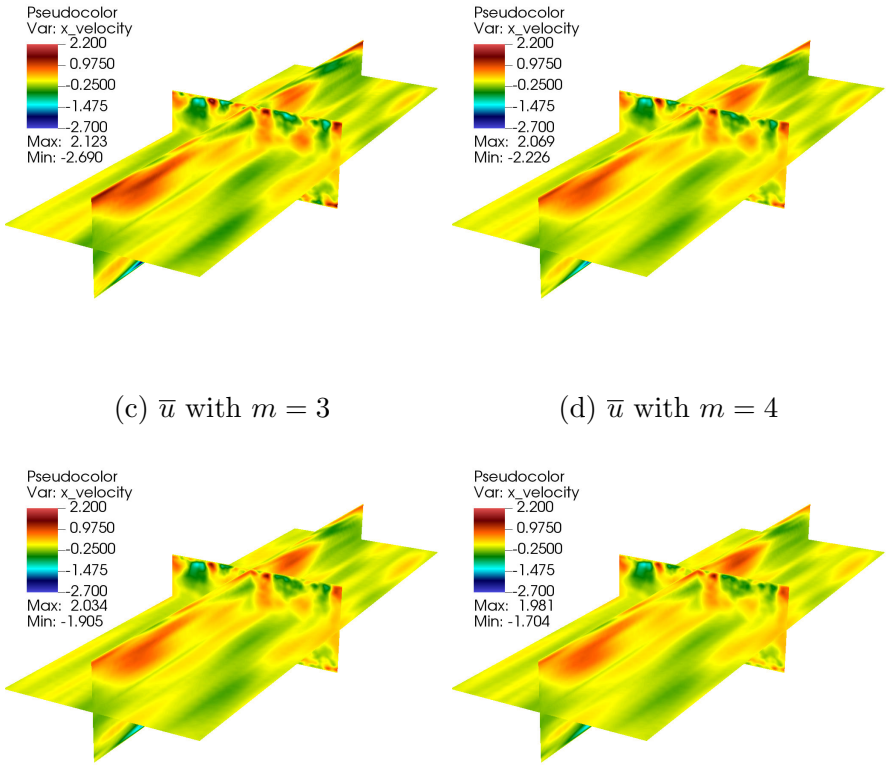

(c) $\overline{u}$ with $m = 3$ (d) $\overline{u}$ with $m = 4$

Figure 4.6: Comparison of streamwise component of the filtered function $\overline{\boldsymbol{u}}$ with $m = 1,\ 2,\ 3,\ 4$, and $\delta = 0.08125$. The display range is fixed to be $[-2.7,\ 2.2]$ and the maximum and minimum magnitudes are reported in the legend.

4.6 Application - Turbulent Channel Flow

In this section, we present numerical results of the three Reg-ROMs presented in Sections 4.1–4.3 in the simulation of the turbulent channel flow. Specifically, we compare L-ROM (4.1), EFR-ROM (4.4), and the novel TR-ROM (4.5). For comparison purposes, we also investigate the standard G-ROM (2.31). As a benchmark for our comparison, we use the FOM results, which correspond to a DNS of the turbulent channel flow. We compare the three Reg-ROMs, the G-ROM and the ROM projection in terms of their accuracy with respect to the FOM benchmark. We expect the three Reg-ROMs to yield significantly more accurate results than the standard G-ROM. We also note that, as mentioned in Section 4.4, the computational cost of the three Reg-ROMs is similar, and is on the same order of magnitude as the G-ROM cost.

The rest of this section is organized as follows: In Section 4.6.1, we present the FOM

computational setting, which is leveraged in Section 4.6.2 to construct the ROMs. In Section 4.6.3, we define the criteria used to evaluate the ROM performance. In Section 4.6.4 we outline the efficient offline-online decomposition of the Reynolds stresses that are used in our numerical investigation. We also outline the ROM projection for the Reynolds stresses, which is used as a benchmark in our numerical investigation. Next, we present numerical results of the Reg-ROM comparison for two regimes: In Section 4.6.5, we present results for the reproduction regime (i.e., when the ROMs are tested on the training time interval). In Section 4.6.6, we present results for the predictive regime (i.e., when the ROMs are tested on a time interval that is different from the training interval). Finally, in Section 4.6.7, we perform a numerical investigation of the Reg-ROMs' sensitivity with respect to the following parameters: (i) time interval; (ii) the relaxation parameter, χ; and (iii) the filter radius, δ. The objective of this sensitivity study is to determine which of the three Reg-ROMs is more robust with respect to parameter changes.

4.6.1 FOM Computational Setting

In this section, we present the computational setting for the FOM, which has two main goals: (i) to generate the snapshots used in Section 4.6.2 to construct the ROMs; and (ii) to serve as a benchmark in the ROM numerical investigation.

The governing equations for the turbulent channel flow are the incompressible Navier-Stokes equations (NSE) with forcing:

$$\frac{\partial \boldsymbol{u}}{\partial t} + (\boldsymbol{u} \cdot \nabla)\boldsymbol{u} = -\nabla p + \frac{1}{\mathrm{Re}}\nabla^2 \boldsymbol{u} + \mathbf{f}(\boldsymbol{u}), \qquad \nabla \cdot \boldsymbol{u} = 0, \tag{4.18}$$

where $\boldsymbol{u}$ is the velocity and p is the pressure. Here, $\mathbf{f}(\boldsymbol{u})$ is a uniform forcing vector field function in the streamwise direction, x, that enforces a time-constant flow-rate on the solution. The initial condition consisted of random noise, which eventually triggered transition to turbulence, and the boundary conditions are periodic in the streamwise and spanwise directions of the channel, and homogeneous Dirichlet in the wall-normal direction.

The FOM is constructed using the Galerkin projection of (4.18) onto the spectral element space with the $\mathcal{P}_q - \mathcal{P}_q$ velocity-pressure coupling. Following [64], a semi-implicit scheme BDFk/EXTk is used for time discretization. Specifically, the kth-order backward differencing (BDFk) is used for the time-derivative term, kth-order extrapolation (EXTk) for the advection and forcing terms, and implicit treatment on the dissipation terms. As discussed in [64], $k = 3$ is used to ensure the imaginary eigenvalues associated with skew-symmetric advection operator are within the stability region of the BDFk/EXTk time-stepper.

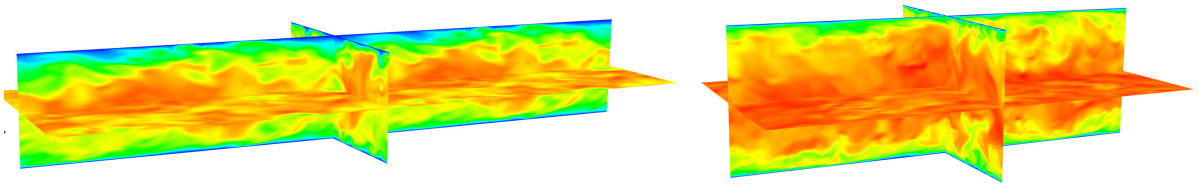

Figure 4.7: Turbulent channel flow: Velocity magnitude snapshot of the full-order model (FOM) at $\mathrm{Re}_\tau = 180$ (left) and 395 (right).

The full discretization leads to solving a linear unsteady Stokes system at each time step, as discussed in Section 2.1. The forcing term effectively adds an impulse-response streamwise velocity field. This impulse response is scaled appropriately at each time step to ensure that the mean velocity at each timestep yields the prescribed flow-rate [117, 118]. The detailed treatment of the constant-flow rate can be found in [16].

Our FOM is a direct numerical simulation (DNS) for the turbulent channel flow at $\mathrm{Re}_\tau = 180$ and $\mathrm{Re}_\tau = 395$ using the spectral element code Nek5000/RS [61, 62]. The friction Reynolds number Re_τ is based on the friction velocity u_τ at the wall, channel half-height h, and the fluid kinematic viscosity ν, with $u_\tau = \sqrt{\tau_w}/\rho$ determined using the wall shear stress τ_w and the fluid density ρ. FOM velocity magnitude snapshots for both Re_τ are shown in Fig. 4.7.

For $\mathrm{Re}_\tau = 180$, we follow the setup in [46], in which the streamwise (i.e, the x-direction) and spanwise (i.e, the z-direction) lengths of the channel are set to $4\pi h$ and $4\pi h/3$, respectively, and the channel half-height is set to $h = 1$. We consider twice as many grid points as in [46], with $E = 5,832$ elements (an array of $18 \times 18 \times 18$ elements in the $x \times y \times z$ directions), of order $q = 9$, for a total of $\mathcal{N} \approx 4.3$ million grid points. FOM statistics are collected over 1000 convection time units (CTUs) and compared against the following two databases: (i) data in [119], which is collected over 3140 CTUs and has 14.2 million grid points; and (ii) data in [46], which has 2.1 million grid points [4].

For $\mathrm{Re}_\tau = 395$, we follow the setup in [47], in which the streamwise and spanwise lengths of the channel are set to 2π and π, respectively, and the channel half-height is set to $h = 1$. We consider twice as many grid points as in [47], with $E = 26,244$ elements (an array of $36 \times 27 \times 27$ elements in the $x \times y \times z$ directions), of order $q = 9$, for a total of $\mathcal{N} \approx 20$ million grid points. FOM statistics are collected over 1500 CTUs and compared against the data in [47], which has 9.5 million grid points.

For both Reynolds numbers, the FOM is run until the solution reaches a statistically steady state prior to gathering statistics. To validate our FOM, in Fig. 4.8, for both Re_τ, we compare the FOM with the reference data with respect to the 2nd order turbulent statistics

[4] We couldn't find out how long the statistics are collected for in [46].

u^+_{rms}, v^+_{rms}, and w^+_{rms} (in wall-units). For both Re_τ, we observe that the FOM's 2nd order statistics are in good agreement with the published results.

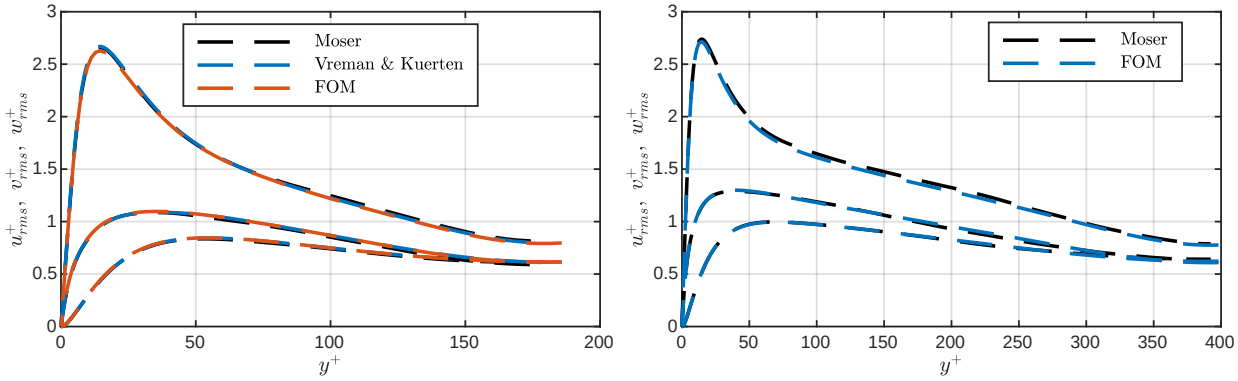

Figure 4.8: FOM 2nd order statistics u^+_{rms}, v^+_{rms}, and w^+_{rms} validation: (Left) $\mathrm{Re}_\tau = 180$, comparison with [46, 119]. (Right) $\mathrm{Re}_\tau = 395$, comparison with [47].

4.6.2 ROM Computational Setting

The POD basis is constructed using $K = 2000$ uniformly distributed snapshots in the statistically steady state region, which spans 500 CTUs for $\mathrm{Re}_\tau = 180$, and 1000 CTUs for $\mathrm{Re}_\tau = 395$.

For each Re_τ, we compare the ROM performance for different ROM parameters in both the reproduction and the predictive regimes. The ROM offline phase, which includes the construction of the POD basis and reduced operators, is performed using NekROM on the NCSA supercomputer Delta. The ROM online phase, which includes loading the reduced operators and solving the ROM systems, is performed using Matlab on a workstation.

The implementation of the three Reg-ROMs (4.1–4.5) is similar: For a given filter order, m, and filter radius, δ, all three Reg-ROMs involve computing the Cholesky factorization of the HOAF (4.14), that is $(I + \delta^{2m}(B^{-1}A)^m) = R^T R$, and storing the inverse of the upper triangular matrix R^{-1}. In each time step, a matrix multiplication $R^{-1}R^{-T}\underline{u}$ is performed to obtain the filtered ROM coefficients, $\overline{u}$. The only difference in the particular Reg-ROM implementation is how $\overline{u}$ is used in the Reg-ROM equation. We also emphasize that, because the most expensive part is to filter the ROM coefficients, the computational overhead is similar for all three Reg-ROMs.

Remark 4.4. Because the zeroth mode has the prescribed flow-rate, the remaining POD basis functions have zero flow-rate, meaning that the test space $\mathbf{X}_0^N = \mathrm{span}\{\boldsymbol{\varphi}\}_{i=1}^N$ contains

only members with zero flow-rate. Hence no additional forcing term is required for the ROM formulation because the forcing term drops out of (2.31):

$$\int_\Omega \boldsymbol{v} \cdot \mathbf{f}\, dV = f_x \left(\int_\Omega v_x dV \right) = 0, \quad \forall\ \boldsymbol{v} \in \mathbf{X}_0^N, \tag{4.19}$$

where f_x and v_x are the streamwise components of $\mathbf{f}$ and $\boldsymbol{v}$, respectively.

4.6.3 Criteria

To evaluate the ROM performance, we use the FOM data as a benchmark and the Reynolds normal stress $\langle u'u' \rangle$ and the Reynolds shear stress $\langle u'v' \rangle$, which are the two dominant terms in the Reynolds stress tensor, as criteria for accuracy evaluation. Specifically, we use the following formula:

$$\varepsilon_{u'u'} \coloneqq \frac{\|\langle u'u' \rangle_\mathrm{r} - \langle u'u' \rangle\|_2}{\|\langle u'u' \rangle\|_2}, \quad \varepsilon_{u'v'} \coloneqq \frac{\|\langle u'v' \rangle_\mathrm{r} - \langle u'v' \rangle\|_2}{\|\langle u'v' \rangle\|_2}, \tag{4.20}$$

where $\langle u'u' \rangle$ and $\langle u'v' \rangle$ are the FOM Reynolds stresses and $\langle u'u' \rangle_\mathrm{r}$, $\langle u'v' \rangle_\mathrm{r}$ are the ROM Reynolds stresses. The FOM Reynolds stresses are defined as follows:

$$\langle u'u' \rangle \coloneqq \left\langle \big(u - \langle u \rangle\big)^2 \right\rangle = \left\langle u^2 - 2u\langle u \rangle + \langle u \rangle^2 \right\rangle = \left\langle \langle u^2 \rangle - \langle u \rangle^2 \right\rangle, \tag{4.21}$$

$$\begin{aligned} \langle u'v' \rangle &\coloneqq \Big\langle \big(u - \langle u \rangle\big)\big(v - \langle v \rangle\big) \Big\rangle \\ &= \Big\langle uv - u\langle v \rangle - v\langle u \rangle + \langle u \rangle\langle v \rangle \Big\rangle = \Big\langle \langle uv \rangle - \langle u \rangle\langle v \rangle \Big\rangle. \end{aligned} \tag{4.22}$$

The ROM Reynolds stresses are computed using (4.21)-(4.22), but with the ROM approximated solution (2.29):

$$\langle u'u' \rangle_\mathrm{r} \coloneqq \left\langle \langle u_\mathrm{r}^2 \rangle - \langle u_\mathrm{r} \rangle^2 \right\rangle, \quad \langle u'v' \rangle_\mathrm{r} \coloneqq \Big\langle \langle u_\mathrm{r} v_\mathrm{r} \rangle - \langle u_\mathrm{r} \rangle\langle v_\mathrm{r} \rangle \Big\rangle. \tag{4.23}$$

Here we ignore the tilde for both the FOM u and ROM u_r for notational simplicity. In this work, an angle bracket $\langle \cdot \rangle$ indicates an average over x, z, and t, and is defined as:

$$\langle u \rangle(y) = \frac{1}{T L_x L_x} \sum_{x,z,t} u(x, y, z, t), \tag{4.24}$$

where T is the length of the time interval, L_x is the dimension of the computational domain in the x-direction, L_z is the dimension of the computational domain in the z-direction, u is a

scalar field, and a prime indicates perturbation from this average.

We note that using (4.23) to compute ROM Reynolds stresses requires accessing the POD basis and reconstructing the ROM quantities $\langle u_{\mathrm{r}}^2\rangle$, $\langle u_{\mathrm{r}}v_{\mathrm{r}}\rangle$, $\langle u_{\mathrm{r}}\rangle^2$, and $\langle u_{\mathrm{r}}\rangle\langle v_{\mathrm{r}}\rangle$, which scale with the FOM dimension, $\mathcal{N}$. Thus, using (4.23) to compute $\langle u'u'\rangle_{\mathrm{r}}$ and $\langle u'v'\rangle_{\mathrm{r}}$ is inefficient.

4.6.4 Efficient Offline-Online Reynolds-Stress Evaluation

To efficiently compute the ROM Reynolds stresses, we use an alternative approach, based on an offline-online splitting. First, we rewrite (4.23) with the POD expansion:

$$\begin{aligned}
\langle u'u'\rangle_{\mathrm{r}} &= \Big\langle \big\langle (\sum_{j=0}^{N} u_{\mathrm{r},j}(t)\varphi_j)(\sum_{k=0}^{N} u_{\mathrm{r},k}(t)\varphi_k)\big\rangle - \big\langle \sum_{j=0}^{N} u_{\mathrm{r},j}(t)\varphi_j\big\rangle^2 \Big\rangle \\
&= \langle \sum_{j=0}^{N}\sum_{k=0}^{N} \langle u_{\mathrm{r},j}(t)u_{\mathrm{r},k}(t)\varphi_j\varphi_k\rangle - \left(\sum_{j=0}^{N}\langle u_{\mathrm{r},j}(t)\varphi_j\rangle\right)\left(\sum_{k=0}^{N}\langle u_{\mathrm{r},k}(t)\varphi_k\rangle\right)\rangle \\
&= \sum_{j=0}^{N}\sum_{k=0}^{N}\langle u_{\mathrm{r},j}u_{\mathrm{r},k}\rangle_t\langle\varphi_j\varphi_k\rangle_{xz} - \sum_{j=0}^{N}\sum_{k=0}^{N}\langle u_{\mathrm{r},j}\rangle_t\langle u_{\mathrm{r},k}\rangle_t\langle\varphi_j\rangle_{xz}\langle\varphi_k\rangle_{xz},
\end{aligned} \tag{4.25}$$

where φ_j and φ_k are the POD basis functions in the streamwise direction, and $\langle\cdot\rangle_t$ and $\langle\cdot\rangle_{xz}$ are the average operators in t and the x-z plane. Then, in the offline stage, for each y coordinate, we compute and store $\langle\varphi_j\varphi_k\rangle_{xz}$ and $\langle\varphi_j\rangle_{xz}$ for all $j,\ k=0,\dots,N$. Finally, in the online stage, we compute $\langle u_{\mathrm{r},j}u_{\mathrm{r},k}\rangle_t$ and $\langle u_{\mathrm{r},j}\rangle_t$ for all $j,\ k=0,\dots,N$. Thus, to evaluate $\langle u'u'\rangle_{\mathrm{r}}$ at a given point y^*, we use (4.25), which is independent of $\mathcal{N}$ and, thus, does not significantly increase the computational cost. The offline-online splitting for $\langle u'v'\rangle$ can be derived similarly.

We also assess the ROM performance with the ROM projection Reynolds stresses $\langle u'u'\rangle_{\mathrm{Proj}}$ and $\langle u'v'\rangle_{\mathrm{Proj}}$:

$$\langle u'u'\rangle_{\mathrm{Proj}} \coloneqq \Big\langle \langle u_{\mathrm{Proj}}^2\rangle - \langle u_{\mathrm{Proj}}\rangle^2\Big\rangle, \tag{4.26}$$

$$\langle u'v'\rangle_{\mathrm{Proj}} \coloneqq \Big\langle \langle u_{\mathrm{Proj}}v_{\mathrm{Proj}}\rangle - \langle u_{\mathrm{Proj}}\rangle\langle v_{\mathrm{Proj}}\rangle\Big\rangle, \tag{4.27}$$

where the ROM-projected solution is defined as:

$$\boldsymbol{u}_{\mathrm{Proj}} = \boldsymbol{\varphi}_0 + \sum_{j=0}^{N}\tilde{u}_{\mathrm{Proj},j}\boldsymbol{\varphi}_j(\mathbf{x}),\ \text{ and } \tilde{u}_{\mathrm{Proj},j} = (\boldsymbol{\varphi}_j, \boldsymbol{u}-\boldsymbol{\varphi}_0). \tag{4.28}$$

The ROM-projected Reynolds stress can be computed using (4.25) but with $\langle\tilde{u}_{\mathrm{Proj},j}\tilde{u}_{\mathrm{Proj},j}\rangle_t$

and $\langle \tilde{u}_{\text{Proj},j} \rangle_t$ quantities and is used to compute the error $\varepsilon_{u'v'}$ (4.20). The ROM projection represents the best theoretical approximation of the training data in the given ROM space and we use it as a benchmark to assess the three Reg-ROMs.

4.6.5 Reproduction Regime

In this section, we perform a numerical investigation of the three Reg-ROMs: L-ROM (Section 4.1), EFR-ROM (Section 4.2), and the new TR-ROM (Section 4.3) for the reproduction regime, the time interval in which the snapshots were collected, at $\text{Re}_\tau = 180$ and $\text{Re}_\tau = 395$. For comparison purposes, we include results for the G-ROM (Section 2.2) and the ROM projection, which represents the best theoretical approximation of the FOM solution in the given ROM space. The Reg-ROM accuracy is expected to be significantly higher than the G-ROM accuracy. To quantify the ROM accuracy, we use $\varepsilon_{u'u'}$ and $\varepsilon_{u'v'}$, which are the relative ℓ^2 error of $u'u'$ and $u'v'$ defined in (4.20).

In our numerical investigation, we also consider the following parameters: For all the ROMs, we utilize 10 values for the ROM dimension, $N \in \{10, 20, \ldots, 90, 100\}$. For each Reg-ROM, we use four HOAF orders: $m = 1$ (which corresponds to the classical DF (4.13)) and $m = 2, 3, 4$ (which correspond to the HOAF (4.14)). For each N and m value, the values of the filter radius, δ, are chosen as follows: For the EFR-ROM and the TR-ROM, 10, 25, and 10 δ values are uniformly sampled from the intervals $[0.001,\ 0.01]$, $[0.01, 0.1]$, and $[0.1, 1]$, respectively. This yields a total of 43 values for δ from the interval $[0.001,\ 1]$. In addition, we choose 4 uniformly sampled values for the relaxation parameter, χ, in the interval $[\Delta t = 0.005,\ 1]$. We chose this χ range because $\chi = \mathcal{O}(\Delta t)$ is commonly used in EFR-ROM simulations [30, 120]. For the L-ROM, we uniformly sample 15 additional δ values from the interval $[0.1,\ 0.2]$, which yields a total of 56 values for δ from the interval $[0.001,\ 1]$ for $\text{Re}_\tau = 180$. For $\text{Re}_\tau = 395$, 30 additional δ values are uniformly sampled from the interval $[0.1,\ 0.3]$, which yields a total of 69 values for δ.

We emphasize that, in our Reg-ROM numerical investigation, we use four parameters: the ROM dimension, N, the filter order, m, the filter radius, δ, and (for the EFR-ROM and the TR-ROM) the relaxation parameter, χ. Thus, to ensure a clear comparison of the three Reg-ROMs, we fix the δ and χ parameters to their optimal values (i.e., the values that yield the most accurate $u'v'$ for each Reg-ROM), and plot $\varepsilon_{u'v'}$ for all the parameter values for N and m. We show $\varepsilon_{u'v'}$ results here and $\varepsilon_{u'u'}$ results in Appendix A. In the end of this section we present a summary of the Reg-ROM comparison in the reproduction regime. For completeness, we included Reg-ROM results for all the δ and χ values in the sensitivity study in Section 4.6.7.

$\mathbf{Re}_\tau = 180$. In Figure 4.9, we plot the relative ℓ^2 error $\varepsilon_{u'v'}$ (4.20) for different ROM dimensions, N, and filter orders, m, for the G-ROM, the ROM projection, and the three Reg-ROMs at $\mathrm{Re}_\tau = 180$. Two sets of ROM-projection results are shown: The solid and the dotted lines represent the errors of $\langle u'v' \rangle_{\mathrm{Proj}}$ (4.27) for the snapshot data and the FOM data, respectively. It is expected that the error $\varepsilon_{u'v'}$ for the snapshot data is smaller than the error for the FOM data, because the POD basis set is constructed using only $K = 2000$ snapshots instead of using all the FOM solutions. For each Reg-ROM, the error is plotted for the optimal δ values and, for EFR-ROM and TR-ROM, for the optimal χ values.

Figure 4.9a displays the G-ROM results. This plot shows that, for all N values, the G-ROM results are very inaccurate. Even with $N = 100$, G-ROM fails to reconstruct $u'v'$ with an error of $\mathcal{O}(10^5)$.

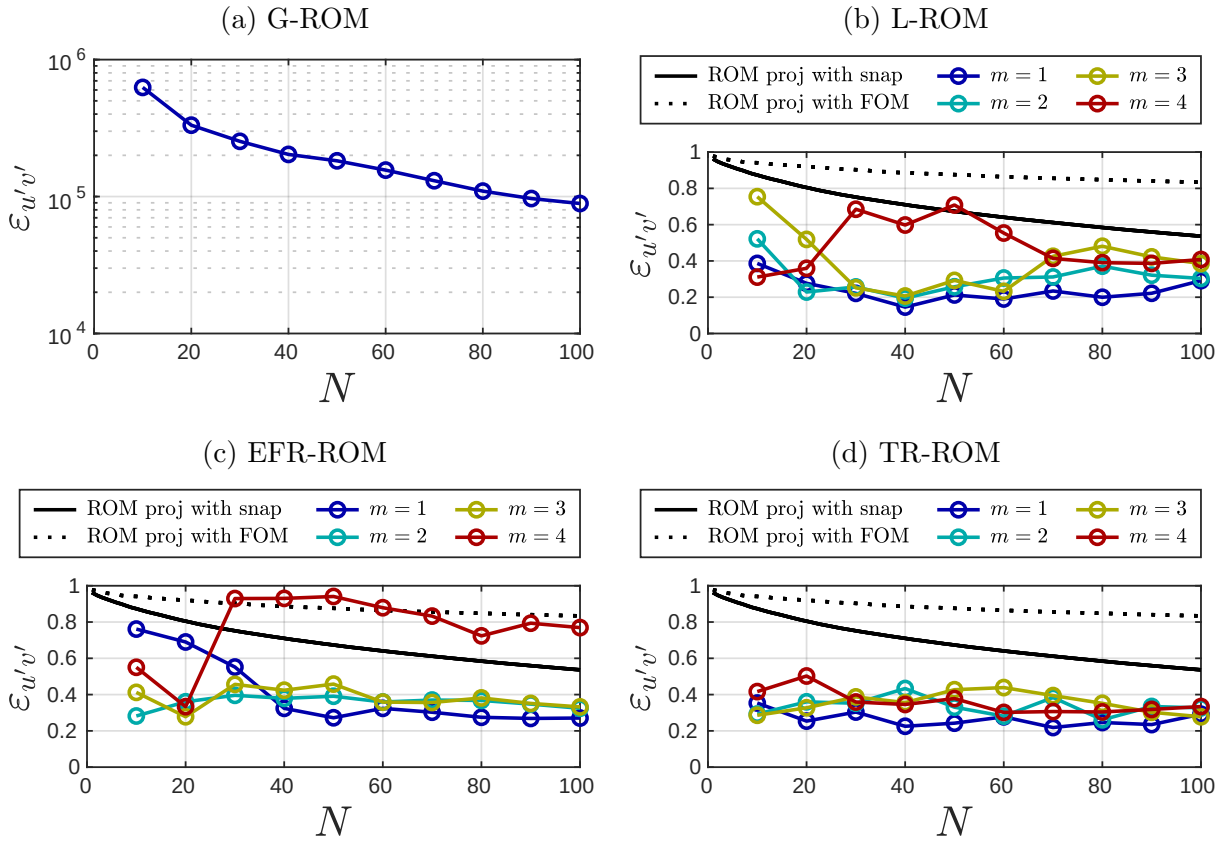

Figure 4.9: The relative error $\varepsilon_{u'v'}$ (4.20) of G-ROM, ROM projection, L-ROM, EFR-ROM and TR-ROM in the *reproduction regime* at $\mathrm{Re}_\tau = 180$ for different N and m values with optimal δ and χ values.

Figure 4.9b displays the L-ROM results for each N and m with the optimal δ, along with the results of the ROM projection for comparison purposes. For $N \geq 30$, $m = 1$

yields the most accurate results, achieving an error of 15% with $N = 40$. Conversely, for $N \leq 20$, a higher-order filter yields better results. Specifically, $m = 4$ achieves an error of 31% for $N = 10$ and $m = 2$ achieves an error of 23% for $N = 20$. With the exception of $(N, m) = (50, 4)$, L-ROM is more accurate than the ROM projection.

Figure 4.9c displays the EFR-ROM results for each N and m with the optimal χ and δ values, along with the results of the ROM projection for comparison purposes. For $N \geq 40$, $m = 1$ yields the most accurate results, achieving an error of 27% for $N = 90$. Conversely, for $N \leq 30$, a higher-order filter yields better results. Specifically, $m = 2$ achieves an error of 28% and 40% for $N = 10$ and $N = 30$, respectively. Additionally, $m = 3$ achieves an error of 45% for $N = 20$. EFR-ROM is more accurate than the ROM projection for all N with $m = 1,\ 2,\ 3$. With $m = 4$, it is only more accurate than the ROM projection for $N \leq 20$.

Figure 4.9d displays the TR-ROM results for each N and m with the optimal χ and δ values, along with the results of the ROM projection for comparison purposes. For $20 \leq N \leq 90$, $m = 1$ yields the most accurate results, achieving an error of 22% for $N = 70$. For $N = 10$ and $N = 100$, $m = 3$ yields the most accurate results, achieving an error of 29% and 28%, respectively. In addition, TR-ROM is more accurate than the ROM projection for all N and m values.

$\mathbf{Re}_\tau = 395$. In Figure 4.10, we plot the relative ℓ^2 error $\varepsilon_{u'v'}$ (4.20) for different N and m values for the G-ROM, the ROM projection, and the three Reg-ROMs at $\mathrm{Re}_\tau = 395$. Two sets of ROM-projection results for the snapshot data and the FOM data are shown. Note that the error $\varepsilon_{u'v'}$ for the snapshot data at $\mathrm{Re}_\tau = 395$ is larger (approximately 70%) compared to the corresponding results at $\mathrm{Re}_\tau = 180$ (approximately 52%). This difference is expected because the $\mathrm{Re}_\tau = 395$ solution exhibits more turbulence and, as a result, requires a greater number of modes to achieve a satisfactory approximation. For each Reg-ROM, the error is plotted for the optimal δ values and, for EFR-ROM and TR-ROM, for the optimal χ values.

Figure 4.10a displays the G-ROM results. Just as in the $\mathrm{Re}_\tau = 180$, for all N values, the G-ROM results are very inaccurate. Even with $N = 100$, $\varepsilon_{u'v'}$ is still about $\mathcal{O}(10^5)$.

Figure 4.10b displays the L-ROM results for each N and m with the optimal δ values, along with the results of the ROM projection for comparison purposes. For all N and m values, the error is found to be much higher compared to the results for $\mathrm{Re}_\tau = 180$. For $N \geq 20$, the most accurate results are achieved with $m = 1$, with an error of 37% for $N = 40$. For $N = 10$, $m = 3$ achieves an error of 43%. Compared to the ROM projection, the L-ROM is more accurate for all values of N and m.

Figure 4.10c displays the EFR-ROM results for each N and m with the optimal χ and δ values, along with the results of the ROM projection for comparison purposes. These results

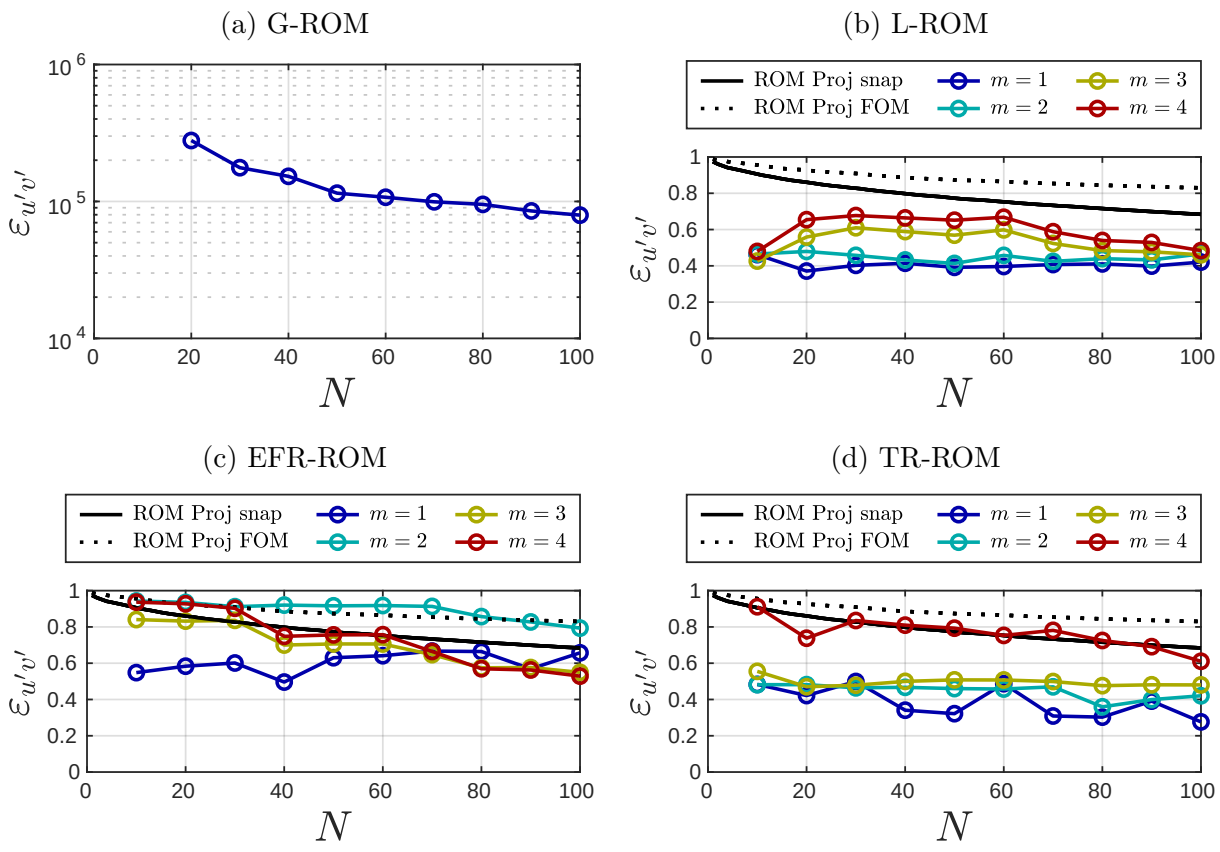

Figure 4.10: The relative error $\varepsilon_{u'v'}$ (4.20) of G-ROM, ROM projection, L-ROM, EFR-ROM and TR-ROM in the *reproduction regime* at $\mathrm{Re}_\tau = 395$ for different N and m values with optimal δ and χ values.

are qualitatively different from the EFR-ROM results for $\mathrm{Re}_\tau = 180$. For $N \leq 60$, $m = 1$ yields the most accurate results and achieves an error of 50% for $N = 40$. For $N \geq 70$, higher-order filter yields better results. Specifically, $m = 4$ achieves an error of 53% for $N = 100$. Moreover, the EFR-ROM is found to be more accurate than the ROM projection for all N with $m = 1$ and for $N \geq 60$ with $m = 3,\ 4$. With $m = 2$, the EFR-ROM only has a similar level of accuracy as the ROM projection.

Figure 4.10d displays the TR-ROM results for each N and m with the optimal χ and δ values, along with the results of the ROM projection for comparison purposes. For almost all N values, $m = 1$ yields the most accurate results, achieving an error of around 28% for $N = 100$. These results also show that $m = 2$ and $m = 3$ yield similar results, while $m = 4$ is found to be the least accurate. Moreover, the TR-ROM is found to be more accurate than the ROM projection for all N and m values.

Summary. Overall, our numerical investigation in the reproduction regime yields the following general conclusions:

All three Reg-ROMs are significantly more accurate than the standard G-ROM. In fact, with respect to several second-order turbulence statistics the three Reg-ROMs' errors are much lower than that of projection through carefully tuned spatial filtering.

Finally, our numerical investigation demonstrates that, for $\mathrm{Re}_\tau = 180$, all three Reg-ROMs with $m = 1$ (i.e., low-order filtering) consistently produce the most accurate results for large N values, while a higher-order filter is more effective for low N values. For $\mathrm{Re}_\tau = 395$, L-ROM and TR-ROM with $m = 1$ yield the most accurate results for all N values, while EFR-ROM yields the most accurate results for low N values with $m = 1$, and for high N values with $m = 3,\ 4$.

To facilitate the comparison of the three Reg-ROMs, in Table 4.1, we rank them based on the error $\varepsilon_{u'v'}$ and $\varepsilon_{u'u'}$ achieved for the N and m values investigated. Specifically, for both Reynolds numbers, we list the Reg-ROMs' rank, the lowest $\varepsilon_{u'v'}$, the corresponding $\varepsilon_{u'u'}$, the ROM dimension N and the filter order m for which the lowest $\varepsilon_{u'v'}$ is achieved. The results in Table 4.1 yield the following conclusions:

For $\mathrm{Re}_\tau = 180$, TR-ROM is the most accurate model with $\varepsilon_{u'v'} \approx 22\%$ and $\varepsilon_{u'u'} \approx 16\%$, followed by EFR-ROM and L-ROM. For $\mathrm{Re}_\tau = 395$, TR-ROM is still the most accurate model with $\varepsilon_{u'v'} \approx 28\%$ and $\varepsilon_{u'u'} \approx 26\%$, followed by L-ROM and EFR-ROM. In addition, we find $\varepsilon_{u'u'}$ is smaller compared to $\varepsilon_{u'v'}$ except for L-ROM for $\mathrm{Re}_\tau = 180$ and $\varepsilon_{u'u'}$ has similar level of accuracy as $\varepsilon_{u'v'}$ for $\mathrm{Re}_\tau = 395$. Moreover, the results in Table 4.1 also show that $m = 1$ (i.e., low-order filtering) yields the most accurate results. Finally, these results show that TR-ROM requires large N values to achieve its best accuracy, whereas L-ROM yields best accuracy with small N. For EFR-ROM, large N is required for $\mathrm{Re}_\tau = 180$ and small N is required for $\mathrm{Re}_\tau = 395$.

In Fig. 4.11, we compare the total, viscous, and Reynolds shear stresses of the optimal Reg-ROMs (listed in Table 4.1) along with the results of the FOM and the ROM projection in the reproduction regime for $\mathrm{Re}_\tau = 180$ and $\mathrm{Re}_\tau = 395$. The total shear stress $\tau(y)$ is the sum of the viscous shear stress $\rho\,\nu\,d\langle u\rangle/dy$ and the Reynolds shear stress $-\rho\,\langle u'v'\rangle$, and its distribution is linear [121]. In each model, the three shear stresses are normalized with the model's wall shear stress $\tau_w \equiv \rho\,\nu\,\left(d\langle u\rangle/dy\right)_{y=-1}$.

In terms of the viscous shear stress, the results of the three Reg-ROMs are in good agreement with those of the FOM and the ROM projection for both Re_τ. In terms of the Reynolds shear stress, for $\mathrm{Re}_\tau = 180$, we observe that the result of the L-ROM is smaller compared to the FOM. On the other hand, the results of the EFR-ROM and the TR-ROM are similar, both have higher values in the boundary layer and lower values outside the

Table 4.1: Reg-ROM accuracy ranking in the reproduction regime for $\mathrm{Re}_\tau = 180$ (top rows) and 395 (bottom rows). The following parameters are listed: Reg-ROMs' rank, the lowest $\varepsilon_{u'v'}$, the corresponding $\varepsilon_{u'u'}$, the ROM dimension N and the filter order m for which the lowest $\varepsilon_{u'v'}$ is achieved.

$\mathrm{Re}_\tau = 180$	L-ROM	EFR-ROM	TR-ROM
Rank	3	2	1
$\varepsilon_{u'v'}$	$\approx 19\%$	$\approx 27\%$	$\approx 22\%$
$\varepsilon_{u'u'}$	$\approx 37.5\%$	$\approx 13\%$	$\approx 16\%$
N	40	90	70
m	1	1	1
$\mathrm{Re}_\tau = 395$	L-ROM	EFR-ROM	TR-ROM
Rank	2	3	1
$\varepsilon_{u'v'}$	$\approx 37\%$	$\approx 50\%$	$\approx 28\%$
$\varepsilon_{u'u'}$	$\approx 40\%$	$\approx 40\%$	$\approx 26\%$
N	20	40	100
m	1	1	1

boundary layer compared to the FOM. Notice that both the EFR-ROM and the TR-ROM are able to capture the slope of the Reynolds shear stress. For $\mathrm{Re}_\tau = 395$, we find the results of the TR-ROM are the best, followed by L-ROM and EFR-ROM. Moreover, although the results of the Reg-ROMs are not perfect, we find the results are much better than the ROM projection. This also indicates that $N = 100$ POD bases are not able to reconstruct the Reynolds stress. Finally, as a results of the discrepancy in the Reynolds shear stress, the total shear stress is not linear in all three Reg-ROMs for both Re_τ.

4.6.6 Predictive Regime

In this section, we perform a numerical investigation of the three Reg-ROMs: L-ROM (Section 4.1), EFR-ROM (Section 4.2), and the new TR-ROM (Section 4.3) for the *predictive regime*, a time interval that is 500 CTUs larger than the snapshot collected time interval, at $\mathrm{Re}_\tau = 180$ and $\mathrm{Re}_\tau = 395$. Hence, 1000 CTU and 1500 CTU time windows are considered for $\mathrm{Re}_\tau = 180$ and 395, respectively. For comparison purposes, we include results for the G-ROM (Section 2.2) and the ROM projection. To quantify the ROM accuracy, we use $\varepsilon_{u'u'}$ and $\varepsilon_{u'v'}$, which are the relative ℓ^2 error of $u'u'$ and $u'v'$ defined in (4.20). The results of $u'u'$ are shown in Section A.

In our numerical investigation, we use the same parameter values for N and m as the values used in Section 4.6.5. For each N and m values, we plot $\varepsilon_{u'v'}$ with $(\delta,\ \chi)_{\mathrm{reprod}}$, that is the δ and χ parameter values that were found to be optimal in the reproduction regime in

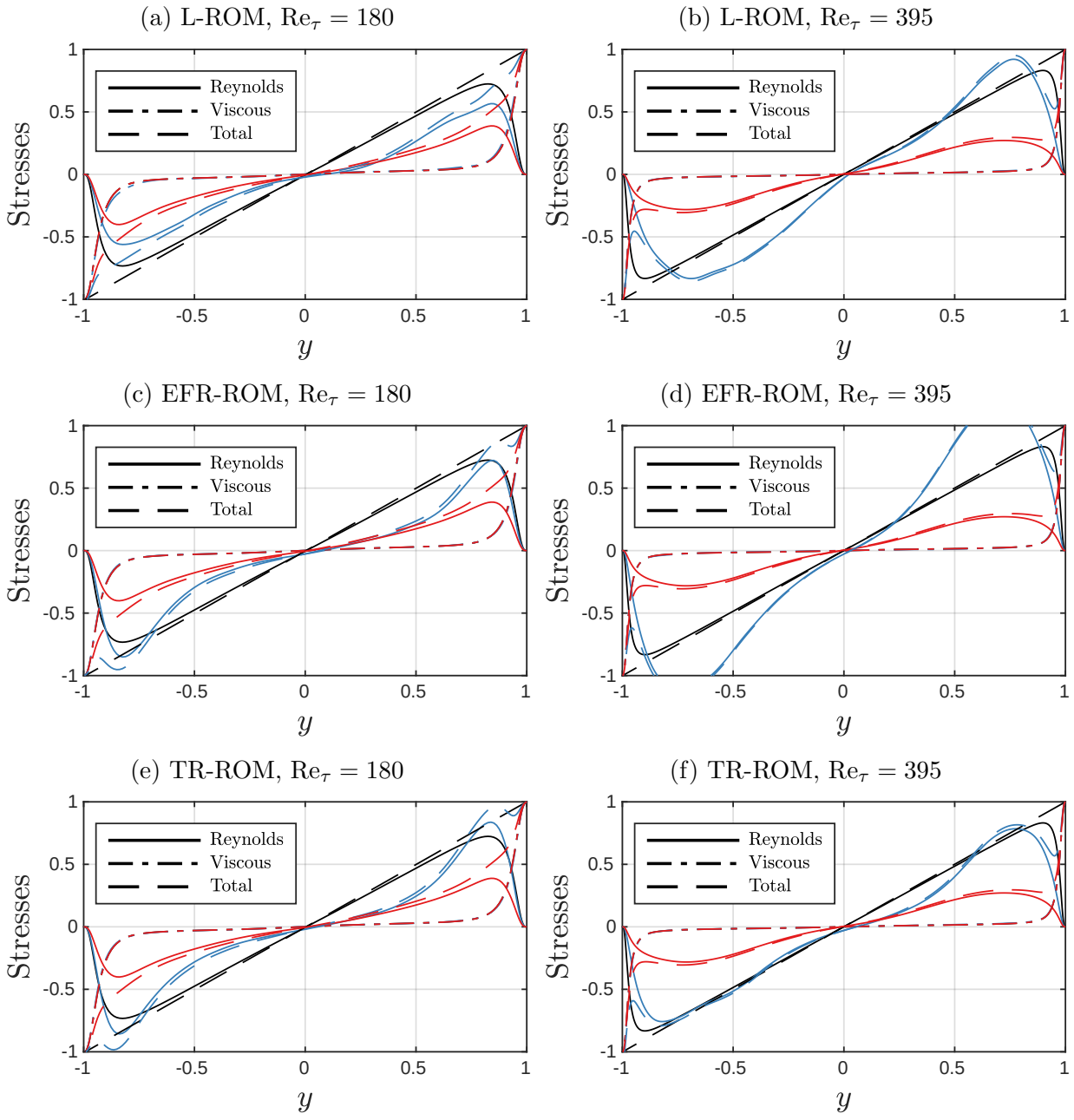

Figure 4.11: Comparison of the total, viscous, and Reynolds shear stresses of the FOM (black), the ROM projection (red) and the optimal Reg-ROMs, listed in Table 4.1 (blue) in the *reproduction regime* for $\mathrm{Re}_\tau = 180$ (left) and $\mathrm{Re}_\tau = 395$ (right). The total shear stress is the sum of the viscous and the Reynolds shear stress.

Section 4.6.5.

We emphasize that our strategy is different from that used in Section 4.6.5: Instead of optimizing the δ and χ values on the entire predictive time interval, we use the values that were optimized over the shorter time interval of the reconstructive regime. Thus, in this

section, we are investigating the predictive power of both the Reg-ROMs *and* their associated parameters.

Finally, in the end of the section, we present a summary of the Reg-ROM comparison in the predictive regime.

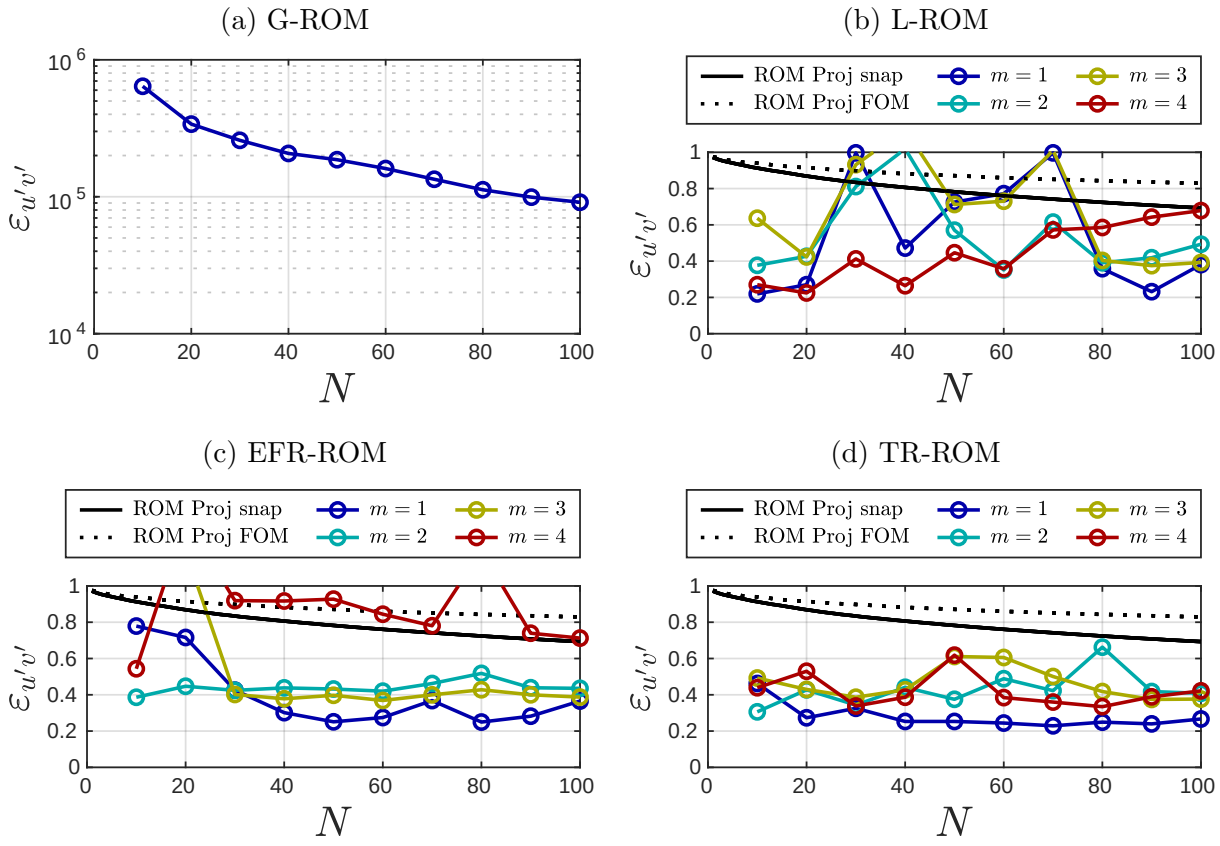

Figure 4.12: The relative error $\varepsilon_{u'v'}$ (4.20) of G-ROM, ROM projection, L-ROM, EFR-ROM and TR-ROM in the *predictive regime* at $\mathrm{Re}_\tau = 180$ for different N and m values with optimal δ and χ values *optimized in the reproduction regime*.

$\mathrm{Re}_\tau = 180$. In Figure 4.12, we plot the relative ℓ^2 error $\varepsilon_{u'v'}$ (4.20) for different N and m values for the G-ROM, the ROM projection, and the three Reg-ROMs at $\mathrm{Re}_\tau = 180$. We emphasize that, to test the predictive capabilities of the Reg-ROM parameters, we plot the error for $(\delta,\ \chi)_{\text{reprod}}$ that were optimized in the *reproduction regime* (Section 4.6.5).

Figure 4.12a displays the G-ROM results. As in the reproduction regime, for all N values, the G-ROM results are very inaccurate.

Figure 4.12b displays the L-ROM results for each N and m with δ_{reprod} along with the ROM projection results for comparison purposes. For $N = 10$ and $N \geq 80$, $m = 1$ yields

the most accurate results, achieving an error of 22% for $N = 10$. For $20 \leq N \leq 70$, $m = 4$ yields the most accurate results, achieving an error of 22% for $N = 20$. For the majority of N and m values, except for specific pairs such as (m, N) with values of $(1, 30)$, $(1, 70)$, $(2, 40)$, $(3, 30)$, $(3, 40)$, and $(3, 70)$, L-ROM is more accurate than the ROM projection.

However, $\varepsilon_{u'v'}$ exhibits a higher sensitivity to changes in N across all m values compared to the results observed in the reproduction regime (as discussed in Section 4.6.5).

Figure 4.12c displays the EFR-ROM results for each N and m with $(\delta,\ \chi)_{\text{reprod}}$ along with the ROM projection results for comparison purposes. For $N \leq 30$, higher-order filter yields better results. Specifically, for $N = 10$ and $N = 20$, EFR-ROM achieves an error of 39% and 45%, respectively, with $m = 2$. Additionally, for $N = 30$, EFR-ROM achieves an error of 40% with $m = 3$. For $N \geq 40$, $m = 1$ yields the most accurate results, achieving an error of 25% for $N = 80$. Compared to the ROM projection, EFR-ROM is more accurate for $m \leq 3$, except for $N = 10$ and $N = 20$ with $m = 3$. For $m = 4$, EFR-ROM is not accurate and has a similar level of accuracy as the ROM projection.

Figure 4.12d displays the TR-ROM results for each N and m with $(\delta,\ \chi)_{\text{reprod}}$ along with the ROM projection results for comparison purposes. For $N = 10$, $m = 2$ yields the lowest error of 30%. For $N \geq 20$, $m = 1$ yields the best results, achieving an error of 23% for $N = 70$. TR-ROM is more accurate than the ROM projection for all N and m values.

$\mathbf{Re}_\tau = 395$. In Figure 4.13, we plot the relative ℓ^2 error $\varepsilon_{u'v'}$ for different N and m values for the G-ROM, the ROM projection, and the three Reg-ROMs at $\text{Re}_\tau = 395$. We emphasize that, to test the predictive capabilities of the Reg-ROM parameters, we plot the error for $(\delta,\ \chi)_{\text{reprod}}$ that were optimized in the *reproduction regime* (Section 4.6.5).

Figure 4.13a displays the G-ROM results. Just as in Section 4.6.6, for all N values, the G-ROM results are very inaccurate with an error of $\mathcal{O}(10^5)$ for $N = 100$.

Figure 4.13b displays the L-ROM results for each N and m with δ_{reprod}, along with the ROM projection results for comparison purposes. For almost all N values, except for $N = 30$ and 40, $m = 1$ yields the most accurate results, achieving an error of 39% with $N = 20$. For $m = 3$ and $m = 4$, the accuracy of L-ROM is improved as N increases but is still larger than the $m = 1$ case. Compared to the ROM projection, L-ROM is more accurate except for the (m, N) pairs $(2, 10), (3, 30)$, $(4, 20)$, and $(4, 30)$.

Figure 4.13c displays the EFR-ROM results for each N and m with $(\delta,\ \chi)_{\text{reprod}}$ along with the ROM projection results for comparison purposes. For $N \leq 60$, $m = 1$ yields the most accurate results, achieving an error of 45% for $N = 40$. For $N \geq 70$ except for $N = 90$, a higher-order filter yields better results. Specifically, $m = 4$ achieves an error of 53% for $N = 80$. For $N = 90$, $m = 1$ achieves an error of 46%. Compared to the ROM projection,

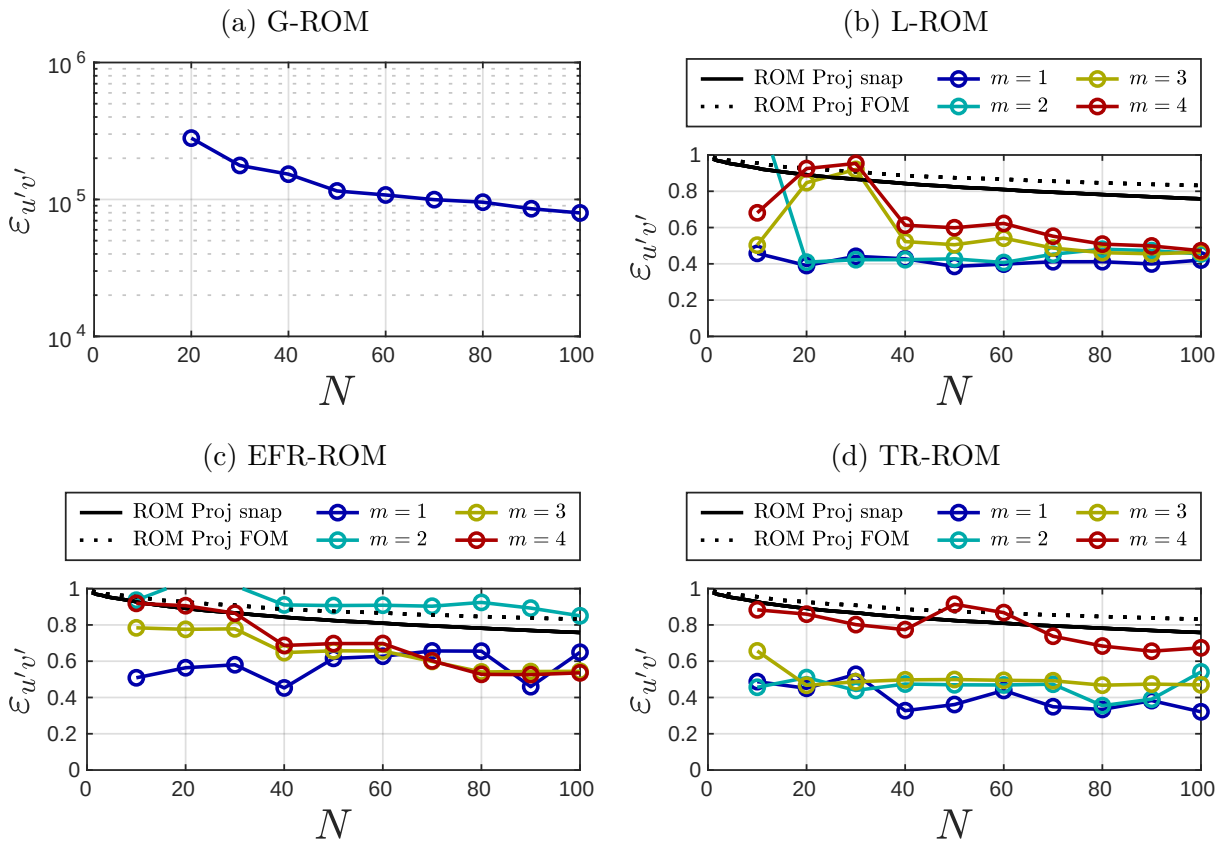

Figure 4.13: The relative error $\varepsilon_{u'v'}$ (4.20) of G-ROM, ROM projection, L-ROM, EFR-ROM and TR-ROM in the *predictive regime* at $\mathrm{Re}_\tau = 395$ for different N and m values with optimal δ and χ values *optimized in the reproduction regime*.

EFR-ROM is more accurate for all N values and $m = 1,\ 3,\ 4$. For $m = 2$, EFR-ROM has a similar level of accuracy as the ROM projection.

Figure 4.13d displays the TR-ROM results for each N and m with $(\delta,\ \chi)_{\text{reprod}}$, along with the ROM projection results for comparison purposes. For all N values except $N = 10$ and $N = 30$, $m = 1$ yields the most accurate results, achieving an error of around 32% for $N = 100$. These results also show that $m = 2$ and $m = 3$ yield similar accuracy and $m = 4$ is the least accurate. TR-ROM is more accurate than the ROM projection for all N and m values, except for (m, N) pairs, $(4, 50)$ and $(4, 60)$.

Summary. Overall, our numerical investigation in the predictive regime yields the following general conclusions:

All three Reg-ROMs are significantly more accurate than the standard G-ROM. In fact, with respect to several second-order turbulence statistics the three Reg-ROMs' errors are much lower than that of projection through carefully tuned spatial filtering.

Finally, our numerical investigation demonstrates that, for $\mathrm{Re}_\tau = 180$, the EFR-ROM and the TR-ROM with $m = 1$ (i.e., low-order filtering) consistently produce the most accurate results for large N values, while a higher-order filter is more effective for low N values. In addition, L-ROM is sensitive to changes in N for all m values. For $\mathrm{Re}_\tau = 395$, the L-ROM and the TR-ROM with $m = 1$ yield the most accurate results for all N values, while the EFR-ROM yields the most accurate results for low N values for $m = 1$, and high N values for $m = 3, 4$.

To facilitate the comparison of the three Reg-ROMs, in Table 4.2, we rank them based on the lowest error achieved for the N and m values investigated. Specifically, for both Reynolds numbers, we list the Reg-ROMs' rank, the lowest $\varepsilon_{u'v'}$, the corresponding $\varepsilon_{u'u'}$, the ROM dimension N and the filter order m for which the lowest $\varepsilon_{u'v'}$ is achieved. The results in Table 4.2 yield the following conclusions:

Table 4.2: Reg-ROM accuracy ranking in the predictive regime for $\mathrm{Re}_\tau = 180$ (top rows) and 395 (bottom rows). The following parameters are listed: Reg-ROMs' rank, the lowest $\varepsilon_{u'v'}$ with δ_{reprod}, the corresponding $\varepsilon_{u'u'}$, the ROM dimension N and the filter order m for which the lowest $\varepsilon_{u'v'}$ with δ_{reprod} is achieved.

$\mathrm{Re}_\tau = 180$	L-ROM	EFR-ROM	TR-ROM
Rank	2	3	1
$\varepsilon_{u'v'}$	$\approx 22\%$	$\approx 25\%$	$\approx 23\%$
$\varepsilon_{u'u'}$	$\approx 23\%$	$\approx 26\%$	$\approx 9\%$
N	10	80	70
Filter order m	1	1	1
$\mathrm{Re}_\tau = 395$	L-ROM	EFR-ROM	TR-ROM
Rank	2	3	1
$\varepsilon_{u'v'}$	$\approx 39\%$	$\approx 45\%$	$\approx 32\%$
$\varepsilon_{u'u'}$	$\approx 39\%$	$\approx 36\%$	$\approx 30\%$
N	50	40	100
Filter order m	1	1	1

For $\mathrm{Re}_\tau = 180$, TR-ROM is the most accurate model with $\varepsilon_{u'v'} \approx 23\%$ and $\varepsilon_{u'u'} \approx 9\%$, followed by L-ROM and EFR-ROM. For $\mathrm{Re}_\tau = 395$, TR-ROM is still the most accurate model with $\varepsilon_{u'v'} \approx 32\%$ and $\varepsilon_{u'u'} \approx 30\%$, followed by EFR-ROM and L-ROM. In addition, the results in Table 4.2 also show that $m = 1$ (i.e., low-order filtering) yields the most accurate results. Moreover, these results show that TR-ROM requires large N values to achieve its best accuracy, whereas L-ROM yields best accuracy with small N. For EFR-ROM, large N is required for $\mathrm{Re}_\tau = 180$ and small N is required for $\mathrm{Re}_\tau = 395$.

Similarly to the reproduction regime (Fig. 4.11), in Fig. 4.14, we compare the total, viscous, and the Reynolds shear stresses of the optimal Reg-ROMs (listed in Table 4.2) along with

the results of the FOM and the ROM projection in the predictive regime for $\mathrm{Re}_\tau = 180$ and $\mathrm{Re}_\tau = 395$.

In terms of the viscous shear stress, the results of the three Reg-ROMs are in good agreement with those of the FOM and the ROM projection for both Re_τ. In terms of the Reynolds shear stress, we find that TR-ROM yields the most accurate results for both Re_τ and the L-ROM is better than the EFR-ROM for $\mathrm{Re}_\tau = 180$. For $\mathrm{Re}_\tau = 395$, L-ROM and EFR-ROM perform similarly. In addition, from the results of the ROM projection, we find $N = 100$ POD bases is insufficient to reconstruct the Reynolds shear stress accurately. Finally, as a results of the discrepancy in the Reynolds shear stress, the total shear stress is not linear in all three Reg-ROMs for both Re_τ.

4.6.7 Sensitivity Study

In this section, we perform sensitivity studies for the three Reg-ROMs: We first present a sensitivity study of the optimal parameter $(\delta,\ \chi)_{\mathrm{reprod}}$ for each N and m in the predictive regime. In addition, we present a sensitivity study of the relative ℓ^2 error $\varepsilon_{u'v'}$ of EFR-ROM and TR-ROM with respect to the relaxation parameter, χ. Moreover, we present a sensitivity study of the relative ℓ^2 error $\varepsilon_{u'v'}$ of the three Reg-ROMs with respect to the filter radius, δ. Finally, we present a sensitivity study of the optimal filter radius, δ_{reprod}, of the three Reg-ROMs with respect to the filter order, m.

Reg-ROM parameter sensitivity in the predictive regime. In Section 4.6.6, for given N and m, we investigated the accuracy of the three Reg-ROMs using $(\delta,\ \chi)_{\mathrm{reprod}}$ in the *predictive regime*, where $(\delta,\ \chi)_{\mathrm{reprod}}$ are the δ and χ values that are optimal in the reproduction regime. In this section, we extend that study and investigate the robustness of the optimal parameter $(\delta,\ \chi)_{\mathrm{reprod}}$ for each N value with four m values by comparing $(\delta,\ \chi)_{\mathrm{reprod}}$ to $(\delta,\ \chi)_{\mathrm{pred}}$, that is, the δ and χ values that are optimal in the predictive regime. In order to find out $(\delta,\ \chi)_{\mathrm{pred}}$, we consider the same parameter sets for δ and χ as those used in the reproduction regime (Section 4.6.5). An additional 500 CTUs FOM simulations are performed for both Re_τ in order to compute $\varepsilon_{u'u'}$ and $\varepsilon_{u'v'}$.

In Fig. 4.15, we plot δ_{reprod} and δ_{pred} for different N and m values for the three Reg-ROMs at both Re_τ. δ_{reprod} is displayed as a smaller filled marker while δ_{pred} is displayed as a larger empty marker. In addition, We use different colors to distinguish filter order m and different markers to distinguish relaxation parameter χ. Hence, for each N value, there will be eight markers total. For a given N and m, if $(\delta,\ \chi)_{\mathrm{reprod}}$ is also optimal for the predictive regime, two markers with different size will be on top of each other.

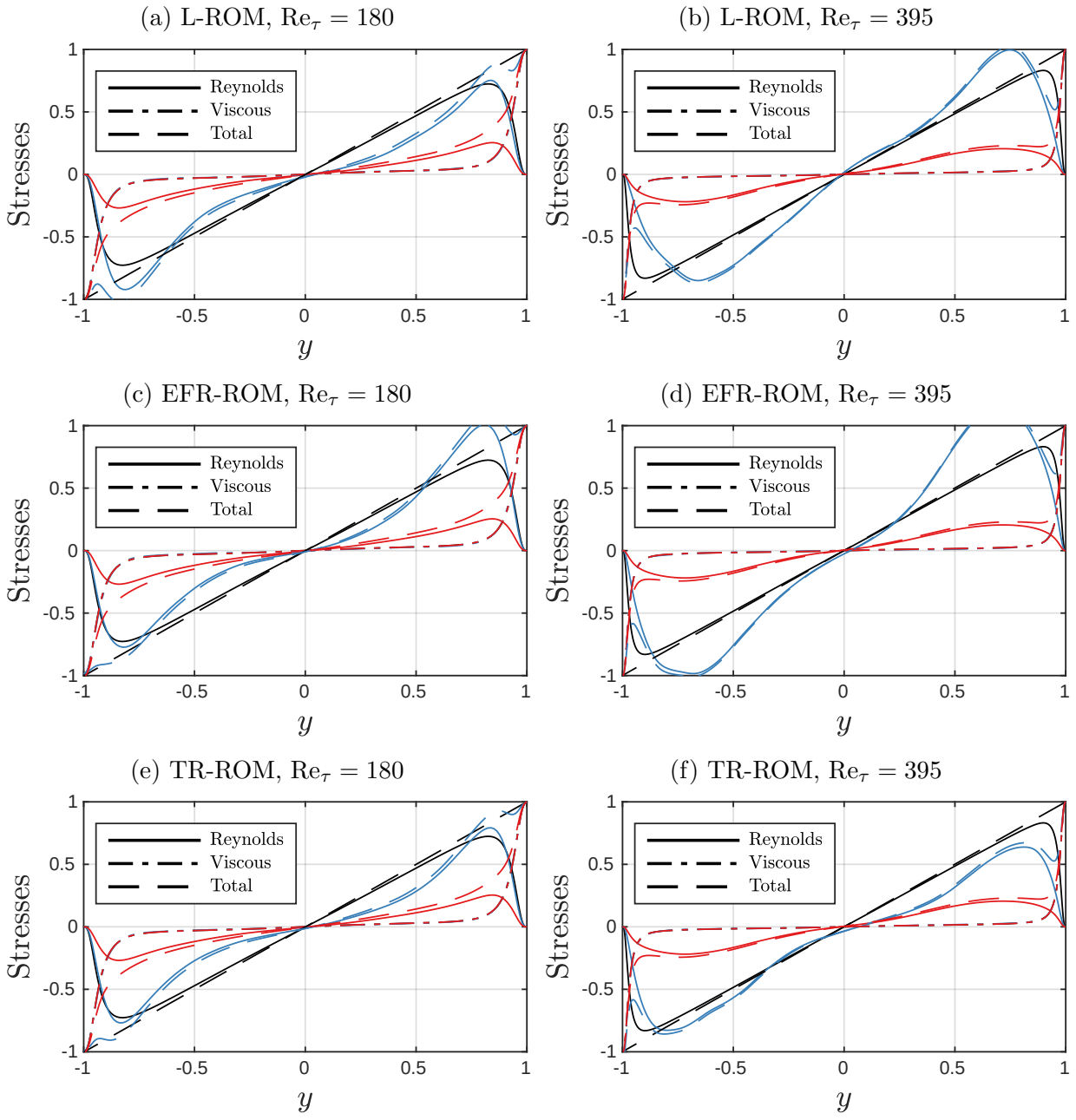

Figure 4.14: Comparison of the total, viscous, and Reynolds shear stresses of the FOM (black), the ROM projection (red) and the optimal Reg-ROMs, listed in Table 4.2 (blue) in the *predictive regime* for $\mathrm{Re}_\tau = 180$ (left) and $\mathrm{Re}_\tau = 395$ (right). The total shear stress is the sum of the viscous and the Reynolds shear stress.

Figs. 4.15a and 4.15b display L-ROM's $(\delta,\ \chi)_{\text{reprod}}$ and $(\delta,\ \chi)_{\text{pred}}$ for each N and m for $\mathrm{Re}_\tau = 180$ and $\mathrm{Re}_\tau = 395$, respectively. Note that χ is simply 0 in L-ROM (4.1). For $\mathrm{Re}_\tau = 180$, we find, for $m = 1$, δ_{reprod} is close to δ_{pred} but not identical for most N. As m increases, δ_{reprod} becomes optimal, i.e., $\delta_{\text{reprod}} = \delta_{\text{pred}}$ for almost all N except $n = 100$. For

$\mathrm{Re}_\tau = 395$, we find δ_{reprod} is in general more robust than $\mathrm{Re}_\tau = 180$: For $m = 1$, δ_{reprod} is already identical to δ_{pred} for most N values, except $N = 20,\ 30,\ 40$. As m increases, the robustness of δ_{reprod} is slightly improved. In addition, for both Re_τ, we find smaller m and larger N both lead to a larger δ_{reprod} and δ_{pred}. Moreover, δ_{reprod} and δ_{pred} are less sensitive to Re_τ with higher-order filter order (larger m).

Figs. 4.15c and 4.15d display EFR-ROM's $(\delta,\ \chi)_{\text{reprod}}$ and $(\delta,\ \chi)_{\text{pred}}$ for each N and m for $\mathrm{Re}_\tau = 180$ and $\mathrm{Re}_\tau = 395$, respectively. For $\mathrm{Re}_\tau = 180$, we find $(\delta,\ \chi)_{\text{reprod}}$ is optimal for almost all (m, N) pairs except for $(1, 20)$, $(2, 10)$, $(2, 40)$, $(3, 10)$, $(3, 20)$, $(4, 20)$, and $(4, 80)$. For $\mathrm{Re}_\tau = 395$, we again find δ_{reprod} is in general more robust than $\mathrm{Re}_\tau = 180$: For $m = 1,\ 3,\ 4$, δ_{reprod} is identical to δ_{pred} for all N values. For $m = 2$, δ_{reprod} is larger and χ_{reprod} is smaller compared to δ_{pred} and χ_{pred}.

In contrast to the results of the L-ROM, in the EFR-ROM case, for the same χ_{reprod}, increasing m leads to larger δ_{reprod} and δ_{pred} for both Re_τ. It is important to note that a larger χ_{reprod} leads to a smaller δ for all m. For instance, at $\mathrm{Re}_\tau = 180$, we observe that the δ_{reprod} and δ_{pred} values for $m = 2$ are smaller compared to the results for other m values. This discrepancy can be attributed to the relatively large value of $\chi_{\text{reprod}} = 0.3367$, which is significantly larger than 0.005. In addition, we find δ of EFR-ROM is less sensitive to N compared to that of L-ROM. Moreover, for the same χ_{reprod}, we find $(\delta,\ \chi)_{\text{reprod}}$ and $(\delta,\ \chi)_{\text{pred}}$ are not sensitive to Re_τ for $m = 1,\ 2,\ 4$. The discrepancy in $m = 3$ is due to a different χ_{reprod}. Finally, we find $\chi = 0.005$ works best for most (N, m) pairs except for $m = 2$ and $m = 3$ with $\mathrm{Re}_\tau = 395$.

Figs. 4.15e and 4.15f display TR-ROM's $(\delta,\ \chi)_{\text{reprod}}$ and $(\delta,\ \chi)_{\text{pred}}$ for each N and m for $\mathrm{Re}_\tau = 180$ and $\mathrm{Re}_\tau = 395$, respectively. For $\mathrm{Re}_\tau = 180$, we find, for $m = 1$ and $m = 4$, δ_{reprod} is robust for all N values except for $N = 40$ with $m = 1$ and $N = 50$ with $m = 4$. For $m = 2$ and $m = 3$, we find at least three $(\delta,\ \chi)_{\text{reprod}}$ is not optimal. For $\mathrm{Re}_\tau = 395$, we again find δ_{reprod} is in general more robust than $\mathrm{Re}_\tau = 180$: The non-optimal δ_{reprod} for all m are very close to their corresponding δ_{pred}. Similar to the results of EFR-ROM, for both Re_τ, we find larger m leads to a larger δ_{reprod}. Compared to the results of L-ROM and EFR-ROM, we find $(\delta,\ \chi)_{\text{reprod}}$ and $(\delta,\ \chi)_{\text{pred}}$ are in general more sensitive to N and Re_τ.

In summary, across all three Reg-ROMs, we find δ_{reprod} is optimal for most N and m values for both Re_τ, demonstrating the predictive capabilities of the three Reg-ROMs and their associated parameters.

Reg-ROM sensitivity to the relaxation parameter χ. In this section, we study the EFR-ROM and TR-ROM sensitivity to the relaxation parameter, χ. To this end, we consider $\varepsilon_{u'v'}$ as the metric. For each N and m, we investigate how $\varepsilon_{u'v'}$ is affected by χ, and what χ

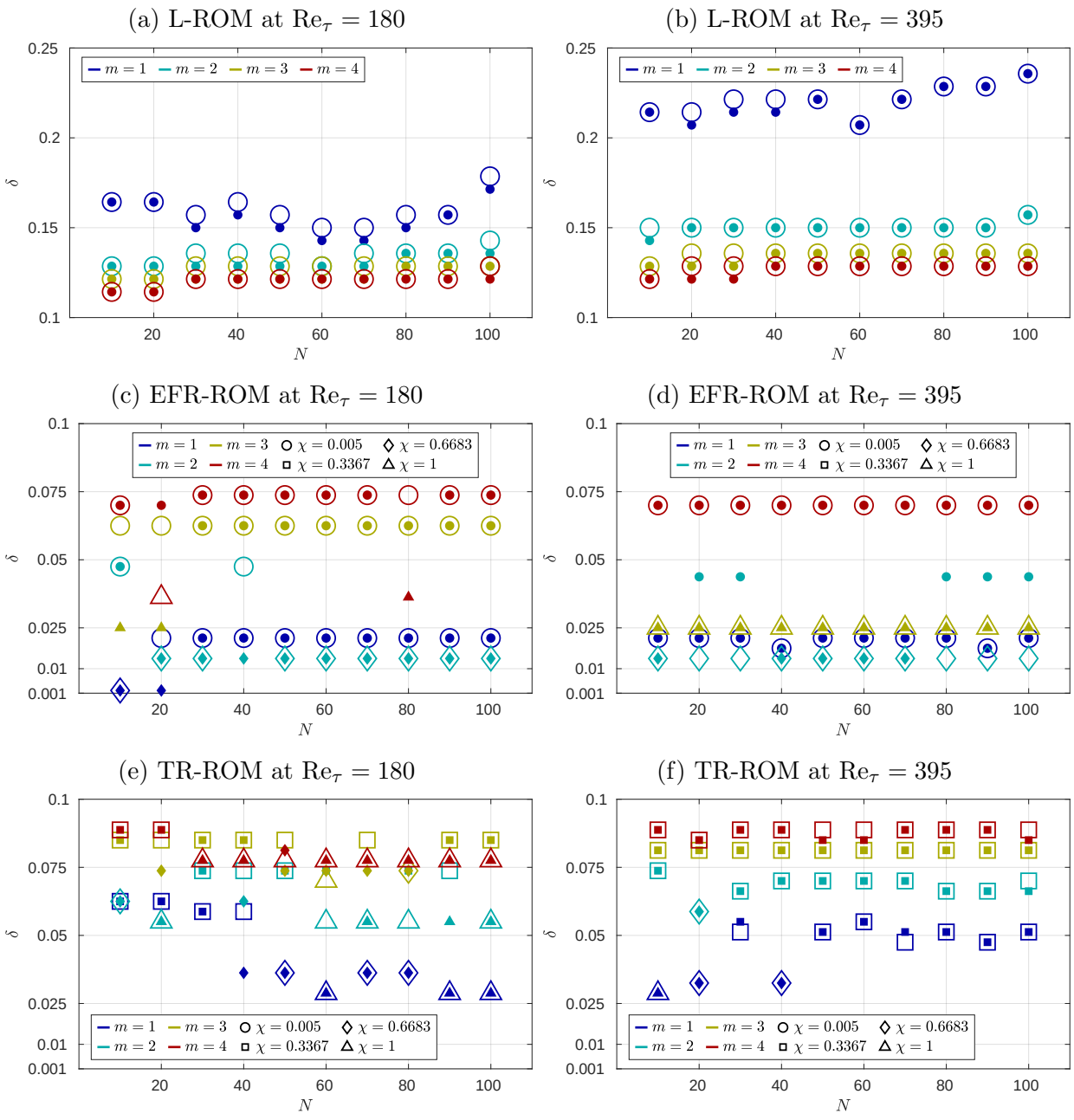

Figure 4.15: $(\delta,\ \chi)_{\text{reprod}}$ (smaller filled marker) and $(\delta,\ \chi)_{\text{pred}}$ (larger empty marker) distributions of the three Reg-ROMs for $m = 1$ and $N = 10, \ldots, 100$ at $\mathrm{Re}_\tau = 180$ (left) and $\mathrm{Re}_\tau = 395$ (right). $(\delta,\ \chi)_{\text{reprod}}$ and $(\delta,\ \chi)_{\text{pred}}$ are the optimal filter radius and relaxation values found in the reproduction and predicitive regime, respectively.

values yield the lowest $\varepsilon_{u'v'}$ values.

We consider four χ values, which are uniformly sampled in the interval $[\Delta t = 0.005,\ 1]$. For each N and χ values, we show $\varepsilon_{u'v'}$ with δ_{reprod} and $m = 1$. We fix the filter order m to be 1 because this is the value that yields the best Reg-ROMs in the reproduction and

predictive regimes (Sections 4.6.5 and 4.6.6).

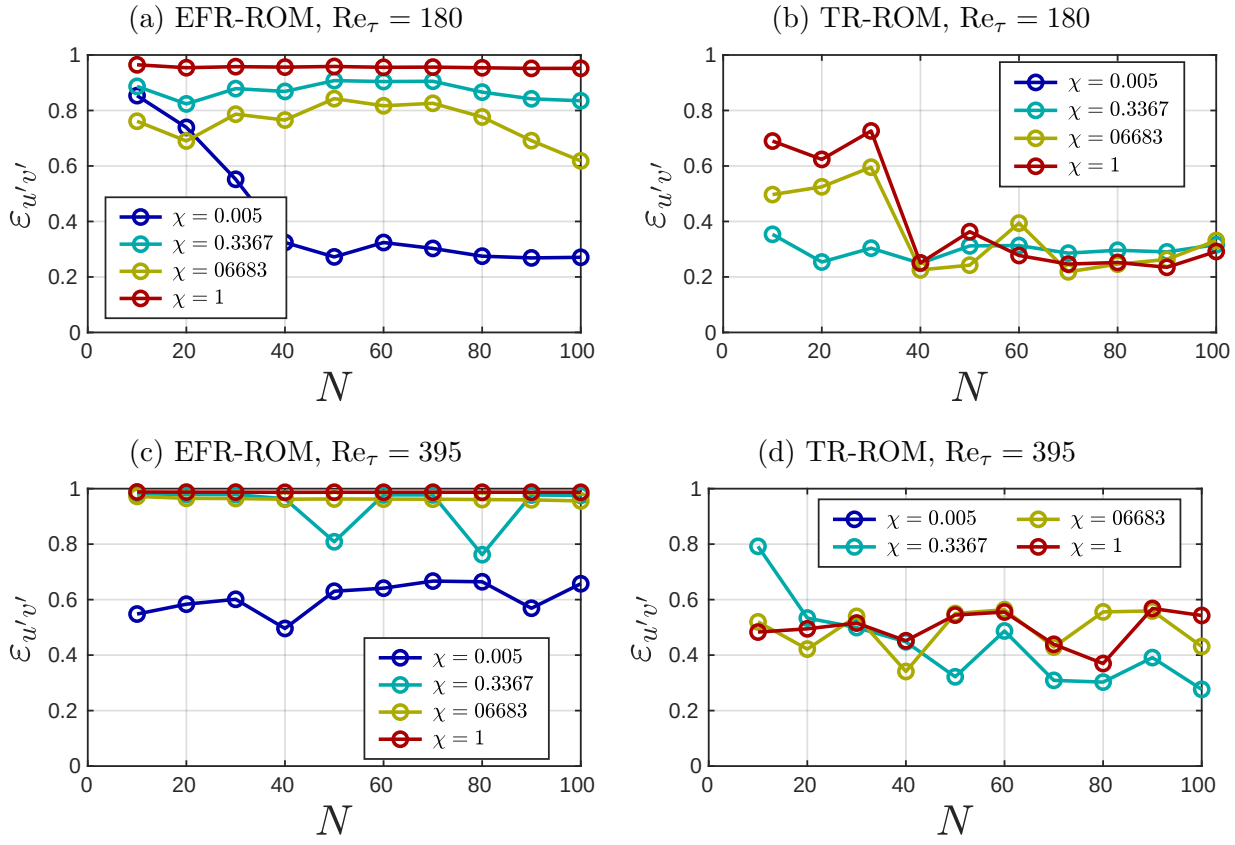

Figure 4.16: The relative error $\varepsilon_{u'v'}$ (4.20) of EFR-ROM and TR-ROM with respect to N and χ for $\mathrm{Re}_\tau = 180$ (4.16a and 4.16b) and $\mathrm{Re}_\tau = 395$ (4.16c and 4.16d) with $m = 1$ and δ_{reprod}. δ_{reprod} is the optimal δ value found in the reproduction regime.

Fig. 4.16a displays the EFR-ROM results at $\mathrm{Re}_\tau = 180$ for each N and for four χ values. We recall that, in EFR-ROM (4.4), χ represents the contribution from the filtered solution at each time step. We find that EFR-ROM with $\chi = \Delta t = 0.005$ yields the best results. For $\chi = 1$, EFR-ROM is too dissipative and leads to an error of around 100% in $u'v'$ for all N values. Although the number of samples we consider for χ is limited due to the training time, it is interesting to see that $\chi = \Delta t$ yields the best EFR-ROM results, just as in the FOM case [30, 120].

Fig. 4.16b displays the TR-ROM results for $\mathrm{Re}_\tau = 180$ for each N and for four χ values. We recall that, in TR-ROM (4.5), χ represents the amount of additional diffusion added to the G-ROM (2.31). This time, we find that TR-ROM with $\chi = \Delta t = 0.005$ yields the worst results. Because the amount of diffusion added to G-ROM is not able to stabilize it, the error $\varepsilon_{u'v'}$ for each N is more than 100%. For the other three χ values, for $N \leq 30$, we find

that smaller χ values lead to better accuracy, and for $N \geq 40$, we find that the error $\varepsilon_{u'v'}$ is similar

Fig. 4.16c displays the EFR-ROM results for $\mathrm{Re}_\tau = 395$ for each N and for four χ values. We again find that EFR-ROM with $\chi = \Delta t = 0.005$ yields the best results. In contrast with the results for $\mathrm{Re}_\tau = 180$, we find that EFR-ROM for the other three χ values leads to an error of around 100% in $u'v'$ for all N values.

Fig. 4.16d displays the TR-ROM results of $\mathrm{Re}_\tau = 395$ for each N and for four χ values. Again, we find that TR-ROM for $\chi = \Delta t = 0.005$ yields the worst results and the error $\varepsilon_{u'v'}$ is more than 100% for each N. For $N \leq 40$, we find that $\chi = 0.6683$ yields the best results for $N = 20$ and 40, and $\chi = 1$ yields the best results for $N = 10$ and $N = 30$. For $N \geq 50$, we find that $\chi = 0.3367$ yields the best results.

In summary, we found that both EFR-ROM and TR-ROM are sensitive to the relaxation parameter χ. Furthermore, for EFR-ROM, we found that $\chi = \Delta t = 0.005$ outperforms the other three values for almost all N. For TR-ROM, we found that $\chi = 0.3367$ outperforms the other values for all N for $\mathrm{Re}_\tau = 180$, and for large N for $\mathrm{Re}_\tau = 395$.

Reg-ROM sensitivity to the filter radius δ. In this section, for the optimal parameters listed in Table 4.1, we study the Reg-ROM sensitivity to the filter radius δ for $\mathrm{Re}_\tau = 180$ and $\mathrm{Re}_\tau = 395$. Our goal is to analyze the impact of δ on the Reg-ROM performance three Reg-ROMs and identify the δ values that yield the best results.

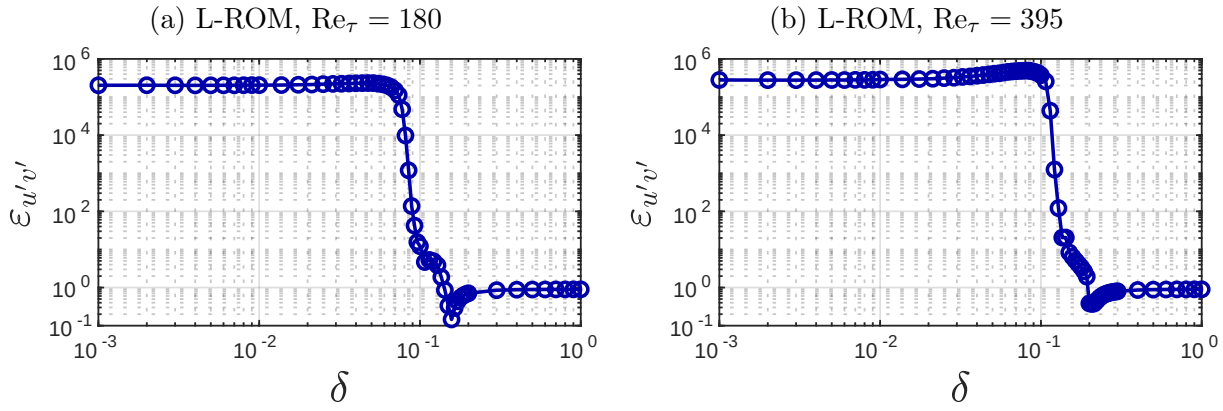

Figure 4.17: The relative error $\varepsilon_{u'v'}$ (4.20) of L-ROM with respect to δ for $\mathrm{Re}_\tau = 180$ (4.17a) and $\mathrm{Re}_\tau = 395$ (4.17b).

Figures 4.17a and 4.17b display the L-ROM's $\varepsilon_{u'v'}$ behavior with respect to the filter radius, δ, for $\mathrm{Re}_\tau = 180$ and $\mathrm{Re}_\tau = 395$. To discuss these results, we can divide the interval $[0.001,\ 1]$ into four subintervals: (i) For $\delta \in [0.001,\ 0.01]$, $\varepsilon_{u'v'}$ is high and does not change with respect

to δ. (ii) For $\delta \in [0.01,\ 0.1]$, $\varepsilon_{u'v'}$ increases as δ increases, and starts decreasing when δ approaches 0.01. A much larger error drop is observed for $\mathrm{Re}_\tau = 180$ than for $\mathrm{Re}_\tau = 395$. (iii) For $\delta \in [0.1,\ 0.2]$, $\varepsilon_{u'v'}$ decreases dramatically from $\mathcal{O}(10^5)$ down to 0.1 and 0.37 for $\mathrm{Re}_\tau = 180$ and $\mathrm{Re}_\tau = 395$, respectively. For both Re_τ, the optimal filter radius, δ_{reprod}, is obtained in the interval $[0.1,\ 0.2]$. (iv) For $\delta \in [0.2,\ 1]$, $\varepsilon_{u'v'}$ increases as δ increases, and eventually plateaus at $\mathcal{O}(1)$ because the L-ROM becomes too dissipative.

Figs. 4.18a and 4.18b display the EFR-ROM's $\varepsilon_{u'v'}$ behavior with respect to the filter radius, δ, for four χ values and for $\mathrm{Re}_\tau = 180$ and $\mathrm{Re}_\tau = 395$. From the results, we can categorize EFR-ROM's $\varepsilon_{u'v'}$ behavior into two types:

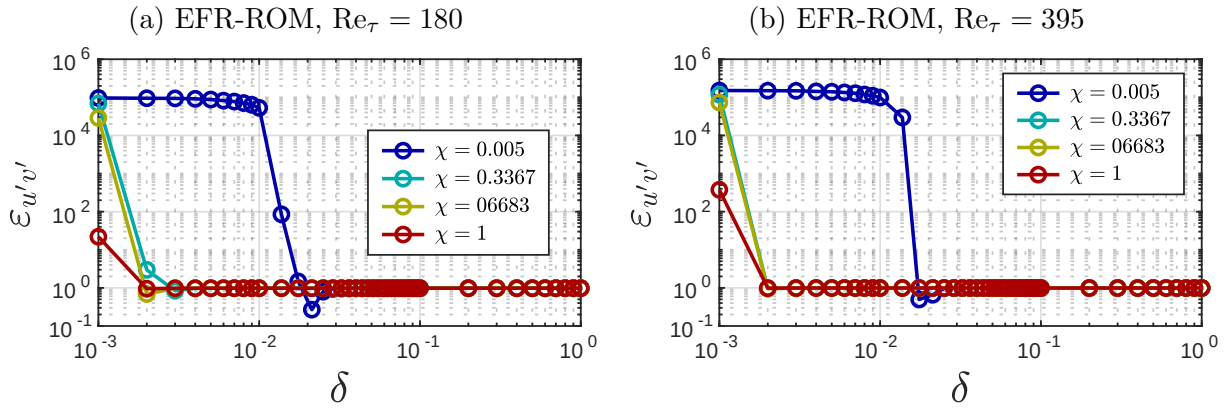

Figure 4.18: The relative error $\varepsilon_{u'v'}$ (4.20) of EFR-ROM with respect to δ for $\mathrm{Re}_\tau = 180$ (4.18a) and $\mathrm{Re}_\tau = 395$ (4.18b).

For $\chi = \Delta t = 0.005$, the behavior of $\varepsilon_{u'v'}$ with respect to δ is similar to that for L-ROM. We can divide the interval $[0.001,\ 1]$ into three subintervals: (i) For $\delta \in [0.001,\ 0.01]$, $\varepsilon_{u'v'}$ decreases slightly as δ increases. (ii) For $\delta \in [0.01,\ 0.03]$, $\varepsilon_{u'v'}$ decreases dramatically from $\mathcal{O}(10^5)$ down to 0.27 and 0.5 for $\mathrm{Re}_\tau = 180$ and $\mathrm{Re}_\tau = 395$, respectively. For both Re_τ values, the optimal filter radius, δ_{reprod}, is obtained in the interval $[0.01,\ 0.03]$. (iii) For $\delta \in [0.03,\ 1]$, $\varepsilon_{u'v'}$ increases as δ increases, and eventually plateaus at $\mathcal{O}(1)$ because EFR-ROM becomes too dissipative.

For the other three χ values, we can divide the interval $[0.001,\ 1]$ into two subintervals: (i) For $\delta \in [0.001,\ 0.003]$, $\varepsilon_{u'v'}$ decreases dramatically to $\mathcal{O}(1)$. However, the fact that there is no δ such that $\varepsilon_{u'v'}$ is below 1 suggests that the optimal filter radius δ_{reprod} is either very sensitive, which requires more sampling points in the interval $[0.001,\ 0.003]$, or it does not exist at all. (ii) For $\delta \in [0.003,\ 1]$, $\varepsilon_{u'v'}$ is mostly $\mathcal{O}(1)$, suggesting that, for these χ values, EFR-ROM is too dissipative regardless of the δ value.

Figs. 4.19a and 4.19b display the TR-ROM's $\varepsilon_{u'v'}$ behavior with respect to the filter radius, δ, for four χ values and for $\mathrm{Re}_\tau = 180$ and $\mathrm{Re}_\tau = 395$. From the results, we can categorize

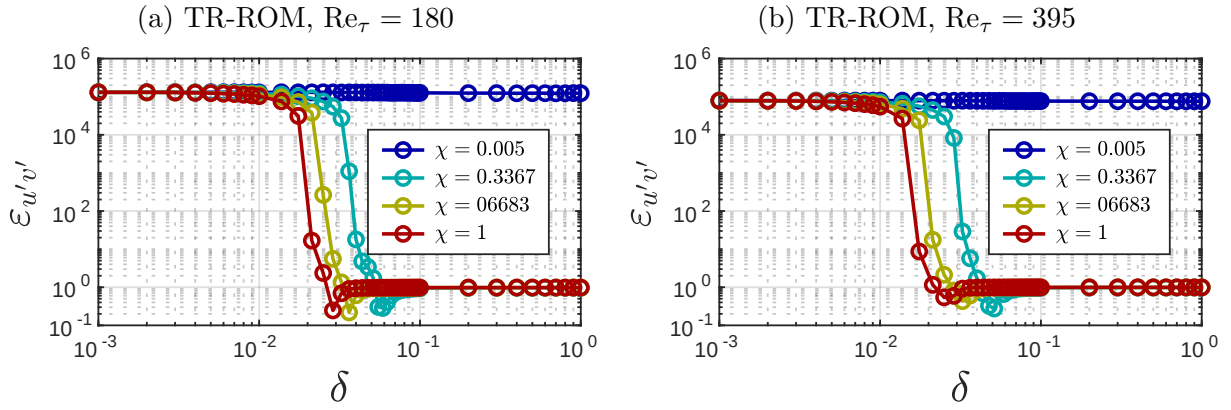

Figure 4.19: The relative error $\varepsilon_{u'v'}$ (4.20) of TR-ROM with respect to δ for $\mathrm{Re}_\tau = 180$ (4.19a) and $\mathrm{Re}_\tau = 395$ (4.19b).

TR-ROM's $\varepsilon_{u'v'}$ behavior into two types:

For $\chi = \Delta t = 0.005$, there is no improvement in $\varepsilon_{u'v'}$ as δ increases. This suggests that χ is so small that, regardless of how large the dissipative term $(\boldsymbol{u}_r - \overline{\boldsymbol{u}}_r)$ (4.6) (determined by δ) is, the total contribution $\chi(\boldsymbol{u}_r - \overline{\boldsymbol{u}}_r)$ is too small to stabilize G-ROM (2.31).

For the other three χ values, the TR-ROM's behavior of $\varepsilon_{u'v'}$ with respect to δ is similar to that of L-ROM and EFR-ROM for $\chi = 0.005$. We can divide the interval $[0.001,\ 1]$ into three subintervals: (i) For $\delta \in [0.001,\ 0.01]$, $\varepsilon_{u'v'}$ decreases slightly as δ increases. (ii) For $\delta \in [0.01,\ 0.1]$, $\varepsilon_{u'v'}$ decreases dramatically from $\mathcal{O}(10^5)$ down to its optimal value. Furthermore, the smaller the χ value, the larger the δ value required to achieve its optimal $\varepsilon_{u'v'}$. This is expected because assuming that the total contribution $\chi(\boldsymbol{u}_r - \overline{\boldsymbol{u}}_r)$ for optimal TR-ROM is fixed, larger χ will then require smaller δ. (iii) For $\delta \in [0.1,\ 1]$, $\varepsilon_{u'v'}$ increases as δ increases, and eventually plateaus at $\mathcal{O}(1)$ because TR-ROM becomes too dissipative.

In summary, we find that all three Reg-ROMs are sensitive to the filter radius, δ. For EFR-ROM and TR-ROM, δ_{reprod} is affected by the relaxation parameter χ, and in the worst-case scenario, δ_{reprod} might not even exist. We also find that the optimal range for δ and the effect of χ are similar for the two Re_τ values.

Sensitivity of the optimal filter radius δ_{reprod} to the filter order m. In this section, we study the sensitivity of the optimal filter radius δ_{reprod} to filter order m for $\mathrm{Re}_\tau = 180$ and $\mathrm{Re}_\tau = 395$ with the three best Reg-ROMs, listed in Table 4.1.

Figs. 4.20a and 4.20b display L-ROM's $\varepsilon_{u'v'}$ behavior with respect to δ for four m values

at $\mathrm{Re}_\tau = 180$ and $\mathrm{Re}_\tau = 395$, respectively. In both Re_τ, we find a higher order filter (larger m) leads to a smaller δ_{reprod}.

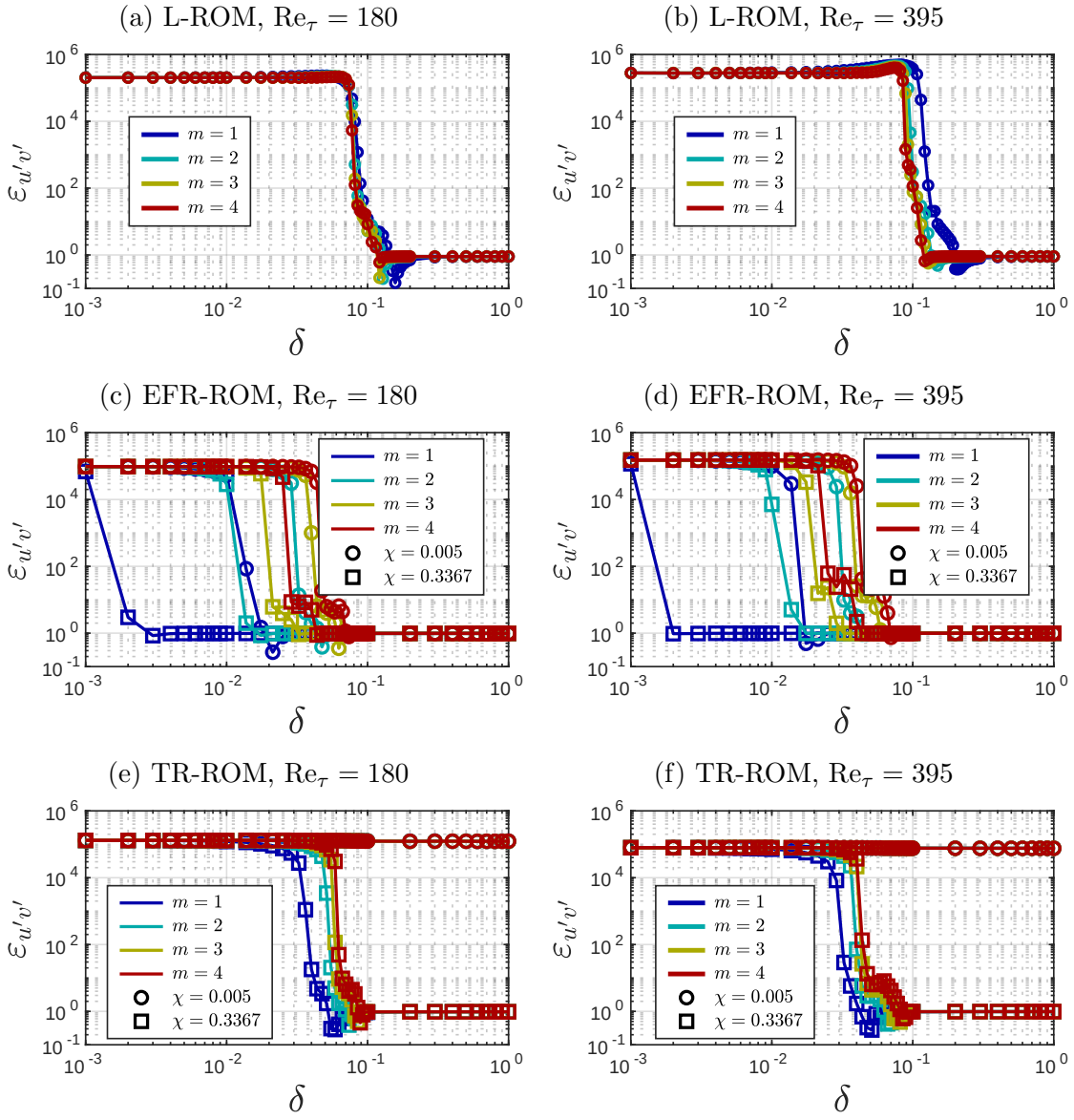

Figure 4.20: The relative error $\varepsilon_{u'v'}$ (4.20) with respect to δ for L-ROM, EFR-ROM and TR-ROM with four m values at $\mathrm{Re}_\tau = 180$ (4.20a, 4.20c, 4.20e) and $\mathrm{Re}_\tau = 395$ (4.20b, 4.20d, 4.20d). For EFR-ROM and TR-ROM, two χ values' results are shown.

Figs. 4.20c and 4.20d display EFR-ROM's $\varepsilon_{u'v'}$ behavior with respect to δ for four m values and two χ values at $\mathrm{Re}_\tau = 180$ and $\mathrm{Re}_\tau = 395$, respectively. The results for different χ values are distinguished by different markers. We choose two χ values because, as explained in Section 4.6.7, there are only two distinct behaviors of EFR-ROM's $\varepsilon_{u'v'}$ for different χ values.

In contrast to the L-ROM results, we observe that, for both Re_τ values, a higher-order filter (larger m) leads to a larger δ_{reprod}. However, it's noteworthy that a higher-order filter does not resolve the issue for $\chi = 0.3367$.

Figs. 4.20e and 4.20f display TR-ROM's $\varepsilon_{u'v'}$ behavior with respect to δ for four m values and two χ values at $\mathrm{Re}_\tau = 180$ and $\mathrm{Re}_\tau = 395$, respectively. The results for different χ values are distinguished by different markers. We choose two χ values because, as explained in Section 4.6.7, there are only two distinct behaviors of TR-ROM's $\varepsilon_{u'v'}$ for different χ values. Similar to the EFR-ROM results, we observe that, for both Re_τ values, a higher-order filter (larger m) leads to a larger δ_{reprod}. However, a higher-order filter does not resolve the issue for $\chi = 0.005$.

4.7 Application - T-junction

In this section, we further test the three Reg-ROMs discussed in the previous sections in a T-junction problem. When streams of rapidly moving flow merge in a T-junction, the potential arises for large oscillations at the scale of the diameter, D, with a period scaling as $\mathcal{O}(D/U)$, where U is the characteristic flow velocity. If the streams are of different

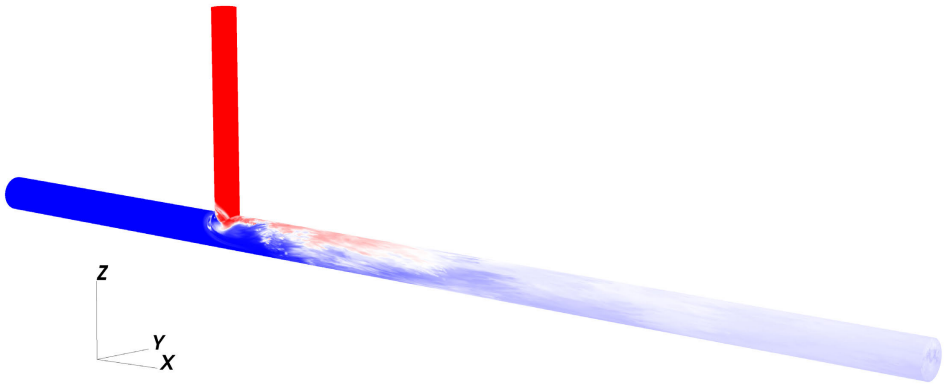

Figure 4.21: Instantaneous temperature field of T-junction simulation at $\mathrm{Re} = 10,000$.

temperatures (see Figure 4.21), the oscillations result in experimental fluctuations (thermal striping) at the pipe wall in the outlet branch that can accelerate thermal-mechanical fatigue and ultimately cause pipe failure. The importance of this phenomenon has prompted the nuclear energy modeling and simulation community to establish T-junction benchmark [103] to test the ability of CFD codes to predict thermal striping.

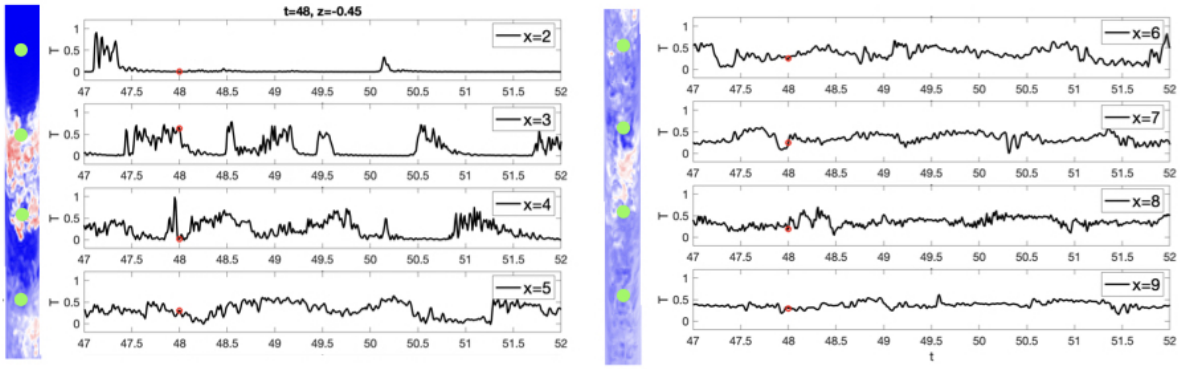

Figure 4.22: Near-wall temperature history at $y = 0,\ z = 0.45$ for several x locations in the outlet branch.

4.7.1 Numerical Results

We consider T-junction problem at the Reynolds number $\mathrm{Re} = 10,000$. The inlet for the main branch is at $x = -9.2143$ and for the hot branch at $z = 6.4286$. The outlet at x=22 was chosen to allow downstream tracking of temperature data at locations provided in the experiment. In terms of the boundary conditions, we have no-slip and insulated boundary everywhere except laminar inflow at the two inlets and outflow at the outlet. The computational mesh for the T-junction consists of $E = 62,176$ spectral elements. Within each element, velocity and pressure are represented as Lagrange interpolating polynomials on tensor products of 7th-order Gauss- Lobatto-Legendre (GLL) points. The FOM degress of freedoms is $\mathcal{N} = EN^3 \approx 21$ million.

The reduced basis $\{\boldsymbol{\varphi}_i, \theta_i\}_{i=1}^N$ for the G-ROM (2.31–2.32) is constructed by applying POD procedure to $K = 1000$ snapshots collected over 10 convective time units. The zeroth mode $\boldsymbol{\varphi}_0$ is set to be the mean velocity field of the snapshot collection time window. The initial condition for the ROMs is obtained by projecting the lifted snapshot at $t = 47$ onto the reduced space.

We test the G-ROM and the Reg-ROMs in the predictive regime, that is, a larger time interval compared to the interval snapshots are collected. We consider $N = 250$ for the G-ROM and $N = 100$ for the Reg-ROMs. To assess ROMs' performance, the near-wall temperature at $(x, \pm 0.5, 0)$, $(x, \pm 0.45, 0)$, $(x, 0, \pm 0.5)$, and $(x, 0, \pm 0.45)$ of the down-stream pipe for $x = 2,\ 3, \ldots, 9$ are measured (Figure 4.22). Unlike the turbulent channel flow, T-junction has high signal-to-noise ratio (NSR) and ROMs are expected to more or less capture the frequency of temperature fluctuations. Figs. 4.23–4.24 show the near-wall $z = 0.45$ temperature of the down-stream pipe at several x locations for the G-ROM, the L-ROM, the EFR-ROM and the TR-ROM. The two vertical red lines denote the time interval in which

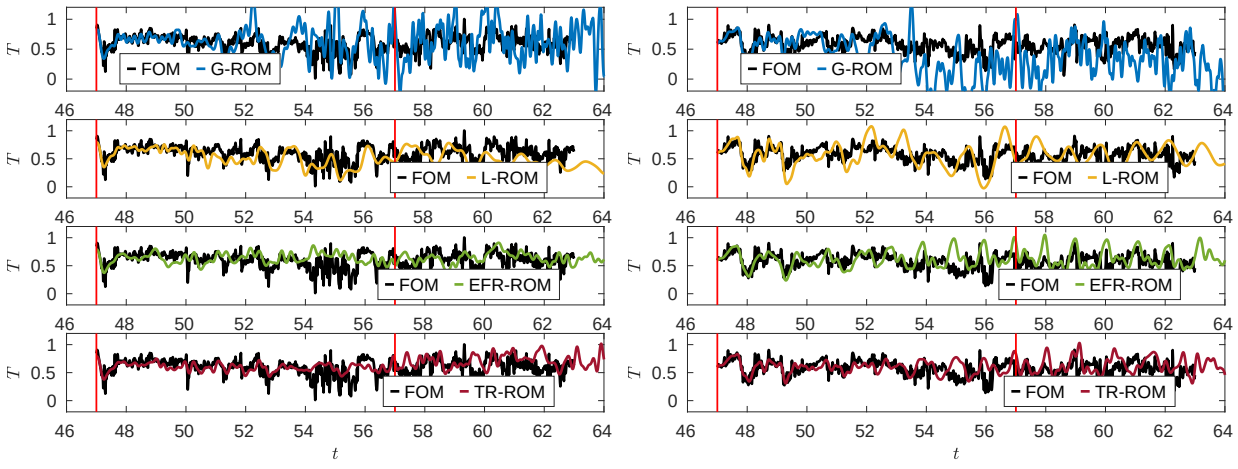

(a) $x = 2,\ y = 0,\ z = 0.45$ (b) $x = 3,\ y = 0,\ z = 0.45$

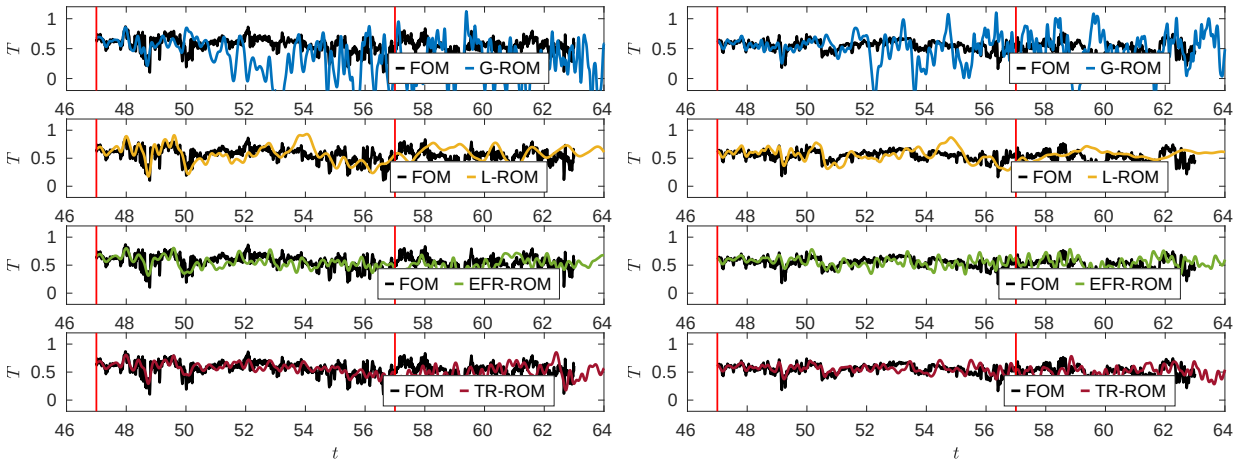

(c) $x = 4,\ y = 0,\ z = 0.45$ (d) $x = 5,\ y = 0,\ z = 0.45$

Figure 4.23: T-junction at $\mathrm{Re} = 10,000$: Comparison of the near-wall temperature history at $z = 0.45$ between the FOM, the G-ROM and the Reg-ROMs for $x = 2,\ 3,\ 4,\ 5$ (outlet branch).

the snapshots are collected.

The results indicate that the near-wall temperature of the G-ROM initially agrees with the FOM but becomes unstable in a relatively short time (≈ 6 CTUs after the initial condition) even with $N = 250$, indicating that it can't even solve the reproduction regime. In addition, a larger fluctuation is observed in upstream of the outlet branch (i.e., small x values). On the other hand, for the thee Reg-ROMs, the near-wall temperature initially agress with the FOM and about the same time as in the G-ROM, the near-wall temperature deviates from the FOM. However, with regularization, the temperature stays on the overall FOM trajectory. Moreover, outside the training time interval (region between the two vertical red lines), all

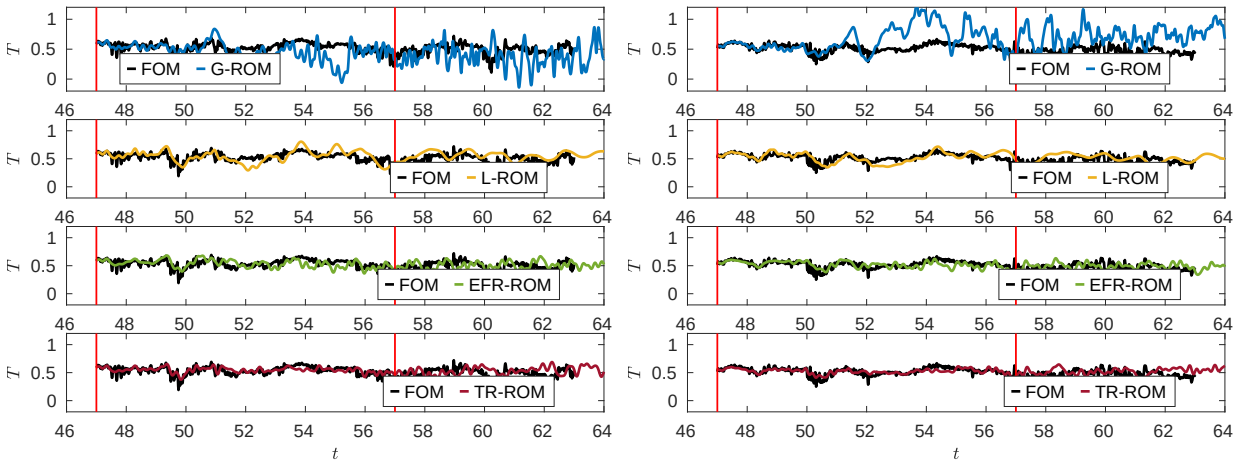

(a) $x = 6,\ y = 0,\ z = 0.45$ (b) $x = 7,\ y = 0,\ z = 0.45$

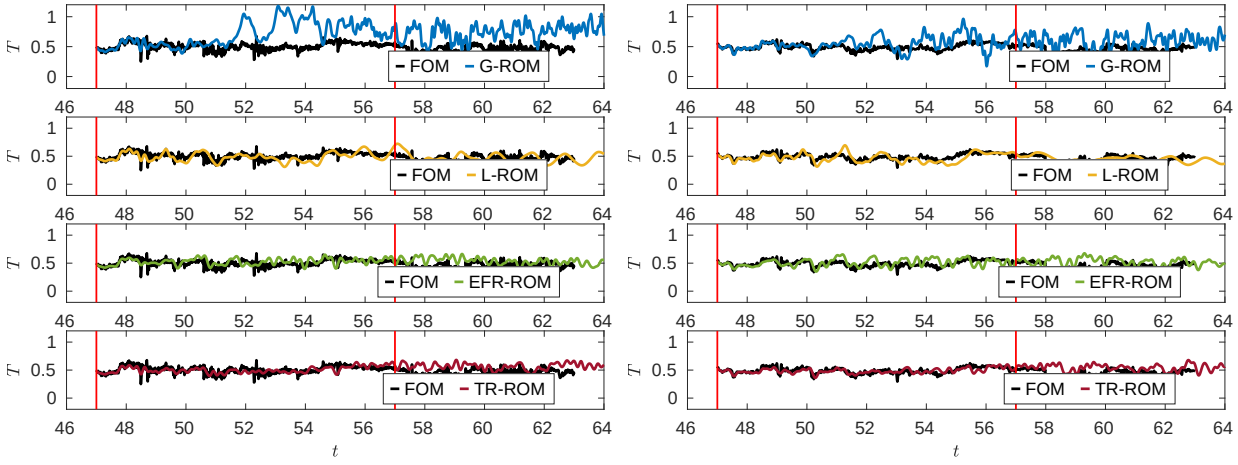

(c) $x = 8,\ y = 0,\ z = 0.45$ (d) $x = 9,\ y = 0,\ z = 0.45$

Figure 4.24: T-junction at $\mathrm{Re} = 10,000$: Comparison of the near-wall temperature history at $z = 0.45$ between the FOM, the G-ROM and the Reg-ROMs for $x = 6,\ 7,\ 8,\ 9$ (outlet branch).

three Reg-ROMs are able to make descent prediction.

4.8 Conclusions

In this chapter, we proposed the time-relaxation ROM (TR-ROM), which is a novel regularized ROM (Reg-ROM) for under-resolved turbulent flows. The TR-ROM employs ROM spatial filtering to smooth out the flow velocity and eliminate the spurious numerical oscillations displayed by the standard Galerkin ROM (G-ROM) (i.e., the ROM that does not use any numerical stabilization). We emphasize that one novel feature of TR-ROM, which

distinguishes it from the other Reg-ROM in current use (i.e., the Leray ROM (L-ROM) and the evolve-filter-relax ROM (EFR-ROM)), is that it introduces different dissipation for the large resolved scales and the small resolved scales. This is in stark contrast with the other two types of Reg-ROMs, i.e, the L-ROM and the EFR-ROM, which use spatial filtering without distinguishing between small and large resolved scales.

To assess the new TR-ROM, we compare it with the L-ROM and the EFR-ROM in the numerical simulation of the turbulent channel flow at $Re_\tau = 180$ and $Re_\tau = 395$ in both the reproduction and the predictive regimes. The spatial filtering in all three Reg-ROMs is performed using the first-order ROM differential filter or the higher-order ROM algebraic filter. We also investigate the sensitivity of the Reg-ROMs with respect to the following parameters: the time interval, the relaxation parameter, and the filter radius. To our knowledge, this is the first numerical comparison of different Reg-ROMs in the numerical simulation of turbulent flows.

Our numerical investigation yields the following conclusions: All three Reg-ROMs are dramatically more accurate than the classical G-ROM without significantly increasing its computational cost. In fact, with respect to several second-order turbulence statistics, the three Reg-ROMs' errors are much lower than that of projection. In addition, with the optimal parameters, the new TR-ROM yields more accurate results than the L-ROM and the EFR-ROM in all tests. Moreover, the HOAF with filter order $m = 1$ yields the best results for most of the N values. On the other hand, the HOAF with $m > 1$ works better for small N, that is, $N \leq 20$, at lower Reynolds number $\mathrm{Re}_\tau = 180$.

From the sensitivity study, we find that the optimal parameters trained in the reproduction regime $(\delta,\ \chi)_{\mathrm{reprod}}$ are also optimal in the predictive regime for most of the N values and for all three Reg-ROMs. Although we find that all three Reg-ROMs are sensitive with respect to the relaxation parameter, χ, and filter radius, δ, we find that the optimal range for δ and the effect of χ are similar for the two Re_τ values.

From the numerical investigation of the HOAF (Section 4.5), we found that the HOAF in the POD setting is indeed a spatial filter, and has a similar behavior as in the SEM setting, that is , the higher-order filter (larger m) tends to damp the higher index modes more, and has less impact on the lower index modes.

Finally, the three Reg-ROMs are investigated for a nuclear engineering application, namely, thermal striping in a T-junction. Our results show that all three Reg-ROMs outperforms the G-ROM and have the capability to reproduce and predict the near-wall temperature at multiple stations along the axis downstream of the T-junction.

Part of the motivation for considering the T-junction is due to it's high signal-to-noise ratio (NSR) which we expect ROMs could capture the large signal with few modes. On

the other hand, the turbulent channel flows has low NSR due to the homogeneity in the x- and z-directions. In fact, from the Fourier analysis, the solution has infinitely many basis functions (sine and cosine functions) in the x- and z-directions. Therefore, it is hard for ROMs.

We also discuss the potential issues that preclude Reg-ROMs from getting more accurate Reynolds shear stress. From our numerical investigation, we found the projection error are high (i.e., at least 55% errors for $\mathrm{Re}_\tau = 180$, and 70% errors for $\mathrm{Re}_\tau = 395$). This indicates the poor approximation capability of the reduced basis for the Reynolds stress $u'v'$. With this approximation error, it is not surprised to find that $\varepsilon_{u'v'}$ of Reg-ROMs is not below 10%. In order to improve the accuracy, one either needs to increase the number of ROM basis functions or consider a ROM basis that is designed for the Reynolds stress approximation. The other potential issue is the necessity of including the modeling Reynolds stress tensor when comparing with the FOM. The idea is inspired from a concept that has been used in the large eddy simulation (LES) community. As pointed out in [122, 123], the Reynolds stresses from a large eddy simulation (LES) can only be compared with those from a direct numerical simulation (DNS) by also taking into account the contribution from the modeling term. As shown in [124], the Leray model of the NSE can be written into the form of filtered NSE with a known subgrid model, only involves the filtered solution and filtering opterators. A further investigation is required to confirm if it is valid to include the modeling Reynolds stress tensor in the context of reduced-order modeling since it is not clear if one could also cast the NSE with ROM solution as the filtered Navier-Stokes equations. In addition, how to compute the modeling Reynolds stress tensor for Reg-ROMs or more general ROMs also needed to be investigated.

The first steps in the numerical investigation of the new TR-ROM for the turbulent flows have been encouraging. There are, however, several other research directions that should be pursued next. For example, one can investigate whether ROM approximate deconvolution [125, 126] can be leveraged to further increase the localization of the dissipation mechanism in the new TR-ROM. One could also compare the approximate deconvolution approach with the effect of increasing the order of the higher-order algebraic filter (4.14) in TR-ROM. Finally, TR-ROM's numerical analysis, which could yield new, robust parameter scalings [127], should be performed.

Chapter 5: Accelerating the Galerkin Reduced-Order Model with the Tensor Decomposition

In this chapter, we propose a novel approach which utilizes the CANDECOMC/PARAFAC decomposition (CPD), a tensor decomposition technique, to accelerate the G-ROM in the scenario of large N values. The CP decomposition reduces the $\mathcal{O}(N^3)$ tensor contraction cost to $\mathcal{O}(NR)$, where R is the CP rank. Our numerical investigation shows that at least a factor of 10 speed-up is established, and the reduction with the CP decomposition allows one to consider a larger N value for turbulent flows. In addition, for stability, we derive two conditions to preserve the skew-symmetry in the CP decomposition and show that the resulting ROM is more stable and achieves the same accuracy with a smaller rank R. Furthermore, we discovered that the advection tensor formed using the H_0^1-POD basis functions has a low-rank structure and this low-rank structure is preserved even in higher Reynolds numbers with the singular value decomposition (SVD) and demonstrate that, for a given level of accuracy, the CP decomposition is more efficient in size and cost than the SVD.

The chapter is organized as follows: In Section 5.1, we revisit the Galerkin reduced order model (G-ROM) and the CANDECOMC/PARAFAC decomposition (CPD) for general and partially symmetric tensors. In Section 5.2, we present the G-ROM with the CP decomposition (CPD-ROM). In addition, we show that the advection tensor is partially skew-symmetric with appropriate boundary and divergence-free conditions and present the CP decomposition for a partially skew-symmetric tensor. Furthermore, we show an underlying CP structure in the advection tensor. Finally, we present the numerical results in Section 5.3. In this section, we also investigate the low-rank structure of the ROM tensors using the SVD, examining their behavior under the L^2 and H_0^1 norms and comparing the performance of the G-ROM with the SVD and the CPD. In Section 5.4, we present the conclusions of our numerical investigation and potential future work.

5.1 Backgrounds

In Section 5.1.1, we revisit the G-ROM introduced in Section 2.2 with a slightly different expression for the ease of the discussion with the CP decomposition. In Sections 5.1.2–5.1.3, we introduce the CANDECOMC/PARAFAC decomposition (CPD) with alternating least squares method (ALS) for general and partially symmetric tensors.

5.1.1 Galerkin Reduced-Order Model (G-ROM)

With the reduced basis functions $\{\boldsymbol{\varphi}_i\}_{i=1}^N$ and the *base state* $\boldsymbol{\varphi}_0$ in hand, the G-ROM is constructed by inserting the ROM basis expansion

$$\widetilde{\mathbf{u}}_{\mathrm{r}}(\mathbf{x}) = \boldsymbol{\varphi}_0(\mathbf{x}) + \sum_{j=1}^{N} u_{\mathrm{r},j}\boldsymbol{\varphi}_j(\mathbf{x}) \tag{5.1}$$

into (2.8): *Find* $\widetilde{\mathbf{u}}_r$ *such that, for all* $\boldsymbol{v} \in \mathbf{X}_0^N$,

$$\left(\boldsymbol{v}_i, \frac{\partial \widetilde{\mathbf{u}}_{\mathrm{r}}}{\partial t}\right) + \nu\ (\nabla \boldsymbol{v}_i, \nabla \widetilde{\mathbf{u}}_{\mathrm{r}}) + \left(\boldsymbol{v}_i, (\widetilde{\mathbf{u}}_{\mathrm{r}} \cdot \nabla)\widetilde{\mathbf{u}}_{\mathrm{r}}\right) = 0, \tag{5.2}$$

where $\mathbf{X}_0^N := \mathrm{span}\{\boldsymbol{\varphi}_i\}_{i=1}^N$ is the ROM space.

With (5.2), a system of differential equations in the coefficients with respect to the reduced bases $u_{\mathrm{r},j}$ are derived:

$$B\frac{d\underline{u}_{\mathrm{r}}}{dt} = -\mathcal{C}(\underline{\widetilde{u}}_{\mathrm{r}})\underline{\widetilde{u}}_{\mathrm{r}} - \nu A\underline{\widetilde{u}}_{\mathrm{r}}, \tag{5.3}$$

where $\underline{u}_{\mathrm{r}} \in \mathbb{R}^N$ is the vector consists of POD coefficients $\{u_{r,j}\}_{j=1}^N$ and $\underline{\tilde{u}}_{\mathrm{r}} \in \mathbb{R}^{N+1}$ is the augmented vector that includes the zeroth mode's coefficient. A, B, and $\mathcal{C}$ represent the reduced velocity stiffness, mass, and advection operators, respectively, with entries defined in (2.35–2.37).

For temporal discretization of (5.3), a semi-implicit scheme with kth-order backward differencing (BDFk) and kth-order extrapolation (EXTk) is considered. The fully discretized reduced system at time t^l is:

$$\begin{aligned}\left(\frac{\beta_0}{\Delta t}B + \nu A\right)\underline{u}_{\mathrm{r}}^{l+1} = &-\sum_{i=1}^{k}\alpha_i\left[\mathcal{C}(\underline{u}_{\mathrm{r}}{}^{l-i})\underline{u}_{\mathrm{r}}{}^{l-i} + (C_1 + C_2)\underline{\bar{u}}_{\mathrm{r}}{}^{l-i} - \underline{c}_0\right] \\ &- B\sum_{i=1}^{k}\frac{\beta_i}{\Delta t}\underline{u}_{\mathrm{r}}^{l-i} - \nu\underline{a}_0,\end{aligned} \tag{5.4}$$

where

$$c_{0,i} = \int_\Omega \boldsymbol{\varphi}_i \cdot (\boldsymbol{\varphi}_0 \cdot \nabla)\boldsymbol{\varphi}_0\, dV, \quad a_{0,i} = \int_\Omega \nabla\boldsymbol{\varphi}_i : \nabla\boldsymbol{\varphi}_0\, dV, \tag{5.5}$$

$$C_{1,ij} = \int_\Omega \boldsymbol{\varphi}_i \cdot (\boldsymbol{\varphi}_0 \cdot \nabla)\boldsymbol{\varphi}_j\, dV, \quad C_{2,ik} = \int_\Omega \boldsymbol{\varphi}_i \cdot (\boldsymbol{\varphi}_k \cdot \nabla)\boldsymbol{\varphi}_0\, dV, \tag{5.6}$$

for all $i = 1, \ldots, N$ and $j,\ k = 0, \ldots, N$.

Remark 5.1. The computational cost of solving (5.4) is dominated by the application of the rank-3 advection tensors, $\mathcal{C}$, which requires $O(N^3)$ operations and memory references on each step. The remainder of the terms are $O(N^2)$ or less. Unfortunately, $O(N^3)$ is a very steep cost and prohibits practical consideration of, say, $N > 200$. In this work, our goal is to mitigate the cost with CP decomposition.

5.1.2 CP Decomposition with ALS

The CP decomposition [128, 129] factories a tensor into a sum of component rank-one tensors. For example, given a third-order tensor $\mathcal{X} \in \mathbb{R}^{s_1 \times s_2 \times s_3}$, its CP decomposition is denoted by

$$\mathcal{X} \approx [\![A^{(1)}, A^{(2)}, A^{(3)}]\!] \equiv \sum_{r=1}^{R} \underline{a}_r^{(1)} \circ \underline{a}_r^{(2)} \circ \underline{a}_r^{(3)}. \tag{5.7}$$

where $[\![\ ]\!]$ is the Kruskal operator [130], which provides a shorthand notation for the sum of the outer products of the columns of a set of matrices. $A^{(i)} = \left[\underline{a}_1^{(i)}, \cdots, \underline{a}_R^{(i)}\right] \in \mathbb{R}^{s_i \times R}$ for $i = 1, 2, 3$ are the factor matrices and refer to the combination of the vectors from the rank-one components, and R is the CP rank. It is noteworthy to point out that solving (5.7) with $R = 1$ is already NP-hard [131].

The rank of a tensor $\mathcal{X}$ is defined as the smallest number of rank-one tensors that generate $\mathcal{X}$ as their sum [129, 132]. One of the major differences between matrix and tensor rank [133] is that determining the rank of a specific tensor is NP-hard [134]. Consequently, the first issue in computing a CP decomposition is choosing the number of rank-one components In this work, we consider the most common strategy by simply fitting multiple CP decompositions with different R until one is "good".

For a given CP rank R, finding a CP decomposition for $\mathcal{X}$ corresponds to a nonlinear least-squares optimization problem:

$$\min_{A^{(1)}, A^{(2)}, A^{(3)}} \|\mathcal{X} - [\![A^{(1)}, A^{(2)}, A^{(3)}]\!]\|_F, \tag{5.8}$$

where $\|\cdot\|_F$ is the Frobenius norm and the Frobenius norm of a tensor $\mathcal{X} \in \mathbb{R}^{s_1 \times s_2 \times s_3}$ is the square root of the sum of the squares of all its elements.

There are many algorithms to compute CP decomposition. In this work, we consider the alternating least squares (ALS) method [128, 135]. The idea behind ALS is that we solve for each factor in turn, leaving all the other factors fixed. In each iteration, three subproblems

are solved in sequence:

$$\min_{B \in \mathbb{R}^{s_1 \times R}} \|\mathcal{X} - [\![B, A^{(2)}, A^{(3)}]\!]\|_F, \tag{5.9}$$

$$\min_{B \in \mathbb{R}^{s_2 \times R}} \|\mathcal{X} - [\![A^{(1)}, B, A^{(3)}]\!]\|_F, \tag{5.10}$$

$$\min_{B \in \mathbb{R}^{s_3 \times R}} \|\mathcal{X} - [\![A^{(1)}, A^{(2)}, B]\!]\|_F. \tag{5.11}$$

Each subproblem corresponds to a linear least squares problem and is often solved via the normal equation [133], which involves tensor contraction to solve the linear system of equations and costs $\mathcal{O}(s^3R)$ if $s_i = s$ for all $i \in \{1, 2, 3\}$.

5.1.3 CP Decomposition for Partially Symmetric Tensor

Symmetric tensor plays an important role in various fields, including chemometrics, psychometrics, econometrics, image processing, biomedical signal processing [136, 137, 138, 139]. A tensor is symmetric if its elements remain the same under any permutation of the indices [133]. Tensors can be partially symmetric in two or more modes as well.

The CP decomposition for partially symmetric tensor has been studied in [135, 140]. Assume the tensor $\mathcal{X}$ is symmetric in the mode-1 and mode-3, its CP decomposition is symmetric if:

$$\mathcal{X} \approx [\![A^{(1)}, A^{(2)}, A^{(3)}]\!] = [\![A^{(3)}, A^{(2)}, A^{(1)}]\!]. \tag{5.12}$$

Typically, one can ensure (5.12) by enforcing the factor matrix $A^{(1)}$ and $A^{(3)}$ to be the same.

For fully symmetric tensors, setting $A^{(1)} = A^{(2)} = A^{(3)}$ results in a decomposition whose rank is referred to as the symmetric rank of a tensor. For such tensors, the symmetric rank is often the same as the CP rank [138].

The factor $A^{(2)}$ is computed as in ALS. For $A^{(1)}$ and $A^{(3)}$, we use an iterative algorithm [141] similar to the Babylonian square root algorithm, which updates $A^{(1)}$ using a series of subiterations. At each subiteration, a linear least squares problem is solved for one of the two repeated factors (with the other fixed),

$$A^{(1)}_{\text{next}} = \operatorname*{argmin}_B \|\mathcal{X} - [\![B, A^{(2)}, A^{(1)}]\!]\|. \tag{5.13}$$

Then, both the first and third factors are updated with momentum, $A^{(1)}_{\text{new}} = \lambda A^{(1)} + (1-\lambda) A^{(1)}_{\text{next}}$.

5.2 Accelerating the G-ROM with the CP Decomposition

The motivation to consider CP decomposition for the G-ROM is demonstrated in Fig. 5.1. Fig. 5.1a shows the behavior of the accumulated POD eigenvalue for 2D periodic to 3D turbulent flows. As problems become advection-dominated, the results indicate that at least $N > 100$ POD modes are required to capture 90% of the total energy. Meanwhile, Figure 5.1b shows the solve time for the reduced system (5.4) for 500 CTUs. The results indicate that the ROM loses efficiency as N increases due to the tensor contraction cost $\mathcal{O}(N^3)$. The rest

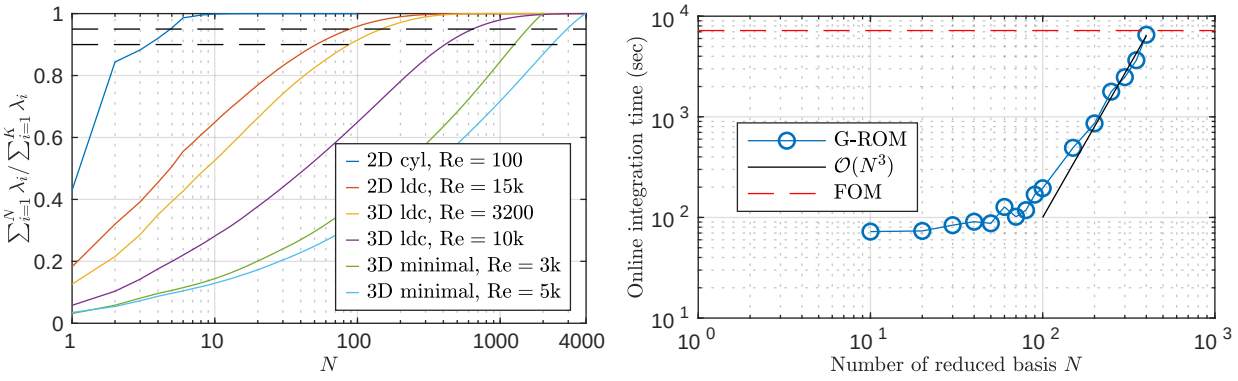

(a) (b)

Figure 5.1: (a): Behavior of the accumulated POD eigenvalues for 2D periodic flow to 3D turbulent flows. Here cyl, ldc and minimal are denoted as flow past a cylinder, lid-driven cavity and minimal flow unit. (b): Behavior of the online solve time of the reduced system (5.4) as a function of N.

of this section is organized as follows: In Section 5.2.1, we present G-ROM with the CP decomposition (CPD-ROM). In Section 5.2.2, we show that the ROM tensor is partially skew-symmetric with divergence-free and certain boundary conditions. In Section 5.2.3, we present CP decomposition for partially skew-symmetric tensor. Finally, in Section 5.2.4, we show that the ROM tensor has an underlying CP structure.

5.2.1 CPD-ROM

To address the $\mathcal{O}(N^3)$ bottleneck, we consider CP decomposition to approximate the convection tensor $\mathcal{C}$ (2.37):

$$\mathcal{C}_{ikj} \approx \tilde{\mathcal{C}}_{ikj} = \sum_{r=1}^{R} a_{ir} b_{kr} c_{jr}. \tag{5.14}$$

With (5.14), the tensor contraction $\mathcal{C}(\underline{u})\underline{u}$ is approximated by three matrix-vector multiplications [5]: $\forall\ i = 1, \ldots, N$,

$$\left[\mathcal{C}(\underline{u}_{\mathrm{r}})\underline{u}_{\mathrm{r}}\right]_i \approx \left[\tilde{\mathcal{C}}(\underline{u}_{\mathrm{r}})\underline{u}_{\mathrm{r}}\right]_i = \sum_{j=0}^{N}\sum_{k=0}^{N}\sum_{r=1}^{R} a_{ir}b_{kr}c_{jr}u_{\mathrm{r},k}u_{\mathrm{r},j} = \sum_{r=1}^{R} a_{ir}(\sum_{k=0}^{N} b_{kr}u_{\mathrm{r},k})(\sum_{j=0}^{N} c_{jr}u_{\mathrm{r},j}). \tag{5.15}$$

The cost is therefore reduced by a factor of $2N^3/6NR = N^2/3R$ in the leading order cost term. Throughout the chapter, CPD-ROM is referred as the G-ROM (5.4) with the approximated tensor $\tilde{\mathcal{C}}$ (5.14).

5.2.2 Partially Skew-Symmetric ROM Tensor

We adapt the analysis in [142] to show that the ROM tensor (2.37) is skew-symmetric in mode-1 and mode-3 with appropriate boundary and divergence-free conditions.

We begin with the definition of the ROM tensor (2.37). Because each POD basis function is a vector field $\boldsymbol{\varphi}_i = (\varphi_{i,x}, \varphi_{i,y}, \varphi_{i,z})$, (2.37) can be further decomposed into three terms (5.17), which represents the x-, y- and z- direction's contribution, respectively:

$$\mathcal{C}_{ikj} = \int_\Omega \boldsymbol{\varphi}_i \cdot (\boldsymbol{\varphi}_k \cdot \nabla)\boldsymbol{\varphi}_j \, dV \tag{5.16}$$

$$= \int_\Omega \varphi_{i,x}(\boldsymbol{\varphi}_k \cdot \nabla)\varphi_{j,x} \, d\Omega + \int_\Omega \varphi_{i,y}(\boldsymbol{\varphi}_k \cdot \nabla)\varphi_{j,y} \, d\Omega + \int_\Omega \varphi_{i,z}(\boldsymbol{\varphi}_k \cdot \nabla)\varphi_{j,z} \, d\Omega. \tag{5.17}$$

Without loss of the generality, we consider the x-direction contribution. With the divergence theorem and the product rule, the following equation is derived:

$$\int_\Omega \varphi_{i,x}(\boldsymbol{\varphi}_k \cdot \nabla)\varphi_{j,x} \, d\Omega = -\int_\Omega \varphi_{j,x}(\boldsymbol{\varphi}_k \cdot \nabla)\varphi_{i,x} \, d\Omega \tag{5.18}$$

$$- \int_\Omega \varphi_{i,x}\varphi_{j,x}(\nabla \cdot \boldsymbol{\varphi}_k) \, d\Omega + \int_{\partial\Omega} \varphi_{i,x}\varphi_{j,x}\boldsymbol{\varphi}_k \cdot \hat{n} dA. \tag{5.19}$$

where $\hat{\mathbf{n}}$ is the outward unit normal on the boundary $\partial\Omega$. If the model problem has Dirichlet or periodic boundary conditions and the velocity reduced basis function $\boldsymbol{\varphi}_k$ is divergence-free, that is, $\nabla \cdot \boldsymbol{\varphi}_k = 0$, the last two integrals vanish, leading to

$$\int_\Omega \varphi_{i,x}(\boldsymbol{\varphi}_k \cdot \nabla)\varphi_{j,x} \, d\Omega = -\int_\Omega \varphi_{j,x}(\boldsymbol{\varphi}_k \cdot \nabla)\varphi_{i,x} \, d\Omega. \tag{5.20}$$

[5] The first two comes from contracting the factor matrices B and C with vector $\underline{u}$, the third is due to contraction of the factor matrix A with the vector $(B^T\underline{u} * C^T\underline{u})$, where $*$ is the element-wise product.

This indicates that the x-direction contribution is skew-symmetric in mode-1 and mode-3. For the y- and z-direction contributions, a similar equations of (5.19)–(5.20) can be derived. Therefore, the ROM tensor (2.37) is skew-symmetric.

Remark 5.2. If the problem has inflow and outflow boundary conditions, the skew symmetry no longer holds.

Remark 5.3. In the case where skew-symmetry is no longer hold, the tensor $\mathcal{C}$ could always be decomposed into a skew-symmetric tensor plus a low-rank tensor contributed from the boundaries, that is, the third term in (5.19).

Remark 5.4. Even if the model problem has appropriate boundary conditions, the ROM tensor (2.37) will not be exactly partially skew-symmetric because of the divergence-free condition $\nabla \cdot \boldsymbol{\varphi}_k = 0$ is not satisfied exactly. This is because each snapshot (FOM solution) only satisfied the divergence-free condition in the weak form, and the condition is enforced to a certain accuracy (10^{-6}–10^{-8}) only in practice. Therefore, a divergence error (albeit small) will be present. In this case, we enforce the partially skew symmetry by doing $\mathcal{C}_{ijk} = 0.5(\mathcal{C}_{ijk} - \mathcal{C}_{kji})$ for all $i, j, k = 1, \ldots, N$.

5.2.3 CP Decomposition for Partially Skew-Symmetric Tensor

Skew-symmetric tensor also arises in many fields, for example, solid-state physics [143, 144], fluid dynamics [142], and quantum chemistry [145, 146, 147]. A tensor is skew-symmetric if its elements alternates sign under any permutation of the indices [148]. Tensors can be partially skew-symmetric in two or more modes as well.

Tensor decomposition for skew-symmetric tensor has been widely studied, see [149] for Tucker decomposition, and [150, 151, 152, 153] for decomposition into directional components (DEDICOM) and its applications. On the other hand, CP decomposition for the skew-symmetric tensor has not been widely studied, in fact, we could only find one related work [154] but with a different approach on enforcing skew-symmetry.

Assume the tensor $\mathcal{X}$ is skew-symmetric in mode-1 and mode-3, its CP decomposition is skew-symmetric if it satisfies:

$$\mathcal{X} \approx [\![A^{(1)}, A^{(2)}, A^{(3)}]\!] = [\![-A^{(3)}, A^{(2)}, A^{(1)}]\!]. \tag{5.21}$$

We impose the following conditions on the CP rank R and the factor matrices so that (5.21)

is satisfied:

$$R \text{ has to be even,} \tag{5.22}$$

$$A^{(1)} \equiv \left[A_1^{(1)}\ A_2^{(1)}\right],\ A^{(2)} \equiv \left[A_1^{(2)}\ A_1^{(2)}\right],\ A^{(3)} \equiv \left[A_2^{(1)}\ -A_1^{(1)}\right], \tag{5.23}$$

where $A_1^{(1)}$ and $A_1^{(1)}$ are of size $N \times R/2$, and the factor matrix $A^{(2)}$ has $N/2$ redundant columns. With (5.23), the CP decomposition can be expressed as:

$$\mathcal{X} \approx [\![A^{(1)}, A^{(2)}, A^{(3)}]\!] = [\![A_1^{(1)}, A_1^{(2)}, A_2^{(1)}]\!] + [\![A_2^{(1)}, A_1^{(2)}, -A_1^{(1)}]\!] = [\![-A^{(3)}, A^{(2)}, A^{(1)}]\!], \tag{5.24}$$

and is skew-symmetric in mode-1 and mode-3.

The factor $A^{(2)}$ is computed as in ALS. For $A^{(1)}$ and $A^{(3)}$, we use an iterative algorithm [141] similar to the Babylonian square root algorithm, which updates $A^{(1)}$ using a series of subiterations. At each subiteration, a linear least squares problem is solved for $A^{(1)}$ with $A^{(3)}$ fixed,

$$A_{\text{next}}^{(1)} = \underset{B}{\operatorname{argmin}} \|\mathcal{X} - [\![B, A^{(2)}, A^{(3)}]\!]\|_F. \tag{5.25}$$

Then both the first and third factors are updated with momentum,

$$A_{\text{new}}^{(1)} = \lambda A^{(1)} + (1-\lambda) A_{\text{next}}^{(1)}, \text{ and } A_{\text{new}}^{(3)} = \left[A_{\text{new},2}^{(1)}\ \ -A_{\text{new},1}^{(1)}\right]. \tag{5.26}$$

5.2.4 Underlying CP Structure in the ROM Tensor

In this section, we demonstrate that CP decomposition is a reasonable low-rank approximation for the advection tensor $\mathcal{C}$ (2.37) by showing there is an underlying CP structure. To see this, recall the definition of $\mathcal{C}$ (2.37) and substitute $\boldsymbol{\varphi}_i$, $\boldsymbol{\varphi}_j$ and $\boldsymbol{\varphi}_k$ with $\boldsymbol{\varphi}_* = (\varphi_{*,x}, \varphi_{*,y})$,

$$\begin{aligned}\mathcal{C}_{ikj} &= \int_\Omega \boldsymbol{\varphi}_i \cdot (\boldsymbol{\varphi}_k \cdot \nabla)\boldsymbol{\varphi}_j \, d\Omega = \int_\Omega \varphi_{i,x}(\boldsymbol{\varphi}_k \cdot \nabla)\varphi_{j,x} \, d\Omega + \int_\Omega \varphi_{i,y}(\boldsymbol{\varphi}_k \cdot \nabla)\varphi_{j,y} \, d\Omega \\ &= \int_{-1}^{1}\int_{-1}^{1} \left(\varphi_{i,x}\varphi_{k,x}\frac{\partial \varphi_{j,x}}{\partial x} + \varphi_{i,x}\varphi_{k,y}\frac{\partial \varphi_{j,x}}{\partial y} + \varphi_{i,y}\varphi_{k,x}\frac{\partial \varphi_{j,y}}{\partial x} + \varphi_{i,y}\varphi_{k,y}\frac{\partial \varphi_{j,y}}{\partial y}\right) dxdy. \end{aligned} \tag{5.27}$$

For simplicity, we assume the problem is two-dimensional and the domain is simply $\Omega = [-1,\ 1]^2$ with one spectral element. For the general form with deformed geometry and multiple elements, we suggest [155] for a detailed review.

(5.27) is used to compute each component of the tensor $\mathcal{C}_{ikj}$ and the two-dimensional

integration is computed using Gaussian quadrature:

$$\int_{-1}^{1}\int_{-1}^{1}\varphi_{i,x}\varphi_{k,x}\frac{\partial\varphi_{j,x}}{\partial x}\,dxdy \simeq \sum_{m=0}^{q}\sum_{n=0}^{q}\omega_m\omega_n\varphi_{i,x}(\xi_m,\xi_n)\varphi_{k,x}(\xi_m,\xi_n)\frac{\partial\varphi_{j,x}(\xi_m,\xi_n)}{\partial x}, \tag{5.28}$$

where $\{\omega_i\}_i^{q+1}$ and $\{\xi_i\}_i^{q+1}$ are the Gauss-Lobatto-Legendre (GLL) quadrature weights and points. Notice that, with $q+1$ GLL quadrature weights and points, the approximated integration is exact if the integrand is a polynomial of at most $2q-1$. However, the overall polynomial order inside the integral is larger than $2q-1$. Usually the exactness of (5.28) is enforced by interpolating the polynomial function onto a finer polynomial space of order $M = 3q/2$, denoted as dealiasing [142]. Dealiasing increases the cost for evaluating (5.28) but the representation stays the same because eventually it is projected back to the original polynomial space of order q.

(5.28) suggests there is an underlying CP structure:

$$\begin{aligned}\int_{-1}^{1}\int_{-1}^{1}\varphi_{i,x}\varphi_{k,x}\frac{\partial\varphi_{j,x}}{\partial x}\,dxdy &= \sum_{m=1}^{q+1}\sum_{n=1}^{q+1}\omega_m\omega_n\varphi_{i,x}(\xi_m,\xi_n)\varphi_{k,x}(\xi_m,\xi_n)\frac{\partial\varphi_{j,x}(\xi_m,\xi_n)}{\partial x}\\ &= \sum_{l=1}^{(q+1)^2}\rho_l a_{i,l}b_{k,l}c_{j,l},\end{aligned} \tag{5.29}$$

where

$$\rho_l := \omega_m\omega_n, \quad a_{i,l} := \varphi_{i,x}(\xi_m,\xi_n), \quad b_{k,l} := \varphi_{k,x}(\xi_m,\xi_n), \quad \text{and} \quad c_{j,l} := \frac{\partial\varphi_{j,x}(\xi_m,\xi_n)}{\partial x}, \tag{5.30}$$

with the index $l := m + (n-1)(q+1)$.

The analysis can be applied to the other three terms in (5.27) and a similar form of (5.29) can be derived. (5.29) suggests a theoretical bound of the CP rank of the advection tensor to be $4E(q+1)^2$ and $9E(q+1)^2$ for 2D and 3D problem, respectively, with E being the number of spectral elements.

5.3 Numerical Results

In this section, we present numerical results for the CPD-ROM introduced in Section 5.2.1. For comparison purposes, we also present the results of G-ROM (5.4) and the FOM. The ROM is constructed through an offline-online procedure: In the offline phase, the FOM is solved using the open-source code Nek5000/RS [61, 62]. The POD basis and the reduced operators (2.37–5.6) are then constructed using NekROM. In addition, the CP decomposition

for the tensor $\mathcal{C}$ is also carried out in the offline phase. In the online phase, the reduced system (5.4) is formed by loading the reduced operators and the CP factor matrices and solved using Matlab. We acknowledge that there are high-performance tools for tensor decomposition with various optimization methods for example [148], however, the primary focus of this work is the application of the tensor decomposition with ROM, hence we implement CP-ALS (5.11) and CP-ALS with quadratically-occurring factors (5.25) in Matlab for easy use and investigation with ROM. We use the campus cluster Delta and Argonne Leadership Computing Facility (ALCF) Polaris for the offline stage and a workstation with Intel Xeon E5-2620 CPU with two threads for the CP decomposition and solving the reduced system.

From the numerical investigation, we would like to address the following questions:

- Without sacrificing too much accuracy, is there any memory saving and speed-up with CPD-ROM?
- Does preserving the skew-symmetry property in the approximated tensor stabilize CPD-ROM?
- Does the advection tensor $\mathcal{C}$ have a low-rank structure, and how does it relate to the parameters such as the number of POD modes N, the Reynolds number Re, the spatial dimension d, the norm used to construct the POD basis?

The rest of this section is organized as follows: In Section 5.3.1, we compare the CPD-ROM with the G-ROM in four model problems, ranging from 2D periodic flow to 3D turbulent flows. We employ the H_0^1-based POD basis functions for both the G-ROM and CPD-ROM across our study, which is motivated by the low-rank structure identified with the H_0^1 norm found in Section 5.3.4. In Section 5.3.2, we investigate the performance of the CPD-ROM with the approximated full tensor and the approximated core tensor. In Section 5.3.3, we investigate if preserving the skew-symmetry for the approximated tensor yields better CPD-ROM. In Section 5.3.4, we investigate the G-ROM with singular value decomposition (SVD). In particular, we investigate the low-rank structure of the tensor under the L^2 and H_0^1 norms using the SVD. Additionally, we investigate the effectiveness of the low-rank approximation between the SVD and CPD and compare the performance of the CPD-ROM with the SVD-ROM, that is, the G-ROM with the singular value decomposition (SVD).

5.3.1 Performance Comparison Between the G-ROM and the CPD-ROM

In this section, we compare the performance of the CPD-ROM (Section 5.2.1) with the G-ROM (5.4) and the FOM across various model problems: 2D flow past a cylinder, 2D

lid-driven cavity, 3D lid-driven cavity, and 3D minimal flow unit. The comparison is based on the accuracy of the quantities of interest (QOIs).

The compression ratio (CR) of the ALS (5.11) and ALS-quad (5.25) are defined based on the ratio of sizes of the original tensor and the size of the CPD models:

$$\mathrm{CR}_{\mathrm{ALS}} = \frac{N^3}{3NR} = \frac{N^2}{3R}, \quad \mathrm{CR}_{\mathrm{ALS\text{-}quad}} = \frac{N^3}{\frac{3}{2}NR} = \frac{2N^2}{3R}. \tag{5.31}$$

A factor of 2 emerges in $\mathrm{CR}_{\mathrm{ALS\text{-}quad}}$ due to the presence of redundant columns in the factor matrix $A^{(2)}$ and the skew-symmetric structure in $A^{(1)}$ and $A^{(3)}$ (Section 5.2.3). These compression ratios ignore the skew-symmetry of the original tensor, since its is difficult to exploit in storage or application of the operator (tensor contraction). Notice that the cost reduction in tensor contraction with ALS-quad is the same as with ALS (i.e., $N^2/3R$), as it still involves three matrix-vector multiplications (5.15)

2D flow past a cylinder Our first example is the 2D flow past a cylinder at the Reynolds number $\mathrm{Re} = 100$, which is a canonical test case for ROMs due to its robust and low-dimensional attractor, manifesting as a von Karman vortex street for $\mathrm{Re} = \mathrm{UD}/\nu > 34.37$ [74]. The computational domain is $\Omega = [-2.5 : 17]D \times [-5 : 5]D$, with the unit-diameter cylinder centered at $[0, 0]$.

The reduced basis functions $\{\boldsymbol{\varphi}_i\}_{i=1}^N$ for the G-ROM (5.3) are constructed by applying POD procedure to $K = 100$ snapshots collected over 100 convective time units (D/U), after von Karman vortex street is developed. The zeroth mode $\boldsymbol{\varphi}_0$ is set to be the mean velocity field of the snapshot collection time window. Already with $N = 20$ POD basis functions, the reduced space contains more than 99% of the total energy of the snapshots. The initial condition for the G-ROM and the CPD-ROM is obtained by projecting the lifted snapshot at $t = 500$ (in convective time units) onto the reduced space.

We test the CPD-ROM in the reconstructive regime, ie., the same time interval in which the snapshots were collected. The total drag on the cylinder is defined as:

$$\boldsymbol{F}_D = \oint_\Gamma (-\nu \nabla \boldsymbol{u} + p) d\boldsymbol{A}, \tag{5.32}$$

where Γ is the surface of the cylinder. We consider the total drag in the x-direction as the QOI. We refer to [16] for computing the pressure drag in the ROM without solving the pressure solution.

Fig. 5.2a displays the relative error in the mean drag and its standard deviation in CPD-ROM with respect to both the FOM and the G-ROM as a function of the CP rank R.

Additionally, it includes the relative error of the G-ROM's results with respect to the FOM for comprehensive comparison. We found the error with respect to the G-ROM decreases as R increases. With $R \geq 200$, the error in both the mean and standard deviation is less than 10^{-8}, indicating the convergence of CPD-ROM to G-ROM. With respect to the FOM, the error decreases initially as R increases and eventually reach to the same level of accuracy as G-ROM (blue dashed line). This is expected because the G-ROM serves as the reference model for the CPD-ROM. Fig. 5.2b shows the total drag history in CPD-ROM at $R = 10$

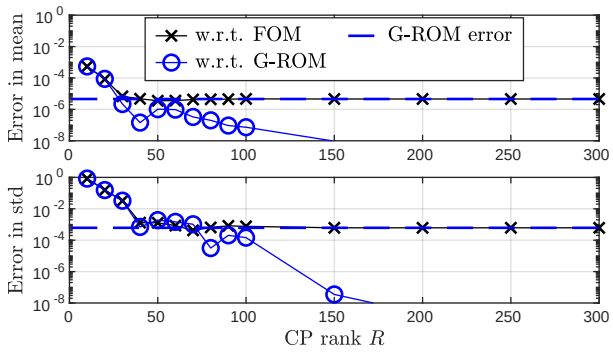

(a) Relative error in mean drag and its standard deviation

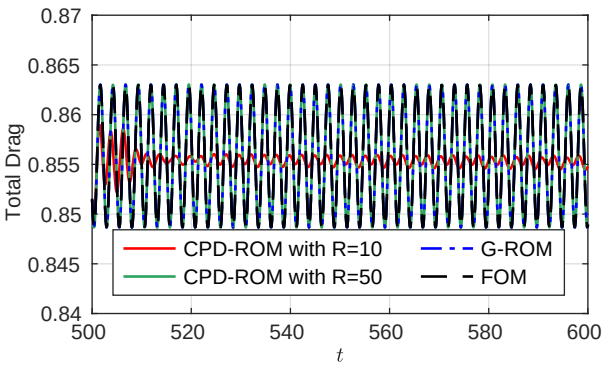

(b) Drag history

Figure 5.2: 2D flow past a cylinder at Re = 100: (a) Relative error in the mean drag and its standard deviation as a function of the CP rank R. The error is presented with respect to both the FOM and G-ROM for each quantity. The relative error of the G-ROM's results with respect to the FOM is also illustrated as a blue dashed line. (b) The total drag history of CPD-ROM at $R = 10$ and $R = 50$, along with the results of the FOM and the G-ROM. The number of POD modes, N, is set to 20 for both the G-ROM and the CPD-ROM.

and $R = 50$ alongside G-ROM and FOM results. With $R = 10$, despite the inaccuracy in the approximated tensor, the total drag in CPD-ROM does not blow up and eventually reaches a constant value. This behavior could be attributed to the model problem having a robust and low-dimensional attractor. With $R = 50$, the total drag in CPD-ROM shows good agreement with the results of both FOM and G-ROM.

2D lid-driven cavity Our next example is the 2D lid-driven cavity (LDC) problem at Re $= 15,000$, which is a more challenging model problem compared to the 2D flow past a cylinder. As demonstrated in [17], the problem requires $N \geq 60$ POD modes for G-ROM to accurately reconstruct the solutions and QOIs. A detailed description on how the FOM is set up for this problem can be found in our previous work [26].

The reduced basis functions $\{\boldsymbol{\varphi}_i\}_{i=1}^{N}$ are constructed by applying POD to $K = 2000$ snapshots in the statistically steady state region in the time interval of [6000.4, 6200] with

sampling time $\Delta t_s = 0.1$. The zeroth mode $\boldsymbol{\varphi}_0$ is set to the mean velocity field of the snapshot collection time window. The initial condition for the G-ROM and the CPD-ROM is obtained by projecting the lifted snapshot at $t = 6000$ (in convective time units) onto the reduced space.

We test both G-ROM and CPD-ROM in the reproduction regime with $N = 200$ for both models. The choice of $N = 200$ ensures that the G-ROM is accurate compared to the FOM. In terms of the QOI, we consider the energy and the energy of the fluctuated velocity:

$$\mathrm{E}(t) = \frac{1}{2}\int_\Omega \|\boldsymbol{u}(x,t)\|_2^2, \quad \mathrm{E}(t)_{\mathrm{fluc}} = \frac{1}{2}\int_\Omega \|\boldsymbol{u}(x,t) - \langle \boldsymbol{u}\rangle(x)\|_2^2, \tag{5.33}$$

where $\|\cdot\|_2$ is the Euclidean norm[6].

Fig. 5.3a displays the relative error in the mean energy and its standard deviation in CPD-ROM with respect to both the FOM and the G-ROM as a function of the CP rank R. Additionally, it includes the relative error of the G-ROM's results with respect to the FOM. Unlike the results of the 2D flow past a cylinder, where the error with respect to G-ROM decreases to machine precision as R increases, we found the error decreases as R increases and starts fluctuating at the level of G-ROM's accuracy after $R \geq 80$. It is not surprising to find this because the model problem is much more chaotic than the 2D flow past a cylinder, and any approximation error could lead to a different solution trajectory. On the other hand, we found the error with respect to the FOM decreases as R increases and eventually reaches the same level of accuracy as G-ROM, as in the case of 2D flow past a cylinder. In fact, we found that the error in the mean of CPD-ROM is smaller than the error of G-ROM with $R \geq 250$.

We further plot the energy history in CPD-ROM with $R = 80$ and $R = 400$, which both have errors less than 0.1% in mean and about 10% in the standard deviation in Fig. 5.3b, along with the results of the FOM and the G-ROM. In both R values, we found the energy in CPD-ROM initially agrees with the G-ROM and departs to a different trajectory at $t \approx 6010$. This is expected due to the approximation error made in the CP decomposition.

Fig. 5.3c displays the relative error in the mean energy of the fluctuated velocity and its standard deviation in CPD-ROM with respect to both the FOM and the G-ROM as a function of the CP rank R. Further, it includes the relative error of the G-ROM's results with respect to the FOM. We found a similar error behavior as in the energy results but with higher errors in general. This is expected because the energy of the fluctuated velocity

[6] $\mathrm{E}(t)_{\mathrm{fluc}}$ in (5.33) is usually referred as the turbulent kinetic energy however, for 2D and 3D low Reynolds number flow, there is no turbulence, therefore we refer (5.33) as the energy of the fluctuated velocity for not confusing the reader.

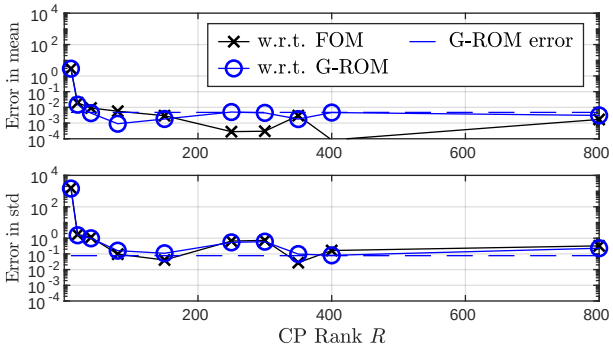

(a) Relative error in mean energy and its standard deviation

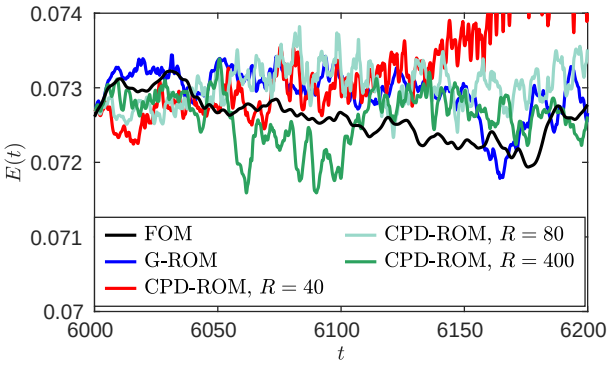

(b) Energy history

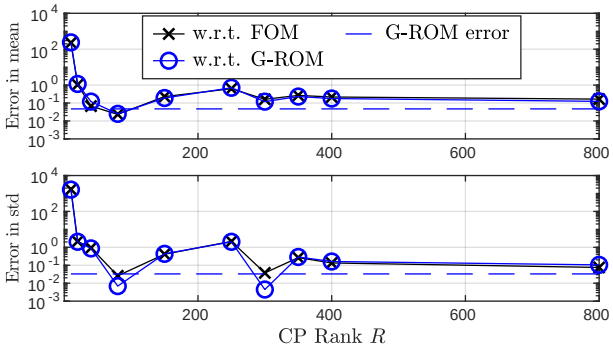

(c) Relative error in mean $\mathrm{E}_{\mathrm{fluc}}$ and its standard deviation

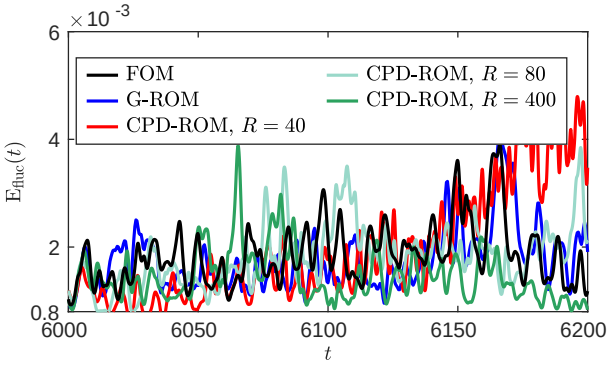

(d) $\mathrm{E}_{\mathrm{fluc}}$ history

Figure 5.3: 2D lid-driven cavity at Re = 15000: Relative error in both (a) mean and standard deviation of the energy and (c) mean and the standard deviation of the energy of the fluctuated velocity as a function of the CP rank R. The error is presented with respect to both the FOM and G-ROM for each quantity. The relative error of the G-ROM's results with respect to the FOM is also illustrated as a blue dashed line; The (b) energy and (d) energy of the fluctuated velocity history of CPD-ROM at $R = 80$ and 400, along with the results of the FOM and the G-ROM. The number of POD modes, N, is set to 200 for both the G-ROM and the CPD-ROM.

is a much harder QOI compared to the energy. Moreover, we also found that the error with respect to the FOM in the CPD-ROM is, in general, larger than the G-ROM's error. Moreover, we are aware of a sudden increase in the error when increasing R from 80 to 150, which could be due to the randomization of the CP decomposition.

We plot the energy of the fluctuated velocity history in CPD-ROM with $R = 80$ and $R = 400$ in Fig. 5.3b, along with the results of the FOM and the G-ROM. Again, in both R values, we found the energy in CPD-ROM initially agree with the G-ROM and depart to a different trajectory at $t \approx 6010$.

In terms of the energy, CPD-ROM with $R = 80$ is sufficient to attain the same level of accuracy as in the G-ROM for the mean and the standard deviation. The compression ratio is CR = 333.3 and the cost of evaluating the nonlinear term is reduced by a factor of 166.6. In terms of the energy of the fluctuated velocity, CPD-ROM with $R = 300$ can attain the same level of accuracy as in the G-ROM for the standard deviation and a factor of 4 in the error of the mean. The compression ratio is CR = 88.9 and the cost of evaluating the nonlinear term is reduced by a factor of 44.4.

Finally, for $200,000$ time steps, the total solve time of the G-ROM with $N = 200$ is about 1167 (secs), and the tensor contraction kernel occupies about 86% of the total solve time, whereas the total solve time of the CPD-ROM with $R = 300$ is about 101 (secs), and the CP kernel (5.15) occupies only 15% of the total solve time. With a factor of 44.4 in reduction, we should observe a factor of 6.25 speedup in the total solve time. In fact, from the numbers reported here, we get a factor of 11.5 speedup. We note this is due to the favorable cache effect. The machine used to run the G-ROM and CPD-ROM has a L1 cache of size 0.384 megabyte (MB), a L2 cache of size 3 MB and a L3 cache shared by all cores of size 30 MB. With $N = 200$, the advection tensor $\mathcal{C}$ is of size 210 MB, whereas the total size of the factor matrices is 4.5 MB with $R = 300$. The additional speedup is because, in the case of CPD-ROM, there is sufficient space in the L3 cache to store the ROM operators. We also note that the numbers reported here are based on the results running with one computing thread in Matlab. We choose to apply this constraint because Matlab optimizes the G-ROM when N is large due to the large tensor, whereas no optimization is used for the CPD-ROM.

3D lid-driven cavity (LDC) We next consider the non-regularized 3D lid-driven cavity (LDC) problem as our first 3D example, which is a much more challenging model problem for the ROM compared to the 2D problems. We consider two Reynolds number Re = 3200 and Re = $10,000$. Following [16], for both Re, the FOM mesh consists of a tensor-product array of $E = 16^3$ elements with a Chebyshev distribution with polynomial order 7 (2 million degrees of freedom).

For Re = 3200, the reduced basis functions $\{\boldsymbol{\varphi}_i\}_{i=1}^N$ are constructed with POD using $K = 4000$ snapshots in the statistically steady state region in the time interval of $[2475.125,\ 2975]$ with sampling time $\Delta t_s = 0.125$. The zeroth mode $\boldsymbol{\varphi}_0$ is set to the mean velocity field of the snapshot collection time window. The initial condition for the G-ROM and the CPD-ROM is obtained by projecting the lifted snapshot at $t = 2475$ onto the POD space.

We test the G-ROM and CPD-ROM in the predictive regime, that is, a larger time interval compared to the interval snapshots are collected. We consider $N = 300$ for both models and the choice of the N value ensures that the G-ROM is accurate compared to the FOM. We

consider the energy and the energy of the fluctuated velocity, defined in (5.33), as the QOIs.

Fig. 5.4a displays the relative error in the mean energy and its standard deviation of CPD-ROM with respect to both the FOM and the G-ROM as a function of the CP rank R. In addition, it includes the relative error of the G-ROM's results with respect to the FOM. We observed the error with respect to both the FOM and the G-ROM decreases as R

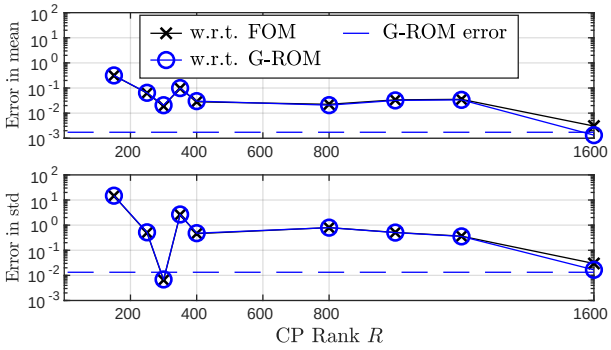

(a) Relative error in mean energy and its standard deviation

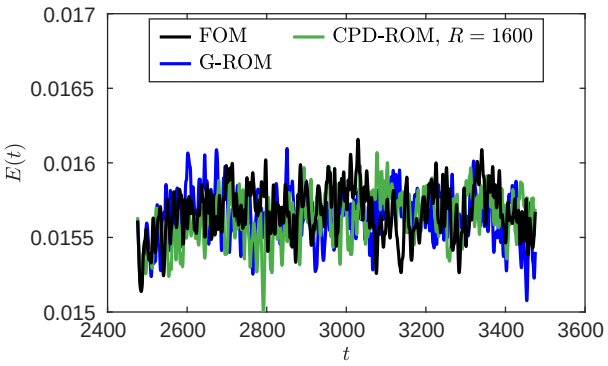

(b) Energy history

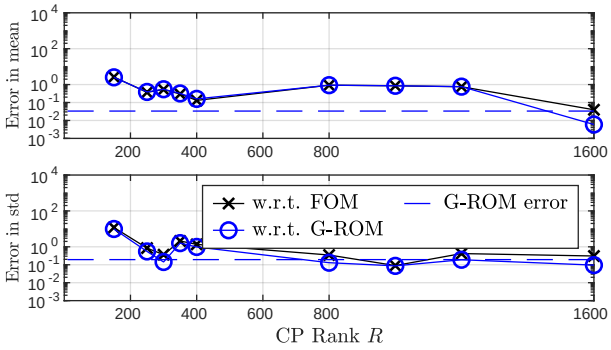

(c) Relative error in mean E_{fluc} and its standard deviation

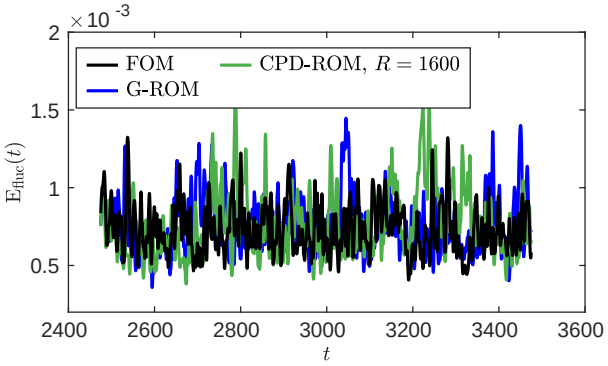

(d) E_{fluc} history

Figure 5.4: 3D lid-driven cavity at Re = 3200: Relative error in both (a) mean and standard deviation of the energy and (c) mean and the standard deviation of the energy of the fluctuated velocity as a function of the CP rank R. The error is presented with respect to both the FOM and G-ROM for each quantity. The relative error of the G-ROM's results with respect to the FOM is also illustrated as a blue dashed line; The (b) energy and (d) energy of the fluctuated velocity history of CPD-ROM at $R = 1600$, along with the results of the FOM and the G-ROM. The number of POD modes, N, is set to 300 for both the G-ROM and the CPD-ROM.

increases. Specifically, CPD-ROM with $R \geq 150$ is able to predict the mean with an error of 10%. In order to accurately predict the standard deviation, $R = 1600$ is required. The energy history of CPD-ROM with $R = 1600$ is shown in Fig. 5.4b, along with the results of

the FOM and the G-ROM. The energy history of CPD-ROM is similar to the results of the FOM and the G-ROM.

Fig. 5.4c displays the relative error in the mean energy of the fluctuated velocity and its standard deviation in CPD-ROM with respect to both the FOM and the G-ROM as a function of the CP rank R. Compared to the results of energy, the error in E_{fluc} is in general larger and to achieve the same level of accuracy as the G-ROM, $R \geq 1600$ is necessary. We plot the energy of the fluctuated velocity history of CPD-ROM with $R = 1600$ in Fig. 5.4d, along with the results of the FOM and the G-ROM. The results of CPD-ROM is similar to the results of the FOM and the G-ROM.

In summary, CPD-ROM with $R = 1600$ is able to accurately predict the statistics of the energy and energy of the fluctuated velocity. With $N = 300$ and $R = 1600$, the compression ratio is CR $= 37.5$ and the cost is reduced by a factor of 18.75.

Finally, for $1,000,000$ time steps, the total solve time of the G-ROM with $N = 300$ is about 16538 (secs) and the tensor contraction kernel occupies about 95.8% of the total solve time whereas, the total solve time of the CPD-ROM with $R = 1600$ is about 1280 (secs) and the CP kernel (5.15) occupies only 57.6% of the total solve time. With a factor of 18.75 in reduction, we should observe a factor of 10.7 speedup in the total solve time. In fact, from the numbers reported here, we get a factor of 13 speedup because of the cache effect.

For Re $= 10,000$, the reduced basis functions $\{\boldsymbol{\varphi}_i\}_{i=1}^N$ are constructed with POD using $K = 4000$ snapshots in the statistically steady state region in the time interval of $[2725.125,\ 3225]$ with sampling time $\Delta t_s = 0.125$. The zeroth mode $\boldsymbol{\varphi}_0$ is set to the mean velocity field of the snapshot collection time window. The initial condition for the G-ROM and the CPD-ROM is obtained by projecting the lifted snapshot at $t = 2725$ onto the POD space.

We test the G-ROM and CPD-ROM in the predictive regime, that is, a larger time interval compared to the interval snapshots are collected. We consider $N = 400$ for both models and the choice of the N value ensures that the G-ROM is accurate compared to the FOM. We consider the energy and the energy of the fluctuated velocity, defined in (5.33), as the QOIs.

Fig. 5.5a displays the relative error in the mean energy and its standard deviation in CPD-ROM with respect to both the FOM and the G-ROM as a function of the CP rank R. In addition, it includes the relative error of the G-ROM's results with respect to the FOM. We found the error with respect to both the FOM and the G-ROM decreases as R increases. In addition, we find at least $R \geq 1600$ is required for CPD-ROM to predict the mean with an error of 10% and in order to predict a reasonable standard deviation, $R = 3200$ is required. We plot the energy history in CPD-ROM with $R = 1600$ and $R = 3200$ in Fig. 5.5b, along with the results of FOM and G-ROM. We found the result with $R = 3200$ is similar to the results of FOM and G-ROM whereas the result with $R = 1600$ has much larger fluctuation.

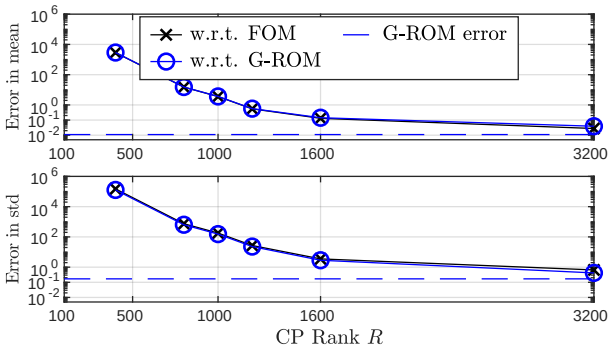

(a) Relative error in mean energy and its standard deviation

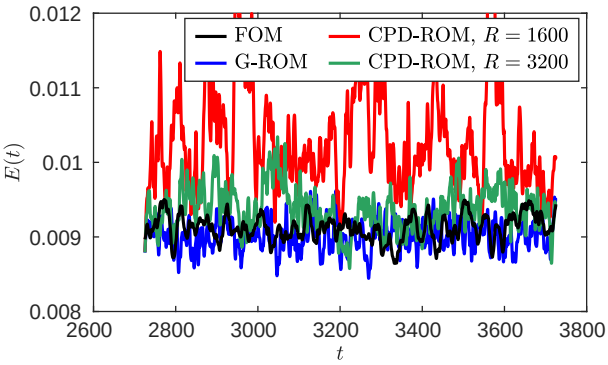

(b) Energy history

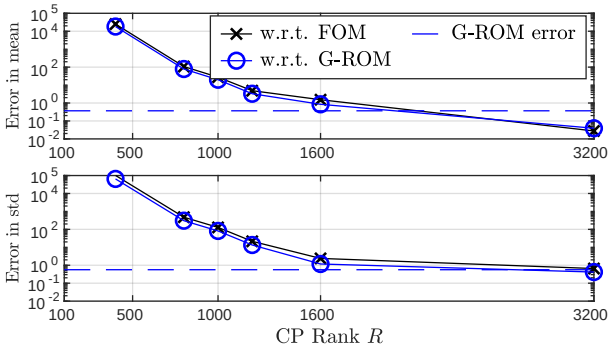

(c) Relative error in mean $\mathrm{E}_{\mathrm{fluc}}$ and its standard deviation

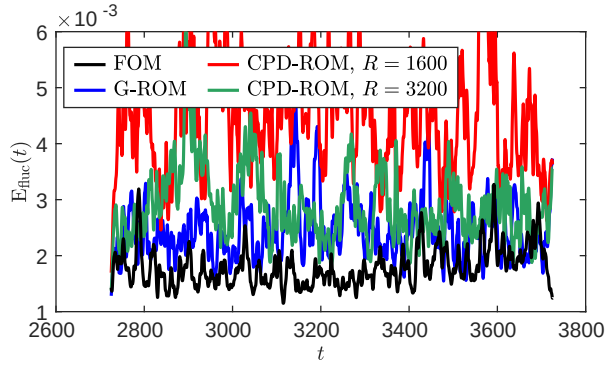

(d) $\mathrm{E}_{\mathrm{fluc}}$ history

Figure 5.5: 3D lid-driven cavity at $\mathrm{Re} = 10,000$: Relative error in both (a) mean and standard deviation of the energy and (c) mean and the standard deviation of the energy of the fluctuated velocity as a function of the CP rank R. The error is presented with respect to both the FOM and G-ROM for each quantity. The relative error of the G-ROM's results with respect to the FOM is also illustrated as a blue dashed line; The (b) energy and (d) energy of the fluctuated velocity history of CPD-ROM at $R = 3200$, along with the results of the FOM and the G-ROM. The number of POD modes, N, is set to 400 for both the G-ROM and the CPD-ROM.

Fig. 5.5c displays the relative error in the mean energy of the fluctuated velocity and its standard deviation in CPD-ROM with respect to both the FOM and the G-ROM as a function of the CP rank R. We found a similar error behavior as in the results of energy but with larger relative errors of the G-ROM in both quantities. In fact, with $R = 3200$, CPD-ROM is able to predict the standard deviation with same level of accuracy as of G-ROM and predict the mean more accurately than the G-ROM.

We plot the energy of the fluctuated velocity history in CPD-ROM with $R = 1600$ and 3200 in Fig. 5.5d, along with the FOM and G-ROM results. The results with $R = 3200$ is

similar to those of the G-ROM and the FOM while the results with $R = 1600$ has larger fluctuation.

In summary, in order to predict the mean energy with an error less than 10%, $R = 1600$ is required for the CPD-ROM. For the mean energy of the fluctuated velocity, a larger CP rank, $R = 3200$, is required. In order to predict the standard deviation with an error less than 10%, $R > 3200$ is required. With $N = 400$ and $R = 3200$, the compression ratio is CR = 33.3 and the cost is reduced by a factor of 16.7. Finally, for $1,000,000$ time steps, the total solve time of the G-ROM with $N = 400$ is about 43819 (secs) and the tensor contraction kernel occupies about 97% of the total solve time whereas, the total solve time of the CPD-ROM with $R = 3200$ is about 4269 (secs) and the CP kernel (5.15) occupies only 64.8% of the total solve time. We get a factor of 10.3 speedup in the total solve time which is close to the theoretical speedup 11.4 with a factor of 16.7 in reduction.

The minimal flow unit (MFU) Our next 3D example is the minimal flow unit (MFU), which presents some strong turbulent features while maintaining simplified flow dynamics, resulting in significantly lower computational costs compared to a full channel flow simulation [156]. Following the setup in [156], we consider two Reynolds numbers Re. For Re = 3000, the streamwise (i.e, the x-direction) and spanwise (i.e, the z-direction) lengths of the channel are set to πh and $0.3\pi h$, respectively. For Re = 5000, the streamwise and spanwise lengths of the channel are set to $0.6\pi h$ and $0.18\pi h$, respectively. The channel half-height is set to $h = 1$ for both Re. For both Re, the FOM mesh consists of an array of $8 \times 18 \times 4$ elements in the $x \times y \times z$ directions), of order $q = 9$, for a total of $\mathcal{N} \approx 420$ thousands grid points.

For both Re = 3000 and Re = 5000, the reduced basis functions $\{\boldsymbol{\varphi}_i\}_{i=1}^{N}$ are constructed with POD using $K = 4000$ snapshots in the statistically steady state region in the time interval of $[3000.125,\ 3500]$ with sampling time $\Delta t_s = 0.125$. The zeroth mode $\boldsymbol{\varphi}_0$ is set to the mean velocity field of the snapshot collection time window. The initial condition for the G-ROM and the CPD-ROM is obtained by projecting the lifted snapshot at $t = 3000$ onto the POD space. The G-ROM and CPD-ROM are tested in the predictive regime, that is, a larger time interval than the interval snapshots are collected. $N = 400$ is considered for both models, and the energy and the energy of the fluctuated velocity, defined in (5.33), are considered as the QOIs.

The results of Re = 3000 are shown in Fig. 5.6. The relative error in the mean energy and its standard deviation in CPD-ROM with respect to both the FOM and the G-ROM as a function of the CP rank R is shown in Fig. 5.6a. We find at least $R \geq 1000$ is required for the CPD-ROM to predict the mean with an error of 10% and in order to predict a reasonable standard deviation, $R = 3200$ is required. We also find that both errors with respect to the

FOM and the G-ROM decreases as R increases but starts fluctuating around the level of G-ROM's accuracy when $R \geq 3200$. The energy history in CPD-ROM with $R = 3200$ is shown in Fig. 5.6b, along with the results of the FOM and the G-ROM. We found that both the CPD-ROM and the G-ROM yield similar results compared to the FOM. The relative

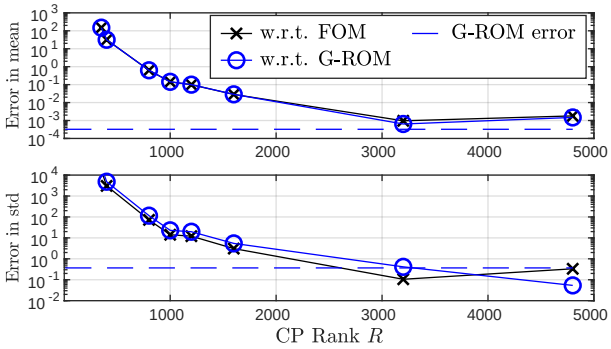

(a) Relative error in mean energy and its standard deviation

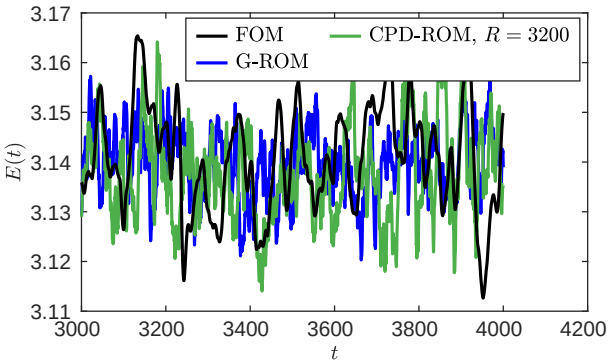

(b) Energy history

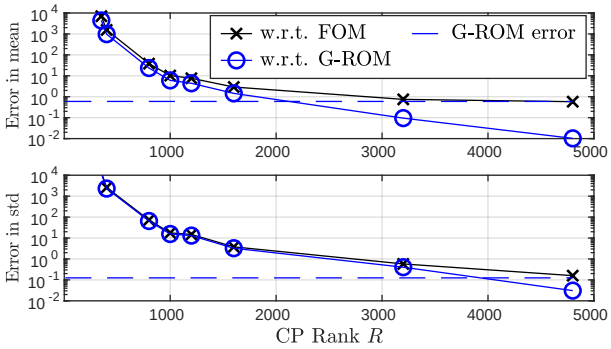

(c) Relative error in mean E_{fluc} and its standard deviation

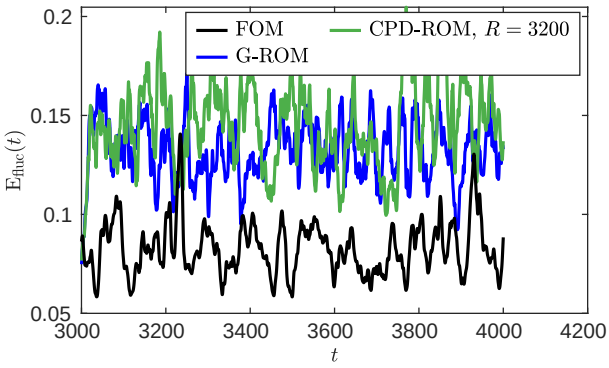

(d) E_{fluc} history

Figure 5.6: MFU at Re = 3000: Relative error in both (a) mean and standard deviation of the energy and (c) mean and the standard deviation of the energy of the fluctuated velocity as a function of the CP rank R. The error is presented with respect to both the FOM and G-ROM for each quantity. The relative error of the G-ROM's results with respect to the FOM is also illustrated as a blue dashed line; The (b) energy and (d) energy of the fluctuated velocity history of CPD-ROM at $R = 3200$, along with the results of the FOM and the G-ROM. The number of POD modes, N, is set to 400 for both the G-ROM and the CPD-ROM.

error in the mean energy of the fluctuated velocity and its standard deviation in CPD-ROM with respect to both the FOM and the G-ROM as a function of the CP rank R in Fig. 5.6c. Again, we observe both the error with respect to the FOM and the G-ROM decreases as R increases and eventually reaches the level of G-ROM's accuracy. However, the error in the

mean is large because the G-ROM itself has an error of 70% in the mean. To further improve the results, $N > 400$ is required for the G-ROM. The E_{fluc} history in the CPD-ROM with $R = 3200$ is shown in Fig. 5.6d, along with the FOM and the G-ROM results. We find that the results of $R = 3200$ are quite similar to the results of the G-ROM; however, both are inaccurate compared to the FOM.

In summary, CPD-ROM with $R = 3200$ can accurately predict the mean energy and its standard deviation. In terms of the energy of the fluctuated velocity, the error in the mean and the standard deviation is large regardless of the R because the G-ROM is inaccurate. To resolve this, a larger N value is required for the G-ROM.

With $N = 400$ and $R = 3200$, the compression ratio is CR $= 33.3$ and the cost is reduced by a factor of 16.7. Finally, for $400,000$ time steps, the total solve time of the G-ROM with $N = 400$ is about 16553 (secs) and the tensor contraction kernel occupies about 97.1% of the total solve time whereas, the total solve time of the CPD-ROM with $R = 3200$ is about 1456 (secs) and the CP kernel (5.15) occupies only 39.6% of the total solve time. We get a factor of 11.4 speedup in the total solve time which agrees with the theoretical speedup with a factor of 16.7 in reduction.

Next, we discuss the results of Re $= 5000$ shown in Fig. 5.7. The relative error in the mean energy and its standard deviation in CPD-ROM with respect to both the FOM and the G-ROM as a function of the CP rank R is shown in Fig. 5.7a. We find that at least $R \geq 1200$ is required for the CPD-ROM to predict the mean with an error of 10% and in order to predict a reasonable standard deviation, $R = 3000$ is required. We also find that the error with respect to the G-ROM decreases as R increases, whereas the error with respect to the FOM starts fluctuating around the level of G-ROM's accuracy when $R \geq 2000$. The energy history in CPD-ROM with $R = 2000$ and $R = 4000$ is shown in Fig. 5.7b, along with the results of the FOM and the G-ROM. We could see that the results of $R = 4000$ is quite similar to the results of the FOM and the G-ROM, whereas the results of $R = 2000$ has a larger fluctuation.

The relative error in the mean energy of the fluctuated velocity and its standard deviation in CPD-ROM with respect to both the FOM and the G-ROM as a function of the CP rank R in Fig. 5.7c. Again we observe that both the error with respect to the FOM and the G-ROM decreases as R increases and eventually reach to the level of G-ROM's accuracy. However, the errors are large because the G-ROM itself is not accurate, with an error of 70% and 21% in the mean and the standard deviation. To further improve the results, $N > 400$ is required for the G-ROM. The E_{fluc} history in the CPD-ROM with $R = 2000$ and $R = 4000$ are shown in Fig. 5.7d, along with the results of the FOM and the G-ROM. We find that the results of $R = 2000$ are not accurate and the results of $R = 4000$ are quite similar to the results of the

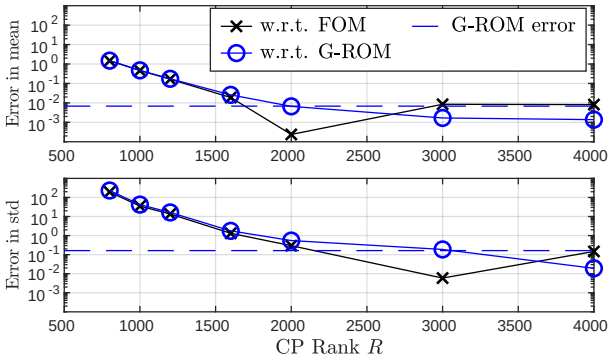

(a) Relative error in mean energy and its standard deviation

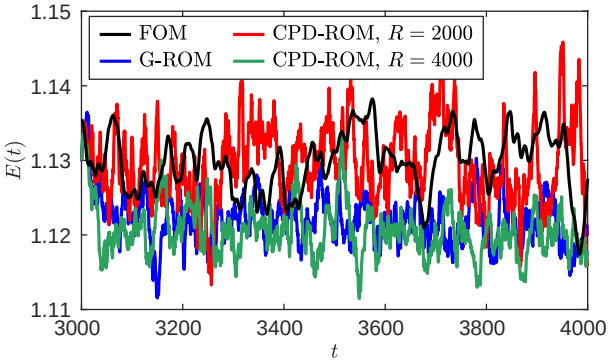

(b) Energy history

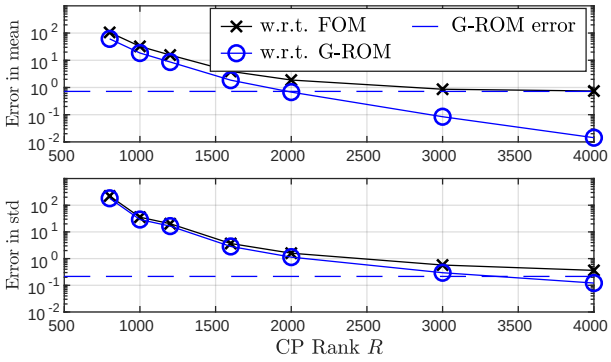

(c) Relative error in mean $\mathrm{E}_{\mathrm{fluc}}$ and its standard deviation

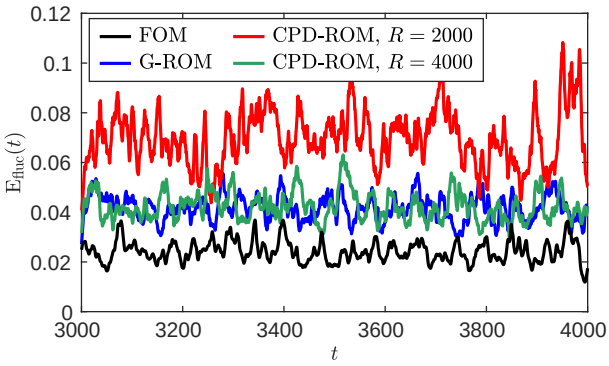

(d) $\mathrm{E}_{\mathrm{fluc}}$ history

Figure 5.7: MFU at Re = 5000: Relative error in both (a) mean and standard deviation of the energy and (c) mean and the standard deviation of the energy of the fluctuated velocity as a function of the CP rank R. The error is presented with respect to both the FOM and G-ROM for each quantity. The relative error of the G-ROM's results with respect to the FOM is also illustrated as a blue dashed line; The (b) energy and (d) energy of the fluctuated velocity history of CPD-ROM at $R = 4000$, along with the results of the FOM and the G-ROM. The number of POD modes, N, is set to 400 for both the G-ROM and the CPD-ROM.

G-ROM however, both are inaccurate compared to the FOM.

In summary, CPD-ROM with $R \geq 3000$ is able to predict the mean energy and its standard deviation with error less than 10%. With $R = 3000$, the compression ratio is of 26.6 and the cost is reduced by a factor of 13.3.

For the energy of the fluctuated velocity, despite CPD-ROM is able to reach to the same level of accuracy as G-ROM with $R = 4000$, the errors with respect to the FOM are large ($> 20\%$). This is due to the inaccuracy in G-ROM and to resolve this issue, one has to consider a larger N.

With $N = 400$ and $R = 3000$, the compression ratio is CR $= 35.5$ and the cost is reduced by a factor of 17.7. Finally, for $400,000$ time steps, the total solve time of the G-ROM with $N = 400$ is about 17470 (secs) and the tensor contraction kernel occupies about 97% of the total solve time whereas, the total solve time of the CPD-ROM with $R = 3000$ is about 1559 (secs) and the CP kernel (5.15) occupies only 64.1% of the total solve time. We get a factor of 11.2 speedup in the total solve time which is close to the theoretical value 11.8 with a factor of 17.7 in reduction.

5.3.2 Performance Investigation of the CPD-ROM with the Approximated Full Tensor and the Approximated Core Tensor

In this section, we investigate the performance of the CPD-ROM with the approximated full tensor (CPD-ROM-Full) and the approximated core tensor (CPD-ROM-Core). Recall the definition of the advection tensor:

$$\mathcal{C}_{ikj} = \int_{\Omega} \boldsymbol{\varphi}_i \cdot (\boldsymbol{\varphi}_k \cdot \nabla)\boldsymbol{\varphi}_j \, dV. \tag{5.34}$$

The full tensor includes the contribution from the zeroth mode $\boldsymbol{\varphi}_0$ and is defined as $\mathcal{C}_{ikj}$ with $i = 1, \ldots, N$ and $j, k = 0, \ldots, N$ whereas the core tensor does not have the zeroth mode contribution and is defined as $\mathcal{C}_{ikj}$ with $i, j, k = 1, \ldots, N$.

Applying the CP decomposition to either the full tensor or the core tensor is valid. However, we expect CPD-ROM-Core outperforms the CPD-ROM-Full, because the zeroth mode contributions, which are the C_1 and C_2 matrices defined in (5.6), remains exact. For fair comparison, we consider ALS for both tensors.

Fig. 5.8a displays the energy history (5.33) of the CPD-ROM-Full and the CPD-ROM-Core at $R = 350$ along with the results of FOM and the G-ROM. We found with $R = 350$, the CPD-ROM-Core is able to reproduce the energy history with relative errors (with respect to the FOM) less than 0.1% in the mean and $\approx 27\%$ in the standard deviation. On the other hand, the CPD-ROM-Full is not stable and its solution blows up after $t > 6030$. Despite we found a significant performance difference between the CPD-ROM-Core and the CPD-ROM-Full with same rank R, the relative residual of the approximated tensor is similar in both case.

Fig. 5.8b displays the energy of the fluctuated velocity $\mathrm{E}_{\mathrm{fluc}}$ history (5.33) of the CPD-ROM-Full and the CPD-ROM-Core at $R = 800$ along with the results of FOM and the G-ROM. $\mathrm{E}_{\mathrm{fluc}}$ is in general a much harder QOI compared to the energy, and we find $R = 800$ is necessary for the CPD-ROM-Core to be accurate. We find CPD-ROM-Core is much

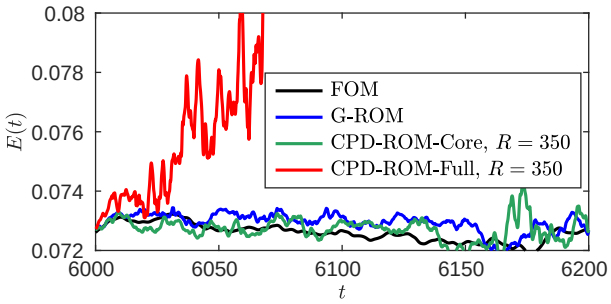

(a) Energy history

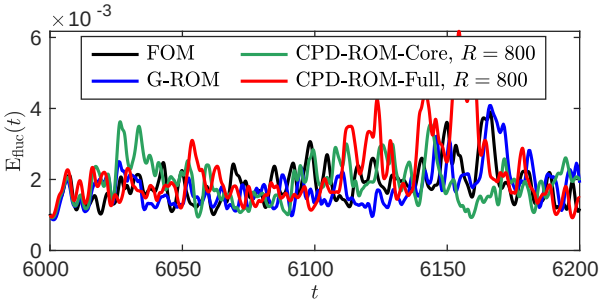

(b) E_{fluc} history

Figure 5.8: 2D lid-driven cavity at Re = 15,000: Comparison of (a) the energy history and (b) the energy of the fluctuated velocity E_{fluc} between the CPD-ROM-Full and the CPD-ROM-Core, along with the results of the FOM and the G-ROM. CPD-ROM-Full and CPD-ROM-Core are denoted as the CPD-ROM with the approximated full tensor and the approximated core tensor.

more accurate than the CPD-ROM-Full. Although the problem is chaotic, The E_{fluc} of CPD-ROM-Core behaves similarly compared to the FOM with relative errors of 4% in both the mean and the standard deviation. On the other hand, the E_{fluc} of CPD-ROM-Full overshoots in later time with relative errors of 16% in the mean and 71% in the standard deviation.

We next investigate the performance of the CPD-ROM-Full and CPD-ROM-Core in the 3D lid-driven cavity at Re = 3200. We test both modes in the reconstructive and the predictive regimes. Fig. 5.9a displays the E_{fluc} history of the CPD-ROM-Full and the CPD-ROM-Core

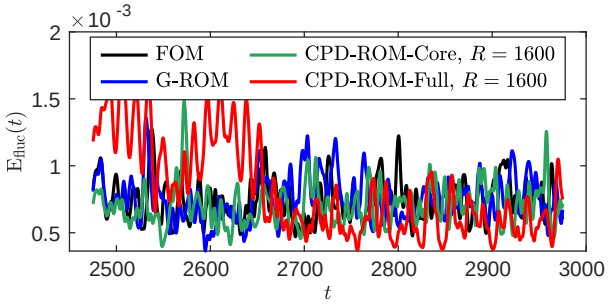

(a) Reconstructive regime

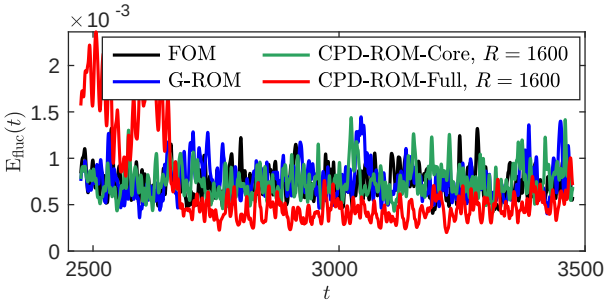

(b) Predictive regime

Figure 5.9: 3D lid-driven cavity at Re = 3200: Comparison of the energy of the fluctuated velocity in (a) the reconstructive and (b) the predictive regimes between the CPD-ROM-Full and the CPD-ROM-Core, along with the results of the FOM and the G-ROM. CPD-ROM-Full and CPD-ROM-Core are denoted as the CPD-ROM with the approximated full tensor and the approximated core tensor.

in the reconstructive regime at $R = 1600$ along with the results of FOM and the G-ROM.

$R = 1600$ is selected so that CPD-ROM-Core is accurate. We found that with $R = 1600$, CPD-ROM-Core is able to reproduce the history with an error (with respect to the FOM) of 5% in the mean and 0.4% in the standard deviation. On the other hand, despite the solution of the CPD-ROM-Full does not blow up, it is less accurate, with an error of 9% in the mean and 127% in the standard deviation.

Fig. 5.9b displays the E_{fluc} history of the CPD-ROM-Full and the CPD-ROM-Core in the predictive regime at $R = 1600$ along with the results of FOM and the G-ROM. We found CPD-ROM-Core is able to accurately predict the QOI with an error of 2% in the mean and 5% in the standard deviation. On the other hand, CPD-ROM-Full is not accurate, with an error of 10% in the mean and 200% in the standard deviation.

5.3.3 Performance Investigation of the CPD-ROM with Skew-Symmetry Preserved

In this section, we investigate if preserving the skew-symmetry for the approximated tensor $\widehat{\mathcal{C}}$ is beneficial for the performance of the CPD-ROM. We compare the performance of the CPD-ROM with skew-symmetry preserved (CPD-ROM-Skew) with the CPD-ROM without preserving the property (CPD-ROM) in the 2D and the 3D lid-driven cavity and the minimal flow unit (MFU). The selection of these model problems is deliberate, as they provide suitable boundary conditions for skew-symmetry (5.20). The ALS-skew, introduced in Section 5.2.3, is employed to ensure the skew-symmetry of the CP decomposition. Additionally, we enforce skew-symmetry in the tensor $\mathcal{C}$ itself, as discussed in Section 5.2.2.

Fig. 5.10 displays the results of the 2D lid-driven cavity at Re = 15000. In Fig. 5.10a, we compare the relative errors in the mean energy and its standard deviation between the CPD-ROM-Skew and the CPD-ROM as a function of CP rank R. In the results of CPD-ROM, the circle marker with a cross marker at several R values, indicate solution blow-up, resulting in NaN errors. We found CPD-ROM-Skew outperforms CPD-ROM for small R values, and as R increases, both behaves similarly. This behavior is expected because skew-symmetry addresses stability, not accuracy. This observation is consistent with the behavior of full-order models, where recovery of skew-symmetry (e.g., through dealiasing) is known to provide stability but does not, in general, improve accuracy. This point was discussed in numerous early works by Orszag and co-authors (e.g., [157, 158, 159]).

In Fig. 5.10b, we compare the energy history between the CPD-ROM-Skew and the CPD-ROM at $R = 80$ and $R = 400$, along with the results of the FOM and the G-ROM. At $R = 80$, we found the CPD-ROM is not stable leading to blowing-up solutions, whereas the CPD-ROM-Skew is stable and has errors of less than 1% in mean and about 10% in

the standard deviation. At $R = 400$, the approximated tensor is accurate enough so that CPD-ROM is stable.

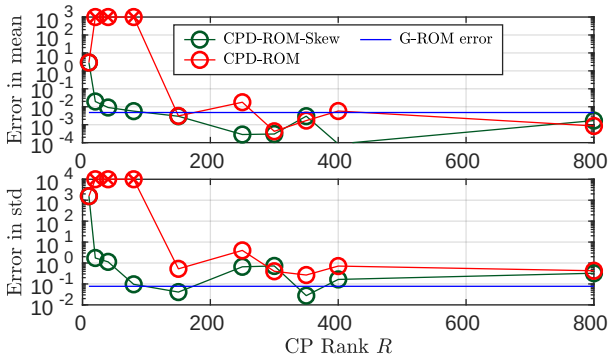

(a) Relative error in mean energy and its standard deviation

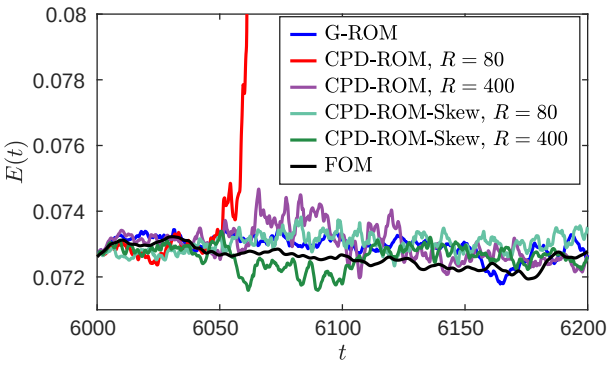

(b) Energy history

Figure 5.10: 2D lid-driven cavity at $\mathrm{Re} = 15,000$: (a) Comparison of the relative error in both the mean and the standard deviation of the energy between CPD-ROM-Skew and CPD-ROM as a function of the CP rank R. The error is presented with respect to the FOM. The relative error of the G-ROM's results with respect to the FOM is also illustrated as a blue dashed line. (b) Comparison of the energy history between CPD-ROM-Skew and CPD-ROM at $R = 80$ and $R = 400$, along with the results of the FOM and the G-ROM. CPD-ROM-Skew is denoted as CPD-ROM with skew-symmetry preserved. The circle marker with a cross marker at several R values, indicate solution blow-up, resulting in NaN errors.

Fig. 5.11 displays the results of the 3D lid-driven cavity. In Figs. 5.11a–5.11b, we compare the relative errors in the mean energy and its standard deviation between the CPD-ROM-Skew and the CPD-ROM as a function of CP rank R for $\mathrm{Re} = 3200$ and $\mathrm{Re} = 10,000$, respectively. The circle marker with a cross marker in the results of CPD-ROM, indicates solution blow-up, resulting in NaN errors. In both Re, we found CPD-ROM-Skew outperforms CPD-ROM for small R values, and as R increases, both behaves similarly. Moreover, with higher Reynolds number, CPD-ROM is unstable with all R values except $R = 3200$. Fig. 5.12 displays the results of the 3D MFU. In Figs. 5.12a–5.12b, we compare the relative errors in the mean energy and its standard deviation between the CPD-ROM-Skew and the CPD-ROM as a function of CP rank R for $\mathrm{Re} = 3000$ and $\mathrm{Re} = 5000$, respectively. The circle marker with a cross marker in the results of CPD-ROM, indicates solution blow-up, resulting in NaN errors. Again, we found CPD-ROM-Skew outperforms CPD-ROM for small R values, and as R increases, both behaves similarly. Moreover, higher Reynolds number requires larger R for the CPD-ROM to be stable.

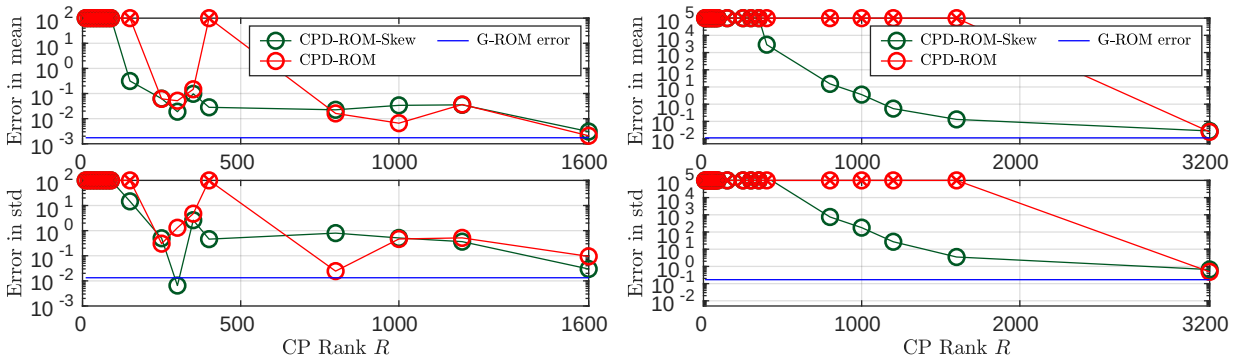

(a) Re = 3200 (b) Re = 10000

Figure 5.11: 3D lid-driven cavity: Comparison of the relative error in both the mean and the standard deviation of the energy between CPD-ROM-Skew and CPD-ROM as a function of the CP rank R for (a) Re = 3200 and (b) Re = 10,000. The error is presented with respect to the FOM. The relative error of the G-ROM's results with respect to the FOM is also illustrated as a blue dashed line. CPD-ROM-Skew is denoted as CPD-ROM with skew-symmetry preserved. The circle marker with a cross marker at several R values, indicate solution blow-up, resulting in NaN errors.

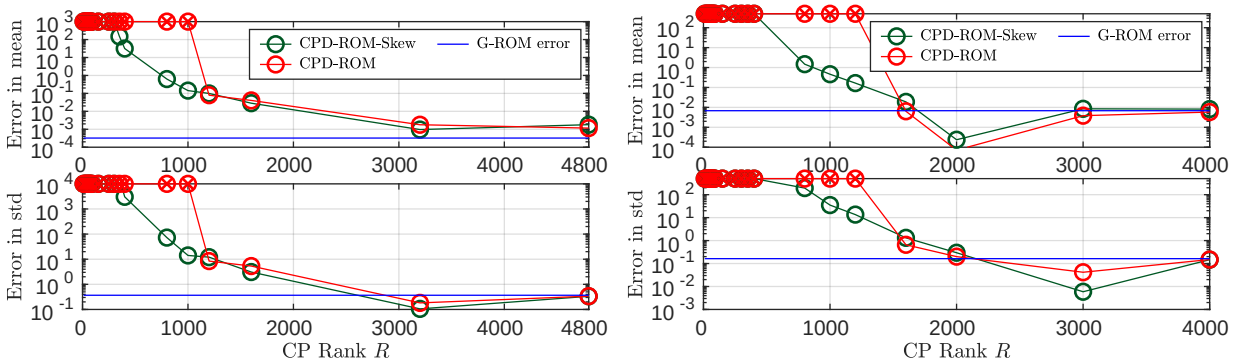

(a) Re = 3000 (b) Re = 5000

Figure 5.12: MFU: Comparison of the relative error in both the mean and the standard deviation of the energy between CPD-ROM-Skew and CPD-ROM as a function of the CP rank R for (a) Re = 3000 and (b) Re = 5000. The error is presented with respect to the FOM. The relative error of the G-ROM's results with respect to the FOM is also illustrated as a blue dashed line. CPD-ROM-Skew is denoted as CPD-ROM with skew-symmetry preserved. The circle marker with a cross marker at several R values, indicate solution blow-up, resulting in NaN errors.

5.3.4 Numerical Investigation of the G-ROM with the Singular Value Decomposition (SVD)

In this section, we explore the use of the singular value decomposition (SVD) in the G-ROM as an alternative low-rank approximation for the tensor $\mathcal{C}$. In Section 5.3.4, we investigate

the low-rank structure of the tensor using the SVD, specifically examining their behavior under the the L^2 and the H_0^1 norms. Additionally, we investigate the effectiveness of the low-rank approximation between the SVD and CPD by examining its relative residual in terms the compression ratio. Subsequently, in Section 5.3.4, we compare the performance of the SVD-ROM with the CPD-ROM.

Low-rank structure ablation In the case of the SVD, we investigate the behavior of the singular values of $C_{(1)}$, $C_{(2)}$ and $C_{(3)}$, representing the mode-1, mode-2 and mode-3 matricized versions of the tensor $\mathcal{C}$. Note that each row of $C_{(3)}$ preserves the skew-symmetric property, unlike $C_{(1)}$ and $C_{(2)}$. For comparison purpose, we normalize the singular value with the first singular value.

In Fig. 5.13, the singular value behavior of $C_{(1)}$, $C_{(2)}$ and $C_{(3)}$ is presented with the POD basis functions using L^2 and H_0^1 norm, denoted as the L^2- and H_0^1-POD basis, respectively, in the 2D flow past a cylinder at $\mathrm{Re} = 100$. We found the singular value of $C_{(3)}$ decays much faster compared to the results of $C_{(1)}$ and $C_{(2)}$ in both norm. This suggests there is a low-rank structure in $C_{(3)}$. In addition, the singular value of all three matricized matrices decays much

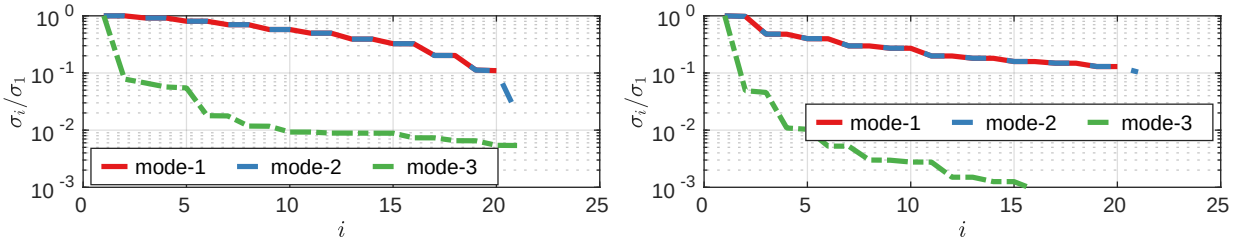

(a) L^2-POD basis function

(b) H_0^1-POD basis function

Figure 5.13: 2D flow past a cylinder at $\mathrm{Re} = 100$: Singular value behavior of mode-1, mode-2, and mode-3 matricized version of $\mathcal{C}$ with (a) the L^2-POD basis and (b) the H_0^1-POD basis.

faster with the H_0^1 norm compared to the L^2 norm. As highlighted in [17], the H_0^1-POD basis is expected to perform better in capturing small-scale structures and distinguishing them from large-scale structures in the solution compared to the L^2-POD basis. Therefore, it is not surprising to find the singular value of all three matrices decay faster with the H_0^1 norm.

Fig. 5.14 shows the singular value behavior of $C_{(1)}$, $C_{(2)}$ and $C_{(3)}$ with L^2- and H_0^1-POD basis in the 2D lid-driven cavity at $\mathrm{Re} = 15000$. We found the singular values of $C_{(1)}$ and $C_{(2)}$ behave similarly regardless of the norm. For the singular value of $C_{(3)}$, we still found it decays much faster compared to the singular value of the other two matrices. However, the results with H_0^1 norm decays much faster compared to the L^2 norm. This indicates there is a low-rank structure in $C_{(3)}$ with H_0^1 but not L^2 norm.

Similar investigations were conducted for the tensors in the 3D lid-driven cavity and MFU, yielding consistent results with those observed in the 2D lid-driven cavity: the matrix $C_{(3)}$ exhibits a low-rank structure under the H_0^1 norm.

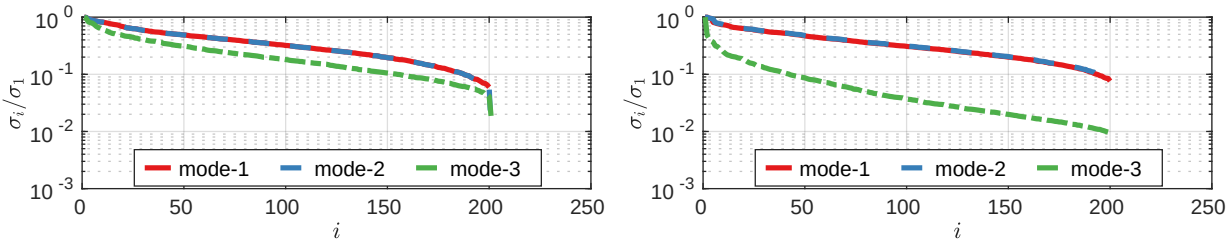

(a) L^2-POD basis (b) H_0^1-POD basis

Figure 5.14: 2D lid-driven cavity at $\mathrm{Re} = 15,000$: Singular value behavior of mode-1, mode-2, and mode-3 matricized version of $\mathcal{C}$ with (a) the L^2-POD basis and (b) the H_0^1-POD basis.

We further investigate the impact of the Reynolds number on the singular values' behavior in the 3D lid-driven cavity and the MFU in Fig. 5.15 with a primary focus on the H_0^1-POD basis. Fig. 5.15a shows the singular value behavior of $C_{(1)}$ and $C_{(3)}$ in the 3D lid-driven cavity at $\mathrm{Re} = 3200$ and $\mathrm{Re} = 10,000$. We found the singular values of both $C_{(1)}$ and $C_{(3)}$ decay slightly faster in the case of higher Reynolds number. Fig. 5.15b shows the singular value behavior of $C_{(1)}$ and $C_{(3)}$ in the MFU at $\mathrm{Re} = 3000$ and $\mathrm{Re} = 5000$. Here we found a faster decay in the singular values of $C_{(1)}$ with the higher Reynolds number. Overall, our results do not reveal a significant difference in the singular values' behavior between low and high Reynolds numbers.

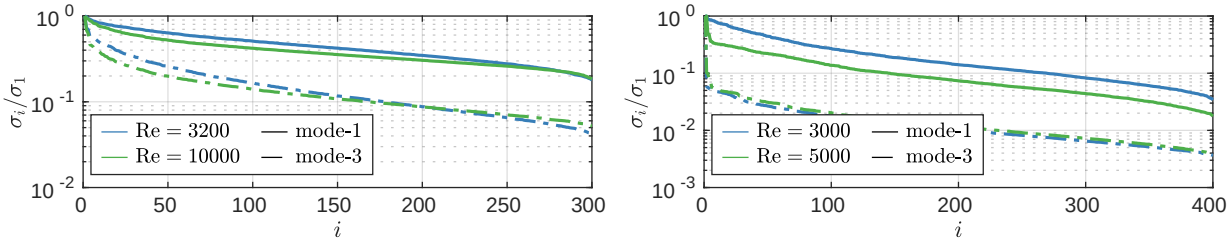

(a) 3D lid-driven cavity (b) Minimal flow unit

Figure 5.15: The effect of the Reynolds number on the singular value behavior of mode-1 and mode-3 matricized version of $\mathcal{C}$ with the H_0^1-POD basis in (a) the 3D lid-driven cavity and (b) the MFU with two Reynolds numbers presented in each case.

We next investigate the behavior of the relative residual as a function of the compression ratio (CR) to study the effectiveness of the SVD and the CPD for approximating the tensor

$\mathcal{C}$. Given a tensor $\mathcal{C}$ and its approximated tensor $\widehat{\mathcal{C}}$, the relative residual is defined as:

$$r_{\text{rel}} := \frac{\|\mathcal{C} - \widehat{\mathcal{C}}\|_F}{\|\mathcal{C}\|_F}. \tag{5.35}$$

For the SVD, the relative residual (5.35) is used to measure the approximation but with $C_{(3)}$ and $\widehat{C}_{(3)}$. In this study, we focus the CP decomposition with skew-symmetry preserved and the compression ratio for the ALS-skew and the SVD are defined as

$$\text{CR}_{ALS-Skew} = \frac{N^3}{\frac{3}{2}NR} = \frac{2N^2}{3R}, \quad \text{CR}_{SVD} = \frac{N^3}{N^2R} = \frac{N}{R}. \tag{5.36}$$

Fig. 5.16 shows the behavior of the relative residual as a function of the CR for the SVD and the CPD in the 3D lid-driven cavity and the MFU. We found for a fixed relative residual, the CPD is much more effective compared to the SVD in terms of the compression ratio. Although the SVD is more robust in achieving a smaller relative residual compared to the CPD, the CR is nearly 1 and therefore use of the SVD achieves almost no speed-up. Moreover, based on our investigation in previous sections, a relative residual between 0.35 to 0.1 is sufficient for the CPD-ROM to perform comparably to the G-ROM.

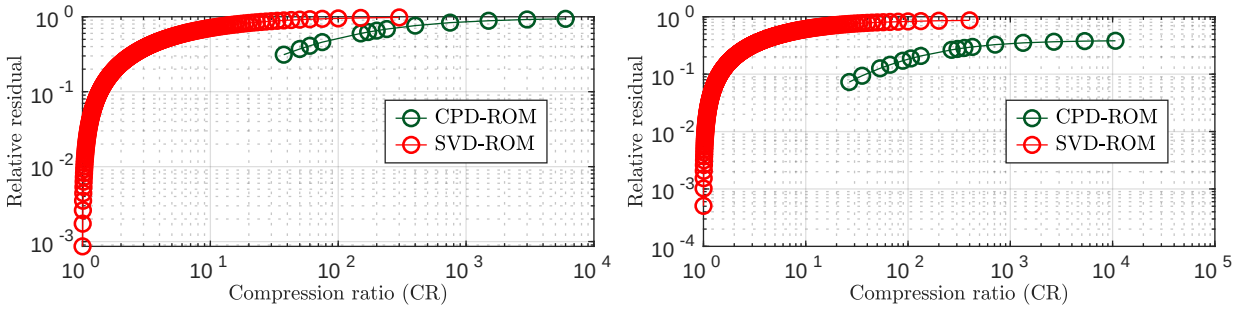

(a) 3D lid-driven cavity (b) MFU

Figure 5.16: The behavior of the relative residual of the approximated tensor with the SVD and the CPD as a function of the compression ratio (CR) in (a) the 3D lid-driven cavity and (b) the MFU. The compression ratio of the CPD and SVD are defined as $2N^2/R$ and N/R, respectively.

Performance investigation of the SVD-ROM with the CPD-ROM In this section, we compare the performance of the SVD-ROM with the CPD-ROM. In the SVD-ROM, the tensor contraction $\mathcal{C}(\underline{u})\underline{u}$ is evaluate using the approximated the mode-3 matricized version

of the tensor $\mathcal{C}$:

$$C_{(3)} \approx \widehat{C}_{(3)} = U_R \Sigma_R V_R^T, \tag{5.37}$$

where U_R and V_R are the left and right singular vector matrices of size $\mathbb{R}^{N\times R}$ and $\mathbb{R}^{N^2\times R}$, respectively. Σ_R is the singular value matrix of size $\mathbb{R}^{R\times R}$.

In Figs. 5.17–5.18, the relative error in the mean and the standard deviation of the energy and energy of the fluctuated velocity is shown as a function of the compression ratio (CR) for the 3D lid-driven cavity and the MFU, respectively. In both the mean and the standard deviation, we found the CPD-ROM has a larger CR compared to the SVD-ROM for a given accuracy. This indicates CPD is more effective than the SVD.

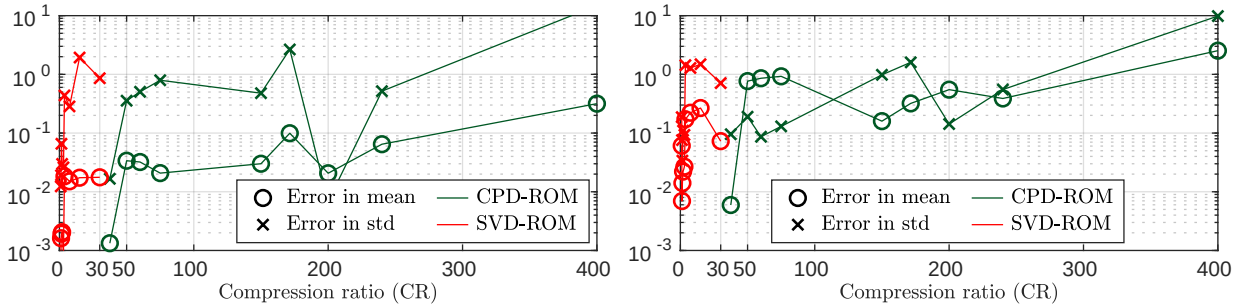

(a) Relative error in the mean energy and its standard deviation

(b) Relative error in the mean E_{fluc} and its standard deviation

Figure 5.17: 3D lid-driven cavity at Re = 3200: Comparison of the relative error in both the mean and the standard deviation of (a) the energy and (b) the energy of the fluctuated velocity between the SVD-ROM and the CPD-ROM as a function of the compression ratio (CR) The compression ratio of the CPD and SVD are defined as $2N^2/R$ and N/R, respectively.

5.4 Conclusions

In this chapter, we proposed a novel approach which utilizes the CANDECOMC/PARAFAC decomposition (CPD) to mitigate the $\mathcal{O}(N^3)$ tensor contraction cost for the scenario of large N values. With the CP decomposition, the reduced advection tensor is approximated by a sum of R rank-1 tensors and the cost is reduced down to $\mathcal{O}(NR)$. Our numerical investigation shows that the G-ROM with the CP decomposition (CPD-ROM) is able to obtain at least a factor of 10 speed-up. Moreover, the reduction obtained with the CP decomposition allows one to consider a larger N value for turbulent flows.

Besides, we derived two conditions on the CP rank and factor matrices to preserve the skew-symmetry in the CP decomposition and show that the CPD-ROM with skew-symmetry

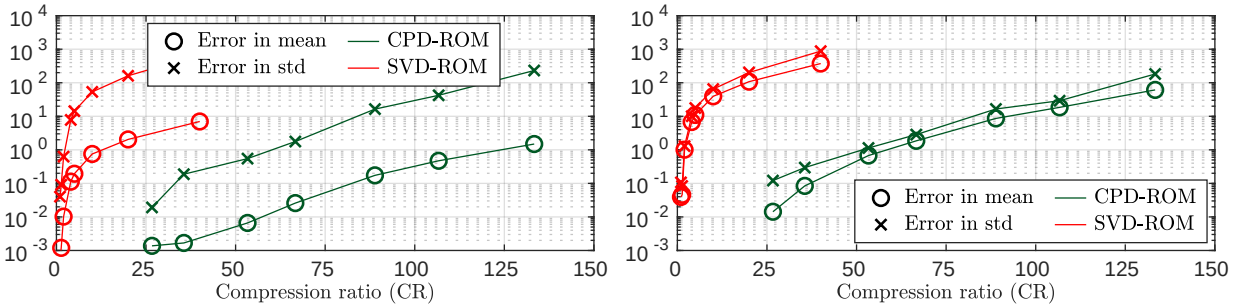

(a) Relative error in the mean energy and its standard deviation

(b) Relative error in the mean E_{fluc} and its standard deviation

Figure 5.18: MFU at Re = 5000: Comparison of the relative error in both the mean and the standard deviation of (a) the energy and (b) the energy of the fluctuated velocity between the SVD-ROM and the CPD-ROM as a function of the compression ratio (CR) The compression ratio of the CPD and SVD are defined as $2N^2/R$ and N/R, respectively.

preserved is more stable and achieves the same accuracy with a smaller CP rank R leading to a larger speed-up.

Furthermore, we investigated the tensor with the singular value decomposition and discovered that the advection tensor with the H_0^1-POD basis functions has a low-rank structure in its mode-3 matricized version and this low-rank structure is preserved even in higher Reynolds numbers. We also compared the CPD-ROM with the SVD-ROM (i.e., the G-ROM with the singular value decomposition (SVD)). For a given accuracy, we show that CPD-ROM outperforms the SVD-ROM in terms of compression ratio.

The first step in the numerical investigation of the CPD-ROM has been encouraging. There are, however, several other research directions that should be pursued next. For example, the CP decomposition can also be applied to the energy equation, potentially leading to further reduction in the computational costs for fluid-thermal applications. Besides, as previously noted, for a general flow problem, the reduced tensor could be decomposed into a skew-symmetric part with a low-rank tensor contributed from the boundaries and it would be intriguing to assess the performance of the CPD-ROM in this context. Moreover, in this work, we used the alternating least squares method (ALS) and its variant for computing the CP decomposition. However, ALS may exhibit slow or no convergence, especially when high accuracy is required [160]. Therefore, it will be interesting to consider other optimization methods to construct the CPD-ROM and investigate if the resulting CPD-ROM is more accurate and is capable of achieving a larger speed-up. Finally, another possibility is to consider other decompositions such as Tucker decomposition.

Chapter 6: Conclusions

This dissertation pushes the state-of-the-art for Galerkin-based ROMs simulation of turbulent flows by tackling three leading challenges.

In Chapter 3, we propose an error-indicated pMOR for buoyancy-driven flows by extending the error indicator proposed in [17] for the energy equation and Leray regularization. Applied to a 2D unsteady natural convection in a tilted high-aspect ratio slot, we demonstrate the error-indicated pMOR with Leray regularization can accurately and efficiently predict several quantities of interests. In addition, we identify spatio-temporal chaos as a source of irreproducibility in both the FOM and the ROM and that the FOM variance in these cases provides a lower bound on the pMOR error.

In Chapter 4, we propose a new regularized ROM, the time-relaxation ROM (TR-ROM), which filters the marginally resolved scales. We compare the TR-ROM with the two existing regularization models, the Leray ROM and the evolve-filter-relax ROM. Our investigation shows that with the optimal parameters, the new TR-ROM yields the most accurate results in both reconstructive and predictive regimes for turbulent channel flow and thermal striping in a T-junction. Moreover, all three Reg-ROMs are dramatically more accurate than the classical G-ROM without a significant increase in computational cost. In fact, with respect to the Reynolds normal stress $\langle u'u' \rangle$ and the Reynolds shear stress $\langle u'v' \rangle$, the three Reg-ROMs' errors are much lower than that of projection.

Our numerical investigation also shows that the differential filter (i.e., higher-order algebraic filter (HOAF) with filter order $m = 1$) yields the best results for most of the N values. On the other hand, the HOAF with $m > 1$ works better for small N, i.e., $N \leq 20$, at lower Reynolds number $\mathrm{Re}_\tau = 180$.

From the sensitivity study, we demonstrate the predictive capability of the Reg-ROMs by showing that the optimal parameters trained in the reconstructive regime $(\delta,\ \chi)_{\text{reprod}}$ are also optimal in the predictive regime for most of the N values. On the other hand, we find that all three Reg-ROMs are sensitive with respect to the relaxation parameter, χ, and filter radius, δ.

In Chapter 5, we propose a novel approach which utilizes the CANDECOMC/PARAFAC decomposition (CPD) to accelerate the G-ROM for N values. The CP decomposition is used to approximate the reduced advection tensor by a sum of R rank-1 tensors, which reduced the $\mathcal{O}(N^3)$ tensor contraction cost down to $\mathcal{O}(NR)$. Our numerical investigation shows that the G-ROM with CP decomposition (CPD-ROM) is able to obtain at least a factor of 10 speed-up, which allows the use of larger N values for turbulent flows. Additionally, we showed

that skew-symmetry-preserving CPD-ROM is more stable and, for a given accuracy, allows a smaller CP rank R, which implies more speed-up. We also compared the CPD-ROM with the SVD-ROM (i.e., the G-ROM with the singular value decomposition). For a given accuracy, we showed that CPD-ROM outperforms the SVD-ROM in terms of the compression ratio. Finally, from the singular value behavior, we showed that the advection tensor with the H_0^1-POD basis functions has a low-rank structure in its mode-3 matricized version.

In summary, this dissertation contributes several strategies for developing parametric model order reduction for turbulent flows. Future directions include combining the methods from the principal chapters to generate accurate (i.e., through the regularization techniques of Chapter 4 and increased N afforded by the CPD-ROM of Chapter 5), error-indicated (through the techniques of Chapter 3) pMOR for cases with more complex geometries and more general boundary conditions. All the techniques developed herein are available in an open-source repository (NekROM), which we hope will foster future collaboration and development in this important approach to thermal-fluid analysis.

References

[1] M. A. Grepl and A. T. Patera, "A posteriori error bounds for reduced-basis approximations of parametrized parabolic partial differential equations," *ESAIM: Mathematical Modelling and Numerical Analysis*, vol. 39, no. 1, pp. 157–181, 2005.

[2] G. Rozza, D. B. P. Huynh, and A. T. Patera, "Reduced basis approximation and a posteriori error estimation for affinely parametrized elliptic coercive partial differential equations: application to transport and continuum mechanics," *Archives of Computational Methods in Engineering*, vol. 15, no. 3, pp. 229–275, 2008.

[3] E. Merzari, H. Ninokata, A. Mahmood, and M. Rohde, "Proper orthogonal decomposition of the flow in geometries containing a narrow gap," *Theoretical and Computational Fluid Dynamics*, vol. 23, no. 5, pp. 333–351, 2009.

[4] E. Merzari, W. D. Pointer, and P. Fischer, "A POD-based solver for the advection-diffusion equation," in *Fluids Engineering Division Summer Meeting*, vol. 44403, 2011, pp. 1139–1147.

[5] A. Quarteroni, G. Rozza, and A. Manzoni, "Certified reduced basis approximation for parametrized partial differential equations and applications," *Journal of Mathematics in Industry*, vol. 1, no. 1, pp. 1–49, 2011.

[6] Z. Wang, I. Akhtar, J. Borggaard, and T. Iliescu, "Proper orthogonal decomposition closure models for turbulent flows: A numerical comparison," *Computer Methods in Applied Mechanics and Engineering*, vol. 237, pp. 10–26, 2012.

[7] K. Kaneko and P. Fischer, "Augmented reduced order models for turbulence," 2022, manuscript submitted for publication.

[8] A. Quarteroni, A. Manzoni, and F. Negri, *Reduced Basis Methods for Partial Differential Equations: An Introduction*. Springer, 2015, vol. 92.

[9] S. Kline and P. Runstadler, "Some preliminary results of visual studies of the flow model of the wall layers of the turbulent boundary layer," 1959.

[10] J. L. Lumley, "The structure of inhomogeneous turbulent flows," *Atmospheric turbulence and radio wave propagation*, pp. 166–178, 1967.

[11] S. L. Brunton and J. N. Kutz, *Data-driven science and engineering: Machine learning, dynamical systems, and control*. Cambridge University Press, 2019.

[12] J. S. Hesthaven, G. Rozza, and B. Stamm, *Certified Reduced Basis Methods for Parametrized Partial Differential Equations*. Springer, 2015.

[13] B. R. Noack, M. Morzynski, and G. Tadmor, *Reduced-Order Modelling for Flow Control*. Springer Verlag, 2011, vol. 528.

[14] S. E. Ahmed, S. Pawar, O. San, A. Rasheed, T. Iliescu, and B. R. Noack, "On closures for reduced order models − A spectrum of first-principle to machine-learned avenues," *Phys. Fluids*, vol. 33, no. 9, p. 091301, 2021.

[15] C. Mou, E. Merzari, O. San, and T. Iliescu, "An energy-based lengthscale for reduced order models of turbulent flows," *Nucl. Eng. Des.*, vol. 412, p. 112454, 2023.

[16] K. Kaneko, "An augmented basis method for reduced order models of turbulent flow," Ph.D. dissertation, 2022.

[17] L. Fick, Y. Maday, A. T. Patera, and T. Taddei, "A stabilized POD model for turbulent flows over a range of Reynolds numbers: Optimal parameter sampling and constrained projection," *Journal of Computational Physics*, vol. 371, pp. 214–243, 2018.

[18] N. Akkari, R. Mercier, G. Lartigue, and V. Moureau, "Stable POD-Galerkin reduced order models for unsteady turbulent incompressible flows," in *55th AIAA Aerospace Sciences Meeting*, 2017, p. 1000.

[19] N. Akkari, F. Casenave, and V. Moureau, "Time stable reduced order modeling by an enhanced reduced order basis of the turbulent and incompressible 3D Navier–Stokes equations," *Math. Comput. Appl.*, vol. 24, no. 2, p. 45, 2019.

[20] X. Xie, M. Mohebujjaman, L. G. Rebholz, and T. Iliescu, "Data-driven filtered reduced order modeling of fluid flows," *SIAM J. Sci. Comput.*, vol. 40, no. 3, pp. B834–B857, 2018.

[21] T. Duriez, S. L. Brunton, and B. R. Noack, *Machine learning control-taming nonlinear dynamics and turbulence*. Springer, 2017, vol. 116.

[22] K. Carlberg, C. Bou-Mosleh, and C. Farhat, "Efficient non-linear model reduction via a least-squares Petrov–Galerkin projection and compressive tensor approximations," *Int. J. Num. Meth. Eng.*, vol. 86, no. 2, pp. 155–181, 2011.

[23] K. Carlberg, C. Farhat, J. Cortial, and D. Amsallem, "The GNAT method for nonlinear model reduction: effective implementation and application to computational fluid dynamics and turbulent flows," *Journal of Computational Physics*, vol. 242, pp. 623–647, 2013.

[24] P. J. Schmid, "Dynamic mode decomposition of numerical and experimental data," *Journal of fluid mechanics*, vol. 656, pp. 5–28, 2010.

[25] C. W. Rowley, I. Mezić, S. Bagheri, P. Schlatter, and D. S. Henningson, "Spectral analysis of nonlinear flows," *Journal of fluid mechanics*, vol. 641, pp. 115–127, 2009.

[26] K. Kaneko, P.-H. Tsai, and P. Fischer, "Towards model order reduction for fluid-thermal analysis," *Nuclear Engineering and Design*, vol. 370, p. 110866, 2020.

[27] P.-H. Tsai and P. Fischer, "Parametric model-order-reduction development for unsteady convection," *Frontiers in Physics*, p. 711, 2022.

[28] D. Wells, Z. Wang, X. Xie, and T. Iliescu, "An evolve-then-filter regularized reduced order model for convection-dominated flows," *International Journal for Numerical Methods in Fluids*, vol. 84, no. 10, pp. 598–615, 2017.

[29] F. Sabetghadam and A. Jafarpour, "α regularization of the POD-Galerkin dynamical systems of the Kuramoto–Sivashinsky equation," *Applied Mathematics and Computation*, vol. 218, no. 10, pp. 6012–6026, 2012.

[30] M. Strazzullo, M. Girfoglio, F. Ballarin, T. Iliescu, and G. Rozza, "Consistency of the full and reduced order models for evolve-filter-relax regularization of convection-dominated, marginally-resolved flows," *Int. J. Num. Meth. Eng.*, vol. 123, no. 14, pp. 3148–3178, 2022.

[31] A. T. Patera and G. Rozza, "Reduced basis approximation and a posteriori error estimation for parametrized partial differential equations," 2006.

[32] L. Machiels, Y. Maday, and A. T. Patera, "Output bounds for reduced-order approximations of elliptic partial differential equations," *Computer methods in applied mechanics and engineering*, vol. 190, no. 26-27, pp. 3413–3426, 2001.

[33] S. Ali, F. Ballarin, and G. Rozza, "Stabilized reduced basis methods for parametrized steady Stokes and Navier–Stokes equations," *Comput. Math. Appl.*, vol. 80, no. 11, pp. 2399–2416, 2020.

[34] N. Ngoc Cuong, K. Veroy, and A. T. Patera, "Certified real-time solution of parametrized partial differential equations," in *Handbook of Materials Modeling*. Springer, 2005, pp. 1529–1564.

[35] K. Veroy and A. T. Patera, "Certified real-time solution of the parametrized steady incompressible Navier–Stokes equations: Rigorous reduced-basis a posteriori error bounds," *International Journal for Numerical Methods in Fluids*, vol. 47, no. 8-9, pp. 773–788, 2005.

[36] S. Deparis, "Reduced basis error bound computation of parameter-dependent Navier–Stokes equations by the natural norm approach," *SIAM Journal on Numerical Analysis*, vol. 46, no. 4, pp. 2039–2067, 2008.

[37] S. Deparis and G. Rozza, "Reduced basis method for multi-parameter-dependent steady Navier–Stokes equations: Applications to natural convection in a cavity," *Journal of Computational Physics*, vol. 228, no. 12, pp. 4359–4378, 2009.

[38] F. Ballarin, T. C. Rebollo, E. D. Ávila, M. G. Mármol, and G. Rozza, "Certified Reduced Basis VMS-Smagorinsky model for natural convection flow in a cavity with variable height," *Computers & Mathematics with Applications*, vol. 80, no. 5, pp. 973–989, 2020.

[39] D. J. Knezevic, N.-C. Nguyen, and A. T. Patera, "Reduced basis approximation and a posteriori error estimation for the parametrized unsteady Boussinesq equations," *Mathematical Models and Methods in Applied Sciences*, vol. 21, no. 07, pp. 1415–1442, 2011.

[40] M. Yano, "A space-time Petrov–Galerkin certified reduced basis method: Application to the Boussinesq equations," *SIAM Journal on Scientific Computing*, vol. 36, no. 1, pp. A232–A266, 2014.

[41] M. Barrault, Y. Maday, N. C. Nguyen, and A. T. Patera, "An empirical interpolation method: Application to efficient reduced-basis discretization of partial differential equations," *Comptes Rendus Mathematique*, vol. 339, no. 9, pp. 667–672, 2004.

[42] S. Chaturantabut and D. C. Sorensen, "Nonlinear model reduction via discrete empirical interpolation," *SIAM Journal on Scientific Computing*, vol. 32, no. 5, pp. 2737–2764, 2010.

[43] S. Chaturantabut and D. C. Sorensen, "Discrete empirical interpolation for nonlinear model reduction," in *Proceedings of the 48h IEEE Conference on Decision and Control (CDC) held jointly with 2009 28th Chinese Control Conference*. IEEE, 2009, pp. 4316–4321.

[44] S. Chaturantabut and D. C. Sorensen, "Application of POD and DEIM on dimension reduction of non-linear miscible viscous fingering in porous media," *Mathematical and Computer Modelling of Dynamical Systems*, vol. 17, no. 4, pp. 337–353, 2011.

[45] P. Astrid, S. Weiland, K. Willcox, and T. Backx, "Missing point estimation in models described by proper orthogonal decomposition," *IEEE Transactions on Automatic Control*, vol. 53, no. 10, pp. 2237–2251, 2008.

[46] J. Kim, P. Moin, and R. Moser, "Turbulence statistics in fully developed channel flow at low Reynolds number," *Journal of fluid mechanics*, vol. 177, pp. 133–166, 1987.

[47] R. D. Moser, J. Kim, and N. N. Mansour, "Direct numerical simulation of turbulent channel flow up to $\mathrm{Re}_\tau = 590$," *Physics of fluids*, vol. 11, no. 4, pp. 943–945, 1999.

[48] D. Xiao, F. Fang, A. G. Buchan, C. C. Pain, I. M. Navon, J. Du, and G. Hu, "Non-linear model reduction for the Navier–Stokes equations using residual DEIM method," *Journal of Computational Physics*, vol. 263, pp. 1–18, 2014.

[49] H. C. Elman and V. Forstall, "Numerical solution of the parameterized steady-state Navier–Stokes equations using empirical interpolation methods," *Computer Methods in Applied Mechanics and Engineering*, vol. 317, pp. 380–399, 2017.

[50] S. Dolgov and M. Stoll, "Low-rank solution to an optimization problem constrained by the Navier–Stokes equations," *SIAM Journal on Scientific Computing*, vol. 39, no. 1, pp. A255–A280, 2017.

[51] W. Guo and J.-M. Qiu, "A low rank tensor representation of linear transport and nonlinear Vlasov solutions and their associated flow maps," *Journal of Computational Physics*, vol. 458, p. 111089, 2022.

[52] L. Einkemmer, A. Ostermann, and C. Piazzola, "A low-rank projector-splitting integrator for the Vlasov–Maxwell equations with divergence correction," *Journal of Computational Physics*, vol. 403, p. 109063, 2020.

[53] Y. Sun and M. Kumar, "Numerical solution of high dimensional stationary Fokker–Planck equations via tensor decomposition and Chebyshev spectral differentiation," *Computers & Mathematics with Applications*, vol. 67, no. 10, pp. 1960–1977, 2014.

[54] A. V. Chikitkin, E. K. Kornev, and V. A. Titarev, "Numerical solution of the Boltzmann equation with S-model collision integral using tensor decompositions," *Computer Physics Communications*, vol. 264, p. 107954, 2021.

[55] O. Koch and C. Lubich, "Dynamical tensor approximation," *SIAM Journal on Matrix Analysis and Applications*, vol. 31, no. 5, pp. 2360–2375, 2010.

[56] A. Nonnenmacher and C. Lubich, "Dynamical low-rank approximation: applications and numerical experiments," *Mathematics and Computers in Simulation*, vol. 79, no. 4, pp. 1346–1357, 2008.

[57] Y. Choi and K. Carlberg, "Space–time least-squares Petrov–Galerkin projection for nonlinear model reduction," *SIAM Journal on Scientific Computing*, vol. 41, no. 1, pp. A26–A58, 2019.

[58] Y. S. Shimizu and E. J. Parish, "Windowed space–time least-squares Petrov–Galerkin model order reduction for nonlinear dynamical systems," *Computer Methods in Applied Mechanics and Engineering*, vol. 386, p. 114050, 2021.

[59] J.-L. Guermond, S. Prudhomme, and J. T. Oden, "An interpretation of the Navier-Stokes-alpha model as a frame-indifferent Leray regularization," *Physica D*, vol. 177, pp. 23–30, 2003.

[60] Y. Maday, A. T. Patera, and E. M. Ronquist, "A well-posed optimal spectral element approximation for the Stokes problem," Tech. Rep., 1987.

[61] P. F. Fischer, J. W. Lottes, and S. G. Kerkemeier, "Nek5000 web page," 2008. [Online]. Available: https://nek5000.mcs.anl.gov

[62] P. Fischer, S. Kerkemeier, M. Min, Y.-H. Lan, M. Phillips, T. Rathnayake, E. Merzari, A. Tomboulides, A. Karakus, N. Chalmers et al., "NekRS, a GPU-accelerated spectral element Navier–Stokes solver," *Parallel Computing*, vol. 114, p. 102982, 2022.

[63] A. Quarteroni and A. Valli, *Numerical Approximation of Partial Differential Equations*, ser. Springer Series in Computational Mathematics. Berlin: Springer, 1994.

[64] P. Fischer, M. Schmitt, and A. Tomboulides, "Recent developments in spectral element simulations of moving-domain problems," in *Recent Progress and Modern Challenges in Applied Mathematics, Modeling and Computational Science*. Springer, 2017, pp. 213–244.

[65] E. M. Rønquist and A. T. Patera, "A Legendre spectral element method for the Stefan problem," *International Journal for Numerical Methods in Engineering*, vol. 24, no. 12, pp. 2273–2299, 1987.

[66] Y. Maday, A. T. Patera, and E. M. Rønquist, "The $P_N \times P_{N-2}$ method for the approximation of the Stokes problem," *Laboratoire d'Analyse Numérique, Paris VI*, vol. 11, no. 4, 1992.

[67] G. Berkooz, P. Holmes, and J. L. Lumley, "The proper orthogonal decomposition in the analysis of turbulent flows," *Annual review of fluid mechanics*, vol. 25, no. 1, pp. 539–575, 1993.

[68] S. Volkwein, "Proper orthogonal decomposition: Theory and reduced-order modelling," *Lecture Notes, University of Konstanz*, 2013, http://www.math.uni-konstanz.de/numerik/personen/volkwein/teaching/POD-Book.pdf.

[69] A. Iollo, S. Lanteri, and J.-A. Désidéri, "Stability properties of POD–Galerkin approximations for the compressible Navier–Stokes equations," *Theoretical and Computational Fluid Dynamics*, vol. 13, no. 6, pp. 377–396, 2000.

[70] P. Fischer, M. Schmitt, and A. Tomboulides, *Recent developments in spectral element simulations of moving-domain problems*. Fields Institute Communications, Springer, 2017, vol. 79, pp. 213–244.

[71] F. Ballarin, A. Manzoni, A. Quarteroni, and G. Rozza, "Supremizer stabilization of POD–Galerkin approximation of parametrized steady incompressible Navier–Stokes equations," *Int. J. Numer. Meth. Engng.*, vol. 102, pp. 1136–1161, 2015.

[72] V. DeCaria, T. Iliescu, W. Layton, M. McLaughlin, and M. Schneier, "An artificial compression reduced order model," *SIAM J. Numer. Anal.*, vol. 58, no. 1, pp. 565–589, 2020.

[73] B. R. Noack, P. Papas, and P. A. Monkewitz, "The need for a pressure-term representation in empirical Galerkin models of incompressible shear flows," *J. Fluid Mech.*, vol. 523, pp. 339–365, 2005.

[74] K. Ding, "Free response of a freely-rotatable eccentric linearly-sprung circular cylinder in or absent a cross-flow," Ph.D. dissertation, 2021.

[75] G. Stabile, S. Hijazi, A. Mola, S. Lorenzi, and G. Rozza, "POD-Galerkin reduced order methods for CFD using Finite Volume Discretisation: vortex shedding around a circular cylinder," *Commun. Appl. Ind. Math.*, vol. 8, no. 1, pp. 210–236, 2017.

[76] M. M. Rai and P. Moin, "Direct simulations of turbulent flow using finite-difference schemes," *Journal of computational physics*, vol. 96, no. 1, pp. 15–53, 1991.

[77] M. R. Malik, T. A. Zang, and M. Y. Hussaini, "A spectral collocation method for the Navier-Stokes equations," *Journal of Computational Physics*, vol. 61, no. 1, pp. 64–88, 1985.

[78] D. Rempfer, "On low-dimensional Galerkin models for fluid flow," *Theoretical and Computational Fluid Dynamics*, vol. 14, no. 2, pp. 75–88, 2000.

[79] J.-L. Guermond, J. T. Oden, and S. Prudhomme, "Mathematical perspectives on large eddy simulation models for turbulent flows," *Journal of Mathematical Fluid Mechanics*, vol. 6, no. 2, pp. 194–248, 2004.

[80] J.-L. Guermond, R. Pasquetti, and B. Popov, "Entropy viscosity method for nonlinear conservation laws," *Journal of Computational Physics*, vol. 230, no. 11, pp. 4248–4267, 2011.

[81] J. Mullen, "Development of a parallel spectral element based large eddy simulation model for the flow of incompressible fluids in complex geometries," Ph.D. dissertation, Brown University, 1999, division of Engineering.

[82] L. Sirovich and A. E. Deane, "A computational study of Rayleigh–Bénard convection. Part 2. Dimension considerations," *Journal of Fluid Mechanics*, vol. 222, pp. 251–265, 1991.

[83] R. Puragliesi and E. Leriche, "Proper orthogonal decomposition of a fully confined cubical differentially heated cavity flow at Rayleigh number $\mathrm{Ra} = 10^9$," *Computers & Fluids*, vol. 61, pp. 14–20, 2012.

[84] F. Busse, "Non-linear properties of thermal convection," *Reports on Progress in Physics*, vol. 41, no. 12, p. 1929, 1978.

[85] Q. Wang, Z.-H. Wan, R. Yan, and D.-J. Sun, "Multiple states and heat transfer in two-dimensional tilted convection with large aspect ratios," *Physical Review Fluids*, vol. 3, no. 11, p. 113503, 2018.

[86] J. L. Eftang, D. J. Knezevic, and A. T. Patera, "An hp certified reduced basis method for parametrized parabolic partial differential equations," *Mathematical and Computer Modelling of Dynamical Systems*, vol. 17, no. 4, pp. 395–422, 2011.

[87] B. Haasdonk and M. Ohlberger, "Reduced basis method for finite volume approximations of parametrized linear evolution equations," *ESAIM: Mathematical Modelling and Numerical Analysis*, vol. 42, no. 2, pp. 277–302, 2008.

[88] B. Haasdonk, "Convergence rates of the POD–Greedy method," *ESAIM: Mathematical Modelling and Numerical Analysis*, vol. 47, no. 3, pp. 859–873, 2013.

[89] A. Karimi and M. R. Paul, "Quantifying spatiotemporal chaos in Rayleigh-Bénard convection," *Physical Review E*, vol. 85, no. 4, p. 046201, 2012.

[90] A. Wolf, J. B. Swift, H. L. Swinney, and J. A. Vastano, "Determining Lyapunov exponents from a time series," *Physica D: Nonlinear Phenomena*, vol. 16, no. 3, pp. 285–317, 1985.

[91] I. Goldhirsch, P.-L. Sulem, and S. A. Orszag, "Stability and Lyapunov stability of dynamical systems: A differential approach and a numerical method," *Physica D: Nonlinear Phenomena*, vol. 27, no. 3, pp. 311–337, 1987.

[92] M. Cross and P. Hohenberg, "Spatiotemporal chaos," *Science*, vol. 263, no. 5153, pp. 1569–1570, 1994.

[93] D. A. Egolf, I. V. Melnikov, W. Pesch, and R. E. Ecke, "Mechanisms of extensive spatiotemporal chaos in Rayleigh–Bénard convection," *Nature*, vol. 404, no. 6779, pp. 733–736, 2000.

[94] M. C. Cross and P. C. Hohenberg, "Pattern formation outside of equilibrium," *Reviews of Modern Physics*, vol. 65, no. 3, p. 851, 1993.

[95] A. Y. Gelfgat, P. Bar-Yoseph, and A. Yarin, "Stability of multiple steady states of convection in laterally heated cavities," *Journal of Fluid Mechanics*, vol. 388, pp. 315–334, 1999.

[96] F. Pichi, "Reduced order models for parametric bifurcation problems in nonlinear PDEs," Ph.D. dissertation, 2020.

[97] W. J. Layton and L. G. Rebholz, *Approximate Deconvolution Models of Turbulence: Analysis, Phenomenology and Numerical Analysis*. Springer Berlin Heidelberg, 2012, vol. 2042.

[98] S. Stolz, N. Adams, and L. Kleiser, "An approximate deconvolution model for large-eddy simulation with application to incompressible wall-bounded flows," *Phys. Fluids*, vol. 13, no. 4, pp. 997–1015, 2001.

[99] S. Stolz, N. Adams, and L. Kleiser, "The approximate deconvolution model for large-eddy simulations of compressible flows and its application to shock-turbulent-boundary-layer interaction," *Phys. Fluids*, vol. 13, no. 10, pp. 2985–3001, 2001.

[100] N. A. Adams and S. Stolz, "A subgrid-scale deconvolution approach for shock capturing," *J. Comput. Phys.*, vol. 178, no. 2, pp. 391–426, 2002.

[101] W. Layton and M. Neda, "Truncation of scales by time relaxation," *J. Math. Anal. Appl.*, vol. 325, no. 2, pp. 788–807, 2007.

[102] P. Schlatter, S. Stolz, and L. Kleiser, "Evaluation of high-pass filtered eddy-viscosity models for large-eddy simulation of turbulent flows," *Journal of Turbulence*, no. 6, p. N5, 2005.

[103] A. Obabko, P. Fischer, T. Tautges, S. Karabasov, V. Goloviznin, M. Zaytsev, V. Chudanov, V. Pervichko, and A. Aksenova, "CFD validation in OECD/NEA t-junction benchmark." Argonne National Lab.(ANL), Argonne, IL (United States), Tech. Rep., 2011.

[104] J. Leray, "Sur le mouvement d'un fluide visqueux emplissant l'espace," *Acta Math.*, vol. 63, pp. 193–248, 1934.

[105] B. J. Geurts and D. D. Holm, "Regularization modeling for large-eddy simulation," *Phys. Fluids*, vol. 15, no. 1, pp. L13–L16, 2003.

[106] C. Foiaş, D. Holm, and E. Titi, "The Navier-Stokes-alpha model of fluid turbulence," *Phys. D*, vol. 152/153, pp. 505–519, 2001, advances in nonlinear mathematics and science.

[107] M. Girfoglio, A. Quaini, and G. Rozza, "A POD-Galerkin reduced order model for a LES filtering approach," *J. Comput. Phys.*, vol. 436, p. 110260, 2021.

[108] M. Girfoglio, A. Quaini, and G. Rozza, "A hybrid projection/data-driven reduced order model for the Navier-Stokes equations with nonlinear filtering stabilization," *J. Comput. Phys.*, vol. 486, p. 112127, 2023.

[109] M. Gunzburger, T. Iliescu, M. Mohebujjaman, and M. Schneier, "An evolve-filter-relax stabilized reduced order stochastic collocation method for the time-dependent Navier-Stokes equations," *SIAM-ASA J. Uncertain.*, vol. 7, no. 4, pp. 1162–1184, 2019.

[110] M. Gunzburger, T. Iliescu, and M. Schneier, "A Leray regularized ensemble-proper orthogonal decomposition method for parameterized convection-dominated flows," *IMA J. Numer. Anal.*, vol. 40, no. 2, pp. 886–913, 2020.

[111] M. Girfoglio, A. Quaini, and G. Rozza, "A linear filter regularization for POD-based reduced-order models of the quasi-geostrophic equations," *C. R. Mech.*, vol. 351, no. S1, pp. 1–21, 2023.

[112] M. Girfoglio, A. Quaini, and G. Rozza, "A novel Large Eddy Simulation model for the Quasi-Geostrophic equations in a Finite Volume setting," *J. Comput. Appl. Math.*, vol. 418, p. 114656, 2023.

[113] J. S. Mullen and P. F. Fischer, "Filtering techniques for complex geometry fluid flows," *Commun. Numer. Meth. Engng.*, vol. 15, no. 1, pp. 9–18, 1999.

[114] M. O. Deville, P. F. Fischer, and E. H. Mund, *High-order methods for incompressible fluid flow*, ser. Cambridge Monographs on Applied and Computational Mathematics. Cambridge: Cambridge University Press, 2002, vol. 9.

[115] M. Strazzullo, F. Ballarin, T. Iliescu, and C. Canuto, "New feedback control and adaptive evolve-filter-relax regularization for the Navier-Stokes equations in the convection-dominated regime," *arXiv preprint, http://arxiv.org/abs/2307.00675*, 2023.

[116] M. Germano, "Differential filters of elliptic type," *Phys. Fluids*, vol. 29, no. 6, pp. 1757–1758, 1986.

[117] N. Ghaddar, G. Karniadakis, and A. Patera, "A conservative isoparametric spectral element method for forced convection; application to fully developed flow in periodic geometries," *Numerical Heat Transfer, Part A: Applications*, vol. 9, no. 3, pp. 277–300, 1986.

[118] S. V. Patankar, C. H. Liu, and E. M. Sparrow, "Fully developed flow and heat transfer in ducts having streamwise-periodic variations of cross-sectional area," 1977.

[119] A. Vreman and J. G. Kuerten, "Comparison of direct numerical simulation databases of turbulent channel flow at Re_τ= 180," *Physics of Fluids*, vol. 26, no. 1, p. 015102, 2014.

[120] V. J. Ervin, W. J. Layton, and M. Neda, "Numerical analysis of filter-based stabilization for evolution equations," *SIAM J. Numer. Anal.*, vol. 50, no. 5, pp. 2307–2335, 2012.

[121] S. B. Pope, *Turbulent flows*. Cambridge university press, 2000.

[122] L. C. Berselli, T. Iliescu, W. J. Layton et al., *Mathematics of large eddy simulation of turbulent flows*. Springer, 2006, vol. 2.

[123] G. Winckelmans, H. Jeanmart, and D. Carati, "On the comparison of turbulence intensities from large-eddy simulation with those from experiment or direct numerical simulation," *Physics of Fluids*, vol. 14, no. 5, pp. 1809–1811, 2002.

[124] B. J. Geurts and D. D. Holm, "Leray and LANS-α modelling of turbulent mixing," *Journal of turbulence*, no. 7, p. N10, 2006.

[125] A. Sanfilippo, I. R. Moore, F. Ballarin, and T. Iliescu, "Approximate deconvolution Leray reduced order model," *arXiv preprint, http://arxiv.org/abs/arXiv:2307.10817*, 2023.

[126] X. Xie, D. Wells, Z. Wang, and T. Iliescu, "Approximate deconvolution reduced order modeling," *Comput. Methods Appl. Mech. Engrg.*, vol. 313, pp. 512–534, 2017.

[127] X. Xie, D. Wells, Z. Wang, and T. Iliescu, "Numerical analysis of the Leray reduced order model," *J. Comput. Appl. Math.*, vol. 328, pp. 12–29, 2018.

[128] R. A. Harshman et al., "Foundations of the PARAFAC procedure: Models and conditions for an" explanatory" multimodal factor analysis," 1970.

[129] F. L. Hitchcock, "The expression of a tensor or a polyadic as a sum of products," *Journal of Mathematics and Physics*, vol. 6, no. 1-4, pp. 164–189, 1927.

[130] T. G. Kolda, "Multilinear operators for higher-order decompositions." Sandia National Laboratories, Tech. Rep., 2006.

[131] C. J. Hillar and L.-H. Lim, "Most tensor problems are NP-hard," *Journal of the ACM (JACM)*, vol. 60, no. 6, pp. 1–39, 2013.

[132] J. B. Kruskal, "Three-way arrays: rank and uniqueness of trilinear decompositions, with application to arithmetic complexity and statistics," *Linear algebra and its applications*, vol. 18, no. 2, pp. 95–138, 1977.

[133] T. G. Kolda and B. W. Bader, "Tensor decompositions and applications," *SIAM review*, vol. 51, no. 3, pp. 455–500, 2009.

[134] J. Håstad, "Tensor rank is NP-complete," *Journal of Algorithms*, vol. 11, no. 4, pp. 644–654, 1990.

[135] J. D. Carroll and J.-J. Chang, "Analysis of individual differences in multidimensional scaling via an N-way generalization of "Eckart-Young" decomposition," *Psychometrika*, vol. 35, no. 3, pp. 283–319, 1970.

[136] L. De Lathauwer, B. De Moor, and J. Vandewalle, "A multilinear singular value decomposition," *SIAM journal on Matrix Analysis and Applications*, vol. 21, no. 4, pp. 1253–1278, 2000.

[137] G. D. Purvis III and R. J. Bartlett, "A full coupled-cluster singles and doubles model: The inclusion of disconnected triples," *The Journal of Chemical Physics*, vol. 76, no. 4, pp. 1910–1918, 1982.

[138] P. Comon, G. Golub, L.-H. Lim, and B. Mourrain, "Symmetric tensors and symmetric tensor rank," *SIAM Journal on Matrix Analysis and Applications*, vol. 30, no. 3, pp. 1254–1279, 2008.

[139] M. Kamiya and S. Hirata, "Higher-order equation-of-motion coupled-cluster methods for electron attachment," *The Journal of chemical physics*, vol. 126, no. 13, 2007.

[140] T. G. Kolda, "Numerical optimization for symmetric tensor decomposition," *Mathematical Programming*, vol. 151, no. 1, pp. 225–248, 2015.

[141] F. Hummel, T. Tsatsoulis, and A. Grüneis, "Low rank factorization of the coulomb integrals for periodic coupled cluster theory," *The Journal of chemical physics*, vol. 146, no. 12, p. 124105, 2017.

[142] J. Malm, P. Schlatter, P. F. Fischer, and D. S. Henningson, "Stabilization of the spectral element method in convection dominated flows by recovery of skew-symmetry," *Journal of Scientific Computing*, vol. 57, pp. 254–277, 2013.

[143] Y. Itin and S. Reches, "Decomposition of third-order constitutive tensors," *Mathematics and Mechanics of Solids*, vol. 27, no. 2, pp. 222–249, 2022.

[144] R. F. Tinder, *Tensor properties of solids: phenomenological development of the tensor properties of crystals*. Morgan & Claypool Publishers, 2008, vol. 4.

[145] P.-O. Löwdin, "Quantum theory of many-particle systems. II. Study of the ordinary Hartree-Fock approximation," *Physical Review*, vol. 97, no. 6, p. 1490, 1955.

[146] P. Lykos and G. Pratt, "Discussion on the Hartree-Fock approximation," *Reviews of Modern Physics*, vol. 35, no. 3, p. 496, 1963.

[147] S. Szalay, M. Pfeffer, V. Murg, G. Barcza, F. Verstraete, R. Schneider, and Ö. Legeza, "Tensor product methods and entanglement optimization for ab initio quantum chemistry," *International Journal of Quantum Chemistry*, vol. 115, no. 19, pp. 1342–1391, 2015.

[148] E. Solomonik, D. Matthews, J. R. Hammond, J. F. Stanton, and J. Demmel, "A massively parallel tensor contraction framework for coupled-cluster computations," *Journal of Parallel and Distributed Computing*, vol. 74, no. 12, pp. 3176–3190, 2014.

[149] E. B. Kovac and D. Kressner, "Structure-preserving low multilinear rank approximation of antisymmetric tensors," *SIAM Journal on Matrix Analysis and Applications*, vol. 38, no. 3, pp. 967–983, 2017.

[150] R. A. Harshman, "Models for analysis of asymmetrical relationships among N objects or stimuli," in *Paper presented at the First Joint Meeting of the Psychometric Society and the Society of Mathematical Psychology, Hamilton*, 1978.

[151] B. W. Bader, R. A. Harshman, and T. G. Kolda, "Temporal analysis of semantic graphs using ASALSAN," in *Seventh IEEE international conference on data mining (ICDM 2007)*. IEEE, 2007, pp. 33–42.

[152] R. Harshman and M. Lundy, "Three-way DEDICOM: Analyzing multiple matrices of asymmetric relationships," in *Annual Meeting of the North American Psychometric Society*, 1992.

[153] M. E. Lundy, R. A. Harshman, P. Paatero, and L. C. Swartzman, "Application of the 3-way Dedicom model to skew-symmetric data for paired preference ratings of treatments for chronic back pain," in *TRICAP 2003 Meeting, Lexington, Kentucky. Citeseer*, 2003.

[154] E. Begovic and L. Perisa, "CP decomposition and low-rank approximation of antisymmetric tensors," *arXiv preprint arXiv:2212.13389*, 2022.

[155] Y.-H. Lan, "On the development of preconditioning the advection diffusion operators with spectral element discretization," Ph.D. dissertation, University of Illinois at Urbana-Champaign, 2023.

[156] J. Jiménez and P. Moin, "The minimal flow unit in near-wall turbulence," *Journal of Fluid Mechanics*, vol. 225, pp. 213–240, 1991.

[157] S. A. Orszag, "Comparison of pseudospectral and spectral approximation," *Studies in Applied Mathematics*, vol. 51, no. 3, pp. 253–259, 1972.

[158] D. G. Fox and S. A. Orszag, "Pseudospectral approximation to two-dimensional turbulence," *Journal of Computational Physics*, vol. 11, no. 4, pp. 612–619, 1973.

[159] S. A. Orszag and M. Israeli, "Numerical simulation of viscous incompressible flows," *Annual Review of Fluid Mechanics*, vol. 6, no. 1, pp. 281–318, 1974.

[160] N. Singh, L. Ma, H. Yang, and E. Solomonik, "Comparison of accuracy and scalability of Gauss–Newton and alternating least squares for CANDECOMC/PARAFAC decomposition," *SIAM Journal on Scientific Computing*, vol. 43, no. 4, pp. C290–C311, 2021.

Appendix A: Streamwise Reynolds Normal Stress Results with Reg-ROMs

In this appendix, we present the results of the streamwise Reynolds normal stress $\langle u'u' \rangle$ in the three Reg-ROMs presented in Sections 4.1–4.3, the G-ROM and the ROM projection in the simulation of the turbulent channel flow.

Notice that, as discussed in Section 4.6, for each N and m values, the Reg-ROMs parameters δ and χ are optimized for the Reynolds shear stress $\langle u'v' \rangle$. Here, we do not retrain the parameters to minimize the error in the streamwise Reynolds normal stress $\langle u'u' \rangle$ but examine how well the normal Reynolds stress $\langle u'u' \rangle$ is reconstructed and predicted with the three Reg-ROMs trained for $\langle u'v' \rangle$.

A.1 Reproduction Regime

In this section, we report the results of the streamwise Reynolds normal stress $\langle u'u' \rangle$ for the three Reg-ROMs: L-ROM (Section 4.1), EFR-ROM (Section 4.2), and the new TR-ROM (Section 4.3) for the reproduction regime, the time interval in which the snapshots were collected, at $\mathrm{Re}_\tau = 180$ and $\mathrm{Re}_\tau = 395$. For comparison purposes, we include results for the G-ROM (Section 2.2) and the ROM projection, which represents the best theoretical approximation of the FOM solution in the given ROM space.

A.1.1 $\mathrm{Re}_\tau = 180$

In Figure A.1, we plot the relative ℓ^2 error $\varepsilon_{u'u'}$ (4.20) for different ROM dimensions, N, and filter orders, m, for the G-ROM, the ROM projection, and the three Reg-ROMs at $\mathrm{Re}_\tau = 180$. Two sets of ROM-projection results are shown: The solid and the dotted lines represent the errors of $\langle u'u' \rangle_{\mathrm{Proj}}$ (4.26) for the snapshot data and the FOM data, respectively. It is expected that the error $\varepsilon_{u'u'}$ for the snapshot data is smaller than the error for the FOM data, because the POD basis set is constructed using only $K = 2000$ snapshots instead of using all the FOM solutions. For each Reg-ROM, the error is plotted for the optimal δ values and, for EFR-ROM and TR-ROM, for the optimal χ values that are trained to yield optimal $\langle u'v' \rangle$.

Figure A.1a displays the G-ROM results. This plot shows that, for all N values, the G-ROM results are very inaccurate. Even with $N = 100$, G-ROM fails to reconstruct $\langle u'u' \rangle$ with an error of $\mathcal{O}(10^5)$.

Figure A.1b displays the L-ROM results for each N and m, along with the results of the ROM projection for comparison purposes. For most N values, $m = 2$ yields the most accurate results among four m values except at $N = 10$ and $N = 40$ where $m = 1$ is better. Among the N and m values, we find $m = 2$ and $N = 60$ yields the smallest error $\varepsilon_{u'v'}$ (17%). This is different from what we found in the results of $\varepsilon_{u'v'}$ reported in Section 4.6.5 where $m = 1$ yields the most accurate results for $N \geq 30$. In addition, compared to the ROM projection, L-ROM is more accurate.

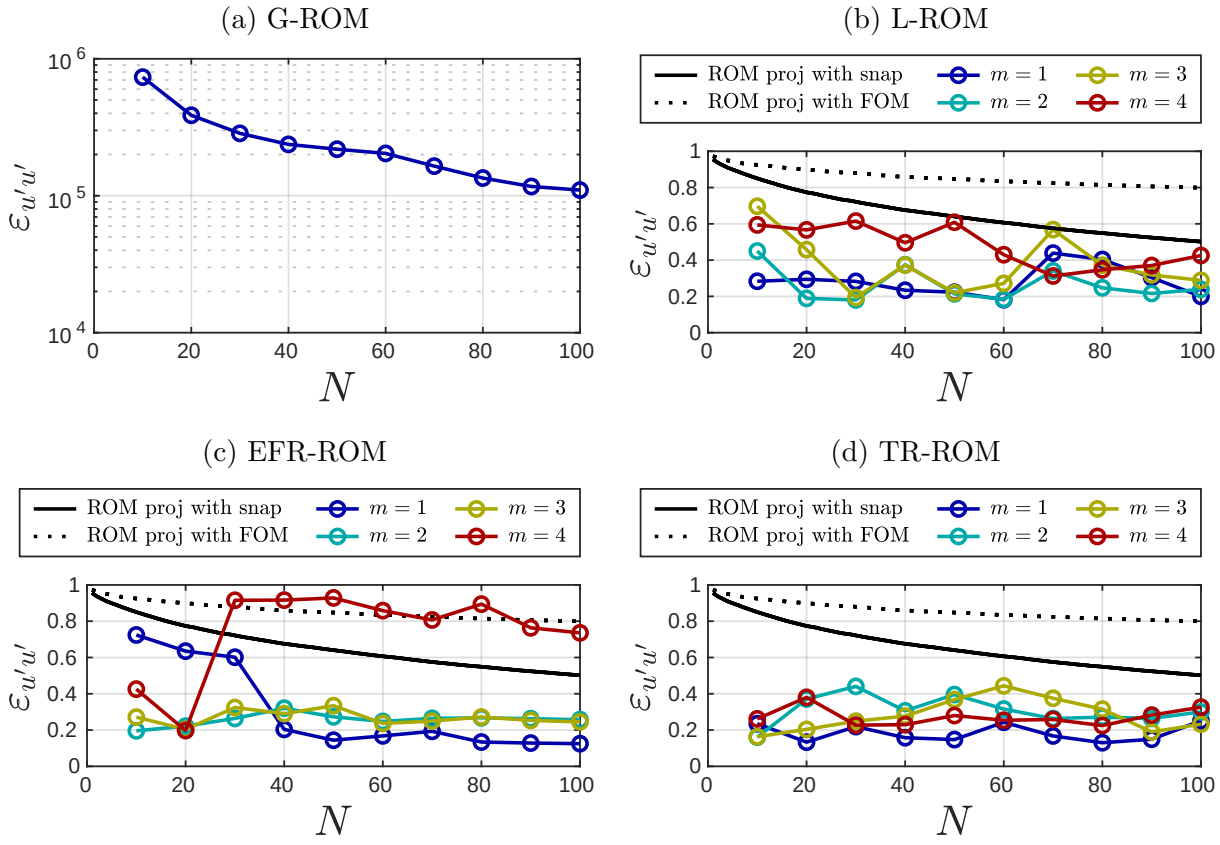

Figure A.1: The relative error $\varepsilon_{u'u'}$ (4.20) of G-ROM, ROM projection, L-ROM, EFR-ROM and TR-ROM in the *reproduction regime* at $\mathrm{Re}_\tau = 180$ for different N and m values with δ and χ values that are trained for optimal $\langle u'v' \rangle$.

Figure A.1c displays the EFR-ROM results for each N and m, along with the results of the ROM projection for comparison purposes. Compared to the results of $\varepsilon_{u'v'}$ in Fig. 4.9c, we find a similar behavior in $\varepsilon_{u'u'}$ for all N and m values and $\varepsilon_{u'u'}$ is smaller than $\varepsilon_{u'v'}$ for all N values with $m = 1,\ 2,\ 3$. For $N \geq 40$, $m = 1$ yields the most accurate results among four m values, achieving an error of 10% for $N = 90$. Conversely, for $N \leq 30$, higher-order filters perform better, with $m = 2$ resulting in 20% and 25% error for $N = 10$ and $N = 30$, respectively, and $m = 3$ in 18% error for $N = 20$.

In addition, EFR-ROM is more accurate than the ROM projection for all N with $m = 1,\ 2,\ 3$. With $m = 4$, it is only more accurate than the ROM projection for $N \leq 20$.

Figure A.1d displays the TR-ROM results for each N and m, along with the results of the ROM projection for comparison purposes. Compared to the results of $\varepsilon_{u'v'}$ in Fig. 4.9d, we find a similar behavior in $\varepsilon_{u'u'}$ for all N and m values but $\varepsilon_{u'u'}$ is smaller than $\varepsilon_{u'v'}$ for all N values only with $m = 1$. For $20 \leq N \leq 90$, $m = 1$ yields the most accurate results among four m values, achieving an error of 10% for $N = 80$. For $N = 10$ and $N = 100$, $m = 3$ achieving an error of 18% and 24%, respectively. In addition, TR-ROM is more accurate than the ROM projection for all N and m values.

A.1.2 $\mathbf{Re}_\tau = 395$

In Figure A.2, we plot the relative ℓ^2 error $\varepsilon_{u'u'}$ (4.20) for different N and m values for the G-ROM, the ROM projection, and the three Reg-ROMs at $\mathrm{Re}_\tau = 395$. Two sets of ROM-projection results for the snapshot data and the FOM data are shown.

Figure A.2a displays the G-ROM results. Just as in the $\mathrm{Re}_\tau = 180$, for all N values, the G-ROM results are very inaccurate. Even with $N = 100$, $\varepsilon_{u'u'}$ is still about $\mathcal{O}(10^5)$.

Figure A.2b displays the L-ROM results for each N and m, along with the results of the ROM projection for comparison purposes. Compared to the results of $\varepsilon_{u'v'}$ in Fig. 4.10b, we find a similar behavior in $\varepsilon_{u'u'}$ for all N and m values. In addition, the $\varepsilon_{u'u'}$ has similar magnitude compared to $\varepsilon_{u'v'}$. For all N and m values, the error is found to be much higher compared to the results for $\mathrm{Re}_\tau = 180$. For $N \geq 60$, the most accurate results are achieved with $m = 1$, with an error of 37% for $N = 60$. For $N = 10$, $m = 3$ achieves an error of 43%. Compared to the ROM projection, the L-ROM is more accurate for all values of N and m.

Figure A.2c displays the EFR-ROM results for each N and m, along with the results of the ROM projection for comparison purposes. Compared to the results of $\varepsilon_{u'v'}$ in Fig. 4.10c, we find a similar behavior in $\varepsilon_{u'u'}$ for all N and m values. In addition, the $\varepsilon_{u'u'}$ has similar magnitude compared to $\varepsilon_{u'v'}$. These results are qualitatively different from the EFR-ROM results for $\mathrm{Re}_\tau = 180$. For $N \leq 60$, $m = 1$ yields the most accurate results and achieves an error of 40% for $N = 40$. For $N \geq 70$, higher-order filter yields better results. Specifically, $m = 4$ achieves an error of 60% for $N = 80$. Moreover, the EFR-ROM is found to be more accurate than the ROM projection for all N with $m = 1$ and for $N \geq 40$ with $m = 3,\ 4$. With $m = 2$, the EFR-ROM only has a similar level of accuracy as the ROM projection.

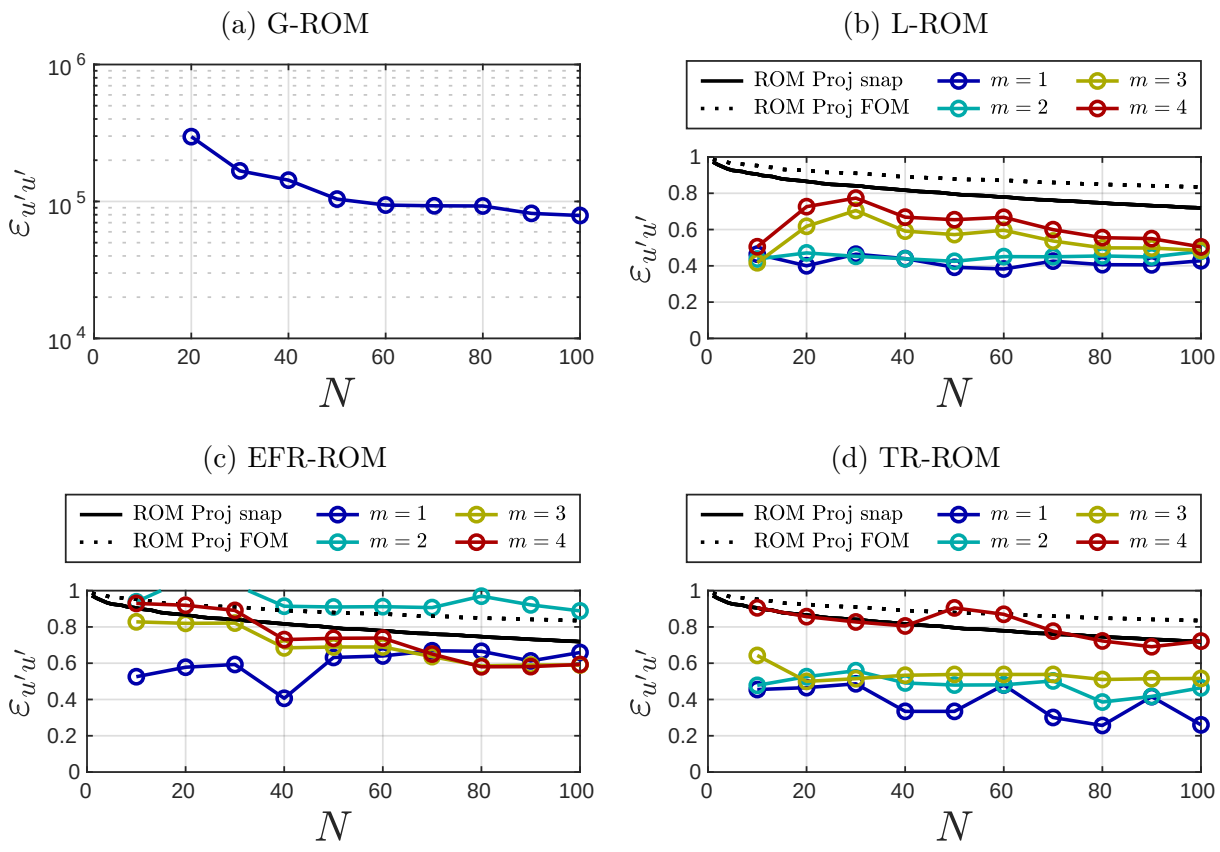

Figure A.2: The relative error $\varepsilon_{u'u'}$ (4.20) of G-ROM, ROM projection, L-ROM, EFR-ROM and TR-ROM in the *reproduction regime* at $\mathrm{Re}_\tau = 395$ for different N and m values with δ and χ values that are trained for optimal $\langle u'v' \rangle$.

Figure A.2d displays the TR-ROM results for each N and m, along with the results of the ROM projection for comparison purposes. Compared to the results of $\varepsilon_{u'v'}$ in Fig. 4.10d, we find a similar behavior in $\varepsilon_{u'u'}$ for all N and m values. However, with TR-ROM, we find the $\varepsilon_{u'u'}$ is smaller compared to $\varepsilon_{u'v'}$ for all N values with $m = 1$. For all N values, $m = 1$ yields the most accurate results, achieving an error of around 22% for $N = 100$. These results also show that $m = 2$ and $m = 3$ yield similar results, while $m = 4$ is found to be the least accurate. Moreover, the TR-ROM is found to be more accurate than the ROM projection for all N and m values.

In Fig. A.3, we compare the streamwise Reynolds normal stress $\langle u'u' \rangle$ of the optimal Reg-ROMs (listed in Table 4.1) along with the results of the FOM and the ROM projection in the reproduction regime for $\mathrm{Re}_\tau = 180$ and $\mathrm{Re}_\tau = 395$.

For $\mathrm{Re}_\tau = 180$, we find TR-ROM accurately predict the $\langle u'u' \rangle$ compared to the FOM.

On the other hand, L-ROM and EFR-ROM overpredict the peak values. For $\mathrm{Re}_\tau = 395$, we find the results of the TR-ROM are the best and it is better in capturing the profile outside the boundary layer compared to the L-ROM and the EFR-ROM. However, all three Reg-ROMs underpredict peak values compared to the FOM. Although the results of the Reg-ROMs are not perfect, we find the results are much better than the ROM projection. This also indicates that $N = 100$ POD bases are not able to reconstruct the Reynolds stress.

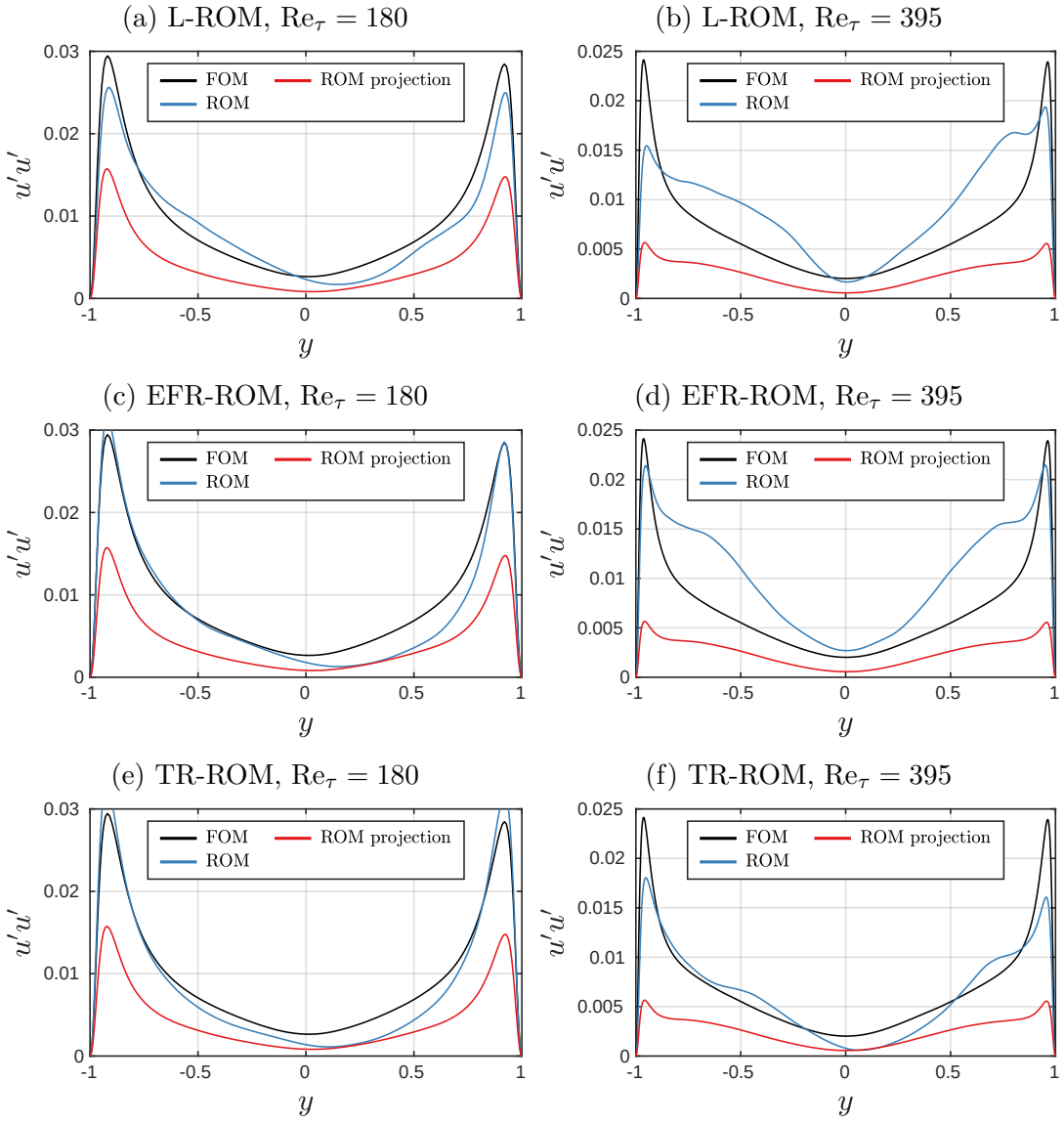

Figure A.3: Comparison of the streamwise Reynolds normal stress $\langle u'u' \rangle$ of the FOM (black), the ROM projection (red) and the optimal Reg-ROMs, listed in Table 4.1 (blue) in the *reproduction regime* for $\mathrm{Re}_\tau = 180$ (left) and $\mathrm{Re}_\tau = 395$ (right).

A.2 Predictive Regime

In this section, we report the results of the streamwise Reynolds normal stress $\langle u'u' \rangle$ for the three Reg-ROMs: L-ROM (Section 4.1), EFR-ROM (Section 4.2), and the new TR-ROM (Section 4.3) for the *predictive regime*, a time interval that is 500 CTUs larger than the snapshot collected time interval, at $\mathrm{Re}_\tau = 180$ and $\mathrm{Re}_\tau = 395$.

A.2.1 $\mathrm{Re}_\tau = 180$

In Figure A.4, we plot the relative ℓ^2 error $\varepsilon_{u'u'}$ (4.20) for different N and m values for the G-ROM, the ROM projection, and the three Reg-ROMs at $\mathrm{Re}_\tau = 180$. We emphasize that, we plot the error for $(\delta,\ \chi)_{\text{reprod}}$ that were optimized in the *reproduction regime* (Section 4.6.5).

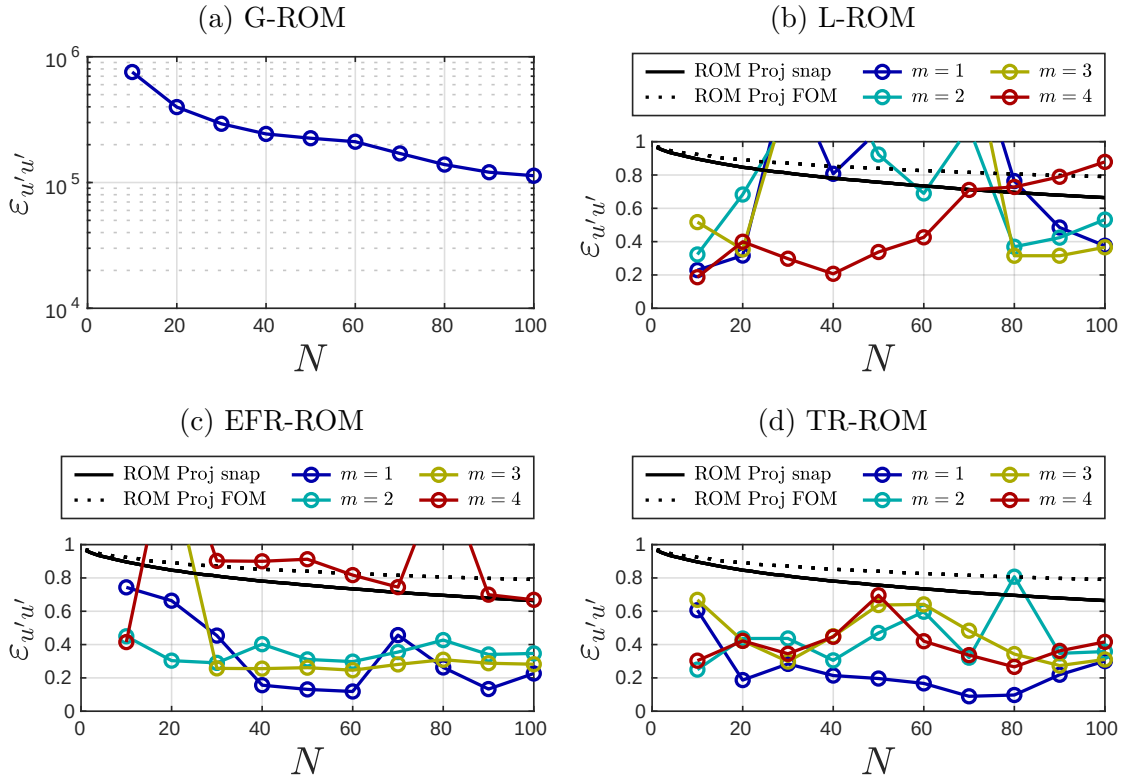

Figure A.4: The relative error $\varepsilon_{u'u'}$ (4.20) of G-ROM, ROM projection, L-ROM, EFR-ROM and TR-ROM in the *predictive regime* at $\mathrm{Re}_\tau = 180$ for different N and m values with δ and χ values *optimized in the reproduction regime* for $\langle u'v' \rangle$.

Figure A.4a displays the G-ROM results. As in the reproduction regime, for all N values, the G-ROM results are very inaccurate.

Figure A.4b displays the L-ROM results for each N and m with δ_{reprod} along with the ROM projection results for comparison purposes. Compared to the results of $\varepsilon_{u'v'}$ in Fig. 4.12b, we also find the behavior of $\varepsilon_{u'u'}$ is sensitive to changes in N across all m values compared to the results observed in the reproduction regime. Except for $N = 20$, higher order filter (i.e., larger m) yields better results, achieving an error of 18% for $N = 10$ and $m = 4$. For the majority of N and m values, we find L-ROM is less accurate than the ROM projection.

Figure A.4c displays the EFR-ROM results for each N and m with $(\delta,\ \chi)_{\text{reprod}}$ along with the ROM projection results for comparison purposes. Compared to the results of $\varepsilon_{u'v'}$ in Fig. 4.13c, we find a similar behavior in $\varepsilon_{u'u'}$ for all N and m values. In addition, $\varepsilon_{u'u'}$ is in general smaller compared to $\varepsilon_{u'v'}$. For $N \leq 30$, $m > 1$ yields better results and achieves an error of 22% for $N = 30$ with $m = 3$. For $N \geq 40$, except at $N = 70$, $m = 1$ yields the most accurate results, achieving an error of 10% for $N = 60$. In addition, compared to the ROM projection, EFR-ROM is more accurate for $m \leq 3$, except for $N = 10$ and $N = 20$ with $m = 3$. For $m = 4$, EFR-ROM is not accurate and has a similar level of accuracy as the ROM projection.

Figure A.4d displays the TR-ROM results for each N and m with $(\delta,\ \chi)_{\text{reprod}}$ along with the ROM projection results for comparison purposes. Compared to the results of $\varepsilon_{u'v'}$ in Fig. 4.12d, we find a similar behavior in $\varepsilon_{u'u'}$ for all N and m values. For $N = 10$, $m = 2$ yields the best results with an error of 22% and for $N \geq 20$, $m = 1$ yields the best results among four m values, achieving an error less than 10% for $N = 70$. In addition, TR-ROM is more accurate than the ROM projection for all N and m values.

A.2.2 $\mathbf{Re}_\tau = 395$

In Figure A.5, we plot the relative ℓ^2 error $\varepsilon_{u'u'}$ for different N and m values for the G-ROM, the ROM projection, and the three Reg-ROMs at $\text{Re}_\tau = 395$. We emphasize that, to test the predictive capabilities of the Reg-ROM parameters, we plot the error for $(\delta,\ \chi)_{\text{reprod}}$ that were optimized in the *reproduction regime* (Section 4.6.5).

Figure A.5a displays the G-ROM results. Just as in Section 4.6.6, for all N values, the G-ROM results are very inaccurate with an error of $\mathcal{O}(10^5)$ for $N = 100$.

Figure A.5b displays the L-ROM results for each N and m with δ_{reprod}, along with the ROM projection results for comparison purposes. Compared to the results of $\varepsilon_{u'v'}$ in Fig. 4.13b, we find a similar behavior in $\varepsilon_{u'u'}$ for all N and m values. For $N = 20,\ 30$ and 40, $m = 2$ yields the most accurate results among four m values and for the rest of the N values, $m = 1$ yields the most accurate results.

Among the N and m values, $m = 1$ with $N = 50$ yields the best error of 39%. For $m = 3$ and $m = 4$, the accuracy of L-ROM is improved as N increases but is still larger than the $m = 1$ case. In addition, compared to the ROM projection, L-ROM is more accurate except for the (m, N) pairs $(2, 10), (3, 20), (3, 30), (4, 20)$, and $(4, 30)$.

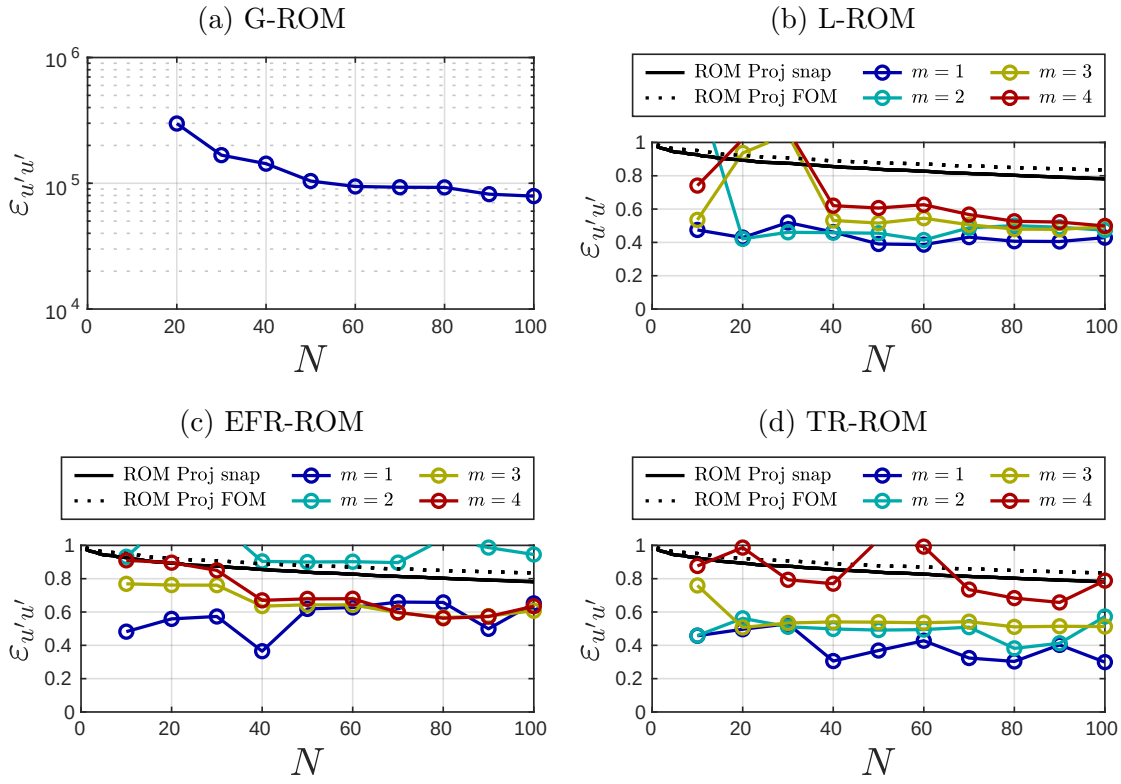

Figure A.5: The relative error $\varepsilon_{u'u'}$ (4.20) of G-ROM, ROM projection, L-ROM, EFR-ROM and TR-ROM in the *predictive regime* at $\mathrm{Re}_\tau = 395$ for different N and m values with δ and χ values *optimized in the reproduction regime* for $\langle u'v' \rangle$.

Figure A.5c displays the EFR-ROM results for each N and m with $(\delta,\ \chi)_{\text{reprod}}$ along with the ROM projection results for comparison purposes. Compared to the results of $\varepsilon_{u'v'}$ in Fig. 4.13c, we find a similar behavior in $\varepsilon_{u'u'}$ for all N and m values. For $N \leq 60$, $m = 1$ yields the most accurate results, achieving an error of 39% for $N = 40$. For $N \geq 70$ except for $N = 90$, a higher-order filter yields better results. In particular, $m = 4$ achieves an error of 60% for $N = 80$. For $N = 90$, $m = 1$ achieves an error of 48%. Compared to the ROM projection, EFR-ROM is more accurate for all N values and $m = 1,\ 3,\ 4$. For $m = 2$, EFR-ROM is in general less accurate than the ROM projection the ROM projection.

Figure A.5d displays the TR-ROM results for each N and m with $(\delta,\ \chi)_{\text{reprod}}$, along with the ROM projection results for comparison purposes.

Compared to the results of $\varepsilon_{u'v'}$ in Fig. 4.13d, we find a similar behavior in $\varepsilon_{u'u'}$ for all N and m values. For all N values except $N = 10$ and $N = 30$, $m = 1$ yields the most accurate results, achieving an error of around 28% for $N = 100$. These results also show that $m = 2$ and $m = 3$ yield similar accuracy and $m = 4$ is the least accurate. Compared to the ROM projection, TR-ROM is more accurate for all N and m values, except for (m, N) pairs, $(4, 50)$ and $(4, 60)$.

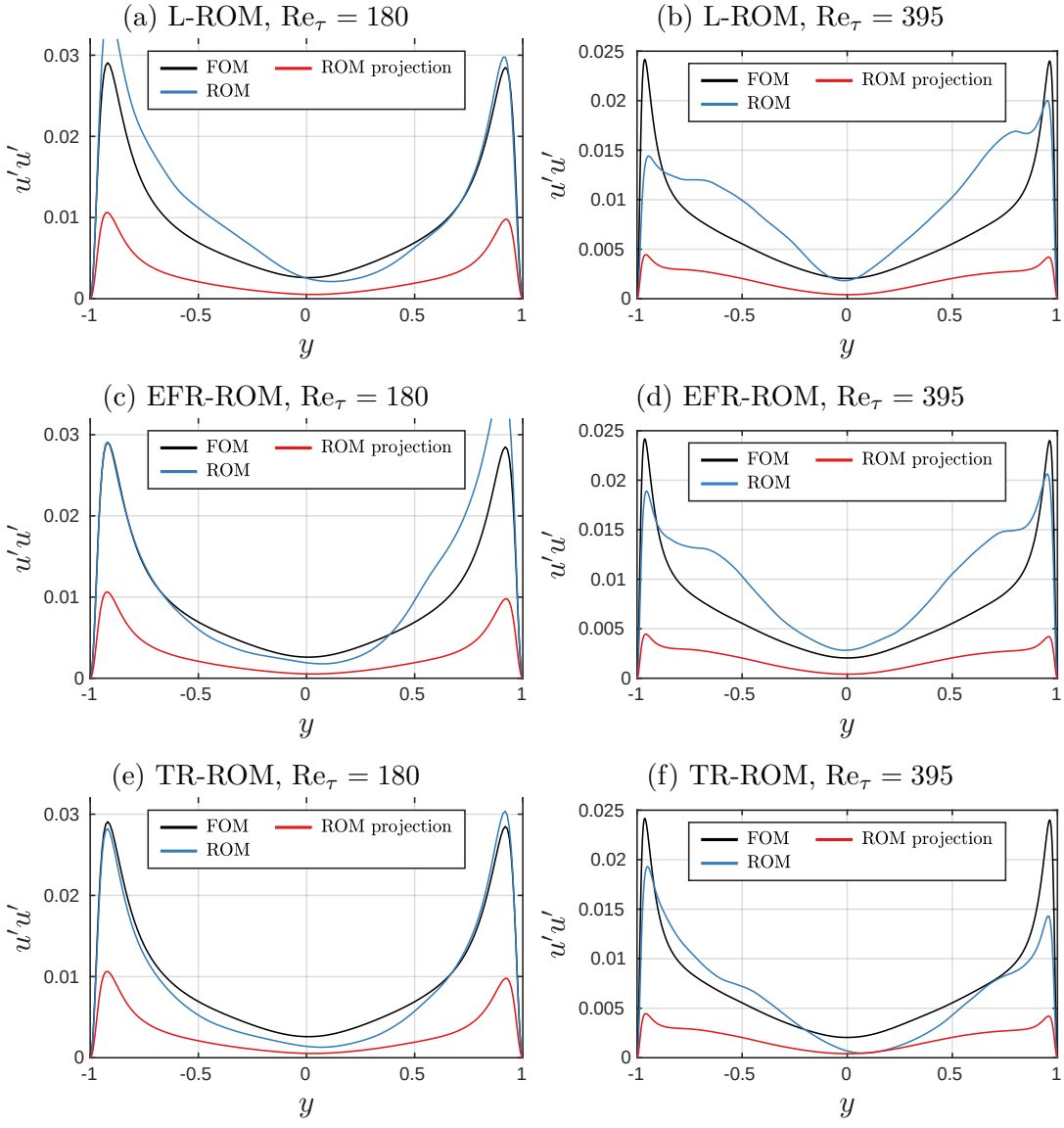

Figure A.6: Comparison of the streamwise Reynolds normal stress $\langle u'u' \rangle$ of the FOM (black), the ROM projection (red) and the optimal Reg-ROMs, listed in Table 4.2 (blue) in the *predictive regime* for $\mathrm{Re}_\tau = 180$ (left) and $\mathrm{Re}_\tau = 395$ (right).

Similarly to the reproduction regime (Fig. A.3), in Fig. A.6, we compare the streamwise Reynolds normal stress $\langle u'u' \rangle$ of the optimal Reg-ROMs (listed in Table 4.2) along with the results of the FOM and the ROM projection in the predictive regime for $\mathrm{Re}_\tau = 180$ and $\mathrm{Re}_\tau = 395$.

For $\mathrm{Re}_\tau = 180$, we find TR-ROM accurately predict the $\langle u'u' \rangle$ compared to the FOM whereas the L-ROM and EFR-ROM overpredict the peak values. For $\mathrm{Re}_\tau = 395$, we again find the results of the TR-ROM are the best and it has better agreement outside the boundary layer compared to the L-ROM and the EFR-ROM. However, all three Reg-ROMs underpredict peak values compared to the FOM. Although the results of the Reg-ROMs are not perfect, we find the results are much better than the ROM projection.